Miloš Petrović

Use of Soft Layers for Seismic Response Modification of Structural Masonry Walls

PhD Dissertation, 2018

DISS. ETH NO. 25092

USE OF SOFT LAYERS FOR SEISMIC RESPONSE MODIFICATION OF STRUCTURAL MASONRY WALLS

A thesis submitted to attain the degree of

DOCTOR OF SCIENCES of ETH ZURICH

(Dr. sc. ETH Zurich)

presented by

MILOŠ PETROVIĆ

MSc, Civil Engineering

Faculty of Civil Engineering of the University of Belgrade, Serbia

born on 29.06.1986

citizen of Serbia

accepted on the recommendation of

Prof. Dr. Božidar Stojadinović (ETH Zurich, Examiner)

Dr. Nebojša Mojsilović (ETH Zurich, Co-examiner)

Prof. Dr. Guido Magenes (University of Pavia, Co-examiner)

2018

Contents

IV

Abstract

The development of the sliding-based modification method for the seismic in-plane behavior of structural unreinforced masonry (URM) walls is the objective of the present research project. This objective is achieved by using engineered deformable (soft) layers, which are already implemented in URM walls, placed at the bottom and/or the top of the wall, however, for the sake of providing a moisture barrier in the form of a damp-proof course membrane, ensuring sound insulation or accommodating the short-term or long-term differential movements between the masonry walls and the floor and ceiling construction. After a comprehensive review of work on response of masonry walls that develop sliding, with a special attention paid to studies on the shear behavior of URM with incorporated soft layers, and after selecting the soft layers from those available on the Swiss market, an experimental investigation was conducted. The first part of the experimental investigation was aimed at providing the information on the in-plane compressive and shear behavior of masonry with a so called multi-layer bed joint, i.e. with a (core) soft layer protected by two layers of elastomer before placed in the middle of the mortar bed joint. The main reason for protecting the core soft layers was to reduce the potential cyclic shear loading-caused damage, i.e. to insure durability of the soft layer bed joint. The second part of the experimental investigation comprised a series of static-cyclic tests on full-scale structural masonry walls with a multi-layer bottom bed joint that were conducted in two phases. The preliminary phase was aimed at determining the most suitable type of core soft layer for the main testing phase. Within the main phase, the influences of the pre-compression level, the aspect ratio and the size effect on the behavior of URM walls with a multi-layer bed joint were investigated. The results obtained indicate that the load-bearing URM walls with a multi-layer bed joint, in spite of the prevailing sliding response, could exhibit a significant shear capacity, which depends on the type of core soft layer material, the applied level of pre-compression and on the loading speed. As compared to the walls without a multi-layer bed joint, URM walls with a multi-layer bed joint have a smaller initial stiffness. Importantly, the multi-layer bed joints provide a significantly large ultimate displacement capacity to the URM walls, thus modifying and improving their seismic response. The ultimate displacement capacity is, however, strongly influenced by the extent of shear cracks that develop in the wall, the occurrence of tensile cracks in the head joints at the bottom block course, and reduction of the

effective area of the wall. In general, it can be concluded that multi-layer bed joints in URM walls act to modify the seismic response of URM structures and improve their seismic performance.

To support design of URM walls with multi-layer bed joints, a method to construct an idealization of the horizontal force-displacement response envelope for the tested URM walls with multi-layer bed joints is proposed. The parameters of this envelope are defined to capture the strength, stiffness and ultimate displacement capacity of the walls, as well as to model sudden drops in wall horizontal force resistance caused by the reduction of the wall effective area. Further, a mechanics-based analytical model of the loading speed-dependent in-plane shear behavior of the masonry multi-layer bed joint with a rubber granulate core soft layer is developed. The model is developed by assuming the elastic-perfectly viscoplastic behavior of the multi-layer bed joint. This model is further extended to describe the horizontal force-displacement behavior of URM walls with a rubber granulate core soft layer in the multi-layer bottom bed joint and validated against the experimental results.

A supplementary investigation on the interaction between the in-plane and transverse URM walls with soft layers that can be regarded as a common element of the URM structures is presented in the last part of the thesis. Two series of static-cyclic shear tests on I-shaped (flanged) URM wallettes with a rubber granulate soft layer in the bottom bed joint were performed. The flanges considerably increased the horizontal force resistance and the initial stiffness of URM wallettes, however, they restrained the motion of the web of the wallettes to some extent, which was detrimental to realizing the intended seismic response modification purpose of the soft layer in bottom bed joints.

Zusammenfassung

Dieses Forschungsprojekt hat das Ziel, eine auf das Gleiten basierte Modifizierungsmethode für das seismische Verhalten in der Ebene (in-plane) beanspruchter, unbewehrter Mauerwerkswände (URM-Wände) zu entwickeln. Dieses Ziel wird durch die Anbringung verformbarer Auflagen, sog. „soft layers", erreicht. Solche Auflagen werden üblicherweise aus Gründen der Gebrauchstauglichkeit (Feuchtigkeitssperrschicht, Schalldämmung, Aufnahmeelemente der kurz- und langfristigen Differenzialbewegungen zwischen Mauerwerkswänden und Decken) eingesetzt. Eine experimentelle Untersuchung wurde nach einer gründlichen Literaturdurchsicht zum Gleitverhalten der URM-Wände durchgeführt. Für diese Untersuchung wurden diverse Auflagen, die auf dem Schweizer Markt erhältlich sind, berücksichtigt. Der erste Teil der experimentellen Untersuchung basierte auf dem „in-plane" Druck- und Schubverhalten des unbewehrten Mauerwerks mit einer mehrschichtigen Lagerfuge. Bei diesem Lagerfugentyp wird die Kernauflage durch zwei in der Mitte der Mörtellagerfuge platzierten Elastomer-Auflagen geschützt. Dies hat den Hintergrund, dass eine allfällige Beschädigung durch die zyklische Schubbeanspruchung reduziert wird und somit die Dauerhaftigkeit der mehrschichtigen Lagerfuge gewährleistet wird. Der zweite Teil der experimentellen Untersuchung umfasste zwei Phasen von statisch-zyklischen Versuchen an den URM-Wänden mit mehrschichtigen Fusslagerfugen. Die erste Phase (Vorphase) diente zur Festlegung eines geeigneten Kernauflagetyps, welches anschliessend in der zweiten Phase (Hauptphase) eingesetzt wurde. In der Hauptphase wurde der Einfluss des Druckvorspannungsniveaus, der Wandgeometrie und des Massstabeffekts auf das Verhalten der unbewehrten Mauerwerkswände mit den mehrschichtigen Fusslagerfugen untersucht. Die Ergebnisse zeigen an, dass URM-Wände mit mehrschichtigen Fusslagerfugen trotz des vorherrschenden Gleitens einen bedeutenden Schubwiderstand aufweisen können. Der Typ der Kernauflage, das Druckspannungsniveau und die Belastungsgeschwindigkeit spielen dabei eine entscheidende Rolle. URM-Wände mit mehrschichtigen Fusslagerfugen weisen im Vergleich zu jenen ohne Fusslagerfugen eine kleinere Horizontalsteifigkeit auf. Zudem erlauben die mehrschichtigen Lagerfugen grosse Verformungsvermögen bei den unbewehrten Mauerwerkswänden, sodass das seismische Verhalten solcher Wände günstig beeinflusst wird. Es ist jedoch zu beachten, dass das

Verformungsvermögen stark vom Ausmass der Schubrisse und der Zugrissbildung in den Stossfugen innerhalb der untersten Wandschicht abhängig ist. Allgemein lässt sich festhalten, dass die mehrschichtigen Lagerfugen bei unbewehrten Mauerwerkswänden das seismische Verhalten von Mauerwerksbauten modifizieren und ihre seismische Performance verbessern.

Eine Methode zur Idealisierung der Horizontalkraft-Verschiebungskurven der geprüften URM-Wände mit mehrschichtigen Fusslagerfugen wird vorgeschlagen, die den Anwender während der Bemessung unterstützen soll. Weiter werden die Parameter dieser Idealisierung definiert, um den Schubwiderstand, die Horizontalsteifigkeit und das Verformungsvermögen der Wände zu ermitteln sowie um plötzliche Absenkungen des Schubwiderstands zu modellieren, die durch die Reduktion der effektiven Wandfläche verursacht werden. Zusätzlich wird ein mechanisches Modell zur Abbildung des von der Belastungsgeschwindigkeit abhängigen Schubverhaltens der mehrschichtigen Mauerwerkslagerfuge mit der Gummigranulat-Kernauflage präsentiert. Dieses Modell beruht auf der Annahme, dass die mehrschichtigen Mauerwerkslagerfugen sich elastisch-perfekt plastisch verhalten. Um das Kraft-Verformungsverhalten der URM-Wände mit den mehrschichtigen Fusslagerfugen beschreiben zu können, wird dieses Modell erweitert und gegen die eigenen Versuchsresultate validiert.

Im letzten Teil dieser Doktorarbeit wird eine ergänzende Untersuchung über die Interaktion zwischen den „in-plane"- und „out-of-plane"-Mauerwerkswänden mit den verformbaren Auflagen dargelegt. Diese Interaktion, bzw. der Verbund zwischen den „in-plane"- und „out-of-plane"- Mauerwerkswänden kann als ein typisches tragendes Element der unbewehrten Mauerwerksbauten betrachtet werden. Insgesamt wurden zwei Serien der statisch-zyklischen Schubversuche an den I-förmigen (geflanschten) URM-Wänden mit den verformbaren Auflagen in den Fusslagerfugen durchgeführt. Die Flansche erhöhen zwar den Querkraftwiderstand und die anfängliche Horizontalsteifigkeit der URM-Wände beträchtlich, beschränken jedoch die Gleitbewegung des Stegs von der Wand, was für die Realisierung der beabsichtigten seismischen Modifikation der verformbaren Auflagen in den Fusslagerfugen ungünstig ist.

Acknowledgments

1 Introduction

1.1 Research motivation

Masonry, thanks to its versatility, high availability, good construction speed, thermal properties and overall cost effectiveness, represents one of the most traditional and widely used construction methods. It is well known that masonry structures are seismically vulnerable and often undergo heavy damage during earthquakes, potentially causing the most fatalities and presenting the biggest obstacle to the post-earthquake recovery of communities. This is a result of several factors that characterize masonry, such as short building vibration periods, large mass, inherent brittleness, lack of tensile strength, lack of ductility etc. Such risks posed by (quasi) brittle masonry structures exposed to seismic hazard have been recognized since ancient times. Looking through the history of the use of masonry structures, several design concepts were developed to improve the seismic behavior of masonry structures and mitigate the seismic risk they pose. Those concepts were either conventional ones, based on preventing collapse by rational strengthening arrangements while allowing for more or less damage to the structural and non-structural components, or the non-conventional ones based on seismic response modification techniques.

Seismic base isolation, now a mature seismic response modification method, consists of decoupling a structure from its base to reduce the effects of the earthquake ground motion. This method is based on diminishing the extent of damage to structures which can be caused by strong earthquakes by introducing a horizontal very deformable base isolation system, i.e. specially designed bearings or other devices at the base level of the structure to allow motion. Deformability of the base isolation system shifts the fundamental period of the isolated structure to a range that is above the predominant period of earthquake ground motion. Moreover, a considerable part of the earthquake input energy is absorbed if hysteretic or viscous energy dissipation devices are installed at the base level of the structure. In this way, both the lateral forces and displacement ductility demand to the elements of the structure are greatly reduced, thus protecting them from damage.

Many base isolation systems utilize multi-layer, laminated rubber elastomeric bearings with steel reinforcing layers. Some isolation systems, particularly those used in

New Zealand and Japan, combine natural rubber bearings with low internal damping and some form of mechanical damper [1]. In the United States the most commonly used isolation system is the lead-plug rubber bearing. These bearings are multi-layer, laminated elastomeric bearings with lead plugs inserted into one or more circular holes to incorporate damping into the isolation system. In spite of capability to successfully limit the earthquake input energy transferred to the structure, many of these systems turned out to be too complex for implementation and/or maintenance, or just too expensive for application in masonry structures, particularly in developing countries. As stated in [2], a seismic isolation system (scheme) for masonry structures is supposed to meet the following requirements: earthquake input energy transferred from the ground to a superstructure should be controlled and limited to the desired level; the scheme should be as simple as possible, feasible for construction at any site location, and by trained but no more skilled labor than for the conventional building construction; and the proposed solution should be cost-effective, as compared to the cost expenses of traditional seismic strengthening arrangements.

An alternative seismic base isolation method, that satisfies all the above-mentioned requirements, is The Pure-Friction Seismic Isolation (PFSI). This method was first proposed by medical doctor Johannes Calantarients in England more than one century ago [1]. PFSI is based on placing the friction isolation materials and/or friction isolation devices between the superstructure and the substructure, i.e. on decoupling the superstructure from its base by means of a friction-sliding joint. Depending on the shape of the friction-sliding joint (surface), the PFSI system can be classified as a continuous or discrete system, see [2]. In principle, this isolation system utilizes friction, while allowing for relative sliding between parts of the structure in the course of an earthquake. Such relative movement in the friction-sliding joint restricts the transmission of seismic waves to the superstructure by dissipating some part of the input seismic energy through friction. However, this system is not without its drawbacks. Fairly high values of frictional coefficient may be required to provide adequate resistance and avoid unnecessary movement under small earthquakes and wind load. Many frictional surfaces have friction characteristics sensitive to vertical (pre-compression) load and to the sliding (loading) speed. Furthermore, any sudden change in the stiffness of the overall structure, e.g. when slipping or sticking occurs, results in high-frequency vibrations in the structure, i.e.

2

vibrations at frequencies that might not be present in the ground motion. Another problem with using PFSI system is the lack of effective restoring force.

1.2 Research objective

The central idea of this research project was to modify the seismic response of individual structural unreinforced masonry (URM) walls by placing engineered deformable (soft) layers in the bottom bed joint of such masonry walls. The idea of using soft layers is an innovative approach to modify the seismic response of URM walls, aimed toward improving the behavior of masonry structures during earthquakes. Soft layers, mainly based on rubber, bitumen, cork or polyvinylchloride (PVC), are already used in Swiss as well in international URM construction. However, the purpose of implementing such layers is unrelated to seismic actions. Soft layers are mainly placed at the base of masonry walls to provide a moisture barrier in the form of a damp-proof course (DPC) membrane, to ensure sound insulation or to accommodate short- or long-term differential movements between the walls and the floors and ceilings, see Figure 1-1. Although it is desirable for the soft layer to be sandwiched in the mortar bed joint, in reality it is usually placed above or below the bed joint mortar. In some cases, such as when it is used as a slip joint, the layer is placed without any mortar.

Figure 1-1. Use of soft layers in Swiss URM construction (from http://www.mageba-group.com)

Results from the preliminary research on masonry elements with a rubber granulate and elastomer based soft layers in bottom bed joints, see [3], indicate that the presence of such layers in the mortar bed joint can significantly alter the mechanical characteristics of URM walls by creating a sliding plane, which, in turn, could influence the seismic response of the entire structure. It appears that the bed joint with a soft layer,

with adequate material properties, could change the typical brittle in-plane shear response of masonry wall to a more desirable quasi-ductile one, and provide for considerable energy dissipation, i.e. to provide the behavior which is desirable for enhanced seismic performance.

In order to develop the basic engineering knowledge for use of soft layers to improve the seismic performance of structural URM structures, a comprehensive experimental investigation was needed both at the material level, i.e. at the level of URM with a soft layer bed joint, as well at the structural element level, i.e. at the level of URM wall with a multi-layer bed joint. The principal research objective was to investigate if the structural unreinforced masonry walls with such soft layers could enable the masonry structure to achieve the following target performance goals in regions of low and moderate seismicity: 1) experience essentially no damage in frequent earthquakes and under high wind loads when the structure is expected to remain elastic; 2) experience controlled damage in design-basis earthquakes through an elongation of the structural response period due to relatively low stiffness in the pre-sliding regime and the stable lateral sliding deformation; and 3) collapse prevention in beyond-design-basis earthquakes through preserving the gravity load-carrying capacity of the structural masonry walls. This research objective was achieved.

1.3 Research approach

The conducted research was focused on developing the basic engineering knowledge for use of soft layers to improve the seismic performance of structural URM walls. The project comprised the following three phases:

1. Investigation of the mechanical properties of soft layers required to achieve the desired performance of structural masonry walls with such layers;
2. Conduct of quasi-static cyclic material- and structural element-level tests to prove the concept and to experimentally investigate the soft layer parameter space;
3. Development of the mechanical model to accurately describe the seismic in-plane response of structural masonry walls with soft layers.

The first research phase was centered on a comprehensive review of work on response of masonry walls that develop sliding, research on low-friction sliding surfaces and thin deformable rubber or polymer layers, as well as the research on seismic isolation

4

of entire masonry structures using engineered and non-engineered pure friction-sliding systems. Special attention was paid to studies on the shear behavior of URM with incorporated soft layers such as soft layer wall bearings and sound and moisture isolation layers made of rubber, cork, plastic and various composite materials. The soft layer mechanical parameter space defined in the first phase was considered in the second phase to select a total of five soft layers from those available on the Swiss market, and to design a portfolio of small masonry specimens (wallettes and triplets) tested to provide the information on the in-plane compressive and shear behavior of masonry with a soft layer incorporated in the bed joint. A rubber granulate, cork-rubber granulate, cork, bitumen and PVC based soft layers were selected. In order to reduce the damage caused by cyclic shear loading, as indicated by the preliminary research, i.e. to insure durability of the soft layer bed joint, all (core) soft layers were protected by two layers of elastomer before placed in the middle of the mortar bed joint, thus making a so-called multi-layer bed joint. Afterwards, a series of static-cyclic tests on full-scale structural masonry walls with a multi-layer bottom bed joint were conducted in two phases. Preliminary phase comprised of four static-cyclic shear tests on 1600 mm high and 1500 mm long, full-scale URM walls. This phase was aimed at determining the most suitable type of core soft layer for the main testing phase. Within the main phase, additional five tests were performed on one-story-high, masonry walls to investigate the influences of the pre-compression level, aspect ratio and size effect on the behavior of URM walls with a multi-layer bed joint. Herein, the rubber granulate was chosen as a core soft layer based on the best overall behavior and seismic performance exhibited within the preliminary testing phase. The last part of the research was directed towards the development of the mechanics-based analytical model to describe, as it appeared, the loading speed-dependent in-plane shear response of the multi-layer bed joint. The model is developed by assuming the elastic-perfectly viscoplastic behavior of a multi-layer bed joint and calibrated for multi-layer bed joints with a rubber granulate core soft layer. Further, the model is extended to be used in URM walls and shows ability to predict the resistance as well to describe the in-plane force-displacement response of URM walls with a multi-layer bed joint with satisfactory accuracy.

1.4 Research significance

The scientific significance of the conducted research lies in establishing the theoretical model framework for predicting of the in-plane behavior of structural URM with a multi-layer bottom bed joint subjected to seismic actions. Since, at a fundamental level very little research in this area has been conducted and reported in the literature, thus leaving numerous theoretical and practical questions unanswered, findings obtained within this research improve this situation considerably. The engineering significant of the conducted research is developing a multi-layer sliding bed joint layer for URM walls that has the mechanical characteristics to facilitate the intended improvement of the seismic response of URM walls by significantly increasing their deformation capacity while maintaining their ability to carry gravity load.

Since the society has only limited resources, it is of the utmost importance to ensure that these resources are used in the most efficient manner possible to ensure a good quality of life. Moreover, it is important to do this in a sustainable way such that the future generations do not carry the burden of today's society. This research was about developing the seismic in-plane response modification of structural masonry walls to make masonry buildings, made using such walls, significantly safer during earthquakes and better suited to fulfil their shelter-in-place function after earthquakes at a minimum increase in cost, environmental burden, and change in current construction practice. It is believed that the findings of the conducted research could contribute for a more efficient allocation of the limited economical resources on construction activities and help preserve the environment by promoting unreinforced structural masonry as an environment-friendly building material of choice for housing and for small to medium office buildings in regions of low and moderate seismic hazard.

1.5 Thesis outline

This thesis is organized into 6 chapters. Chapter 1 comprises the above presented introduction with the research motivation, objective, approach and significance. Chapter 2 summarizes the previous experimental and theoretical work on the response of masonry walls that develop sliding, with a special attention on studies on the shear behavior of URM with incorporated soft layers such as soft layer wall bearings and sound and moisture isolation layers made of rubber, cork, plastic and various composite materials. The results

of an extensive experimental work on the in-plane shear behavior of URM elements with a multi-layer bed joint, as well discussion of the test outcomes, are given in Chapter 3. Chapter 4 presents a mechanical model of the in-plane force-displacement response of the URM walls with a multi-layer bed joint. The behavior of the I-shaped URM walls with a rubber granulate soft layer in the bottom bed joint, subjected to the in-plane static-cyclic shear load is addressed in Chapter 5. A detailed summary as well the conclusions are provided at the end of each Chapter. Finally, Chapter 6 provides the brief summary of the findings as well as the recommendations for future research.

2 Literature review

2.1 Introduction

Risk posed by quasi-brittle URM structures when exposed to seismic hazard has been recognized since ancient times. Different seismic isolation methods were developed to enhance the seismic performance of URM structures and mitigate the seismic risk they pose. This chapter summarizes the previously conducted research on PFSI systems for URM structures, based on engineered and non-engineered masonry joints enabling friction-sliding behavior. In order to provide a useful database of available test results and to identify the governing parameters, special attention was devoted to studies on the shear behavior of URM with incorporated soft layers such as soft layer wall bearings and sound and moisture isolation layers. The findings presented within this chapter have already been partly published in [4,5].

2.2 Pure friction seismic isolation systems for URM structures

It can be said that PFSI is the seismic response modification method which evolved from on-site observations of masonry structural response to severe earthquakes. A friction-sliding was documented as the primary mechanism that significantly reduced building damage in earthquakes in India that occurred between 1897 and 1950 in Assam, see [6]. Similar was documented after series of earthquakes occurred in China between 1960 and 1976, see [7]. Two three-story masonry buildings, designated as building No. 3 and No. 4, were only 10 m apart and exposed to the same soil condition. After a strong Tangshan earthquake (July 26th, 1976), building No. 3 survived, but No. 4 was reduced to rubble. The reason for such contrast was found in the continuous horizontal crack at the base of the walls of the surviving building, which was probably formed at the beginning of the earthquake and permitted the whole building to slide on it. Another example is Sanjusangen-do Buddhist Temple in Kyoto built on the horizontal sliding surface comprised of superimposed layers of sand and clay. It stood for more than 750 years though it has experienced many strong earthquakes, see [8]. Inspired by these observations, research workers started studying a friction-sliding as a method of base isolation to achieve better performance of masonry structures during earthquakes. Some selected experimental studies are presented in following.

Qamaruddin et al. [9] reported results of pilot shaking table tests, performed as a part of feasibility study of the PFSI method on two small, one-fourth scale, single room masonry building models. Different sliding materials such as graphite powder, dry sand, and wet sand were used, placed between the building models and their bases. The specimens were exposed to a horizontal motion with a frequency ranging between 8 Hz and 26 Hz. The recorded sliding displacement and acceleration values at the base and at the roof level of the specimens are summarized in Table 2-1. It can be seen that, as compared to the fixed-base model, in case of base isolated models there were no amplifications of roof acceleration, thus indicating a significant reduction of the effective seismic force.

Table 2-1. Results of the tests conducted on one-fourth scale building models (Qamaruddin et al. [9])

Specimen type	Sliding material	Friction coefficient	Recorded acceleration [g]			Sliding displacement
			Base	Roof	Ratio	[mm]
Fixed	-	∞	0.38	0.89	2.34	-
Sliding	Graphite powder	0.25	0.32	0.20	0.63	2.0
Sliding	Dry sand	0.34	0.86	0.60	0.70	0.5
Sliding	Wet sand	0.41	0.86	0.77	0.90	0.5
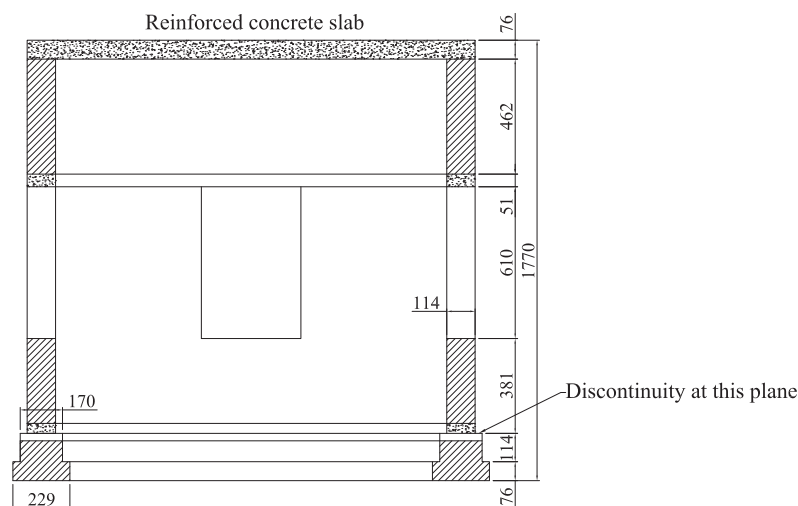
Figure 2-1. House model with the sliding base (according to Qamaruddin et al. [9])

In the same course, additional series of tests were performed to investigate the dynamic behavior and performance both of the PFSI-isolated and conventional half-scale, single-story house models. A total of eight models, six conventional and two isolated were tested to ultimate state through gradually increased shock loading. Sliding joint was

provided just above the plinth band by using burnt oil as a sliding layer, see Figure 2-1. As compared to the fixed base house models, house models with the sliding base exhibited the following features: they had a significantly reduced response and behaved adequately up to the very high imposed base accelerations; they had much less extent of cracking.

A similar, and very simple, PFSI technique was proposed and investigated by Li [7]. The system consisted of laying a thin layer of specially selected sand grains between terrazzo plates. Five small-scale house models were tested on a shaking table. The superstructures were made of adobe while the bases were made of better quality small bricks and cement mortar, with the sliding layer placed between them. All five house models survived the shaking table tests. It was noticed that sliding of the superstructure began after the base acceleration reached a level of 0.2g.

Lou et al. [10] reported results of horizontal load tests on brick walls made with and without a sliding joint under different levels of vertical load. Graphite powder, asphalt felt, screened gravel (fine sand) and paraffin wax were selected as sliding materials. Test results showed that the horizontal load that caused forming of diagonal cracks in conventional masonry wall was about two times larger than the horizontal load resisted by walls with sliding joint. Further, shaking table tests were carried out on 32 I-shaped brick walls with same types of sliding material, but different interface materials and height-width ratio of specimens. Due to low cost, high bearing capacity and stable sliding behavior under dry and wet conditions, the graphite powder appeared as an ideal low-friction material to make a sliding joint. Screened gravel did not show satisfactory sliding behavior, since gravel particles tended to break during sliding, causing a considerable increase of the friction coefficient. Because of its condensation cohesiveness, which led to rather rocking vibration, paraffin wax was found inappropriate as a sliding joint material.

Findings of a comprehensive experimental research project on the effectiveness of the PFSI technique for multi-story masonry buildings were reported in [2]. A total of 13 shaking table tests were carried out to assess the performance of both fixed-base and isolated three-story-high masonry building models built at one-third scale. In order to construct an isolated model, eighteen Teflon/Stainless steel sliders were installed at wall corners and junctions at the base (plinth) level of the building model, while a continuous grease/concrete sliding joint was placed at the second story floor level, see Figure 2-2.

10

Experimentally obtained values of static friction coefficient of Teflon/steel and grease/concrete sliding joints were 0.1 and 0.4, respectively.
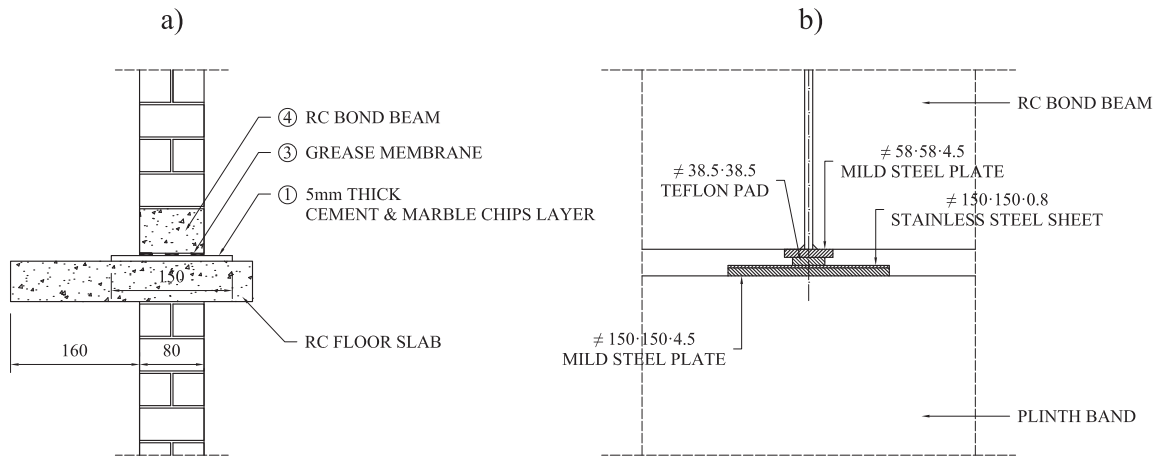
Figure 2-2. Construction detail of the implemented isolation system: a) continuous, b) discrete system (according to Nikolić-Brzev [2])

A single artificially generated earthquake motion was used for all conducted tests. In some test runs, a vertical base motion was induced simultaneously with a horizontal base motion. A fixed-base model was tested in the first phase of six test runs, while the second phase comprised seven test runs on sliding models. Sliding of the second story isolation system was not observed in any of tests. Similar levels of acceleration amplifications ratios were attained in test runs with only horizontal and simultaneous horizontal and vertical base excitations, thus indicating that the seismic response of the isolated structure was not significantly affected by vertical base excitation. Experiments have shown that, as compared to the conventional multi-story masonry building, the response acceleration level of isolated buildings was appreciably reduced (by 30% on average). This was particularly pronounced in the cases of higher excitation. Moreover, it was revealed that with the increase of horizontal excitation level, the amount of input energy transmitted to the fixed-base system was constantly increasing, whereas for the isolated system an opposite trend was observed. This indicated that the proposed isolation method was more effective at higher excitation levels.

Nanda et al. [11–13] investigated the frictional characteristics of different types of green marble-based sliding interface for seismic protection of masonry buildings by performing a series of friction and shaking table tests. Both static and dynamic displacement controlled friction tests were conducted on round specimens with the

diameter of 200 mm. Four types of sliding interfaces, such as green marble-High Density Poly Ethylene (HDPE), green marble-green marble, green marble-geosynthetic and green marble-natural rubber were selected. A loading speed was kept constant for the static friction tests, while the dynamic tests were performed under changing loading speeds. Three levels of vertical load were considered, namely 10 kN, 20 kN, and 50 kN, which corresponded to the pre-compression stress levels of 0.32 MPa, 0.64 MPa and 1.59 MPa, respectively. Obtained tests results are summarized in Table 2-2. No significant influence of the pre-compression level on the coefficient of static friction was observed. Similarly, the coefficient of dynamic friction was found to be insensitive to the variations of the loading speed (the loading speed variation range was 12.5-50 mm/s).

Table 2-2. Friction coefficients for different sliding interfaces (Nanda et al. [11])

Sliding interface type	Coefficient of static friction for different vertical load				Coefficient of dynamic friction for different loading speed [vertical load of 50 kN]		
	10 kN	20 kN	50 kN	Mean	12.5 mm/s	50 mm/s	Mean
Green marble-HDPE	0.08	0.07	0.09	0.08	0.07	0.07	0.07
Green marble-green marble	0.08	0.09	0.09	0.09	0.09	0.08	0.08
Green marble-geosynthetic	0.11	0.11	0.11	0.11	0.10	0.10	0.10
Green marble-rubber	0.17	0.16	0.16	0.16	0.20	0.17	0.18

Further, the effectiveness of these sliding interfaces in reducing the seismic response of a half-scale single-story masonry building was investigated on a servo-controlled shaking table. An artificial accelerogram with effective peak ground acceleration of 0.36g was used as the base excitation in the horizontal direction, while the vertical motion was considered as two-thirds of the horizontal one. The results showed that, in the case of the fixed-base building, the maximum roof acceleration was amplified by 168% with respect to the maximum base acceleration, whereas for the buildings with marble-marble, marble-HDPE, marble-rubber, and marble-geosynthetic sliding interface the maximum roof acceleration amounted to 53%, 41%, 87% and 60% of the maximum base acceleration, respectively. This reduction in the roof acceleration response of the sliding-base system appeared at the cost of relative displacement between the superstructure and the substructure. However, the measured relative displacements in case of models with marble-marble, marble-rubber, and marble-geosynthetic sliding interfaces, were well within the range limited by the plinth level size (plinth projection of 75 mm).

12

Therefore, it was concluded that the investigated low-friction sliding materials allowed the superstructure to slide with equal effectiveness to previously recommended materials such as graphite, screened gravel, Teflon-steel, fine sand-terrazzo plates, whose use is restricted because of their high cost, construction complications, and poor durability [12].

Sassu [13] presented the design criteria for a proposed low-cost base dissipation technique for masonry buildings together with the results of numerical analyses. The proposed system, termed as "reinforced cut wall" (RCW), was built of 50 mm thick (weak) mortar and 4 mm thick elastomer layer laid between the foundation and base of the wall, which is further reinforced and connected to the foundation by a series of vertical steel bars (Ø8-12 mm). Series of static-cyclic shear tests have been performed to establish the mechanical properties of such dissipators and define suitable assembly techniques. Numerical simulations were conducted on several building schemes to determine the benefits in their structural response caused by implementing the RCW. The results indicate that, when implemented, the RCW system can significantly reduce the relative horizontal displacements in the masonry superstructure as well provide for the moderate decrease of the fundamental vibration period of masonry structures.

Beside the experimental investigations, several mathematical models for single- and multi-story masonry buildings with a friction-sliding joint at the base were proposed, validated and analyzed under different unidirectional and bidirectional, horizontal and vertical base excitations by researchers in the past, e.g. [2,9,11,14–16]. All models are in principle the same, and are based on the following assumptions: building is idealized as the multiple-degree of freedom system with the masses lumped at the base and each floor level; the base mass is assumed to rest on a plane with a sliding interface to permit sliding of the system; the stiffness and damping are provided by the structural masonry walls, which remain linear-elastic; geometric non-linear effects are small and neglected; the coefficient of friction remains constant (Coulomb's type friction); contribution of overturning is small and neglected; the ground is assumed as stiff. The response of such idealized system was separated in two different response regimes, namely sliding and non-sliding regime, with the defined transition point. It was shown that such analytical models could give results in good agreement with the experimental observations and could be used for the assessment of the seismic response of masonry buildings with friction-sliding joints.

2.3 Unreinforced masonry with a soft layer in bed joint

In today's construction practice various types of soft layer membrane are used in URM structures. Depending on their purpose, soft layers are often placed at the bottom and/or the top of masonry walls, being incorporated in a bed joint, either placed between two mortar layers (centric) or laid directly on the masonry units or underlying concrete slab with the mortar layer placed atop. In some applications, such as when it is used as a slip joint, soft layers are placed in the bed joint without mortar. Bed joints with built-in soft layers are designed to meet serviceability design criteria such as providing a moisture barrier in the form of a damp-proof course (DPC) membrane or ensuring sound insulation at the base and/or the top of the masonry walls, as well as accommodation of short-term or long-term differential movements between the masonry walls and the floor construction. However, due to the presence of a soft layer in the bed joint, the shear and tensile characteristics of the joint can be significantly altered. Since these material parameters could be governing for the masonry behavior, especially under seismic, i.e. cyclic loading it is of the utmost importance to investigate and understand the influence of such layers incorporated in a bed joint of a masonry wall. A relatively modest amount of research data is available on the shear behavior of URM walls containing soft layer membranes. The majority of the previous research has been focused on the investigation of the behavior of various types of soft layer at different pre-compression levels. Attention has been paid to the assessment of the shear parameters and the overall performance of bed joints containing soft layers by conducting static, static-cyclic and dynamic tests on small URM elements (mostly triplets), see [17–24]. The behavior of larger URM elements (wallettes) with soft layers has been also investigated, see [3,25–27]. The research findings indicate, that a shear force can be transmitted through the joints containing soft layer and that due to sliding failure along the soft layer a considerable amount of energy dissipation and quasi-ductile behavior could be expected for URM with soft layers. However, neither analytical nor numerical models capable of describing the observed behavior were reported in the published literature. A common observation is that the relationship between the applied pre-compression and the shear strength is linear and can be quantified using the Mohr-Coulomb's law with the cohesion, c, and the friction coefficient, $\tan\varphi$, as parameters. A summary of the material parameters that characterize the bed joint shear resistance obtained from reviewed experimental work is presented in Table 2-3.

14

Table 2-3. Summary of the bed joint shear strength parameters (according to Mojsilović et al. [5])

Reference	Soft layer position	Soft layer type	tanφ Loading type Monotonic	Cyclic	Dynamic	c [MPa]
Suter et al. [17]	Centric (no mortar)	Polyethylene	0.2633	-	-	0.0310
		Dual polycrepe	0.2200	-	-	0.0583
		Copperfibreen	0.2383	-	-	0.0603
	Centric	Polyethylene	0.3517	-	-	0.0930
		Dual polycrepe	0.3733	-	-	0.0637
		Copperfibreen	0.3633	-	-	0.2503
	Lying on brick	Polyethylene	0.2717	-	-	0.0953
		Polythene	0.2767	-	-	0.0787
		Copperfibreen	0.2083	-	-	0.1150
Zhuge et al. [18]	Centric	Embossed polythene	0.293	-	-	0.3467
		Aluminium-cored polyethylene	0.152	-	-	0.2558
		Bitumen-coated fabric	0.312	-	-	0.1552
	Lying on brick	Embossed polythene	0.361	-	-	0.14
		Aluminium-cored polyethylene	0.180	-	-	0.17
		Bitumen-coated fabric	0.171	-	-	0.14
Griffith et al. [19]	Lying on brick	Bitumen-coated aluminium	0.460	0.520	0.430	-
		2 layers of bitumen-coated aluminium	0.470	0.569	0.460	-
		Embossed polythene	0.304	0.267	0.410	-
		2 layers of greased galvanized steel	0.074	0.108	0.110	-
	Centric	Bitumen-coated aluminium 0.85 mm	-	-	0.440	-
		Bitumen-coated aluminium 0.99 mm	0.527	0.541	0.470	-
		Polythene/bitumen-coated aluminium	0.259	0.317	0.370	-
		Embossed polythene	0.397	0.329	0.360	-
Trajkovski et al. [21]	Centric	Reinforced polyvinylchloride	1.124[a]	-	0.647[a]	-
			0.488[b]	-	0.394[b]	-
Mojsilović et al. [23]	Mortar Joint	-	0.87	-	-	0.30
	Centric	Elastomer	0.68	-	-	0.06
		Bitumen	0.02	-	-	0.26
		Polyester	0.69	-	-	0.15
	Lying on brick	Elastomer	0.71	-	-	0.01
		Bitumen	0.07	-	-	0.12
		Polyester	0.74	-	-	0.09
	Lying on concrete brick	Elastomer	0.74	-	-	0.03
		Bitumen	0.09	-	-	0.14
		Polyester	0.83	-	-	0.09
Mojsilović et al. [24]	Centric	Embossed polythene	-	0.28	-	0.04
			0.29	-	-	0.07
	Lying on brick	Embossed polythene	-	0.26	-	0
			0.25	-	-	0.02
Mojsilović et al. [26]	Centric	Embossed polythene	-	0.409	-	0.051
	Lying on concrete slab	Embossed polythene	-	0.441	-	0.025
Vögeli et al. [3]	Lying on brick	Rubber granulate	-	0.410	-	0.017

[a] Loading speed of 250 mm/s

[b] Loading speed of 0.006 mm/s

Suter et al. [17] performed monotonic tests on masonry triplets with three different types of DPC material, i.e. polyethylene, polycrepe and copperfibreen in bed joints. Zhuge et al. [18] performed two sets of experiments aimed at determining the in-plane shear strength of masonry containing a DPC membrane. A total of eighteen typical masonry triplets were tested. As soft layer materials different types of DPC membrane were considered (embossed polyethylene, bitumen-coated fabric and aluminium-cored polyethylene). In order to evaluate the performance of masonry joints containing soft layers under dynamic loading, as well as to assess their seismic integrity and establish their friction capacity, Griffith and Page [19] performed a series of monotonic, static-cyclic and dynamic shear tests on masonry triplets with different types of DPC membranes (bitumen-coated aluminium; polythene/bitumen-coated aluminium and embossed polythene) and reported the corresponding friction coefficients, see Table 2-3. The DPC membranes were placed in both mortar joints of the triplet. In one series, the middle brick was made of concrete in order to simulate the concrete floor slab. Test specimens were initially subjected to a foreseen level of pre-compression, which was kept constant during the test. The shear load was applied in the out-of-plane direction. In order to expand the abovementioned findings, Simundic et al. [20] investigated the long-term shear behavior of the masonry triplets subjected to monotonic loading. Their results indicated that all tested sliding joints, besides a proven potential to transmit short-term transient seismic loads, had the potential to accommodate long-term moisture and thermal movements. Trajkovski and Totoev [21] reported the results of an experimental investigation on the shear capacity of masonry triplets with reinforced polyvinylchloride (PVC) as a damp-proof course. The PVC membrane was placed in the bed joint mortar. The research aimed to clarify the correlation between the sliding (loading) speed and value of the friction coefficient. Two different displacement rates were considered. The obtained average values of the maximum and residual shear strength, as well as dynamic and static friction coefficients were reported, cf. Table 2-3. Totoev and Simundic [22] carried out monotonic tests on DPC membrane slip joints placed at the interface between concrete and masonry. As DPC materials, bitumen-coated aluminium and embossed polythene were used. This research addressed the pseudo viscosity of the joints containing DPC, i.e. dependence of the joint response on different strain rates. Mojsilović [23] performed monotonic tests on ten series of masonry triplet specimens with three different soft layers: elastomer-, bitumen- and polyester-based membranes. The friction coefficients found for bed joints

16

with soft layer membranes are presented in Table 2-3. Shear behavior of the specimens was highly influenced by the applied pre-compression level, while the influence of the position of the DPC membrane was much smaller. A series of monotonic and static-cyclic tests were performed on masonry triplets with an incorporated embossed polythene DPC membrane, placed either in the middle of the bed joints or between the bed joint mortar and the brick, see Mojsilović et al. [24]. Test results on the mechanical characteristics, energy dissipation and the overall behavior of the masonry elements with a DPC subjected to static-cyclic loading were reported (see Table 2-3 for the mechanical characteristics obtained). At the same time, static cyclic tests were performed on 21 masonry wallettes subjected to static-cyclic shear loading with an embossed polythene DPC placed either in a mortar joint or at the masonry-concrete slab interface, see [25,26]. Masonry materials used were characteristic for Australian masonry construction (extruded clay bricks and cement-lime mortar). Three levels of pre-compression, namely 0.7, 1.4 and 2.8 MPa were considered. Results from this investigation confirmed the good performance of the DPC soft layers subjected to cyclic loading. The behavior of the wallettes was highly influenced by the pre-compression level. Furthermore, the presence and position of the DPC had a considerable influence on the behavior of the wallettes, especially on the failure mode. Two types of failure were observed, namely sliding along the bed joint containing the DPC for low and moderate pre-compression and compression failure, i.e. toe crushing, for higher levels of pre-compression. Wallettes that failed in compression exhibited limited energy dissipation, while those that failed by sliding displayed considerable energy dissipation and behaved in a quasi-ductile manner. The mechanical characteristics relevant for the present work are shown in Table 2-3. Within the preliminary research on masonry elements with a rubber granulate and elastomer based soft layers in bottom bed joint, see [3,27], a total of 16 static-cyclic shear tests on clay block masonry wallettes were performed. A soft layer was placed either directly on the first block course, covered with a layer of mortar before the next course of blocks was laid, or in the middle of the bottom mortar bed joint. It appeared that the rubber granulate soft layers placed in a bed joint have the potential to enhance the seismic performance of URM walls producing a more desirable, quasi-ductile behavior with higher deformation capacity. Extruded elastomer layers had a higher friction coefficient that precluded the occurrence of sliding. The friction coefficient for the rubber granulate layer was damage-dependent. With an increasing number of cycles, the degradation of the soft layer increased and the friction

coefficient decreased. The mechanical shear properties relevant to the present work are shown in Table 2-3.

The range of variation of the friction coefficient values presented in this review is quite wide, from as low as 0.06 for bitumen-based soft layers to as high as 0.83 for polyester-based soft layers. The friction coefficient ranges between about 0.2 and 0.4 for polymer-based soft layers used for hydro or acoustic insulation. The measured friction coefficient for rubber granulate soft layer wall bearings is 0.41. Test observations show that the sliding rate, i.e. the loading speed, affects the behavior of some soft layers, making their friction coefficient loading speed-dependent, see also [4].

In general, a load-bearing unreinforced masonry with a soft layer in the bed joint exhibit significant shear capacity that depends on the type of soft layer material and its position within the bed joint, as well as on the loading speed. Therefore, in order to apply the Mohr-Coulomb's failure criterion to determine the shear strength of unreinforced load-bearing masonry walls with incorporated soft layers, needed friction properties have to be determined experimentally for the particular soft layer material and the particular soft layer bed joint configuration using a cyclic loading protocol with varying loading magnitude and speed.

3 Experimental investigation

3.1 Introduction

The central idea of the conducted research project was to modify the seismic in-plane response of individual structural URM walls by placing engineered deformable (soft) layers it the bottom bed joint. Soft layers, mainly based on rubber, bitumen, cork or polyvinylchloride (PVC), have already been used in Swiss URM construction. However, the purpose of implementing such layers is mainly unrelated to seismic actions. Soft layers are used to provide a moisture barrier in the form of a damp-proof course membrane, to ensure sound insulation or to accommodate short- or long-term differential movements between the walls and floor constructions. Results from the preliminary research on masonry wallettes with rubber granulate and elastomer based soft layers, see [3], indicated that the presence of such layers in the mortar bed joint can significantly alter the mechanical characteristics of URM walls by creating a sliding plane, which, in turn, could influence the seismic response of the entire structure. A bed joints with soft layers, with adequate material properties, could change the typical brittle in-plane shear response of masonry to a more desirable quasi-ductile one, and provide for considerable energy dissipation, i.e. to provide the behavior which is desirable for enhanced seismic performance. It was revealed that the rubber granulate soft layers were in some cases heavily damaged during the cyclic loading, whereas the elastomer layers were found to be significantly more durable. This certainly influence the mechanical characteristics, namely the friction coefficient of the bed joint. In order to protect the soft layer and insure its durability, the conducted research investigated a so called multi-layer bed joints in which the core soft layer is protected by two adjacent 2.2 mm thick extruded elastomer layers and placed in the middle of mortar joint.

After selecting a typical Swiss hollow clay units and standard cement mortar as masonry components for the planned experimental research, since this combination covers most of the masonry construction in Switzerland, soft layer types were chosen. Five different core soft layers, namely rubber granulate, cork, cork-rubber granulate, bitumen and PVC based membranes were selected. After determining the masonry and soft layer components to be used, the standard material-level tests were performed to investigate the mechanical properties and the behavior of the selected soft layer components. Firstly, a

series of monotonic and static-cyclic in-plane shear tests on masonry triplets were carried out to assess the friction coefficient and apparent cohesion of the multi-layer bed joints and the dependence of these parameters on the pre-compression stress and the loading speed. The extent of the cyclic loading-caused degradation of the soft layers was of special interest. Secondly, the effect of the multi-layer bed joint on the compressive strength and vertical deformation of URM was determined. Further, a total of 9 static-cyclic shear tests on structural, full-scale URM walls with a multi-layer bed joint were conducted in two phases. Those structural element level tests were performed to gain an insight into the in-plane seismic behavior of URM walls with multi-layer bottom bed joints. The preliminary testing phase was aimed at choosing the most suitable core soft layer type for the main testing phase. The main testing phase comprised five tests on storey-high URM walls with rubber granulate core soft layers performed to investigate the influence of the wall size, the pre-compression level and the aspect ratio on the seismic behavior of URM with a multi-layer bottom bed joint. Finally, additional series of monotonic shear and relaxation tests were performed on masonry triplets with a rubber granulate core soft layer in multi-layer bed joints to assess the mechanical parameters of such multi-layer bed joints needed for the modelling purpose. Figure 3-1 depicts schematically the experimental investigation and further use of the experimental results in the theoretical phase of the research project (see the "List of symbols" for the parameters shown in Figure 3-1).
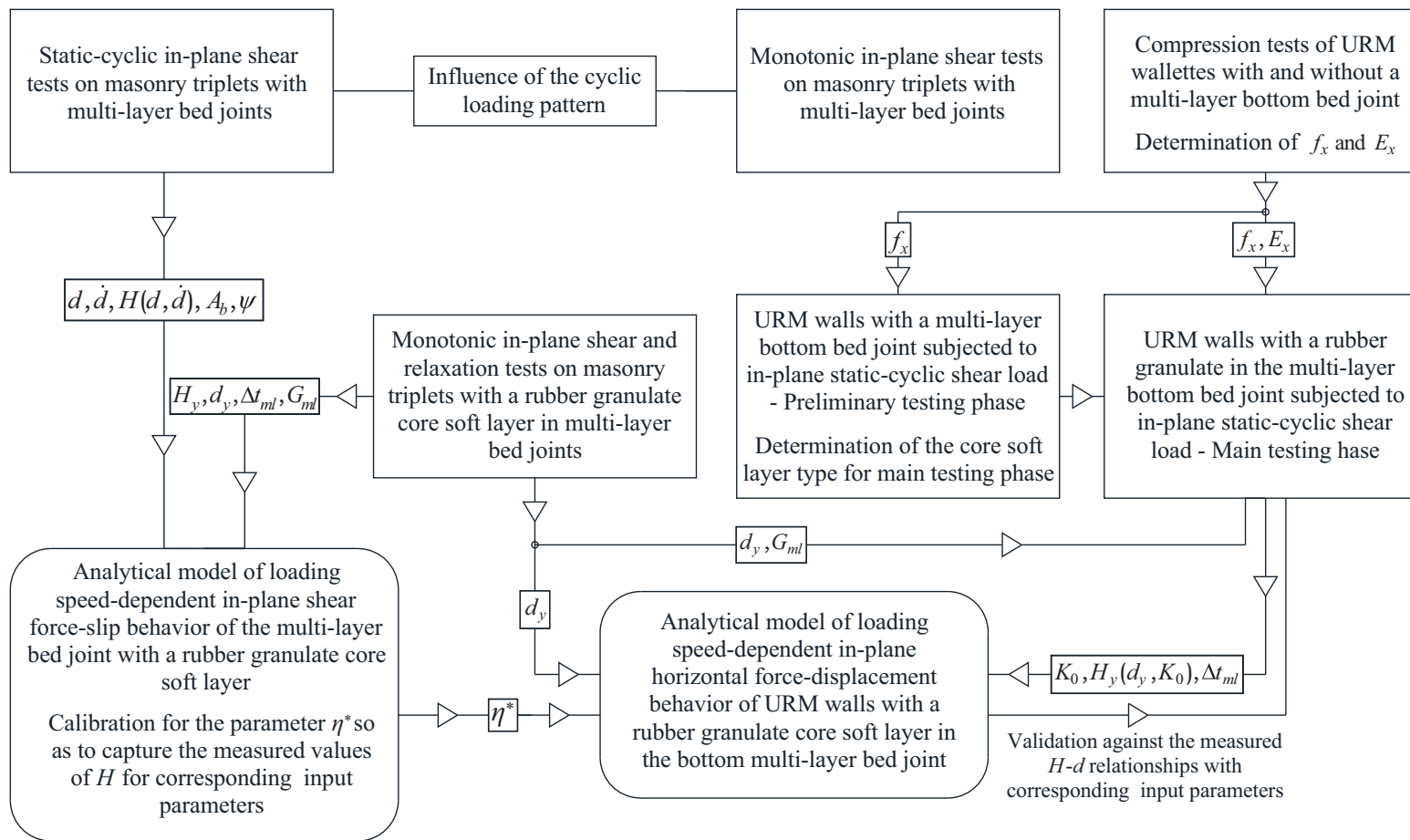
Figure 3-1. Schematic preview of the research project

3.2 Monotonic and static-cyclic in-plane shear tests on masonry triplets with multi-layer bed joints

In order to investigate the influence of the multi-layer bed joint on the behavior of masonry under monotonic and static-cyclic shear, to assess the mechanical shear properties as well the durability of multi-layer bed joints with different core soft layers, and to establish the potential of a multi-layer bed joint to modify the lateral load resistance mechanism of URM walls, a total of 57 monotonic and static-cyclic tests on URM triplets made of Swiss masonry materials and having five different commercial built-in core soft layers were performed. The increase of the pre-compression as well the loading speed leads to higher values of shear resistance of the multi-layer bed joint, regardless to the core soft layer type and the loading protocol type. The applicability of Mohr-Coulomb's failure criterion to determine the shear resistance of the multi-layer bed joint requires the friction properties to be experimentally determined for the particular soft layer material and the particular soft layer bed joint configuration using a loading protocol with varying loading magnitudes and speeds. The intended protective role of the elastomer layers is largely fulfilled. The findings presented within this section have already been partly published in [5,28].

3.2.1 Test programme and masonry materials

Typical Swiss extruded clay blocks of nominal size 250x120x90 mm and five different types of core soft layer, namely rubber granulate, cork-rubber granulate, cork, bitumen and PVC, have been used to prepare test specimens, see Figure 3-2. Selected soft layers are commonly used as DPCs (bitumen), as sound insulation (cork, cork-rubber granulate, elastomer) and as wall bearings or to accommodate the differential movements between the masonry wall and the floor construction (rubber granulate, PVC, elastomer). Dry ready-mixed general-purpose cement mortar, with the sand grain size up to 4 mm for standard masonry was mixed with water in the laboratory and used to produce mortar bed joints. The average compressive strength of cement mortar was determined according to the European standard EN 1015-11 [29]. The measured values were 14.84 MPa with standard deviation of 0.52 MPa, and 6.68 MPa with standard deviation of 0.43 MPa, for mortar specimens stored in the climatic chamber and in open air in the laboratory, respectively. The average compressive strength of the extruded block, determined

22

according to the European standard EN 772-1 [30] amounted to 19.37 MPa with standard deviation of 1.68 MPa. Specimens were classified into six series according to type of built-in core soft layer. The test programme is summarized in Table 3-1.

Figure 3-2. Materials used for specimen preparation [5]

Table 3-1. URM triplets with multi-layer bed joints: test programme [5]

Series	(Core) soft layer type	Soft layer thickness [mm]	Pre-compression level [MPa]		
			0.2	0.6	1.0
M	No soft layer	-	M1	M2	M3
G	Rubber granulate	3.0	G1	G2	G3
GK	Cork-rubber granulate	3.2	GK1	GK2	GK3
K	Cork	3.5	K1	K2	K3
B	Bitumen	2.0	B1	B2	B3
F	PVC	2.5	F1	F2	F3

Soft layers, together with two protective outer layers of 2.2 mm thick extruded elastomer were placed in the middle of each bed joint (series G, GK, K, B and F), but for 6 specimens of series M that served as control specimens and were constructed without a soft layer, see Figure 3-3. All specimens were constructed by experienced bricklayers and were kept in the open air in the laboratory, cf. Figure 3-4.

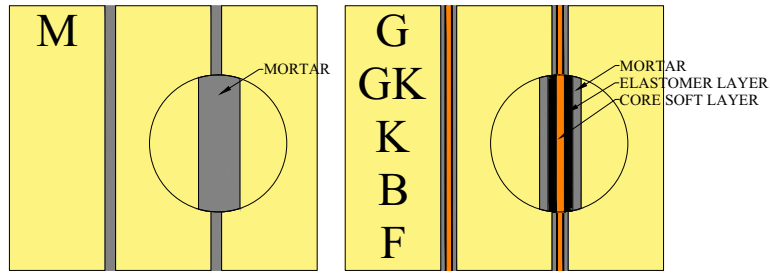**Figure 3-3. Schematic preview of prepared specimens [5]**

Figure 3-4. Construction and storage of the specimens

3.2.2 Test set-up, testing procedure and measurements

The test set-up, which was designed based on the European Standard EN 1052-3 [31], used for performing both monotonic and static-cyclic tests is shown in Figure 3-5.
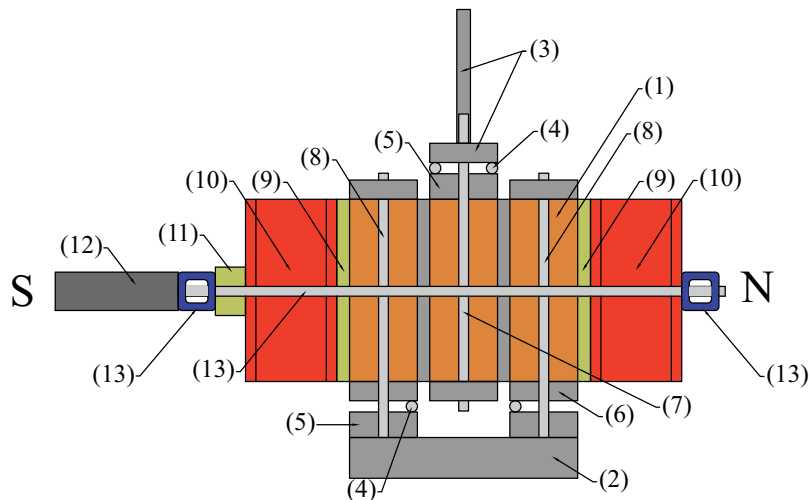

Figure 3-5. URM triplets with multi-layer bed joints: test set-up [5]

After the prescribed curing time and applied pre-compression force, each specimen (1) was placed in the universal testing machine between two load transmission elements and centered to avoid any bending influence. The shear load was applied by means of the massive steel plate (2) fixed to the lower transmission element, while the upper load transmission element remained static during testing. Each static-cyclic test started with an upward motion of the lower transmission element (pushing semi-cycle). Monotonic tests were performed with a unidirectional pushing motion. In order to properly introduce shear load into the specimen, steel cylinders, (4), and two sets of steel plates, (5) and (6), were used. Two steel rods, (7), symmetrically placed on both opposite sides of the specimen, were used to connect the middle block with the set of steel plates, (3), which in turn were clamped to the upper load transmission element of the universal testing machine. Cyclic movement of the outer blocks was ensured by means of steel rods, (8), which were placed on both sides of the specimen and fixed to the massive steel plate, (2). It should be noted that for the monotonic tests there was no need to fix either middle block or outer blocks, since they were performed with a unidirectional pushing motion, and therefore the steel rods, (7) and (8), were not used. Two plywood plates, (9), were used to ensure a good contact between the specimens and the steel profiles, (10), which in turn were used to introduce the pre-compression force. A hydraulic jack, (11), together with a pendulum manometer was used to apply the pre-compression force and maintain a constant level during testing. Load cells, (12), were used to monitor the level of applied pre-compression. A set of two steel rods together with two steel profiles, (13), was used to keep the hydraulic jack and the load cells in their correct position.
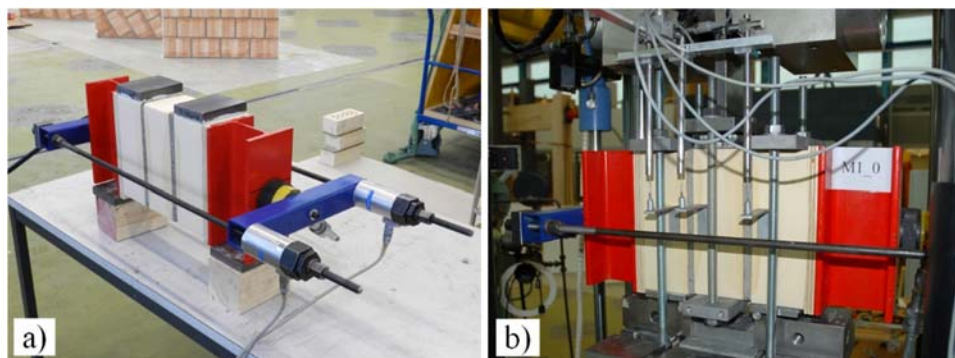

Figure 3-6. Measuring devices: a) loading cells; b) LVDTs

All measured data, i.e. vertical shear load, vertical displacements of each block, pre-compression force, were recorded and processed in real time. As mentioned before,

load cells were used to monitor the level of the applied pre-compression force, see Figure 3-6a, which was also controlled by observing the oil pressure in the hydraulic system of the pendulum manometer. Vertical displacements of the blocks were measured by means of three linear variable differential transformer displacement transducers (LVDTs) on the West side of the specimen. All LVDTs had the measuring span of 100 mm and rested on L-shape aluminium plates, which in turn were glued to the blocks, see Figure 3-6b. Both static-cyclic and monotonic tests were performed applying computer-controlled displacement steps. Monotonic tests were performed either at a constant loading speed of 0.25 mm/min or at a constant loading speed of 0.5 mm/min. Each displacement step during static-cyclic tests was applied twice per cycle in the form of a sinusoidal wave. Data on the target displacements and the duration of the period for each step are given in Table 3-2. Using this procedure the maximum test duration was about 160 min.

Table 3-2. Loading history for static-cyclic shear tests [5]

Travel [mm]	0.5	1	2	3	5	10	15	20	30
Loading speed [mm/min]	0.5	0.5	0.5	1	3	5	10	10	10
Period [min]	4.0	8.0	16.0	12.0	6.67	8.0	6.0	8.0	12.0

3.2.3 Test results and specimen behavior

After preparation and prescribed curing time of at least 28 days, each specimen was firstly subjected to a pre-compression load and subsequently subjected either to a monotonic or to a static-cyclic shear load. Three different levels of pre-compression were considered, namely 0.2, 0.6 and 1.0 MPa. Figure 3-7 depicts exemplarily the variation of the pre-compression over time for selected specimens. For each level of pre-compression four replicates of series G, GK, K, B series were tested, among which two replicates, 0 and 3, were subjected to a monotonic and two replicates, 1 and 2, were subjected to a static-cyclic shear load. Further, for testing the control specimens (M series), only one replicate for each level of pre-compression was subjected to a monotonic and static-cyclic shear load. Finally, the specimens of F series were subjected only to a static-cyclic shear load and one replicate for each level of pre-compression was tested. It should be noted that in the replicates notation their numbers (0, 1, 2 and 3) are preceded by the underscore.

Typical shear deformation, i.e. sliding in the bed joints, was observed during testing in all cases, see Figure 3-8 for the deformation of specimens G2_0, GK2_2 and

26

K3_1. Although the shear deformation for the observed sliding failure mode is theoretically unlimited, monotonic tests were stopped after reaching a considerable shear deformation, while static-cyclic tests were stopped after the ultimate shear strength was reached.
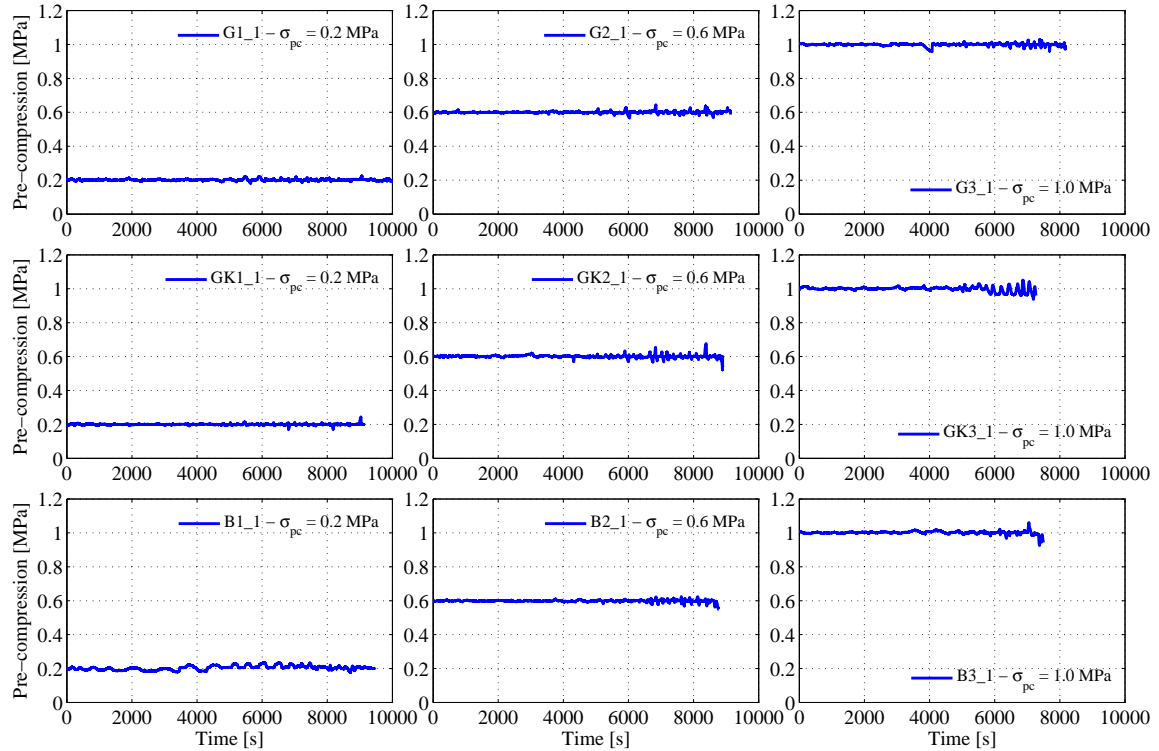

Figure 3-7. Pre-compression load vs. time
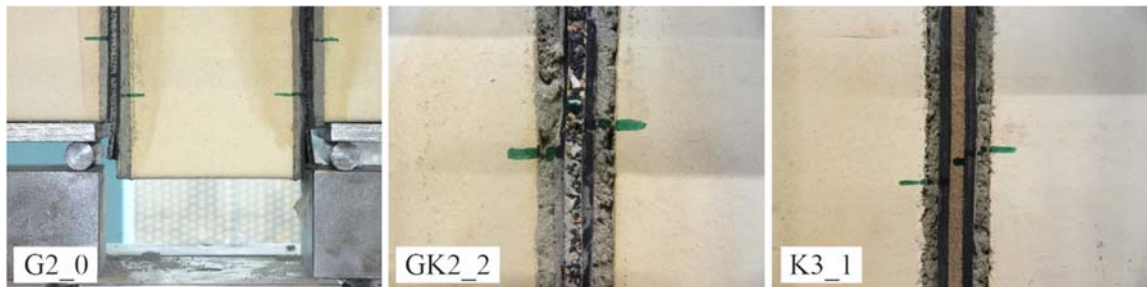
Figure 3-8. Typical shear-sliding deformation: specimens G2_0; GK2_2 and K3_1

Values of the maximum shear force per bed joint recorded during the monotonic and static-cyclic tests are summarized in Tables 3-3 and 3-4, respectively. The same results are reported in [5,28]. As mentioned before, both monotonic and static-cyclic tests started with a push cycle (positive values of shear force and displacement). It can be seen that the maximum recorded values of shear force for the specimens with multi-layer bed joints are lower than those for the specimens without multi-layer bed joints (series M),

both for monotonic and static-cyclic loading. Furthermore, the values of the maximum shear forces obtained for monotonic loading were significantly lower than the values obtained for static-cyclic loading. Finally, the values of the maximum shear force obtained for monotonic loading with a higher loading speed (replicates 3) were higher than those obtained from tests with a lower loading speed (replicates 0), especially in case of higher levels of the applied pre-compression. The only exceptions are the specimens of Series GK, where these values were of similar magnitude.

Table 3-3. Monotonic shear test on masonry triplets: test results [5]

	Replicates 0 [loading speed 0.25 mm/min]				Replicates 3 [loading speed 0.5 mm/min]		
σ_{pc} [MPa]	0.2	0.6	1	σ_{pc} [MPa]	0.2	0.6	1
Series	Maximum shear force [kN]			Series	Maximum shear force [kN]		
M	9.71	14.94	21.72	-	-	-	-
G	2.21	4.29	5.32	G	1.99	5.40	7.42
GK	2.77	6.78	12.72	GK	2.83	6.56	12.78
K	3.27	6.38	7.18	K	3.17	8.15	10.30
B	3.08	8.42	9.04	B	3.62	9.65	12.75

Table 3-4. Static-cyclic shear test on masonry triplets: test results [5]

		Replicates 1					Replicates 2		
	σ_{pc} [MPa]	0.2	0.6	1		σ_{pc} [MPa]	0.2	0.6	1
Series	Loading direction	Extreme values of shear force [kN]			Series	Loading direction	Extreme values of shear force [kN]		
M	Push	8.87	16.10	27.30	-	-	-	-	-
	Pull	-9.64	-18.18	-28.06		-	-	-	-
G	Push	4.58	12.11	13.93	G	Push	5.28	11.82	17.51
	Pull	-4.45	-10.93	-13.37		Pull	-4.83	-11.50	-16.69
GK	Push	4.90	12.31	17.88	GK	Push	4.59	12.39	15.18
	Pull	-4.54	-11.70	-17.50		Pull	-4.85	-12.80	-15.68
K	Push	4.34	11.51	15.29	K	Push	4.38	11.56	17.53
	Pull	-3.93	-10.17	-14.66		Pull	-4.13	-11.45	-15.72
B	Push	4.88	12.18	17.53	B	Push	4.38	12.47	15.96
	Pull	-4.61	-11.10	-15.52		Pull	-4.45	-10.95	-14.71
F	Push	0.47	1.12	2.30	-	-	-	-	-
	Pull	-0.65	-1.50	-2.83		-	-	-	-

3.2.3.1 Shear load-deformation characteristics: monotonic tests

Typical shear load-deformation relationships obtained from the monotonic tests on replicates 0 and 3 are shown in Figure 3-9 (see Appendix A1 for details). The deformation value shown in the diagram is the relative displacement (slip) between the middle and outer blocks. An average value of both values on the South and North sides is presented. It is clear from Figure 3-9 that the specimens without soft layers in bed joints (series M) behaved linear-elastically with a high stiffness up to the maximum attained shear force. Afterwards, softening behavior with changing slope was observed. All specimens with multi-layer bed joints (G, GK, K and B series) exhibited a non-linear behavior from the beginning. As compared to the other series, specimens of series G exhibited a somewhat softer initial response. After reaching the maximum value of the shear force, an initial softening branch was observed for some of the specimens (Series M and B) and eventually all specimens developed the plastic plateau. The maximum shear force for all specimens was reached at the value of slip that was less than 2 mm.
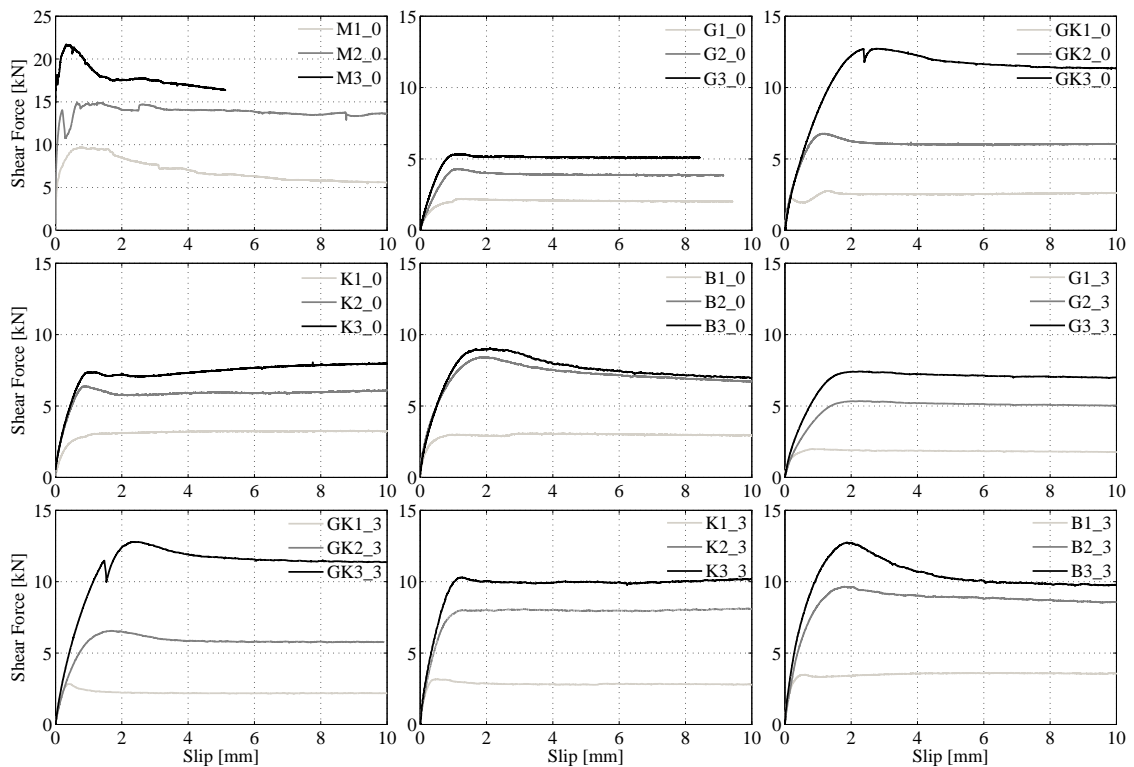

Figure 3-9. Shear force-slip relationships: monotonic tests

3.2.3.2 Shear load-deformation characteristics: static-cyclic tests

As can be seen from Figures 3-10 and 3-11, which show the shear load-slip relationships of the specimens subjected to static-cyclic loading, all specimens exhibited typical hysteretic behavior for all levels of pre-compression (see Appendix A1 for details). The initial response of the specimens of series M (control specimens) was linear-elastic with high stiffness, which subsequently evolved into an ideal-plastic horizontal branch (plateau). Specimens of series with multi-layer bed joints exhibited non-linear behavior from the beginning. Here, too, as the deformation increased, the response of the specimens evolved into an ideal-plastic horizontal branch. Generally, all specimens with multi-layer bed joints exhibited a considerable energy dissipation capacity and behaved in a quasi-ductile manner. It should be emphasized that the recorded value of shear force for the specimens of the series G, GK, K and B increased as the number of performed cycles increased. This means that the increase of the level of target displacement and loading speed had a significant influence on the shear strength of the specimens. On the other hand, specimens of series M and F, reached a maximum shear force after the first or second cycle, i.e. their strength degraded with an increasing number of cycles.
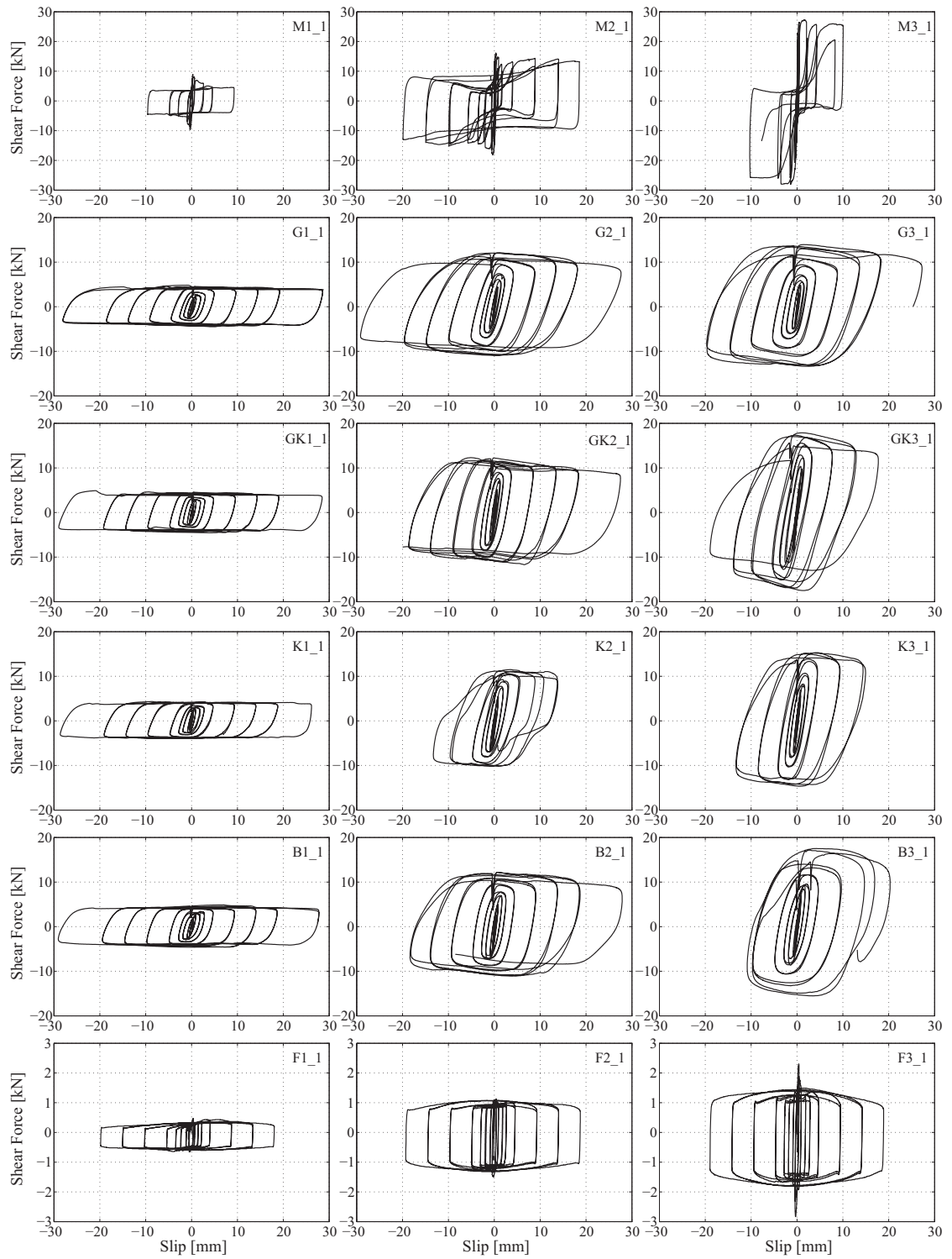
Figure 3-10. Shear force-slip relationships: static-cyclic tests of replicates 1
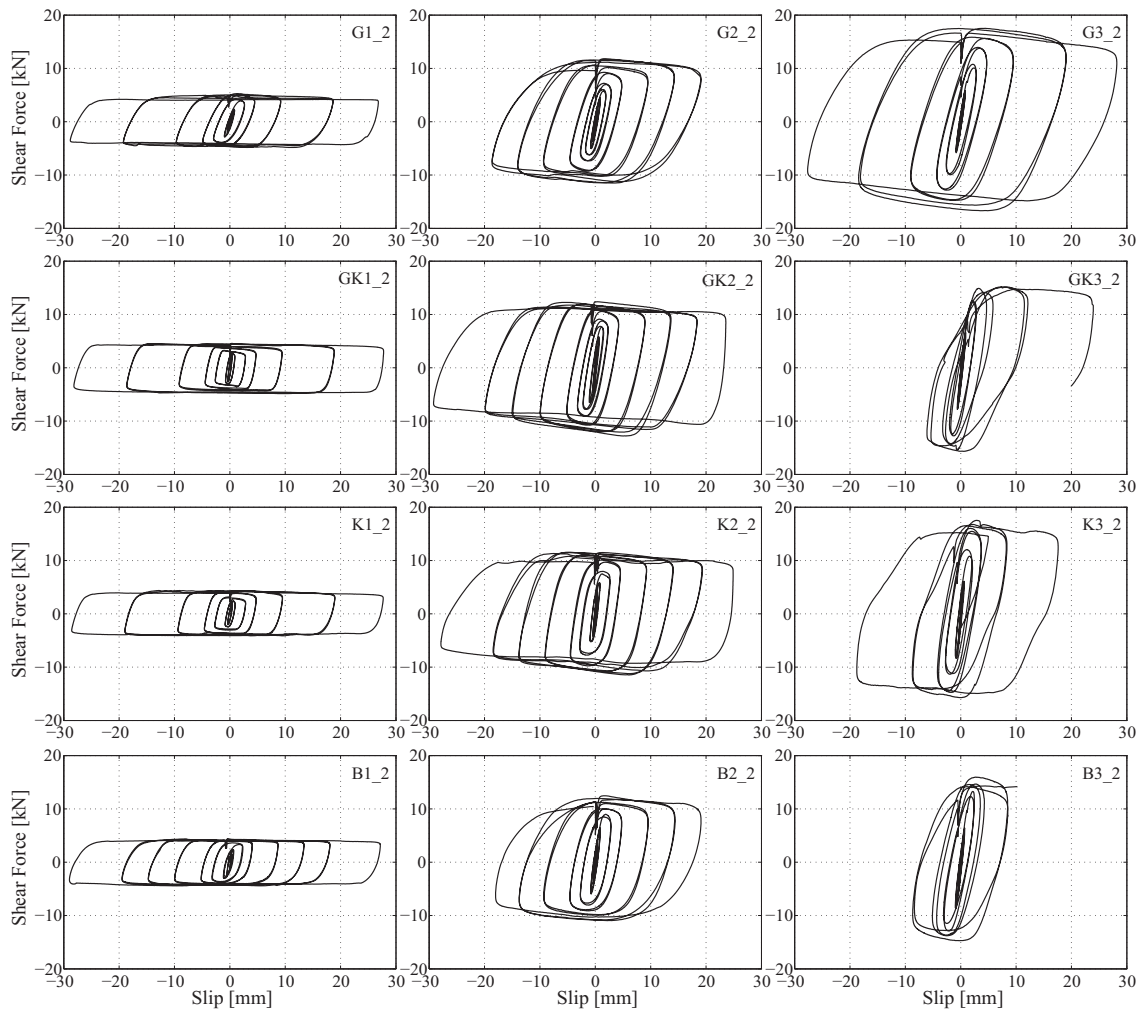
Figure 3-11. Shear force-slip relationships: static-cyclic tests of replicates 2

3.2.3.3 Behavior at ultimate load

All observed failure patterns were characteristic for masonry failing in a sliding mode. Failure of the specimens of series M has been caused by the failure of the bond between mortar and units. In general, bed joint mortar was delaminated from the units. Lateral tension failure of the clay blocks was observed in the latter phase of monotonic and static cyclic tests conducted under higher levels of pre-compression. Specimens of the series G, GK, K and B behaved very similarly to each other. Sliding planes were formed along the interface between a core soft layer and the protective elastomer layers. For some static-cyclic tests, after a certain level of deformation, failure of the bond between elastomer and joint mortar occurred, i.e. a new sliding plane was formed, and sliding deformation continued as a combined one. Similar to the control specimens, lateral tension failure of the clay blocks was observed in the latter phase of the static-cyclic tests conducted under

32

higher levels of pre-compression. As expected, failure of the specimens of series F took place at the greased interface between two layers of PVC and no additional failure planes were formed during testing. After completion of the static-cyclic tests the majority of core soft layers were moderately damaged. The mode and extent of the degradation of soft layers will be discussed in Section 3.2.4.3 in more details. In no case did shear failure occur through the units, both for monotonic and static-cyclic loading. In addition, for none of the series with multi-layer bed joints was any damage to the clay blocks observed during monotonic tests.

3.2.4 Discussion

The presented test results will be discussed in the following section. Firstly, a comparison of the shear load-deformation response of the triplets subjected to monotonic and static-cyclic loading will be discussed. Further, the applicability of a simple linear relation between normal (pre-compression) and shear stress, i.e. Mohr-Coulomb's failure criterion, is investigated. Then, the influence of the applied pre-compression level on the behavior of the specimens and the degradation of soft layers is discussed. Finally, a special attention is given to the influence of the loading speed on the mechanical characteristics and overall behavior of masonry specimens.

3.2.4.1 Load-deformation characteristics: monotonic vs. static-cyclic loading

The load and the deformation are represented by the measured shear force and the slip between the middle and outer blocks (average value), respectively. The observed slip consisted on the one hand of the shear deformation of the soft layers, and on the other hand, of the relative displacement of the core soft layer to the elastomer layers or to the joint mortar. With this in mind and considering the possible (small) lost motion within the test set-up it is clear that slip cannot be equal to the applied displacement. The values obtained from a static-cyclic tests show that the slip is (almost) always smaller than the applied displacements and that the difference becomes larger with the increase of pre-compression. It seems that the horizontal cracking of the blocks was mainly responsible for this effect. The lateral deformation of the soft layers (induced by the applied pre-compression) imposed splitting stresses in adjacent blocks and thus caused the above-mentioned cracking and further crushing of the blocks.
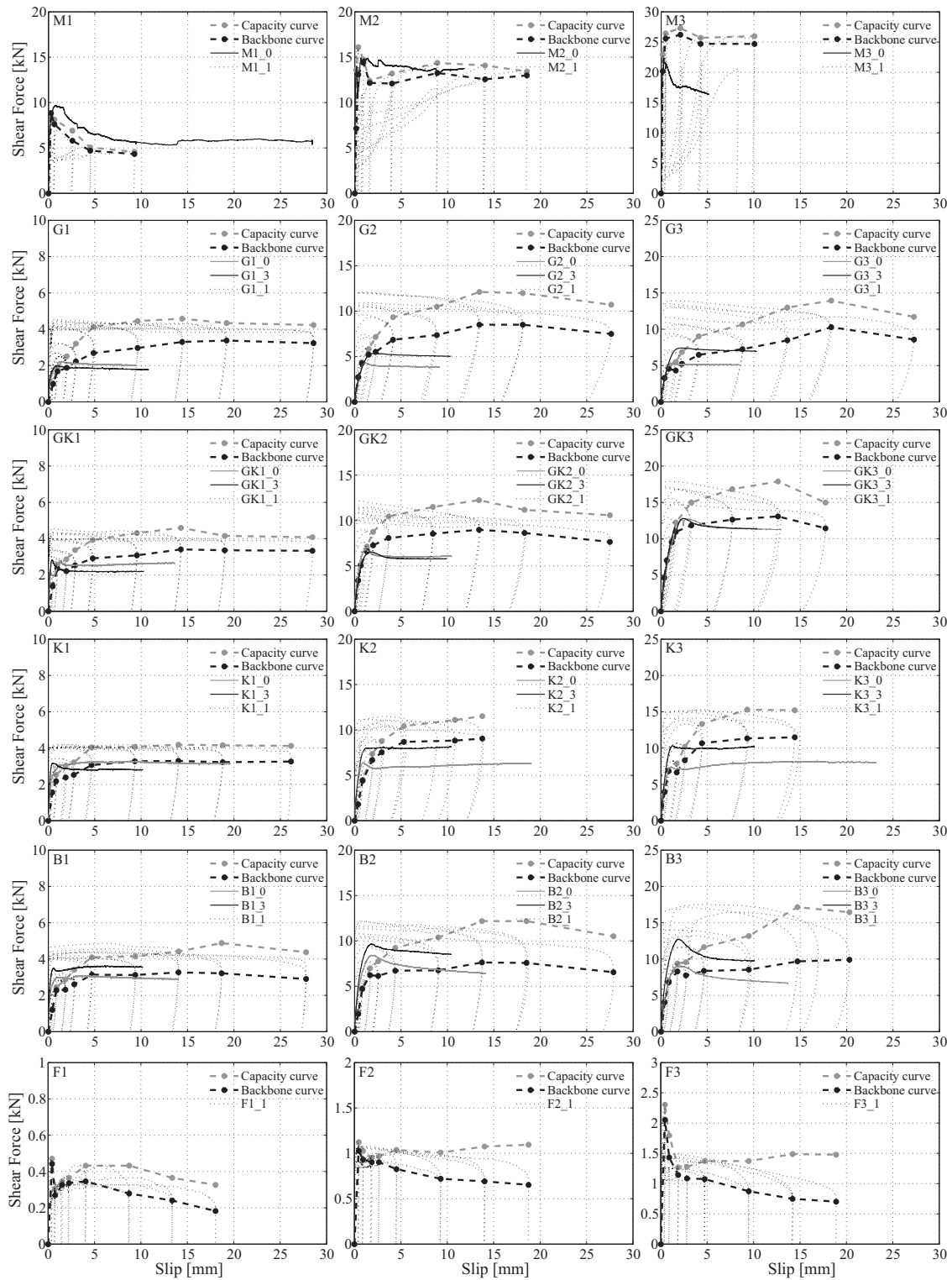
Figure 3-12. Shear force-slip relationships and corresponding backbone and capacity curves

Figure 3-12 show the load-deformation characteristics for all tested series (see also [5]). Each of the diagrams depicts the behavior of specimens subjected to monotonic loading (two solid lines, for both replicates 0 and 3), the hysteresis curve (first quadrant,

i.e. positive values of the shear force and slip) for the corresponding specimen subjected to static-cyclic loading (thin dashed line, for replicate 1). In order to allow for a better comparison, using the hysteretic data the backbone and capacity curves were extracted (dashed lines with markers). The backbone curve connects the points, which pair the maximum slip and the corresponding shear force for each first applied displacement step. Thus, these points lie on the hysteresis curve but do not necessarily show the maximum shear force reached. The maximum shear force values are presented in Figure 3-12 through so called capacity curves. The capacity curves contain points that pair the maximum shear force and the maximum slip in each first applied displacement cycle. The capacity curve points do not lie on the hysteresis curve since these values are not reached simultaneously. In this sense the introduced capacity curves lack a mechanical background, but give useful information on a specimen's behavior. It is clear from Figure 3-12 (see in Appendix A1 for details) that in case of Series G, GK, K and B, specimens subjected to static-cyclic loading could reach a higher shear resistance than those subjected to monotonic loading. Moreover, except for the GK Series, the specimens subjected to monotonic loading with a higher loading speed of 0.5 mm/min (replicates 3) exhibited a higher shear resistance compared to the specimens subjected to monotonic loading with a loading speed of 0.25 mm/min (replicates 0). Figure 3-12 clearly depicts that, for both Series M and F the unloading branch of the hysteresis curve is vertical, which was not the case for the specimens in the other series.

3.2.4.2 Shear stress-normal stress relationship

As previous research indicates, sliding failure of the triplet specimens can be described by the classical Mohr-Coulomb's failure criterion: $\tau = c + \sigma_{pc} \cdot \tan\varphi$, where c denotes the cohesion, φ is the angle of internal friction, i.e. $\tan\varphi$ is a friction coefficient and σ_{pc} is the pre-compression (normal) stress. The friction coefficient in the bed joint can be estimated from the levels of compression and measured bed joint shear resistance by applying linear regression. The resulting linear shear stress-normal stress graphs are shown in Figure 3-13 together with the data obtained from the tests. Note that stresses were calculated using the gross cross-section area of the blocks, $A_b = 120 \times 250$ mm^2, and that for static-cyclic loading only results on the shear resistance from the push cycles were used, cf. Table 3-4. A very good agreement, independent of the built-in core soft layer type, between the test results and a theoretical linear relationship can be clearly seen from Figure 3-13.
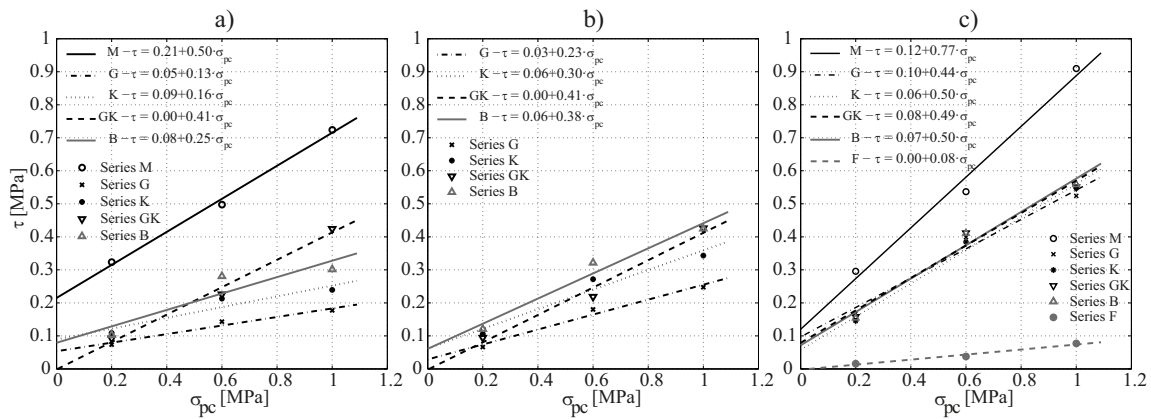
Figure 3-13. Shear stress-normal stress relationships: a) monotonic loading-replicates 0; b) monotonic loading-replicates 3; c) static-cyclic loading (average from both replicates)

Calculated values of the friction coefficient and cohesion in the bed joints for all test series are summarized in Tables 3-5 and 3-6 (see also [5]). For all specimens, except for series M, the obtained values of the cohesion were very small. The (small) apparent cohesion is due to the pre-compression stress. Thus, for practical applications, the small cohesion value can be neglected and the shear resistance of the masonry with multi-layer bed joints could be defined by the product of friction coefficient and existing pre-compression load.

In previous tests on triplets with a bitumen soft layer placed in a bed joint mortar (without protective elastomer layers) and subjected to monotonic loading a considerable apparent cohesion of 0.17 MPa was obtained and the corresponding friction coefficient was 0.06 [23]. Both parameters differ from those obtained in the present tests, see Table 3-5, and show the influence of the applied protective elastomer layers. Inspecting graphs on Figure 3-13c it is striking that the graphs for series GK, K and B are almost congruent and that all three types of multi-layer bed joint have a friction coefficient of about 0.5.

Table 3-5. Shear strength parameters: monotonic tests [5]

	Replicates 0			Replicates 3	
Series	$\tan\varphi$	c [MPa]	Series	$\tan\varphi$	c [MPa]
M	0.50	0.21	-	-	-
G	0.13	0.05	G	0.23	0.03
GK	0.41	0	GK	0.41	0
K	0.16	0.09	K	0.30	0.06
B	0.25	0.08	B	0.38	0.06

36

Table 3-6. Shear strength parameters: static-cyclic tests [5]

Replicates 1			Replicates 2			[a] Average values		
Series	$\tan\varphi$	c [MPa]	Series	$\tan\varphi$	c [MPa]	Series	$\tan\varphi$	c [MPa]
M	0.77	0.12	-	-	-	M	0.77	0.12
G	0.38	0.12	G	0.51	0.08	G	0.44	0.10
GK	0.54	0.06	GK	0.44	0.09	GK	0.49	0.08
K	0.46	0.07	K	0.55	0.04	K	0.50	0.06
B	0.53	0.07	B	0.48	0.07	B	0.50	0.07
F	0.08	0	-	-	-	F	0.08	0

[a] Average from Replicates 1 and 2

3.2.4.3   Influence of the pre-compression level

The applied levels of pre-compression were chosen based on the provisions of the European standard EN 1052-3 [31]. These ensured that the possible (negative) influence of tensile stresses due to bending on the shear stress distribution along the critical shear cross-section (bed joint) was eliminated. It can be seen from Figure 3-5 that the masonry triplet acted as a deep beam subjected to four point bending. Keeping the distance between the loading point and support to a minimum, and applying the pre-compression, which in our case acts as a post-tensioning of the deep beam, it was possible to achieve a proper shear stress distribution in the beam sections subjected to shear, see e.g. [32] for a detailed analysis of this issue.

The influence of the applied pre-compression level on the behavior of the specimens can be seen by comparing the corresponding graphs in Figures 3-9, 3-10 and 3-11. It is clear from such a comparison that the specimens tested under higher pre-compression could reach a higher shear resistance. The relatively large difference in the stiffness and the shear resistance between the specimens with and without multi-layer bed joints can be also clearly seen from the above-mentioned figures.

3.2.4.4   Soft layer degradation

In a previous investigation on monotonically loaded masonry triplets with a soft layer in the bed joints, but without the protective elastomer layers, see [23], it was found out that with the increase of pre-compression level, the degradation of the soft layers also increased. After completing the monotonic tests on masonry triplets with multi-layer bed joints, a modest damage of the soft layers was detected even for the highest level of pre-

compression, see Figure 3-14. Only the surface of the bitumen-based core soft layers was found slightly damaged. However, signs of the sliding motion were visible on the surface of the soft layers for each series and were more pronounced for higher levels of applied pre-compression. Thus, the behavior of soft layers was similar to that from previous investigations and has confirmed that the degradation of the soft layers during monotonic loading is not an issue of concern.
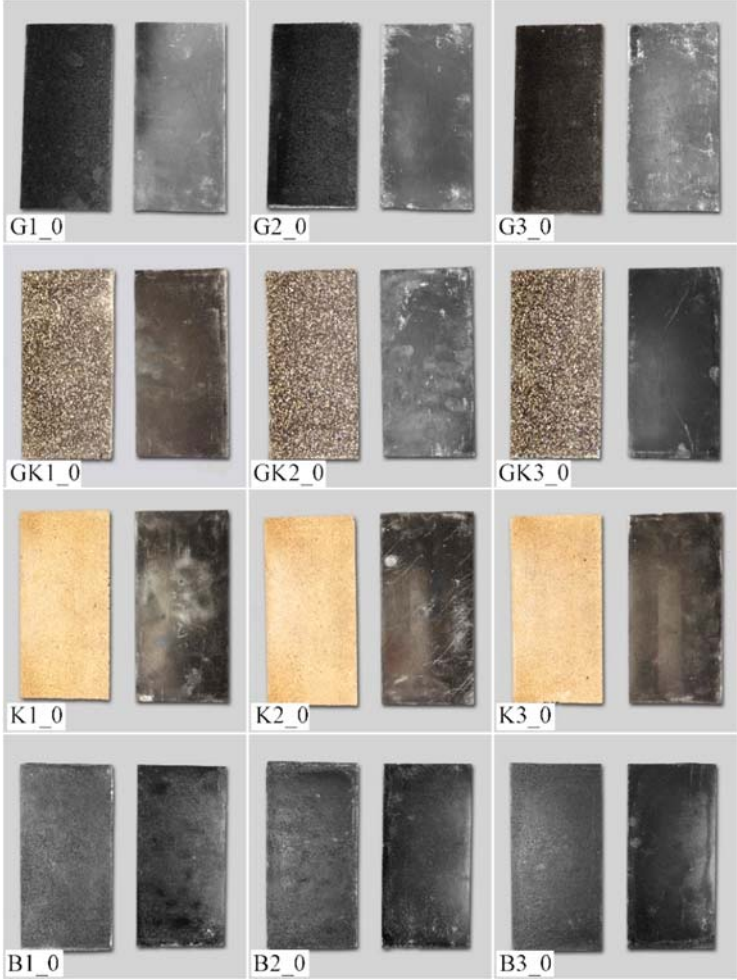

Figure 3-14. Degradation of soft layers: monotonic test (Replicates 0)

On the other hand, in case of static-cyclic shear tests, the extent of the degradation of the soft layers was much higher, and was more severe as the level of pre-compression increased, see Figure 3-15. Previous static-cyclic tests on masonry wallettes with bed joint soft layers made of rubber granulate and extruded elastomer revealed rather large cyclic loading-caused soft layer degradation, especially for rubber granulate layers [3,27]. This was one of the reasons for introducing the multi-layer bed joint, where the core soft layer

is placed between two layers of extruded elastomer that are intended to limit the deterioration of the core layer, as described in Section 3.1.
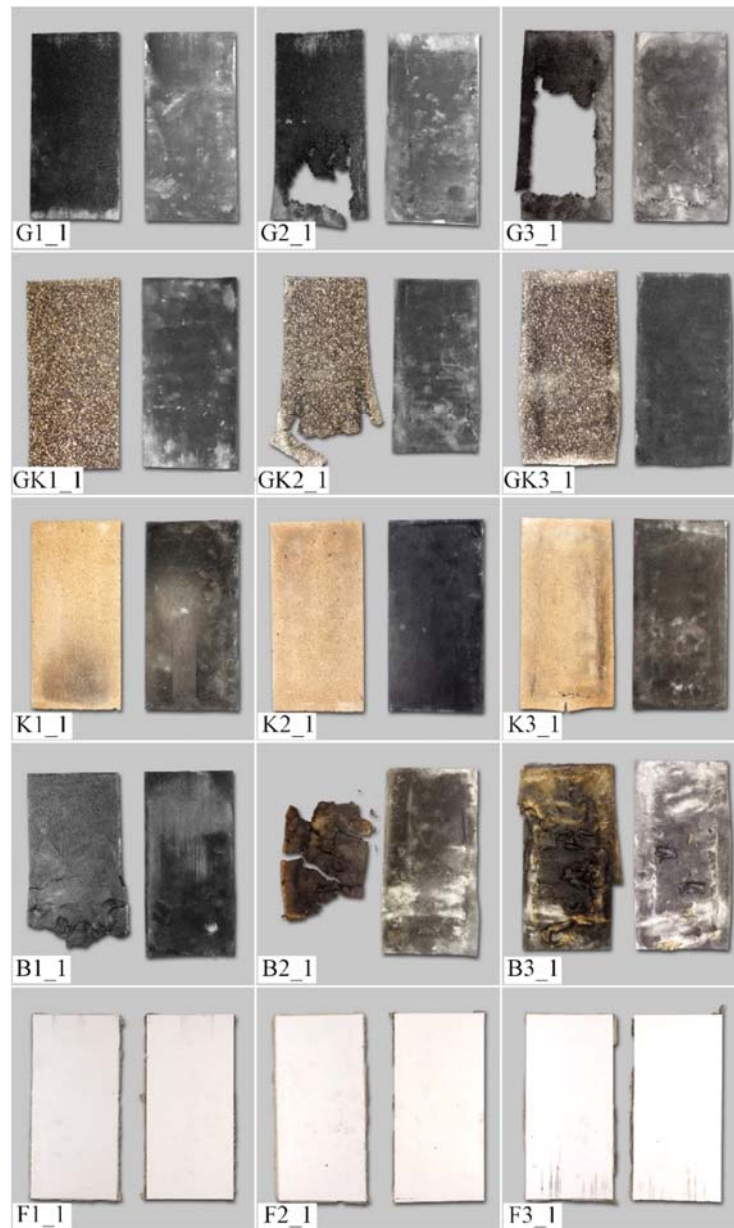

Figure 3-15. Degradation of soft layers: static-cyclic test (Replicates 1)

In the current investigation, as can be seen from Figure 3-15, the most pronounced degradation was noticed for the bitumen and rubber granulate soft layers. Bitumen soft layers were fragmented after completing the static-cyclic tests under higher levels of pre-compression. Similarly, rubber granulate soft layers were significantly damaged after a certain number of loading cycles. As compared to the bitumen and rubber granulate soft layers, cork-rubber granulate and cork soft layers were found as more resistant during the

cyclic loading. They exhibited only local deterioration caused by the damage of the clay blocks. Significant deformation, but not the damage of the protective elastomer layers, was visible for all specimens, especially in case of specimens in which, beside the initial core/elastomer sliding plane, another sliding plane at the interface between the elastomer and mortar was formed. In summary, the protective layers were able to limit but not to eliminate the deterioration of all core soft layers.

3.2.4.5 Influence of the loading speed

A comparison of the results obtained from the monotonic and static-cyclic tests, given as average values from both replicates, indicate the following. First, the values of the shear strength obtained from monotonic tests were lower than those obtained from static-cyclic tests, cf. Tables 3-3 and 3-4. The difference is more pronounced for some types of soft layers and becomes larger as the level of pre-compression increases. Second, for the specimens of series G, GK, K and B subjected to static-cyclic load, the value of the recorded shear force increased as the number of performed cycles increased and that in spite of the fact that sliding occurred already at the small (less than 2 mm) applied displacements. This can be clearly seen from the capacity curves given in Figure 3-12. The capacity curves contain points that pair the maximum shear force and the maximum slip in each first applied displacement cycle, which have different loading speed. Moreover, the shear strength obtained from monotonic tests on specimens subjected to monotonic loading at higher loading speed (0.5 mm/min) was higher than that obtained from tests performed at lower loading speed (0.25 mm/min), cf. Table 3-3. The only exceptions were the tests on the specimens with a cork-granulate core soft layer (Series GK). From these findings it is clear that the loading speed, i.e. the speed of the applied displacements in our case, had a considerable influence on the overall behavior of masonry with multi-layer bed joints, and especially on the friction coefficient and thus on the shear strength. This fact has also been reported in previous investigations, e.g. [21] where it was found that the loading speed affected the shear characteristics of masonry elements with bitumen- and polyester-based DPCs as soft layers placed in bed joints. Figure 3-16 depicts the influence of the loading speed on the value of friction coefficient. Shown shear stress-normal stress relationships are obtained for the second replicates of series G subjected to the static-cyclic load (Specimens G1_2, G2_2 and G3_2) by considering the maximum shear forces measured for each first pushing semi-cycle.
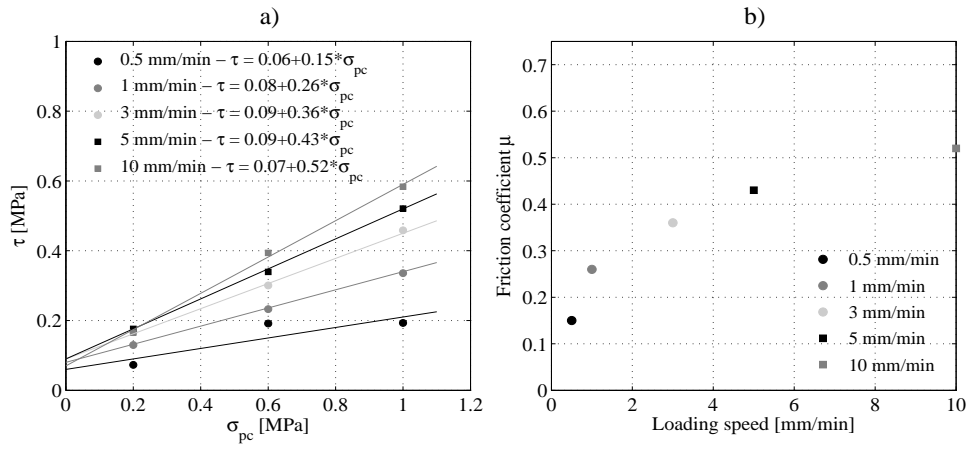
40

Figure 3-16. Shear strength parameters for series G-replicates 2: a) shear stress vs. normal stress for different levels of loading speed; b) friction coefficient for different levels of loading speed

3.3 Compression tests of URM wallettes with a multi-layer bottom bed joint

The main goal of the conducted series of material-level tests was to investigate the effect of a multi-layer bed joint on the compressive strength and vertical deformation of URM. A total of 15 URM wallettes, made with or without a multi-layer bottom bed joint, were subjected to compression up to failure. The compression load was applied in direction perpendicular to the bed joints. It appears that only the multi-layer bed joint with a rubber granulate core soft layer leads to the somewhat lower compressive strength of masonry, while the vertical deformability of masonry is influenced by all types of considered multi-layer bed joints. The findings presented within this section have already been partly published in [33].

3.3.1 Test programme and masonry materials

A total of 12, nominally 600 mm wide, 1000 mm high and 150 mm thick URM wallettes with four different types of a multi-layer bottom bed joint, have been prepared for testing (three replicates for each type of a multi-layer bed joint). The same types of core soft layer were used as in case of in-plane shear tests on masonry triplets, namely rubber granulate, cork-rubber granulate, cork and bitumen soft layer, cf. Figure 3-2. In addition, three wallettes with the same dimensions, but without a multi-layer bed joint were constructed to serve as control specimens. All wallettes were built in running bond using a typical Swiss perforated clay blocks with nominal dimensions 290x190x150 mm and a void area of 42%, see Figure 3-17.

Figure 3-17. Swiss perforated clay block used for the construction of the wallettes

The average compressive strength of the perforated block, determined according to the European standard EN 772-1 [30] amounted to 31.5 MPa with standard deviation of 2.38

42

MPa. A standard cement mortar, with values of mean compressive strength of 10.46 MPa with standard deviation of 0.90 MPa, and 6.92 MPa with standard deviation of 0.39 MPa, measured for mortar specimens stored in the climatic chamber and in open air in the laboratory, respectively, was used to produce bed and head joints. All bed and head joints were 10 mm thick except the multi-layer bottom bed joint, whose thickness, including the mortar layers, was larger and varied between about 16.5 mm and 18 mm, depending on the thickness of the core soft layer, cf. Table 3-7. The used mortar did not allow for mortar layers thinner than about 5 mm.

Figure 3-18. Construction and storage of the wallettes

All specimens were constructed by experienced bricklayers and were kept in the open air in the laboratory. The curing time before testing was at least 28 days. During the construction of the wallets with a multi-layer bed joint, each core soft layer, together with two protective outer layers of 2.2 mm thick extruded elastomer, was placed in the middle of the mortar layer of the bottom bed joint, see Figure 3-18. Than the wallettes were built as usual. A summary of the test programme is given in Table 3-7.

Table 3-7. URM wallettes with a multi-layer bed joint: test programme

Series	(Core) soft layer type	Soft layer thickness [mm]	Number of replicates
R	No soft layer	-	3
RG	Rubber granulate	3.0	3
RGK	Cork-rubber granulate	3.2	3
RK	Cork	3.5	3
RB	Bitumen	2.0	3

3.3.2 Test set-up, testing procedure and measurements

The specimens were tested in the laboratory of the Institute of Structural Engineering of ETH Zurich using a universal testing machine, see Figure 3-19. The tests were performed

according to the European Standard EN 1052-1 [34]. To ensure a uniform load distribution, a soft wood, i.e. a wood-fiber plates were placed between the specimen and spreader beams in each test. The spreader beams were fixed to the testing machine. The vertical (compressive) load was applied at the constant speed of 27 kN/min up to failure of the specimen. The loading speed was determined in such a way so as to attain the specimen failure after 15-20 min of testing. Apart from the applied vertical load, measurements included vertical and horizontal deformations of the specimen. Vertical and horizontal deformations were measured by means of three LVDTs both on North and South side of the specimen, see Figure 3-19. All measuring devices were connected to a computer, which processed the data in real time. It should be noted that LVDTs were removed after reaching about 60% of the ultimate vertical load.
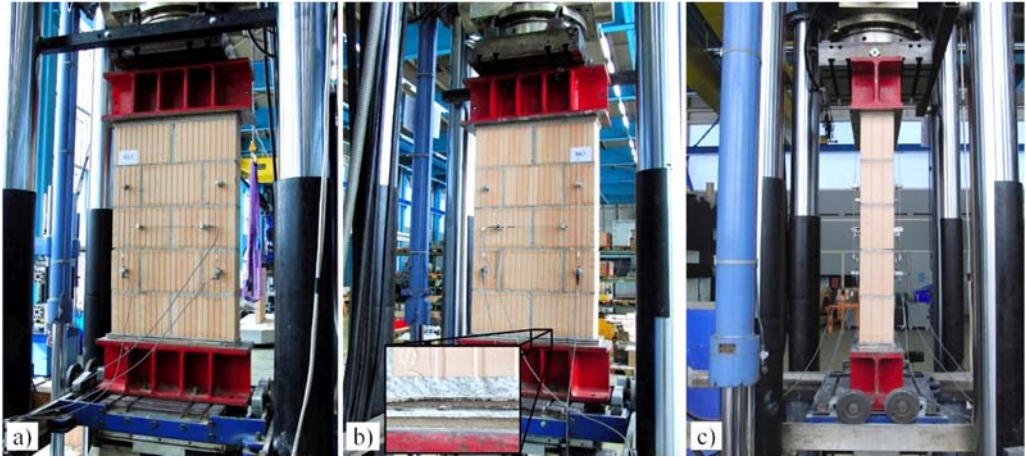

Figure 3-19. Test set-up and measuring devices: a) South specimen's side; b) North specimen's side; c) West specimen's side
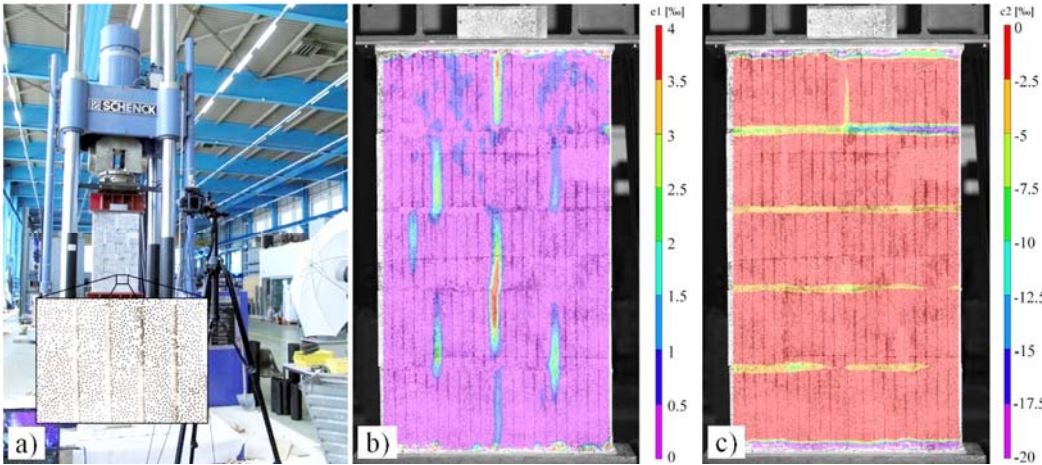

Figure 3-20. Specimen RB3: a) implemented 2D-DIC measurement system and the applied pattern; b) major principal strain field; c) minor principal strain field

44

Besides a conventional hard-wired measuring system (LVDTs), a 2D Digital Image Correlation (DIC) measurement system was used to obtain the information on the strain field on the surface of a specimen during the tests on third replicate of series RG, RGK and RB. DIC is a non-contact optical system that measures displacements directly by comparing consecutive digital images of the specimen's surface obtained before and after deformation. This measurement system requires a random pattern to be applied on the surface of tested object. The same DIC system was used throughout the whole research project. More details about the implemented DIC system can be found in [35,36]. The computer used for data acquisition triggered the DIC camera every 10 seconds. Figure 3-20 shows exemplarily the details of the applied pattern (circles of 1.5 mm diameter on the area of 140x95 mm) and the evaluated strain fields of specimen RB3. The strain fields depicted correspond to the vertical load of 360 kN (about 75% of the ultimate load).

3.3.3 Test results and specimen behavior

Table 3-8 shows the values of the masonry compressive strength perpendicular to the bed joints, f_x, and values of the modulus of elasticity, E_x, for each tested specimen (see also [33]).

Table 3-8. Compression tests on URM wallettes: test results

Specimen	f_x [MPa]	f_{xm} [MPa]	COV [%]	E_x [MPa]	E_{xm} [MPa]	COV [%]	E_{xm}/f_{xm}
R1	4.9			5499			
R2	5.4			4738			
R3	5.3	5.2	3.9	5579	5272	7.2	1014
RG1	4.9			6054			
RG2	4.1			3793			
RG3	4.9	4.6	8.5	4894	4914	18.8	1068
RGK1	5.4			4116			
RGK2	4.9			5138			
RGK3	5.5	5.3	4.4	4459	4571	9.3	862
RK1	4.8			5444			
RK2	4.9			5724			
RK3	5.3	5	4.2	5800	5656	2.7	1131
RB1	4.9			4321			
RB2	5.1			5251			
RB3	5.3	5.1	1.9	4548	4707	8.4	923

Further, their mean values, f_{xm} and E_{xm}, for each test series and corresponding coefficients of variation, COV, are also given. Values of f_x are calculated by dividing the measured ultimate vertical loads with the wallette nominal horizontal cross-section area = 600x150 mm^2. Modulus of elasticity is determined as a secant modulus by considering the strains measured at the vertical load level equal to one third of the ultimate load.
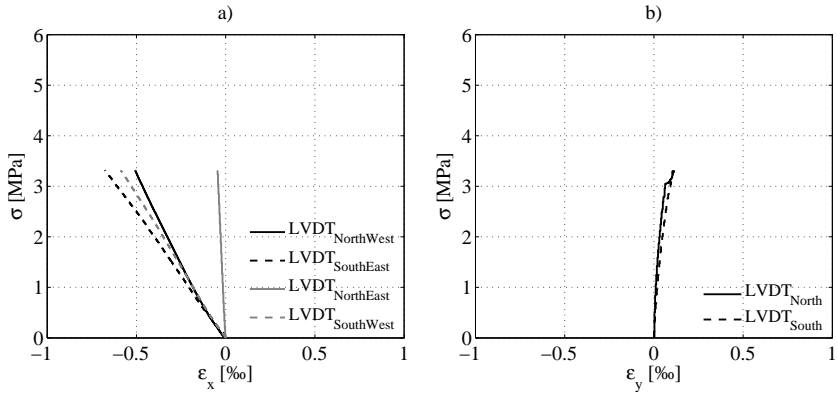

Figure 3-21. Vertical stress-strain curves for Specimen R3: a) vertical strains ε_x; b) horizontal strains ε_y
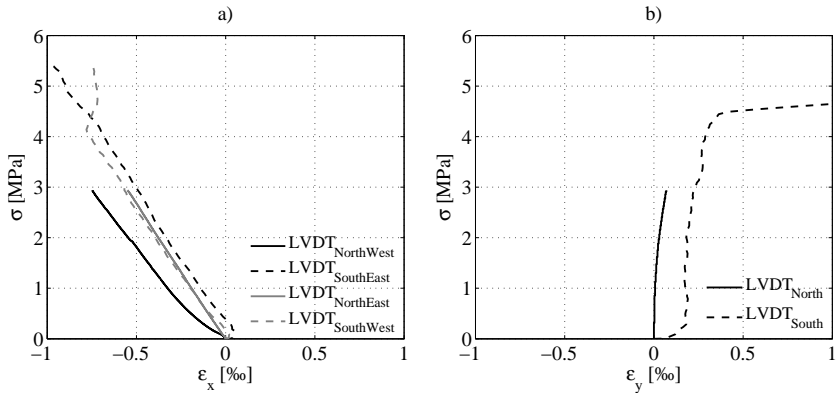
Figure 3-22.Vertical stress-strain curves for Specimen RGK3: a) vertical strains ε_x; b) horizontal strains ε_y
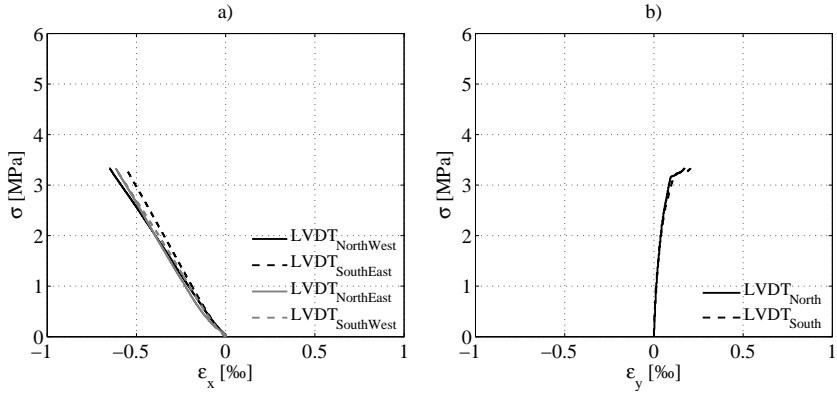
Figure 3-23. Vertical stress-strain curves for Specimen RB2: a) vertical strains ε_x; b) horizontal strains ε_y

46

Figures 3-21, 3-22 and 3-23 show exemplarily the relationships between the nominal vertical (normal) stress, σ, and measured vertical and horizontal strains, ε_x and ε_y, obtained for wallettes R3, RGK3 and RB2 (the direction perpendicular to the bed joints of the wallette is considered as vertical one). Note that the strains at the South side of the specimen RGK3, see Figure 3-22, are obtained using the DIC software VIC-2D [37]. VIC-2D software allows for positioning of the virtual LVDT at any place of the specimen's surface, whose digital images taken before and after deformation are correlated. Those positions are chosen to match the positions of corresponding LVDTs on the North side of the wallette.
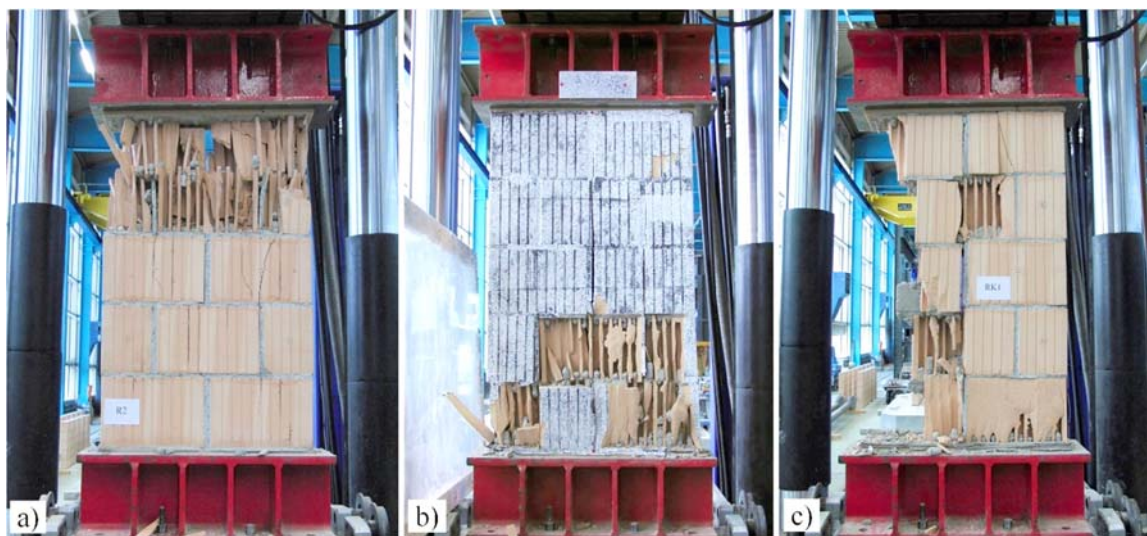

Figure 3-24. Failure pattern: a) Specimen R2; b) Specimen RB3; c) Specimen RK1

The failure patterns observed during the tests were characteristic for clay block masonry failing in compression and were, in general, governed by the tensile strength of the units, see Figure 3-24. Subjected to the vertical load, the specimen failed when the tensile strength in one of the directions orthogonal to the applied vertical load was exceeded. In some tests, a typical vertical cracking and dividing of a specimen into several pillars was observed, cf. Figure 3-24c. A larger number of cracks as well as larger openings of the vertical cracks were observed for specimens with a multi-layer bed joint than for those without soft layers. For all specimens without a multi-layer bed joint, the cracks appeared first in the upper portion of the specimen and progressed towards the bottom of the specimen in the course of the test, see Figure 3-24a. For specimens with a multi-layer bed joint, the cracks appeared first in the lower portion of the wall (adjacent to the multi-layer bed joint) and subsequently progressed towards the top of the specimen,

see Figure 3-24b. This can be explained by the fact that, since consisted of rubber-based materials, a multi-layer bed joint have a higher Poisson's ratio than the conventional mortar bed joint, which in turn has a higher Poisson's ratio than the clay block. This difference between the Poisson's ratios of the clay block and the bed joint induces tensile splitting of the blocks in the lateral direction(s) and eventually causes the failure of the specimen (larger difference induces larger tensile stresses).

3.3.4 Discussion

In the following, the test results are discussed in respect to the influence of the multi-layer bed joint on the specimen's response characteristics. In addition, the degradation of elastomer and core soft layers during testing is addressed.

3.3.4.1 Influence of the multi-layer bed joint

It can be seen from Table 3-8 that specimens with a rubber granulate core soft layer in the multi-layer bed joint (Series RG), had around 10% less compressive strength as compared to the control specimens (Series R), while specimens with other core soft layer types showed only minor differences. Such a reduction in the strength is usually neglected in practical applications and masonry code provisions. However, the recently revised Swiss Structural masonry code SIA 266 [38] introduced the new provision, which require that this reduction has to be taken in account in structural masonry design. Moreover, values of modulus of elasticity given in Table 3-8 indicate that the multi-layer bed joint influenced the vertical deformation of specimens. That influence depended on the type of the core soft layer. With respect to the specimens without a multi-layer bottom bed joint (R series), specimens from RG, RGK and RB series had 6.8%, 13.3% and 10.7% lower modulus of elasticity, respectively, while the modulus of elasticity of specimens from RK series was higher for 7.3%.

3.3.4.2 Degradation of elastomer and core soft layers

Figure 3-25 shows exemplarily the soft layers after the tests on specimens RG1, RGK1, RK1 and RB1. Degradation was similar for all replicates. A permanent deformation in shape of prints of the block cross-section could be observed both on elastomer and core soft layers. In addition, a vertical stress concentration-caused local damage of the elastomer and/or core soft layers was detected in specimens from series RG and RB. Those stress concentrations resulted from the lateral tensile cracking of the specimen's bottom

48

block course and reduction of the horizontal cross-section area. In general, all four types of multi-layer bed point exhibited satisfactory behavior under applied compressive load.
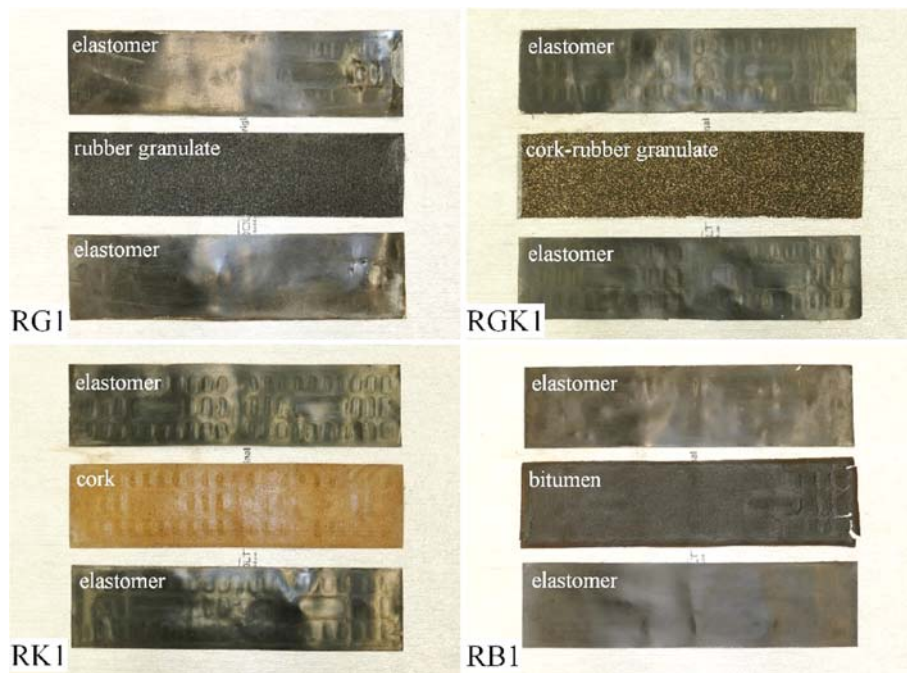

Figure 3-25. Degradation of soft layers

3.4 URM walls with a multi-layer bottom bed joint subjected to in-plane static-cyclic shear load

In order to gain an insight into the behavior of masonry structural elements with a multi-layer bed joint, a total of 9 URM walls with a multi-layer bottom bed joint were tested under the combined action of vertical and static-cyclic shear load up to failure. The preliminary testing phase was conducted to choose the most suitable core soft layer type among the four types considered (rubber granulate, cork, cork-rubber granulate and bitumen). The main testing phase comprised five tests on storey-high URM walls with rubber granulate core soft layers. Those structural element-level tests allowed investigating the influence of the wall size, the pre-compression level and the aspect ratio on the seismic behavior of URM walls with a multi-layer bed joint. Sliding occurred in all tests performed. However, the final failure mode as well as the displacement capacity of tested walls were governed by the extent of shear cracks that develop in the wall as well as by the appearance of (vertical) tensile cracks in the head joints at the bottom block course, which further tended to reduce the effective area of the wall. A method to construct an idealization of the horizontal force-displacement response envelope for the tested URM walls with multi-layer bed joints is proposed and the equations to estimate the idealization parameters are given. The findings presented within this section have already been partly published in [39,40].

3.4.1 Test programme and masonry materials

Table 3-9 summarizes the test programme, where l_w, h_w and t_w are the length, height and thickness of the specimens (see Figure 3-26), σ_{pc} is the pre-compression stress computed with reference to the nominal wall cross-section area $A_w = l_w \cdot t_w$, t_{csl} is the thickness of core soft layer, and f_x is the mean compressive strength of the masonry perpendicular to the bed joints. It should be noted that the value measured for wallettes without a multi-layer bed joint is considered as f_x, see Section 3.3.3. All walls were tested under fixed-end boundary conditions. Within the first phase of the experimental programme and according to findings from shear tests on masonry triplets and compression test on masonry wallettes, which are presented in Sections 3.2 and 3.3, respectively, four different core soft layer types, namely rubber granulate, cork rubber granulate, cork and bitumen, were tested. The objectives of the preliminary phase were to determine the most promising type of core soft

layer for the main testing phase, and to verify the applied vertical pre-compression levels and the measurement system. For that purpose, a total of four static-cyclic tests on 1600 mm high and 1500 mm long, full-scale URM walls were performed.

Table 3-9. URM walls with a multi-layer bed joint: test programme [40]

Phase	Specimen	Core soft layer	t_{csl} [mm]	Dimensions l_wxh_wxt_w [mm]	Aspect ratio	σ_{pc}/f_x
Preliminary	WG	Rubber granulate	3	1500x1600x150	0.94	0.10
Preliminary	WGK	Cork-rubber granulate	3.2	1500x1600x150	0.94	0.10
Preliminary	WK	Cork	3.5	1500x1600x150	0.94	0.10
Preliminary	WB	Bitumen	2	1500x1600x150	0.94	0.10
Main	Z1	Rubber granulate	3	2700x2600x150	1.04	0.10
Main	Z2	Rubber granulate	3	2700x2600x150	1.04	0.05
Main	Z3	Rubber granulate	3	2700x2600x150	1.04	0.20
Main	Z5	Rubber granulate	3	1800x2600x150	0.69	0.10
Main	Z6	Rubber granulate	3	3600x2600x150	1.38	0.10

The main phase comprised another five tests on large, story-high walls with a multi-layer bed joint. A rubber granulate soft layer was chosen as a core layer based on the overall behavior and performance exhibited during the preliminary testing phase. Comparison of the tests results with the results of the test on Specimen Z1, chosen as the reference specimen, enables the investigation of the influence of the pre-compression level (Specimens Z2 and Z3) and the aspect ratio (Specimens Z5 and Z6) on the seismic behavior of URM walls with a multi-layer bed joint. Moreover, the results obtained from the preliminary and the main test phases allow for an investigation of the size effect.

Specimens were constructed in running bond with nominally 10 mm thick mortar fully filled bed and head joints. Figure 3-26 shows the structure of the multi-layer bed joint, comprising the mortar layers, the 2.2 mm thick protective layers made of extruded elastomer and the core soft layer. Four different types of core soft layers investigated in this study are also shown in Figure 3-26. The thickness of the multi-layer bed joint, excluding the mortar layers, ranged between 6.4 and 7.9 mm depending on the type of the core soft layer, while the total thicknesses of a multi-layer bed joints, including the mortar layers, ranged between 15 and 18 mm. The specimens of both test phases were built by experienced bricklayers in separate batches, but with the same materials (except mortar),

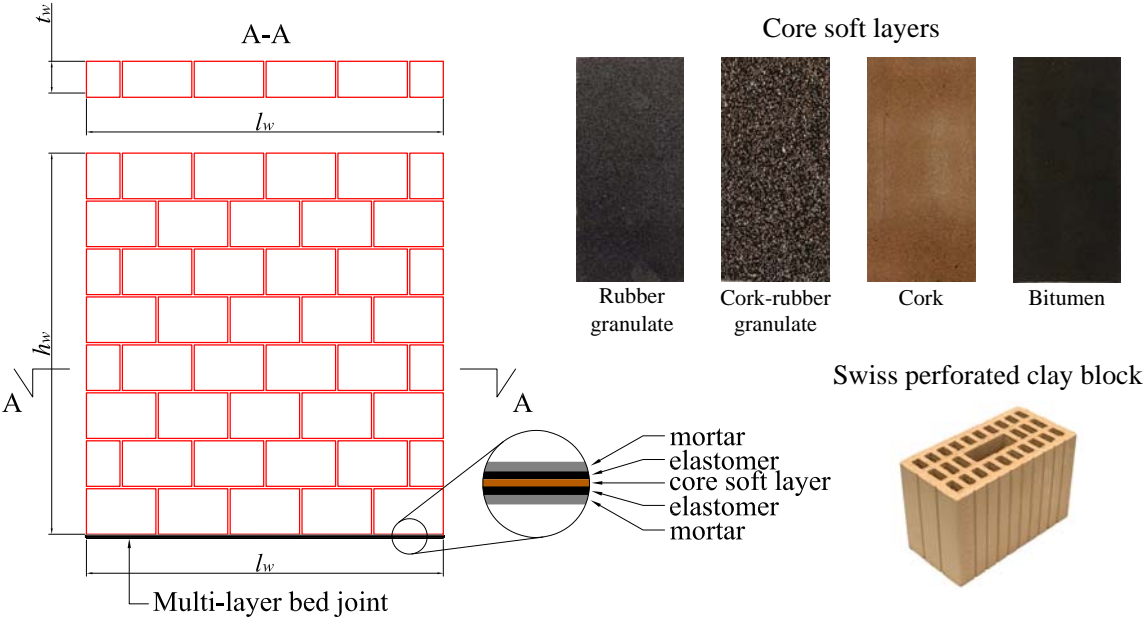see Figure 3-27, and were kept in open air in the laboratory for a minimum of 28 days before testing.

Figure 3-26. Specimen layout and materials [40]

Figure 3-27. Construction of the specimens

Typical Swiss perforated clay blocks, with nominal dimensions of 290x150x190 mm and void area of 42%, were used to build the specimens for both testing phases, cf.

Figure 3-26. As reported in Section 3.3.1, the measured compressive strength of the blocks was equal to 31.5 MPa with standard deviation of 2.38 MPa. The compressive strength of standard cement mortar used to produce the bed and head joints was determined by testing the mortar prisms with dimensions of 40x40x160 mm. The prisms were tested according to EN 1015-11 [29] after a curing period of at least 28 days. The same mortar was used to build the specimens of the preliminary phase and the wallettes for the compression tests addressed in Section 3.3. As reported in Section 3.3.1, the values of mean compressive strength of 10.46 MPa with standard deviation of 0.90 MPa, and 6.92 MPa with standard deviation of 0.39 MPa, were measured for mortar specimens stored in the climatic chamber and in open air in the laboratory, respectively. The measured values of mean compressive strength of mortar used to prepare the specimens of the main phase were 11.23 MPa with standard deviation of 1.93 MPa, and 7.90 MPa with standard deviation of 0.96 MPa, for mortar specimens stored in the climatic chamber and in open air in the laboratory, respectively. The masonry compressive strength perpendicular to the bed joint direction, f_x, determined from the compression tests (Section 3.3), is assumed as valid for masonry from both testing phases.

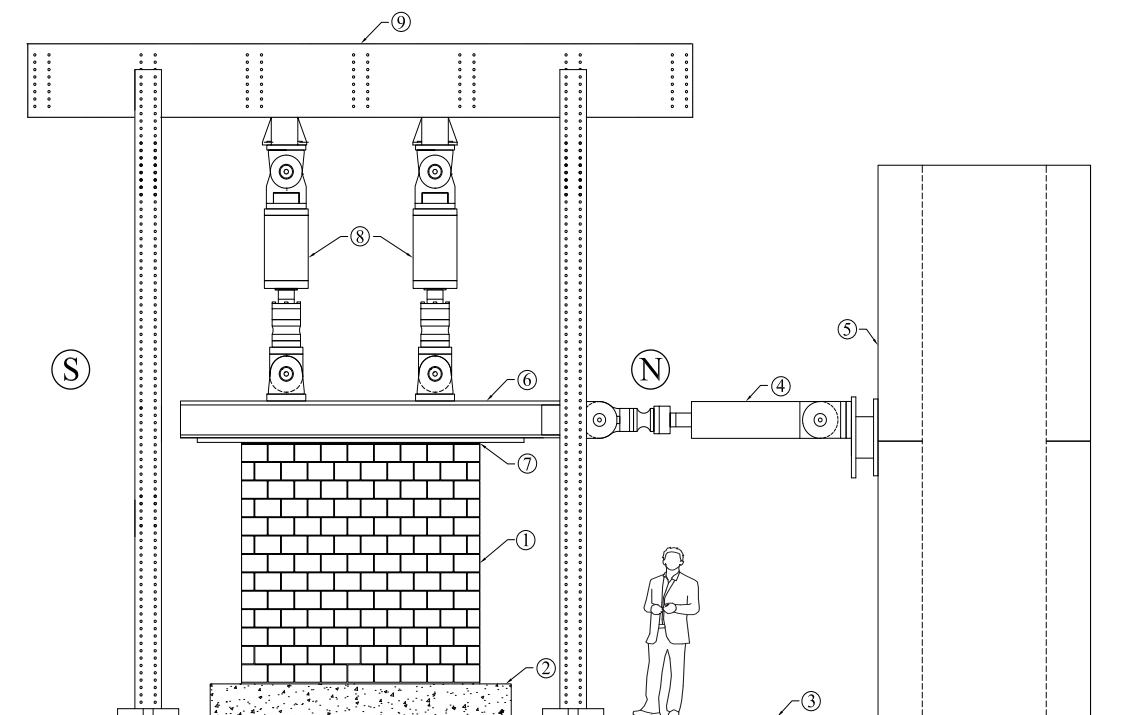## 3.4.2 Test set-up, testing procedure and measurements

Figure 3-28. URM walls with a multi-layer bed joint: drawing of the test set-up [40]

The drawing of the test set-up is shown in Figure 3-28. The specimens (1) were built on 350 mm thick reinforced concrete pedestals (2), which in turn were clamped to the laboratory strong floor (3) by means of post-tensioned steel bars. The horizontal servo-hydraulic actuator (4), connected to the reaction wall (5), was used to apply horizontal displacements to the top of the walls through a stiff horizontal steel loading beam (6). The loading beam was connected to the walls by a layer of mortar (7). The mortar layer also ensured uniform vertical load distribution. The vertical load was applied by means of two servo-hydraulic actuators (8) reacting on the reaction frame (9). In order to prevent any out-of-plane movement of the loading beam, an auxiliary, low friction sliding system (not shown in Figure 3-28) was used to guide the web of the loading beam (6) during the tests.

Table 3-10. Loading history for static-cyclic shear tests

Preliminary testing phase (h_w = 1600 mm)			Main testing phase (h_w = 2600 mm)		
Target drift ratio [%]	Loading speed [mm/min]	Period [sec]	Target drift ratio [%]	Loading speed [mm/min]	Period [sec]
0.025	0.4	240	0.015	0.37	250
0.05	0.8	240	0.025	0.62	250
0.075	1.2	240	0.05	1.25	250
0.1	1.6	240	0.075	1.87	250
0.15	2.4	240	0.1	2.5	252
0.2	3.2	240	0.15	3.74	250
0.25	3.2	300	0.2	4.99	250
0.3	3.6	320	0.25	5.67	275
0.35	3.6	373.3	0.3	5.76	325
0.4	3.6	426.7	0.35	5.82	375
0.5	4.5	426.7	0.4	5.87	425
0.6	5.4	426.7	0.5	7.34	425
0.8	5.8	529.6	0.6	8.81	425
1	6	640	0.8	9.51	525
1.2	7.5	640	1	9.6	650
1.5	8	720	1.5	13.87	675
1.75	8	840	2	17.21	725
2	8	960	3	24.96	750

For each test, a specimen was first pre-compressed to the designated stress level, simulating the gravity load supported by the wall. The pre-compression load was applied in the force-controlled manner with a constant force speed of 1-3 kN/s, depending on the

target magnitude (higher force speed for was used for higher pre-compression load magnitude), and was kept constant during the test. Subsequently, a specimen was subjected to the static-cyclic shear load that was applied using computer-controlled displacement steps chosen to have the form of a sinusoidal wave. Each step was repeated three times. All tests started with a push cycle (positive horizontal displacement and force). The loading speed was determined by the corresponding target displacement, i.e. the loading speed increased with increasing target displacement. Loading histories used for the preliminary and main testing phase are presented in Table 3-10, where the target drift ratio is the value of target displacement divided by the specimen's height.

All specimens were tested under fixed-end boundary conditions, i.e. the rotation at the top and the bottom of the specimen was restricted. The fixed-end boundary conditions were ensured by a mixed force-displacement control of the vertical actuators which, besides the role of keeping the pre-compression level constant during the tests, have been used to keep the loading beam horizontal. More detailed information about the test controlling system can be found in [41]. Each test was stopped either due to critical damage conditions or when the response of the specimen was stable and no difference in response quantities between several consecutive loading history steps was observed.

All measured data were recorded and processed in real time. Apart from the applied vertical and horizontal loads and the displacements of the servo-hydraulic actuators, measurements comprised vertical, horizontal and diagonal deformations of the specimens, cf. Figure 3-29. Vertical deformations were measured by means of a pair of potentiometers (POTs), WVN and WVS. Potentiometers WHB, WHM and WHT measured horizontal deformations (WHM was not implemented during the preliminary testing phase). Further, diagonal deformations of the walls were captured using another two POTs, WD1 and WD2. Linear variable differential transformers (LVDTs) NS, MSN, MSS and SS were applied to measure the sliding displacement (slip) of the specimen along the multi-layer bed-joint with respect to the reinforced concrete pedestal. The vertical (uplift) displacement along the multi-layer bed-joint was measured by means of NU1, NU2, SU1 and SU2 (an additional pair was used for the test on the longest specimen, Z6), while LVDTs TSD1-4 were used for measuring the vertical displacements at the top of the specimen. The horizontal displacement of the top of the specimen was measured on the North side (WTLaser). Another laser measuring device (CTRLaser) was used to

control the horizontal displacement of the loading beam. The vertical displacement of the loading beam on the North and the South sides was captured by means of NVD and SVD, respectively. These two LVDTs were part of the test controlling system. LVDTs WBSN and WBSS were installed to detect the (possible) slip between the loading beam and the specimen, while the slip between two constituent parts of the loading beam was tracked by means of LVDT PBS. Finally, potentiometers CUN, CUS and CS were installed to monitor the vertical as well the horizontal displacement of the concrete pedestal.
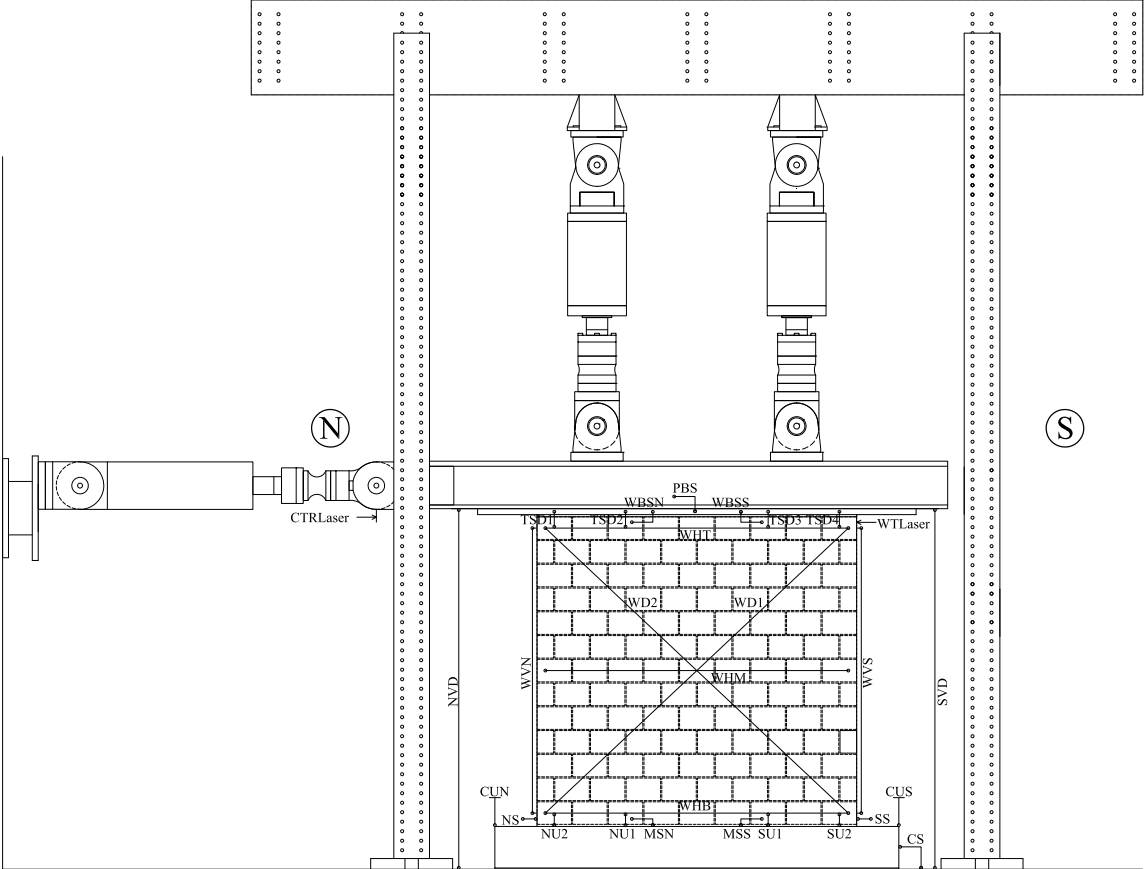
Figure 3-29. Plan of measuring devices [40]

Besides a conventional hard-wired measuring system (LVDTs and POTs), a 2D DIC measurement system was used to obtain the information on the deformation field on the surface of a specimen during a test, see Figure 3-30. The computer used for data acquisition triggered the DIC cameras at the predefined displacement levels in each cycle performed. Figures 3-31 and 3-32 show example of the details of the applied patterns and the evaluated global and local strain fields of specimens WK and Z3.
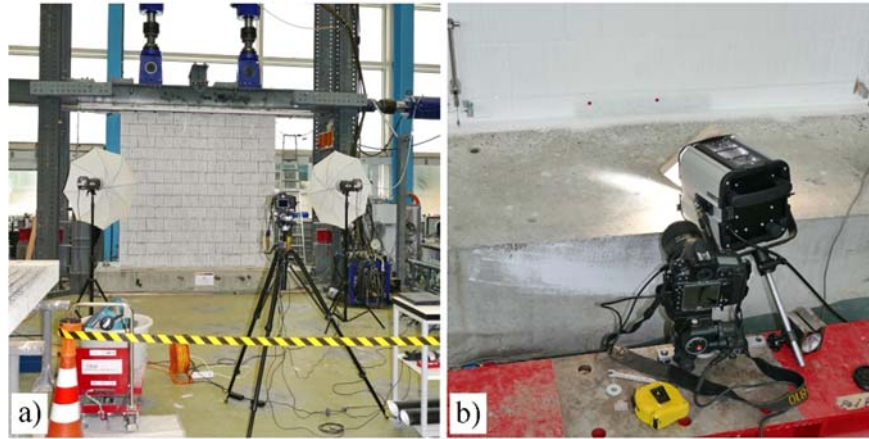
Figure 3-30. Used 2D-DIC measurement system: a) global (East face); b) local (West face) [40]
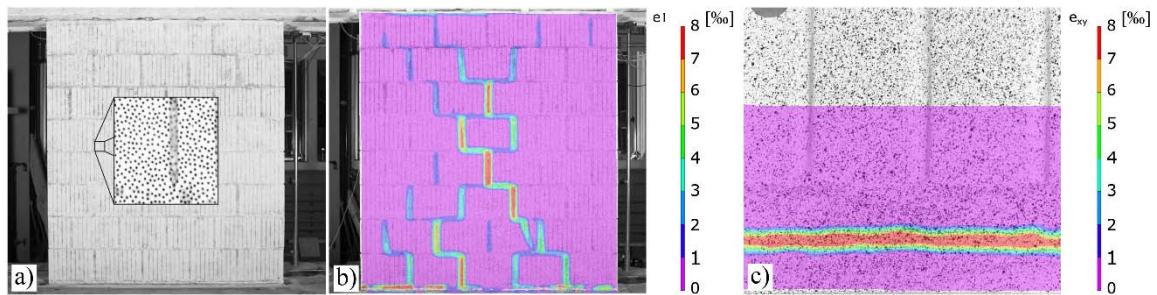
Figure 3-31. Specimen WK: a) applied pattern; b) major principal strain field at the target displacement of 3.2 mm; c) local shear strain field at the target displacement of 0.4 mm [40]
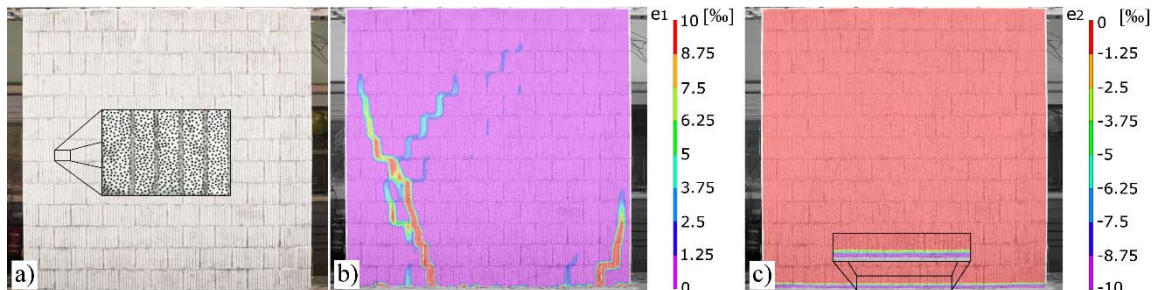

Figure 3-32. Specimen Z3: a) applied pattern; b) major principal strain field at the target displacement of 5.2 mm; c) minor principal strain field at the pre-compression stress of 1.04 MPa [40]

3.4.3 Test results and specimen behavior

The values of the extreme (maximum and minimum) horizontal force, H_{max} and H_{min}, and horizontal displacement, d_{max} and d_{min}, recorded during testing are summarized in Table 3-11. Further, the extreme horizontal displacements in terms of drift ratio δ (i.e. displacement values normalized by the specimen height), as well as the values of the specimen's initial (tangent) stiffness, K_0, and displacements $d_{t,\,max}$ and $d_{t,\,min}$ corresponding to the occurrence of significant loss of horizontal force resistance are also reported.

57

Table 3-11. Measured response characteristics [40]

Specimen	H_{max} [kN]	H_{min} [kN]	d_{max} [mm]	d_{min} [mm]	$d_{t,\,max}$ [mm]	$d_{t,\,min}$ [mm]	δ_{max} [%]	δ_{min} [%]	K_0 [kN/mm]
WG	57.71	-63.86	12.8	-12.8	6.4	-6.4	0.8	-0.8	43.95
WGK	59.19	-69.19	9.6	-9.6	6.4	-5.6	0.6	-0.6	54.06
WK	55.74	-65.97	6.4	-6.4	4.8	-4.8	0.4	-0.4	53.92
WB	56.08	-59.51	9.6	-9.6	-	-	0.6	-0.6	65.54
Z1	103.70	-95.53	39	-39	-	-	1.5	-1.5	98.59
Z2	77.63	-71.45	52	52	-	-	2.0	-2.0	81.80
Z3	141.17	-140.81	13	-13	9.1	-9.1	0.5	-0.5	100.10
Z5	68.09	-69.68	9.1	-9.1	-	-	0.35	-0.35	44.49
Z6	171.41	-164.68	15.6	-15.6	7.8	-7.8	0.6	-0.6	107.80

The horizontal force-displacement response hysteresis curves of the tested specimens are shown in Figure 3-33 (see Appendix A2 for details). The deformation value shown in the diagrams is the horizontal displacement of the loading beam, which can be considered as representative of the displacement of the top of the walls, since, in each test, no slip between the loading beam and the wall was recorded. Note the different axis scaling for some of the presented hysteresis curves: this was chosen to present clearly the development of the hysteretic response.
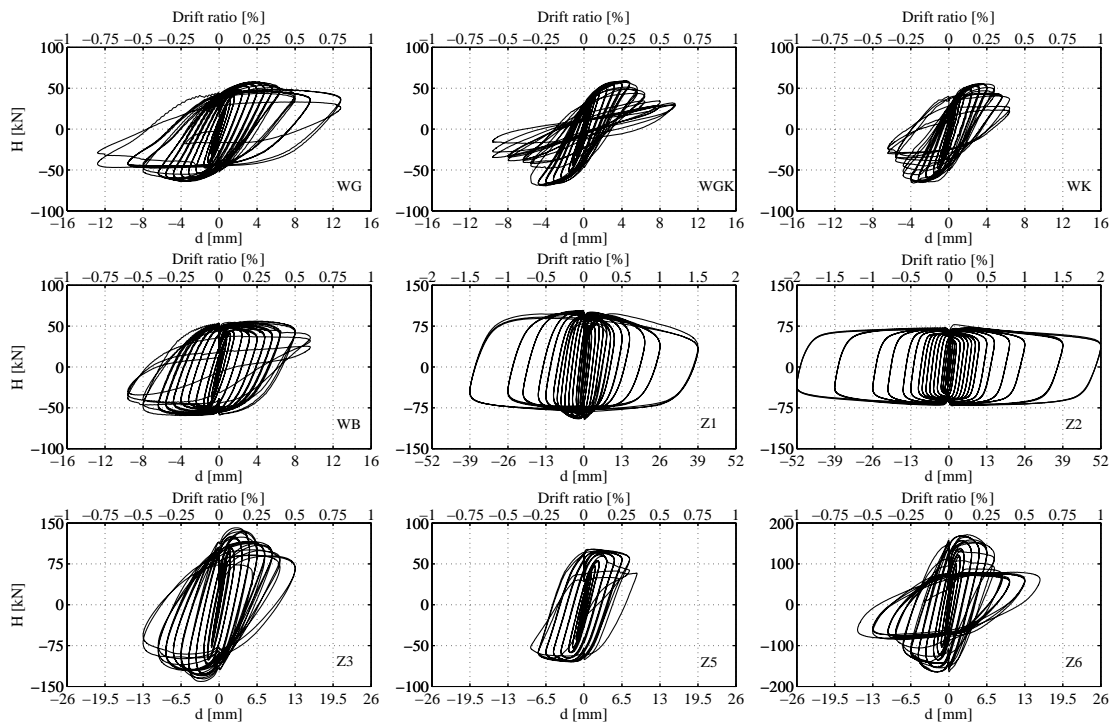

Figure 3-33. Horizontal force-displacement response hysteresis curves for both testing phases [40]

Figure 3-34 shows the values of the equivalent viscous damping ratio, ξ_{eq}, used to measure the energy dissipation characteristics. As stated in [42], the most common method for defining equivalent viscous damping is to equate the energy dissipated in a vibration cycle of the actual structure (the area enclosed by the hysteresis loop) and an equivalent viscous system (a function of the strain energy). The values given are calculated for each first cycle applied and plotted against the corresponding target displacement. Evidently, a well-developed sliding response in Specimens Z2, Z1 and WB results in almost ideal elastic-plastic horizontal force-displacement response hysteresis loops (cf. Figure 3-33) and very high values of equivalent viscous damping ratios. Somewhat less energy is dissipated when shear and/or flexure of the masonry contributes more to the overall response (e.g. Specimens Z3 and Z5). It should be noted that for calculating the strain energy, the horizontal force values were chosen as 90% of the maximum horizontal force attained within the cycle considered, since the horizontal force values corresponding to the maximum applied displacement led to an underestimate of the actual strain energy, cf. Figure 3-33.
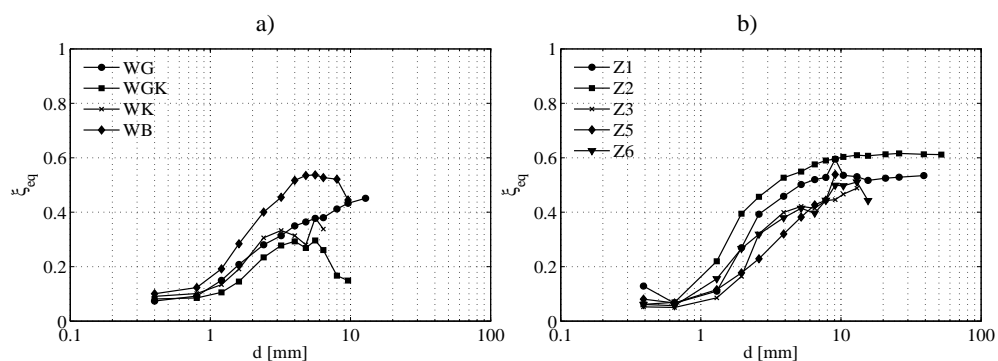
Figure 3-34. Equivalent viscous damping ratio: a) preliminary testing phase; b) main testing phase
[40]

3.4.3.1 Preliminary testing phase

All specimens tested in the preliminary phase responded quite similarly. Generally, the response was non-linear almost from the beginning and more pronounced when the horizontal displacement exceeded 1 mm. Subsequently, with increasing deformation the response evolved into an ideal plastic horizontal branch (more pronounced for Specimens WG and WB). All specimens exhibited large energy dissipation (Specimens WG and WB to a greater extent, cf. Figure 3-34a) and behaved in a quasi-ductile manner. Sudden changes in values of the equivalent viscous damping ratio, and thus the slope change of

the lines given in Figure 3-34a, correspond to the occurrence of significant (shear and/or vertical tensile) cracks. Each test was stopped when critical damage conditions occurred.
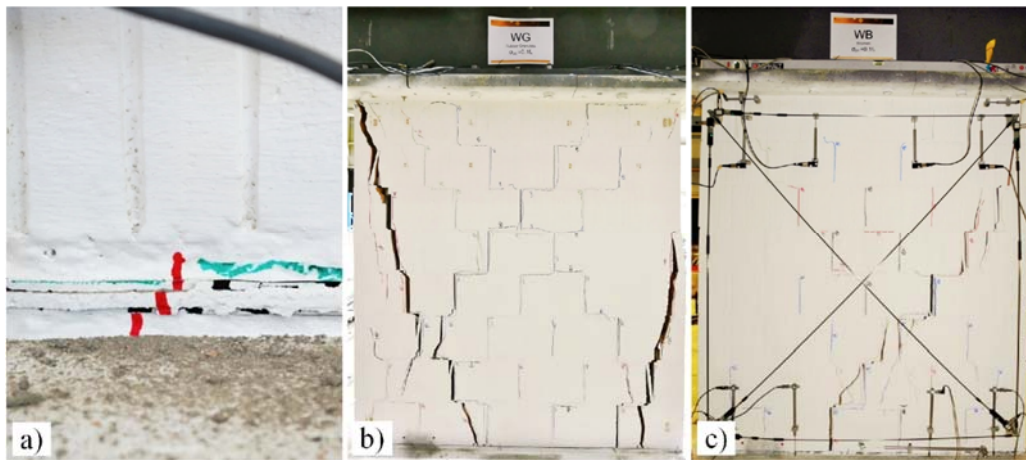

Figure 3-35. Failure modes of selected specimens from the preliminary testing phase: a) sliding in the multi-layer bed joint of specimen WGK; b) reduced wall's effective area of specimen WG; c) reduced wall's effective area of specimen WB [40]

The initial response of all specimens primarily originated from the soft layer deformability. Besides the shear deformation of the soft layer (cf. Figure 3-31c), a soft layer's vertical deformability allowed for rigid body rotation of the walls. During the loading step with the target displacement of 1.6 mm (corresponding to a horizontal drift ratio of 0.1%), sliding at the interface between the core soft layer and the elastomer appeared, see Figure 3-35a. In spite of the fact that sliding had already occurred, values of the recorded horizontal force increased as the number of performed cycles increased, cf. Figure 3-33. The same was noticed during the static-cyclic shear tests on masonry triplets with a multi-layer bed joint, addressed in Section 3.2.4.5. Further sliding motion caused lateral tensile stresses at the bottom block course of the specimen, which led to vertical tensile cracks in the head joints and eventually to the separation of the head joint mortar from the blocks. The problem of tensile cracking at the bottom block is addressed in Section 3.4.5. Simultaneously with the sliding motion, which amounted to between 60% and 80% of the applied horizontal displacement, depending on the displacement step and specimen considered, diagonal shear cracks formed along the bed and head joints (step-wise cracking) starting from the middle of the wall with subsequent extension through the clay units (cf. Figure 3-31b the for major principal strain field concentrated in the joints). The aforementioned tensile cracks in the bottom block course spread to the upper courses

60

of the wall as the tests progressed and caused the reduction of the effective area of the bottom cross-section of the specimen, cf. Figures 3-34b and 3-34c.

Figure 3-36. Final crack patterns of the specimens in the preliminary testing phase [40]

The level of the reduction of the wall effective area, which in turn depended on the position of the tensile cracks in the bottom block course, determined the subsequent behavior of the specimen. Moreover, due to the separation of the specimen along the step-wise cracks into individual parts, another sliding interface between the mortar and the upper elastomer layer of the multi-layer bed joint occurred. Specimens WB and WG slid more than Specimens WGK and WK. Nevertheless, shear was finally the common failure mode for all specimens. Figure 3-36 shows the final crack patterns of the tested specimens.

3.4.3.2 Main testing phase

The response of specimens of the main testing phase was initially non-linear, more significantly so after exceeding 0.64 mm of horizontal displacement (0.025% drift ratio). Subsequently, the response evolved into an ideal plastic horizontal branch. Specimens of the main testing phase exhibited a considerable energy dissipation capacity and behaved in a quasi-ductile manner, cf. Figure 3-34b. The final crack patterns are shown in Figures 3-37 and 3-38.

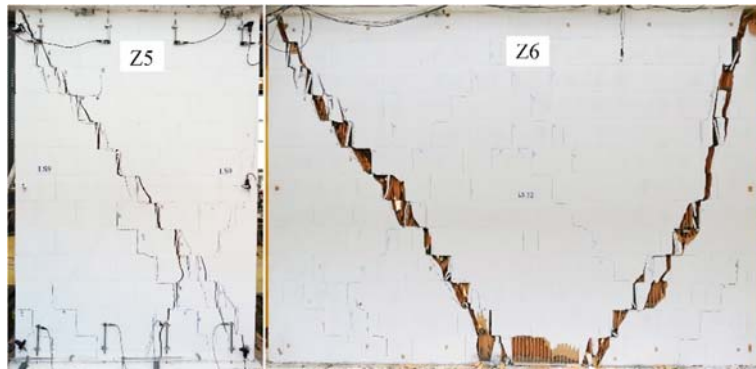**Figure 3-37. Final crack patterns of specimens Z1, Z2 and Z3** [40]

Figure 3-38. Final crack patterns of specimens Z5 and Z6 [40]

Before sliding at the interface between the rubber granulate core soft layer and the elastomer started during the cycle with the target displacement of 1.3-3.9 mm (0.05-0.15% drift ratio), depending on the specimen aspect ratio or the level of pre-compression, the wall response was concentrated at the soft layer level (shear deformation of the soft layer and rotation allowed by the soft layer's vertical deformability). Here too, although limited, as indicated from the test on Specimen Z2, the influence of the loading speed on the value of the recorded horizontal force was apparent, cf. Figure 3-33. It was observed that, in spite of further increasing the loading speed, over the value of 9.5 mm/min (a cycle with the target drift ratio of 0.8%), there was no increase of the horizontal force. Sliding measured at the bottom of each wall was around 60-100% of the applied horizontal displacement. However, except in the case of Specimen Z2, which responded in pure sliding with almost no cracks (cf. Figure 3-37), a stable pure sliding response mechanism was interrupted by the appearance of (vertical) tensile cracks at the bottom layer of the blocks (see Section 3.4.5) . These cracks, as mentioned before, progressed to the upper part of the walls causing the reduction of the effective areas of the walls (see Figures 3-37 and 3-38) and thus influenced the subsequent response of the walls. In the case of the Specimen Z1 the sliding continued with minor shear cracks, which formed in the middle of the wall, see Figure 3-37.

With increasing level of pre-compression (Specimen Z3) further sliding response was limited since the remaining effective part of the wall failed in shear (the cycle with the drift ratio of 0.5%). The wall with the higher aspect ratio (Specimen Z5) also failed in shear, after responding prevalently in sliding, at a horizontal displacement of 7.8 mm (drift ratio of 0.3%). Finally, Specimen Z6 (the 3.6 m long specimen) behaved similar to the reference wall. However, the sliding response was interrupted by the shear failure of the

remaining effective part of the wall. Thereafter, another sliding mechanism was established in the multi-layer bed joint, and the middle part of the wall continued to slide up to the final compressive failure of the remaining bottom block course (at the horizontal drift ratio of 0.6%), see Figure 3-38.

3.4.4 Discussion

In the following section, the behavior of the tested URM walls with a multi-layer bed joint is discussed in terms of the horizontal force resistance and the size effect, horizontal force-displacement response stiffness and horizontal displacement capacity. Then, the horizontal force-displacement response idealization is proposed. Further, the influence of the core soft layer type, pre-compression level, aspect ratio on the observed response is considered. Furthermore, the degradation of the implemented soft layers caused by cyclic loading is addressed.

3.4.4.1 Horizontal force resistance and the wall size effect

The shear strength of the tested URM walls with multi-layer bed joints can be quantified using the classical Mohr-Coulomb's failure criterion $\tau = c + \sigma_{pc} \cdot \tan\varphi$, where c and φ are the cohesion and the angle of internal friction, respectively. The pre-compression stress is $\sigma_{pc} = V/A_w$, where V is the vertical (pre-compression) load of the specimen and $A_w = t_w \cdot l_w$ is the nominal cross-section area of the wall. Then, the maximum calculated horizontal force resistance of URM walls with multi-layer bed joints is:

$$H_{max,\,calc} = A_w \cdot (c + \sigma_{pc} \cdot \tan\varphi) \tag{3-1}$$

Using the average values of friction coefficient, $\tan\varphi$, determined from the results of static-cyclic shear tests on masonry triplets with a multi-layer bed joint, see Table 3-6, while neglecting the small cohesion values and taking into account the applied pre-compression stress level, the experimentally obtained values of the maximum horizontal force resistance of specimens of the preliminary testing phase could be predicted well, cf. Table 3-12. However, the correlation between the experimental and the calculated values of the maximum force resistance of specimens of the main testing phase is not that good. This is, likely, caused by the size effect.

Table 3-12. Comparison of the experimentally obtained and calculated values of the horizontal force resistance [40]

Specimen	H_{max}	[a] $\tan\varphi$	$H_{max, calc}$	$H_{max}/H_{max, calc}$	[b] $\tan\varphi$	[b] c	$H_{max, calc}$	$H_{max}/H_{max, calc}$
	[kN]	[-]	[kN]	[-]	[-]	[MPa]	[kN]	[-]
WG	57.71	0.44	52.02	1.11	0.2	0.15	57.15	1.01
WGK	59.19	0.49	57.45	1.03	-	-	-	-
WK	55.74	0.50	58.76	0.95	-	-	-	-
WB	56.08	0.50	59.06	0.95	-	-	-	-
Z1	103.7	0.44	93.63	1.11	0.2	0.15	102.87	1.01
Z2	77.63	0.44	46.82	1.66	0.2	0.15	81.81	0.95
Z3	141.17	0.44	187.27	0.75	0.2	0.15	144.99	0.97
Z5	68.09	0.44	62.42	1.09	0.2	0.15	68.58	0.99
Z6	171.41	0.44	124.84	1.37	0.2	0.15	137.16	1.25

[a] Average values from Table 3-6
[b] Values estimated from the present tests

Results obtained by testing Specimens WG and Z1, which had (almost) the same aspect ratio and were tested under the same pre-compression stress level (10% of the masonry compressive strength) but have different size allow one to assess the (wall) size effects. Both specimens responded in sliding in the multi-layer bed joint. However, the amount of sliding, expressed as a percentage of the applied wall horizontal displacement, was smaller for Specimen WG, thus indicating a larger contribution of the shear deformation of the masonry. This can be seen by comparing the crack patterns shown in Figures 3-36 and 3-37. Compared to Specimen Z1, Specimen WG exhibited more extensive shear cracks. These cracks governed the specimen behavior after the reduction of wall effective area occurred. Specimen WG failed in shear at the drift ratio value of 0.8%. On the other hand, Specimen Z1 continued to slide without failing in shear until the test was stopped at the drift ratio of 1.5%. Such behavior can be attributed to the size effect, i.e. to the ratio between the size of a single block and the size of a specimen. When this ratio is smaller (for taller specimens with the same aspect ratio), the stress distribution is more uniform and there are fewer cracks. Further, the stiffness of the larger specimen (Z1) is higher than that of the smaller one (WG), the difference being even more pronounced than in the case of similar walls without layers, see [43] or [44].
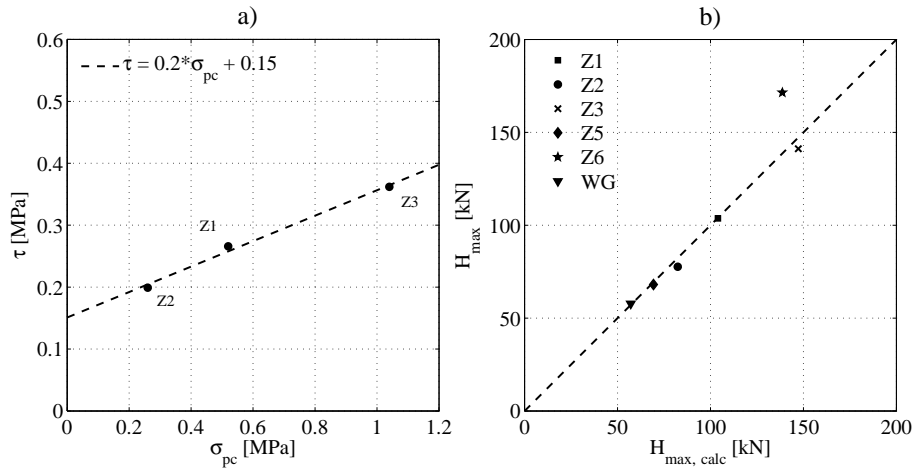
Figure 3-39. Mohr-Coulomb's failure criterion: a) shear vs. normal stress for specimens Z1, Z2 and Z3; b) correlation between the measured and the calculated values of the horizontal force resistance [40]

The effect of the multi-layer bed joint length on the horizontal force resistance of the specimens is assessed by considering the shear stress vs. normal stress data determined from the results of static-cyclic shear tests on masonry triplets with a multi-layer bed joint, given in Table 3-6, and the shear stress vs. normal stress data for specimens Z1, Z2 and Z3 that have the same aspect ratio but different pre-compression levels, plotted in Figure 3-39a. A line fitted through the latter data is used to estimate the Mohr-Coulomb's failure criterion parameters: a friction coefficient of $\tan\varphi=0.2$ and a corresponding apparent cohesion of $c=0.15$ MPa. The estimates of the maximum horizontal force resistance of the specimens tested in the main test phase made using these results (instead of those from Table 3-6) in equation (3-1) are listed in Table 3-12. Evidently, the observed maximum horizontal force resistance of Specimens Z5, Z6 and WG is predicted fairly well, cf. also Figure 3-39b. Thus, increasing the length of the multi-layer bed joint, the friction coefficient reduces, while the contribution of the apparent cohesion to the force resistance rises and cannot be neglected anymore.

3.4.4.2 Horizontal force-displacement response stiffness

The value of elastic horizontal force-displacement response stiffness K_{el} of a masonry wall can be adequately estimated using the elastic beam theory incorporating both shear and flexure masonry deformation, see e.g. [45]. Vögeli et al. [3] extended the calculation of K_{el} for the URM walls with a soft layer bed joint, where the additional soft layer shear deformation was considered. However, neither the influence of the pre-compression level

nor the contribution of the wall base rotation allowed by the vertical deformability of the soft layer bed joint are included in this extension. Vertical deformability of the multi-layer bed joint soft layers allows the wall to rotate, i.e. allows for a rocking deformation, and therefore has a significant influence on the initial stiffness of the specimens.
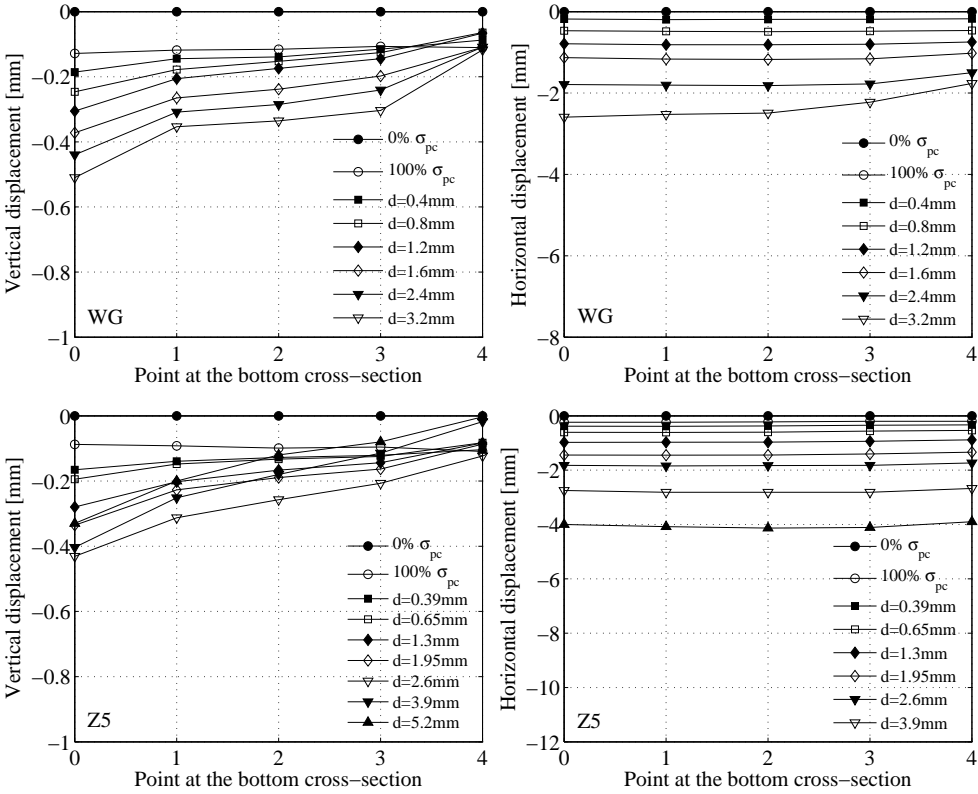

Figure 3-40. DIC-obtained horizontal and vertical displacement at the bottom cross-section level of Specimens WG and Z5

Figure 3-40 shows the horizontal and the vertical displacements at the level of the bottom cross-section of Specimens WG and Z5. Points 0 and 4, shown on the horizontal axis of graphs in Figure 3-40, correspond to the very end points of the bottom wall cross-section. All consecutive points have the same mutual distance (450 mm in case of Wall Z5 and 375 mm in case of Wall WG). The horizontal and the vertical displacements were obtained from DIC for different levels of the pre-compression load (0 and 100% of the total applied load) and for different positive peak horizontal displacements in the subsequent horizontal load cycles. In order to transform the vertical displacements into base rotation and further to the wall top displacement, one needs to assume that: the deformation of the multi-layer bed joint mortar is relatively small as compared to the deformation of soft layers and thus negligible; the bottom cross-section of the wall remains plane. The first assumption can

be justified by comparing the values of the deformation moduli of the mortar and the soft layer: the elastic and shear moduli of the soft layer are three orders of magnitude less than the typical values for mortar. The latter assumption can be considered as justified up to a certain peak horizontal displacement, at which the reduction of the effective area was initiated, changing the displacements distribution at the bottom cross-section. This displacement limit lies between 2.4 and 5.2 mm, depending on the specimen considered. A decomposition of the DIC-measured wall top displacements indicates that the displacement components derived from the multi-layer shear/sliding deformation, and the multi-layer vertical deformability are the governing ones. For example, if calculated for the first loading cycle with the target displacement of 0.65 mm, those components together amount to 65-90% of the total wall top displacement, depending on the specimen considered. More details about the wall deformation components and their contribution are given in Chapter 4.

Based on these observations, equation (3-2) is proposed to calculate the elastic stiffness K_{el} of URM walls with a multi-layer bed joint that has a thickness t_{ml}, and shear modulus G_{ml}:

$$K_{el} = \frac{1}{\kappa \cdot \dfrac{h_w}{G_m \cdot A_w} + \dfrac{h_w^3 \cdot \left(\alpha^3 + (1-\alpha)^3\right)}{3 \cdot E_x \cdot I_w} + \dfrac{(t_{ml} - \Delta t_{ml})}{G_{ml} \cdot A_w} + \alpha \cdot \dfrac{h_w^2 \cdot \Delta t_{ml}}{\sigma_{pc} \cdot I_w}} \tag{3-2}$$

Note that the equation (3-2) is written in such manner to distinguish between the components which contribute to the total wall deformation. Looking from left to right, the following deformation components are given: masonry shear deformation, masonry flexure deformation, multi-layer bed joint shear deformation and rocking deformation, respectively. In equation (3-2), A_w and I_w denote the area and moment of inertia of the wall horizontal cross-section, respectively; G_m and E_x correspond to the shear and elastic moduli of masonry. Coefficient κ is the shear coefficient and equals to 1.2 for the rectangular cross-section. The level of pre-compression σ_{pc} is included through its influence on the thickness of the multi-layer bed joint. The thickness of the multi-layer bed joint that effectively deforms in shear before sliding begins is the original thickness (excluding the mortar layers), t_{ml}, reduced by the amount of vertical deformation of the multi-layer bed joint due to the pre-compression load, Δt_{ml}. Now, the relationship between the pre-compression (normal) stress and Δt_{ml} is of interest. Those relationships, obtained

from all tests performed, are shown in Figure 3-41 (the measurements of uplift sensors are shown, cf. Figure 3-29 for the position of the sensors).
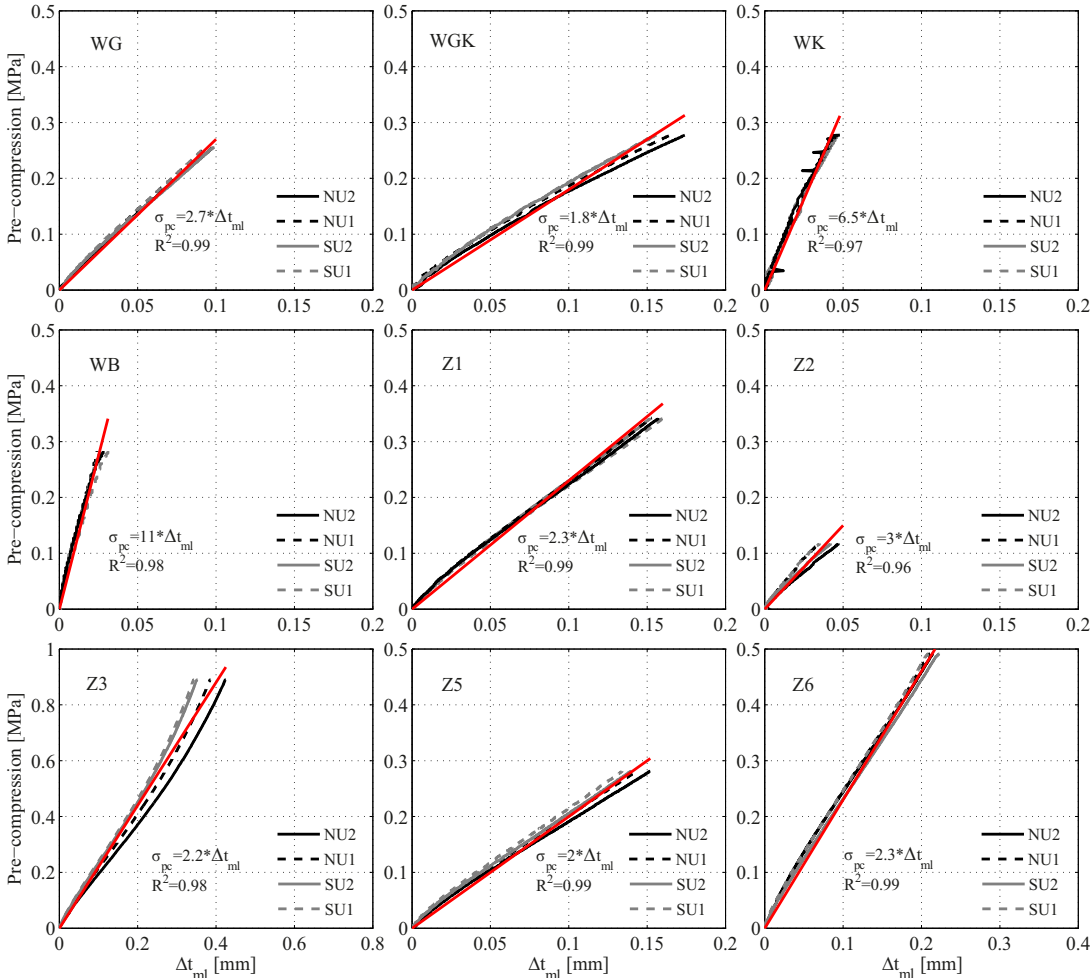

Figure 3-41. Pre-compression (normal stress) vs. multi-layer bed joint thickness contraction

The σ_{pc} - Δt_{ml} relationships are linear, and can be described by the parameters given in Figure 3-41 and Table 3-13. It is noteworthy that the first intention was to derive the values of elastic moduli of multi-layer bed joints values from the values of Δt_{ml} and implement it into equation (3-2). However, it was noticed that the values of Δt_{ml} of the multi-layer bed joint with a rubber granulate core soft layer, obtained from vertical load phases of the tests on the URM walls, are much smaller than the values of Δt_{ml} obtained from the tests on masonry triplets for the same level of pre-compression, see Section 3.5.4.3, and those values should be the same and indicate the elastic modulus of the multi-layer bed joint. This is likely caused by the relatively high deformability of the interface between the multi-layer bed joint mortar and the clay block that increases the total deformability of the multi-layer bed joint due to pre-compression load. In case of masonry triplets with a rubber

68

granulate core soft layer in multi-layer bed joints, the mortar-block interface deformation was included in the measurements of Δt_{ml}, cf. Figure 3-54a, while in case of URM walls with a multi-layer bottom bed joint, due to wall self-weight and the weight of the test set-up parts placed above the wall (elements (6) and (8) in Figure 3-28), the mortar-block interface deformation was already finished before measuring Δt_{ml}. The rocking deformation is estimated as follows: knowing the relationship between the pre-compression (normal stress) and Δt_{ml}, and assuming a linear normal stress distribution at the bottom cross-section of the wall, wall base rotation caused by the bending moment at the bottom cross-section is calculated and further transformed to the wall top displacement. The estimation of the shear modulus G_{ml} of the multi-layer bed joint with a rubber granulate core soft layer, which is assumed as the same for each type of multi-layer bed joint, is given in Section 3.5.4.3. Coefficient α accounts for the influence of the position of the zero bending moment (inflection) point, i.e. the shear span, h_0, on the value of masonry flexure deformation and rocking deformation. The fixed-end boundary conditions, both in the preliminary and the main testing phase, were ensured by a mixed force-displacement control of the vertical actuators. Therefore, the distribution of the bending moment along the wall height is not necessarily symmetric. Figure 3-42 shows the values of coefficient α, i.e. the position of zero bending moment with respect to the bottom cross-section, $h_s = h_w - h_0$, normalized with the corresponding wall height, for walls from both testing phases. Those values are calculated from the values of bending moment at the top and the bottom wall cross-section, at the point of peak positive horizontal force for each first pushing semi-cycle performed, and plotted against the corresponding target horizontal displacement. Such a calculation is plausible until the wall keeps its integrity, i.e. until the significant shear cracking or the reduction of the wall effective area appears. As can be seen from Figure 3-42, the distribution of the bending moment along the height of each wall is asymmetric. This is because of the multi-layer bed joint, which, with respect to the conventional mortar bed joint on top, has a significantly higher vertical deformability, thus providing for higher rotation capacity. The positions of the zero bending moment calculated for the first pushing semi-cycle performed for walls WG, Z1, Z5 and Z6, which have the same type of core soft layer, and which are tested under the same level of pre-compression, are close to value $0.2 \cdot h_w$. However, in case of Wall Z2 the zero moment point is somewhat lower, around $0.15 \cdot h_w$, while in case of Wall Z3 it lies higher, around $0.3 \cdot h_w$, see Figure 3-42b. This can be explained as influence of the pre-

compression. Similarly, less deformable multi-layer bed joint, as one with a bitumen-based or with a cork core soft layer (cf. Table 3-13 for values of $\sigma_{pc}/\Delta t_{ml}$), increase the position of the zero bending moment, see Figure 3-42a. The influence of the pre-compression and the multi-layer vertical deformability on the position of the zero bending moment in the wall, i.e. on the wall shear span, is addressed in more details in Section 3.4.4.5 and Section 3.4.4.7, respectively.
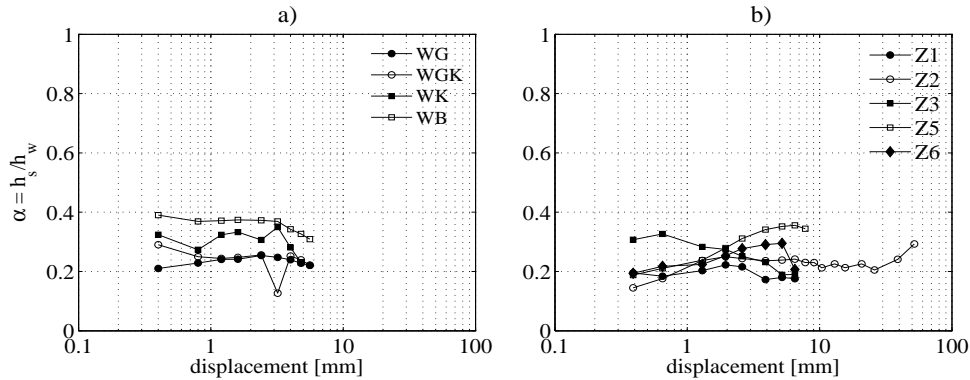

Figure 3-42. Zero bending moment position: a) walls from the preliminary testing phase; b) walls from the main testing phase

Values of the elastic stiffness of each wall with a rubber granulate core soft layer calculated using equation (3-2) are shown in Table 3-14, while the parameters used for the calculation are summarized in Table 3-13. The deformation contribution factors of each deformation component in the equation (3-2) are given in Table 4-5. The calculated values of K_{el} are very well correlated to the measured values of the initial stiffness, $K_0 = 1.4 \cdot K_{el}$ with $R^2 = 0.8$, see Figure 3-43.

Table 3-13. Parameters used to calculate the elastic stiffness K_{el} of the specimens

Specimen	E_x [MPa]	G_m [MPa]	G_{ml} [MPa]	A_w [mm²]	t_{ml} [mm]	[a] $\sigma_{pc}/\Delta t_{ml}$ [MPa/mm]	α [-]
WG	5272	2108.8	2	$2.25 \cdot 10^5$	7.4	2.7	0.2
WGK	5272	2108.8	2	$2.25 \cdot 10^5$	7.6	1.8	0.3
WK	5272	2108.8	2	$2.25 \cdot 10^5$	7.9	6.5	0.3
WB	5272	2108.8	2	$2.25 \cdot 10^5$	6.4	11	0.4
Z1	5272	2108.8	2	$4.05 \cdot 10^5$	7.4	2.3	0.2
Z2	5272	2108.8	2	$4.05 \cdot 10^5$	7.4	3	0.15
Z3	5272	2108.8	2	$4.05 \cdot 10^5$	7.4	2.2	0.3
Z5	5272	2108.8	2	$2.70 \cdot 10^5$	7.4	2	0.2
Z6	5272	2108.8	2	$5.40 \cdot 10^5$	7.4	2.3	0.2

[a] In walls with a rubber granulate core soft layer an average value of $\sigma_{pc}/\Delta t_{ml}=2.4$ was used to calculate K_{el}

70

Table 3-14. Computed response characteristics

Specimen	Response idealization	H_u [kN]	$1.4 \cdot K_{el}$ [kN/mm]	d_y [mm]	δ_y [%]	d_t/d_y [-]	d_u/d_y [-]	H_r/H_u [%]
WG	multilinear	51.44	49.55	1.04	0.06	6.17	12.33	95
WGK	multilinear	51.70	42.84	1.21	0.08	5.30	7.95	65
WK	multilinear	52.88	52.84	1.00	0.06	4.80	6.39	80
WB	bilinear	53.16	63.68	0.83	0.06	-	11.50	-
Z1	bilinear	92.58	81.59	1.13	0.04	-	[a] 22.91	-
Z2	bilinear	73.63	81.58	0.90	0.03	-	[a] 28.81	-
Z3	multilinear	130.49	80.65	1.62	0.06	5.62	8.03	70
Z5	bilinear	61.72	40.66	1.52	0.06	-	5.14	-
Z6	multilinear	123.44	123.37	1.00	0.04	7.80	15.59	60

[a] d_u is limited to 26 mm due to interaction with other structural and non-structural elements of the building
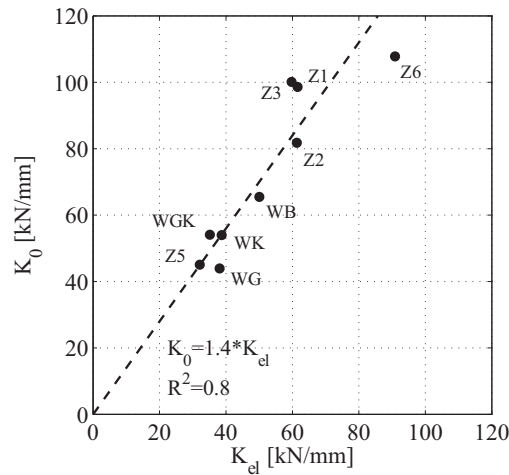
Figure 3-43. Tangent stiffness vs. calculated elastic stiffness for all specimens

A minor inconsistency can be noticed when comparing the values of calculated elastic stiffness of walls Z1, Z2 and Z3. Wall Z3 has the smallest elastic stiffness. This is because the expected attenuation of increment of the contraction of the multi-layer bed joint thickness, cf. Figure 3-41 for the difference between measured σ_{pc} - Δt_{ml} relationships obtained for Wall Z3 and for other walls, which appears after exceeding a certain value of the pre-compression stress, is not considered in the equation (3-2). The σ_{pc}-Δt_{ml} relationship is modeled as linear, i.e. with the constant increment of the contraction of the multi-layer bed joint thickness with the increase of the pre-compression stress, and therefore slightly overestimate the rocking deformation component in Wall Z3.

3.4.4.3 Horizontal displacement capacity

The stiffness of all tested specimens remained close to their initial stiffness until they reached their maximum horizontal force resistance. Then, they deformed (plastically) without an increase in resistance. However, the maximum horizontal displacements achieved during different tests depend on the specimen failure modes (cf. Table 3-11). Specimens Z1 and Z2 responded predominantly in sliding along the multi-layer bed joint, cf. Figure 3-33 (the former one did so in spite of the reduction of the wall effective area). These two tests were terminated, even though the sliding capacity of the multi-layer bed joint was not exhausted. Even though the ultimate horizontal displacement of such walls is large, it is practically limited due to the interaction of the wall with other structural and non-structural components of the building. The ultimate drift ratio limit of 0.8% [46] to 1% [47] for the predominantly sliding type of response, is also acceptable for URM walls with multi-layer bed joints. Other specimens, after developing some sliding in the multi-layer bed joints, failed in shear either before (Specimen WGK, WK, Z5) or after the wall effective cross-section areas were reduced due to separation into individual segments (Specimens WG, WB, Z3 and Z6). Some specimens exhibited a sudden drop in horizontal force resistance. The displacements $d_{t,\,max}$ and $d_{t,\,min}$ corresponding to such sudden loss of resistance in the push and pull test directions are given in Table 3-11.

3.4.4.4 Horizontal force-displacement response idealization

In general, the response of URM walls subjected to cyclic shear is non-linear and depends on several parameters, such as the pre-compression level, the wall aspect ratio and the wall boundary conditions. Moreover, a cycling-induced reduction of the strength and the stiffness of masonry wall is presents. Usually, the horizontal force-displacement response hysteresis of a masonry wall under reversed cyclic loading is simplified by idealizing the envelope of the hysteresis using a bilinear (linear elastic-perfectly plastic) or multilinear relations. Different approaches to determine this bilinear idealization, i.e. its parameters (the effective stiffness, ultimate displacement and the ultimate horizontal force resistance), could be found in the literature. For example, Tomaževič [45] calculates the ultimate horizontal force resistance from the condition that the areas (the work) under the actual cyclic response envelope and its idealization are the same. Further, based on numerous tests, the ultimate horizontal force resistance assigned to the idealized response, H_u, is approximately equal to 90% of the maximum horizontal force resistance attained during

the cyclic tests (max{H_{max}, |H_{min}|} in Table 3-11). However, the force-displacement response curves obtained from the present tests do not allow for a straight-forward application of the procedure described above. As mentioned before, the point where the maximum horizontal force is attained is not the same as the point of the maximum horizontal displacement due to the change of the loading speed during a sine-wave loading cycle.
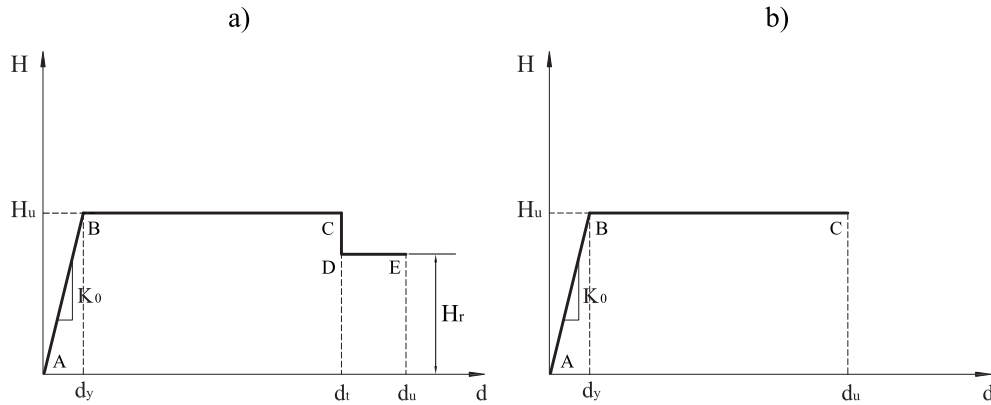
a)   b)

Figure 3-44. Idealization of the horizontal force-displacement hysteretic response: a) multilinear; b) bilinear

Therefore, an idealization of the envelope of the horizontal force-displacement hysteretic response of a URM wall with a multi-layer bed joint is proposed in Figure 3-44a. The value of the ultimate horizontal force resistance is $H_u = 0.9 \cdot H_{max, calc}$, where $H_{max, calc}$ is computed using equation (3-1). As it is mentioned before, the stiffness of all tested specimens remained close to their initial stiffness until they reached their maximum horizontal force resistance, and can be approximated by K_{el} while considering the K_0-K_{el} correlation coefficient of 1.4, see Section 3.4.4.2. Consequently, the displacement d_y when the response of a URM wall with a multi-layer bed joint ceases to be elastic (i.e. apparent yield displacement), can be computed, see Table 3-14. Past displacement d_y the response is assumed to be perfectly plastic, with the horizontal force resistance equal to H_u, until displacement d_t is attained, when a sudden drop of horizontal force resistance occurs. The ratios of the observed displacements d_t, given in Table 3-11, and the computed values of displacement d_y, are shown in Table 3-14. They are consistently about 6.0 for all specimens. The ultimate displacements d_u of specimens, that had or did not have a sudden drop of horizontal force resistance, except of walls Z1 and Z2, are 5 to 15 times larger than d_y, cf. Table 3-14. The remaining horizontal force resistance, H_r, of the specimens with a rubber granulate soft layer (WG, Z3 and Z6) varies, but is larger than $0.6 \cdot H_u$. It

73

should be noted here that a similar general horizontal force-deformation response envelope for URM walls is suggested by Figure 7-1 of FEMA 356 [46]. The parameters of this envelope are specified in Table 7-4, see [46].
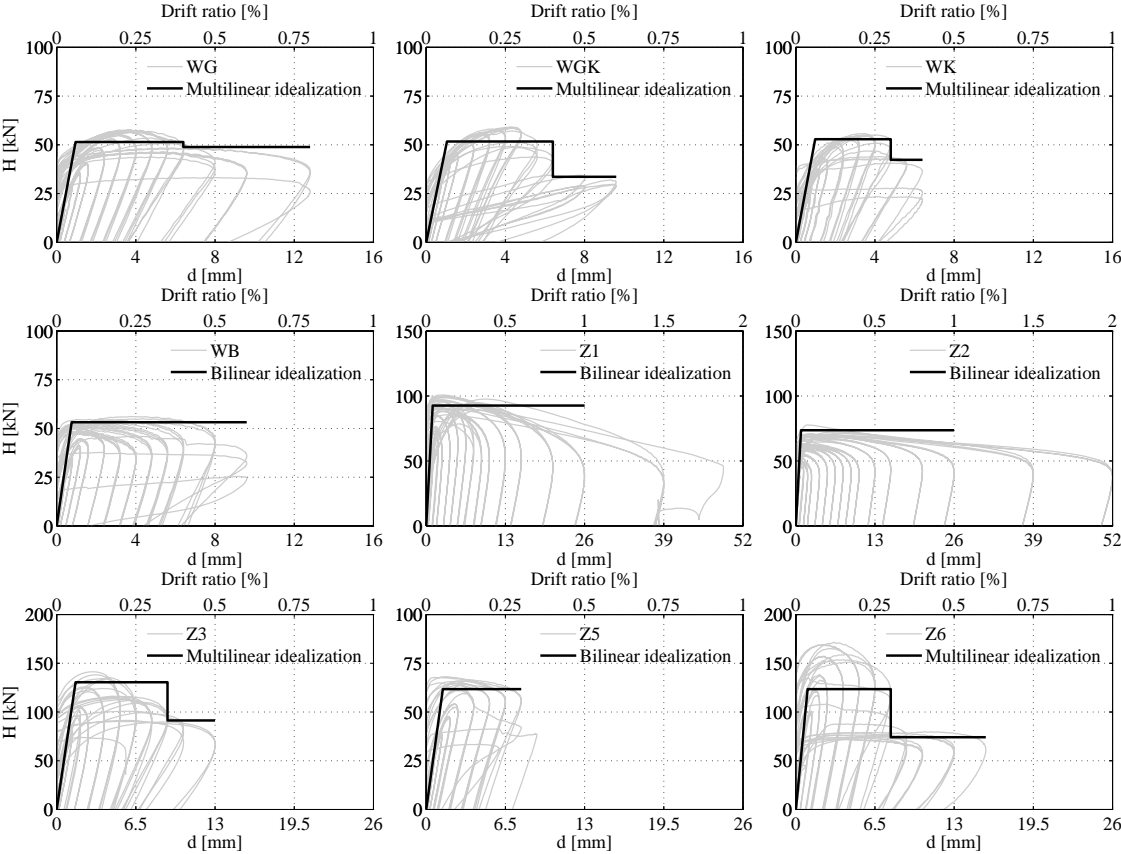
Figure 3-45. Measured vs. idealized horizontal force-displacement hysteretic response

The specimens whose response was dominated by sliding (WB, Z1, Z2 and Z5) did not experience a drop in strength. The idealization of their horizontal force-displacement response is simpler, elastic-plastic, as shown in Figure 3-44b. The ultimate displacement of specimens Z1 and Z2 is limited by the interaction with other structural and non-structural elements of the building and is set to a drift value of 1% (Table 3-14). The idealized envelopes of the hysteretic horizontal force-displacement responses for all specimens in the first quadrant computed using the procedures stated above are shown in Figure 3-45 (see Appendix A2 for details).

3.4.4.5 Influence of the pre-compression level

The influence of the pre-compression level can be assessed by comparing the results obtained for Specimens Z1, Z2 and Z3. The results indicate that as the level of pre-

74

compression increased, the stiffness, the apparent yield displacement and the horizontal force resistance increased, cf. Tables 3-11 and 3-14. Further, the position of the zero bending moment, i.e. the shear span of the specimens was influenced by the pre-compression level: higher pre-compression level leads to more contraction of the thickness of the multi-layer bed joint, which decreases the remaining vertical deformation capacity, and therefore the remaining rotation capacity, thus increasing the position of the zero bending moment, and vice versa (see Figure 3-42b in Section 3.4.4.2). Furthermore, an increase of the level of pre-compression influenced the reduction of the wall effective area, cf. Figure 3-37. Specimens Z1 and Z3 (tested under the pre-compression level of 0.52 MPa and 1.04 MPa, respectively) underwent such a reduction during cycles with the target drift ratio of 0.3% and 0.2%, respectively. In the case of Specimen Z3 the horizontal force resistance degraded, while such degradation was negligible for Specimen Z1, cf. Figure 3-33. Thereafter, the (remaining) effective parts of Specimens Z1 and Z3 continued to respond in sliding. However, Specimen Z3 failed in shear at a drift ratio of 0.5%, while the sliding mechanism of Specimen Z1 was stable until the test was interrupted at a drift ratio of 1.5%. Specimen Z2, tested under the lowest pre-compression level of 0.26 MPa, did not exhibit an effective area reduction and responded steadily in pure sliding (the test was stopped at a drift ratio of 2%).

3.4.4.6 Influence of the aspect ratio

Specimens Z5 and Z6 were tested to investigate the influence of the wall aspect ratio (h_w/l_w) on the specimen behavior by comparing the results obtained with the results of the reference test Z1, which had aspect ratio of 1. The test results show that, as also indicated from previous studies on the conventional URM walls (e.g. [43]), the horizontal force resistance and the stiffness increases with decreasing aspect ratio. Further, the values of the apparent yield displacement were slightly affected by changing the aspect ratio. In spite of the same initial behavior, Specimen Z6 developed a 60% smaller value of horizontal displacement prior to failure compared to Specimen Z1. This was mostly due to the reduction of the wall effective area. Specimen Z5, with the highest aspect ratio, failed in shear during the cycle with the target drift ratio of 0.35% (about 76% lower displacement capacity than that of Specimen Z1). Given the above, it can be concluded that either increasing or decreasing the aspect ratio with respect to the reference value of $h_w/l_w = 1$, the displacement capacity of URM walls with a multi-layer bed joint decreases.

However, by lowering the aspect ratio, the probability of establishing a new and stable sliding response regime, after the wall effective area is reduced, increases. This could possibly improve the deformation capacity of URM walls with multi-layer bed joints.

3.4.4.7 Influence of the core soft layer type

Results from the preliminary testing phase allow investigating the influence of the core soft layer type on the specimen response, cf. Tables 3-11 and 3-14. It can be seen that the effect of the core layer type on the stiffness, apparent yield displacement and the horizontal force resistance of the specimens with a multi-layer bed joint is almost negligible. On the other hand, the deformation capacity of the tested specimens exhibits some variability. Moreover, as mentioned in 3.4.4.2, the vertical deformability of the multi-layer bed joint, which is in turn dependent on the core soft layer type, cf. Table 3-13 for values of $\sigma_{pc}/\Delta t_{ml}$, influence the position of the zero bending moment, i.e. the shear span: higher vertical deformability of the core soft layer ensures the higher rotation capacity of the multi-layer bed joint, thus leading to the lower position of the zero bending moment, i.e. to the higher shear span, see Figure 3-42a. A relatively less deformable multi-layer bed joint, as one with a bitumen-based or with a cork core soft layer, increases the position of the zero bending moment. The initial values of α calculated for the specimen with a cork-rubber granulate soft layer (WGK) show inconsistency. However, after loading cycles with the target horizontal displacement of 0.65 mm, values of α are close to the values measured for the specimen with a rubber granulate core soft layer in the multi-layer bed joint, whose vertical deformability is similar to that of the multi-layer bed joint with a cork-rubber granulate core soft layer.

Considering the intended purpose of a multi-layer bed joint to modify the seismic in-plane response of URM walls, it can be concluded that the smallest benefits are obtained when using a cork core soft layer (Specimen WK), since the ultimate horizontal displacement is significantly smaller than that of the other specimens. For Specimens WGK and WK, the crack pattern, characteristic for the walls failing in shear, started developing at an early stage in the tests causing degradation of both the horizontal force resistance and the stiffness, cf. Figure 3-33. Specimens WG and WB exhibited more favorable behavior, albeit with different levels of core soft layer damage. Finally, the rubber granulate core soft layer was chosen for the main testing phase, since it exhibited a higher durability under repeated cycles than the bitumen core soft layer.

3.4.4.8 Soft layer degradation

Figures 3-46 and 3-47 show the layers (elastomer and core soft layers) of the multi-layer bed joints after testing in both the preliminary and the main phases, respectively. As can be seen, there was almost no degradation of the core soft layers of Specimens WG, WGK and WK. Only local damage to the core soft layers and elastomer was detected at the location where the tensile cracks in the bottom block course appeared. However, the bitumen based core soft layer (Specimen WB) underwent considerable damage during cycling and became stuck to the sheets of the elastomer, cf. Figure 3-46.

Figure 3-46. Degradation of the soft layers: preliminary testing phase [40]

Figure 3-47. Degradation of the soft layers: main testing phase [40]

For the main phase full-scale specimens, which were tested at the higher levels of pre-compression, a soft layer degradation depended on the extent of sliding motion: the

smaller the sliding motion (e.g. relatively early shear failure of Specimens Z3 and Z5), the less the degradation of soft layers. An extensive sliding motion of Specimen Z2 caused only wrinkling deformation at the outer edges of the elastomer layers. However, in the case of Specimens Z1 and Z6 (both developed reduced effective areas), local damage to the rubber granulate core soft layer, i.e. crumbling caused by normal stress concentration in combination with the sliding motion, was detected at the location of the tensile cracks in the bottom block course. Moreover, the elastomer layers underwent tensile cracks (rupture) at the same position, cf. Figure 3-47. The abraded surface of the elastomer sheets, observed in all specimens, clearly indicated the pronounced sliding at the interface between the elastomer and the core soft layer. Finally, one can conclude that the implemented protective extruded elastomer layers were able to limit the deterioration of all core soft layers, except for the bitumen layer.

3.4.5 Vertical tensile cracks at the bottom block course of the walls

As it is already mentioned, except in case of Wall Z2 a stable pure sliding response mechanism of all walls with a rubber granulate core soft layer in multi-layer bed joint was interrupted by the appearance of vertical tensile cracks in head joints at the bottom layer of the blocks, and their further progression to the upper part of the walls causing the reduction of the effective areas of the walls, thus influencing the subsequent response of the walls. Specimen Z1 continued to slide even after a certain part of the wall separated, with minor shear cracks formed in the middle of the wall and without a significant change in horizontal force-displacement characteristics. The test was stopped at the drift ratio of 1%. However, walls WG, Z3 and Z6 underwent a significant change in resistance as well the stiffness after the reduction of the wall effective area and could develop significantly smaller horizontal displacement prior to failure. Therefore, it is of high importance to investigate the potential source, which causes such vertical cracks in head joints of bottom block course of masonry walls.

One can assume that, when subjected to the combination of vertical and horizontal load acting at its top, a masonry wall with a multi-layer bed joint and with a fixed-end boundary conditions initially behaves elastically (cf. Chapter 4). In addition, the linear distribution of normal stresses, $\sigma(y)$, i.e. the parabolic distribution of shear stresses, $\tau(y)$, at the top and the bottom cross sections of the wall with a multi-layer bed joint, can be assumed, see Figure 3-48.
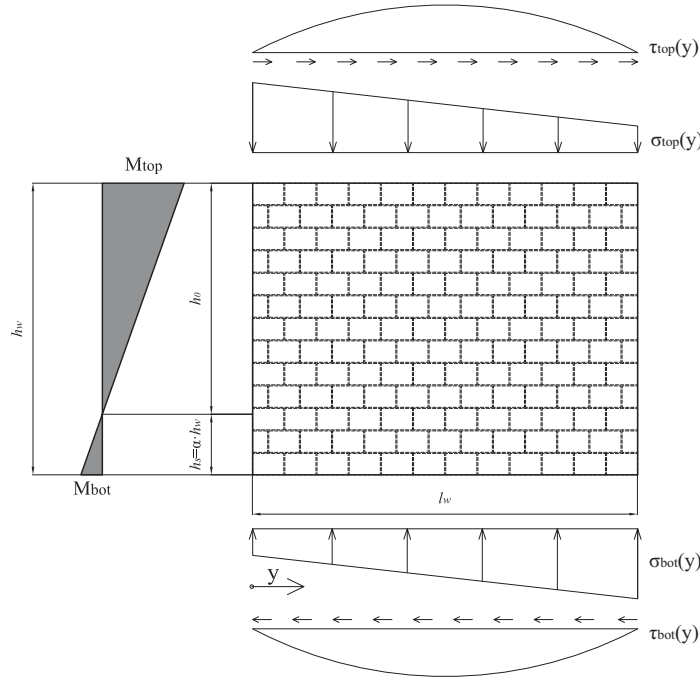
Figure 3-48. Wall subjected to the combination of vertical and horizontal load acting at its top

As indicated by DIC results, the tensile and compressive longitudinal strain concentrations started appearing in head joints of bottom block course of masonry walls once sliding in a multi-layer bed joint was initiated. The functions of normal and shear stresses at the bottom cross sections of the wall, $\sigma_{bot}(y)$ and $\tau_{bot}(y)$, and the corresponding force functions called the resistance force, $R(y)$, providing the (Mohr-Coulomb-type) resistance, and the demand force, $D(y)$, at the onset of sliding are:

$$\sigma_{bot}(y) = \sigma_{pc} - \frac{H \cdot \alpha \cdot h_w}{W_w} + 2 \cdot \frac{H \cdot \alpha \cdot h_w}{W_w \cdot l_w} \cdot y \tag{3-3}$$

$$\tau_{bot}(y) = 6 \cdot H \cdot \frac{y \cdot (l_w - y)}{l_w^3 \cdot t_w} \tag{3-4}$$

$$R(y) = t_w \cdot \int_0^y \left(\mu_{sl} \cdot \sigma_{bot}(y) + c_{sl} \right) dy = t_w \cdot \mu_{sl} \cdot \left(\sigma_{pc} \cdot y - \frac{H \cdot \alpha \cdot h_w}{W_w} \cdot y + \frac{H \cdot \alpha \cdot h_w}{W_w \cdot l_w} \cdot y^2 \right) + t_w \cdot c_{sl} \cdot y \tag{3-5}$$

$$D(y) = t_w \cdot \int_0^y \tau_{bot}(y) dy = \frac{6 \cdot H}{l_w^2} \cdot \left(\frac{y^2}{2} - \frac{y^3}{3 \cdot l_w} \right) \tag{3-6}$$

where H and V are, in terms of forces given, applied horizontal and vertical load, t_w and h_w are the thickness and the height of the wall, respectively, σ_{pc} is pre-compression stress estimated as V/A_w, W_w is the resistance moment of the wall horizontal cross section, α is the coefficient which accounts for the influence of the position of the moment inflection

point (cf. Figure 3-42) and μ_{sl} and c_{sl} are the Mohr-Coulomb's criterion parameters for the multi-layer bed joint, i.e. the friction coefficient and cohesion at the onset of sliding. The latter parameters can be determined from the test on walls Z1, Z2 and Z3 while considering the pre-compression applied and measured values of horizontal force, i.e. the (average) shear stress, at the onset of sliding, cf. Table 3-15. The target displacements of loading cycles during which the sliding occurred and corresponding values of the coefficient α are also given in Table 3-15. Figure 3-49 depicts the shear stress versus the normal stress data for specimens Z1, Z2 and Z3, together with the line fitted through this data used to estimate the Mohr-Coulomb's criterion parameters at the onset of sliding: a friction coefficient of $\mu_{sl} = 0.2$ and a corresponding apparent cohesion of $c_{sl} = 0.06$ MPa.

Table 3-15. Response characteristics at the onset of sliding

Specimen	l_w [mm]	σ_{pc} [MPa]	H_{sl} [kN]	τ_{sl} [MPa]	d [mm]	α [-]	R_{sl} [kN]
WG	1500	0.52	40	0.18	1.6	0.24	36.9
Z1	2700	0.52	75	0.19	2.6	0.2	66.4
Z2	2700	0.26	40	0.1	2.6	0.24	45.4
Z3	2700	1.04	105	0.26	2.6	0.25	108.5
Z5	1800	0.52	60	0.22	3.9	0.34	44.3
Z6	3600	0.52	100	0.19	1.3	0.22	88.6
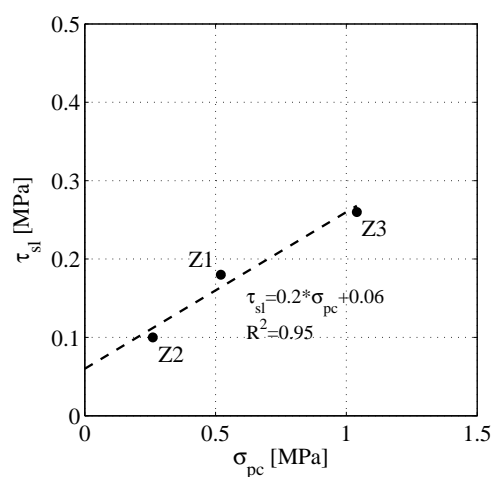
Figure 3-49. Shear vs. normal stress at the onset of sliding for specimens Z1, Z2 and Z3

Knowing the pre-compression load for each wall, values of a total resistance force $R_{sl} = R(y = l_w)$, that should be exceeded in order to initiate sliding, can be calculated using equation (3-5), cf. Table 3-15 for the values calculated. It can be seen that as compared to the measured values of horizontal force at the onset of sliding, excluding values obtained

for walls Z1, Z2 and Z3, the calculated values are conservative, but still reasonable. With known values of R_{sl}, i.e. having $H=R_{sl}$, resistance and demand force functions in the multi-layer bed joint at the onset of sliding, given in equations (3-5) and (3-6), are determined. Since the tensile cracks appears in the head joints, i.e. between the blocks of the bottom block course, the values of resistance and demand forces, which correspond to each block of the bottom block course and have opposite directions, are of interest. Figure 3-50 shows the calculated values of resistance and demand forces at the onset of sliding, i.e. the values calculated for $H=R_{sl}$ and per each block in the bottom block course of each wall. The block length is assumed as 300 mm. Note that the directions of loading cycle during which the sliding occurred are considered and indicated by an arrow above each graph.
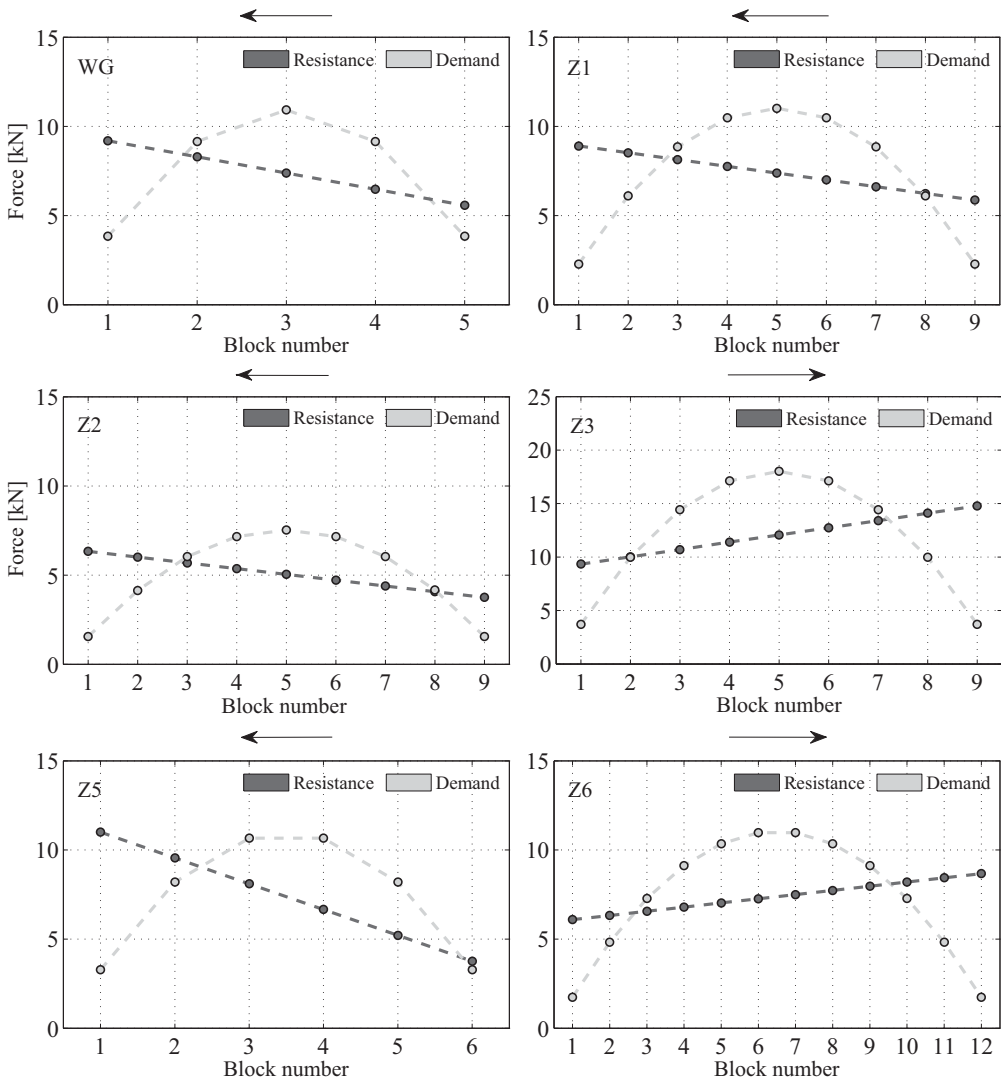
Figure 3-50. Calculated values of resistance and demand force per each block in the bottom block course at the onset of sliding

As it is mentioned before, a wall is at the onset of sliding regime. However, the positive difference between the resistance and the demand forces, which correspond to each block, indicate that some (outer) blocks tend to stop sliding, while the remaining (middle) blocks tend to keep sliding, thus making conditions for the occurrence of either tensile or compressive stresses in head joints between them, depending on the blocks position with respect to the loading direction. Table 3-16 shows the predicted locations of tensile and compressive stresses in head joints for each wall (according to Figure 3-50).

Table 3-16. Predicted locations of tensile and compressive stresses in head joints for each wall

Wall	Tensile stress location [between the blocks number]	Compressive stress location [between the blocks number]
WG	4-5	1-2
Z1	7-8 and 8-9	1-2 and 2-3
Z2	8-9	1-2 and 2-3
Z3	2-3	7-8 and 8-9
Z5	5-6	1-2 and 2-3
Z6	2-3	9-10, 10-11 and 11-12

The predicted locations of stress concentration can be compared with the DIC obtained results on the longitudinal (horizontal) strain field on the surfaces of the walls, see Figure 3-51. The strain fields depicted correspond to the target horizontal wall top displacements of the loading cycles during which the sliding occurred, cf. Table 3-15, except in case of Wall Z2, where the strain field corresponds to the wall top displacement of 13 mm, until which there were no stress concentrations detected. It can be seen from Figure 3-51, where the head joins at the bottom block course can be recognized, that the locations of the stress (strain) concentrations are well predicted (the block numeration is the same as given in Figure 3-50).

Figures 3-36, 3-37 and 3-38 show that in case of walls WG, Z1 and Z3, the tensile cracks were initiated at the predicted locations, and further progressed to the upper part of the walls causing the reduction of the effective areas of the walls. In case of Wall Z6, the tensile crack opened at the predicted location at first, i.e. between the 2nd and 3rd block, however a new crack opened later between the 4th and 5th block and further progressed towards the wall top.
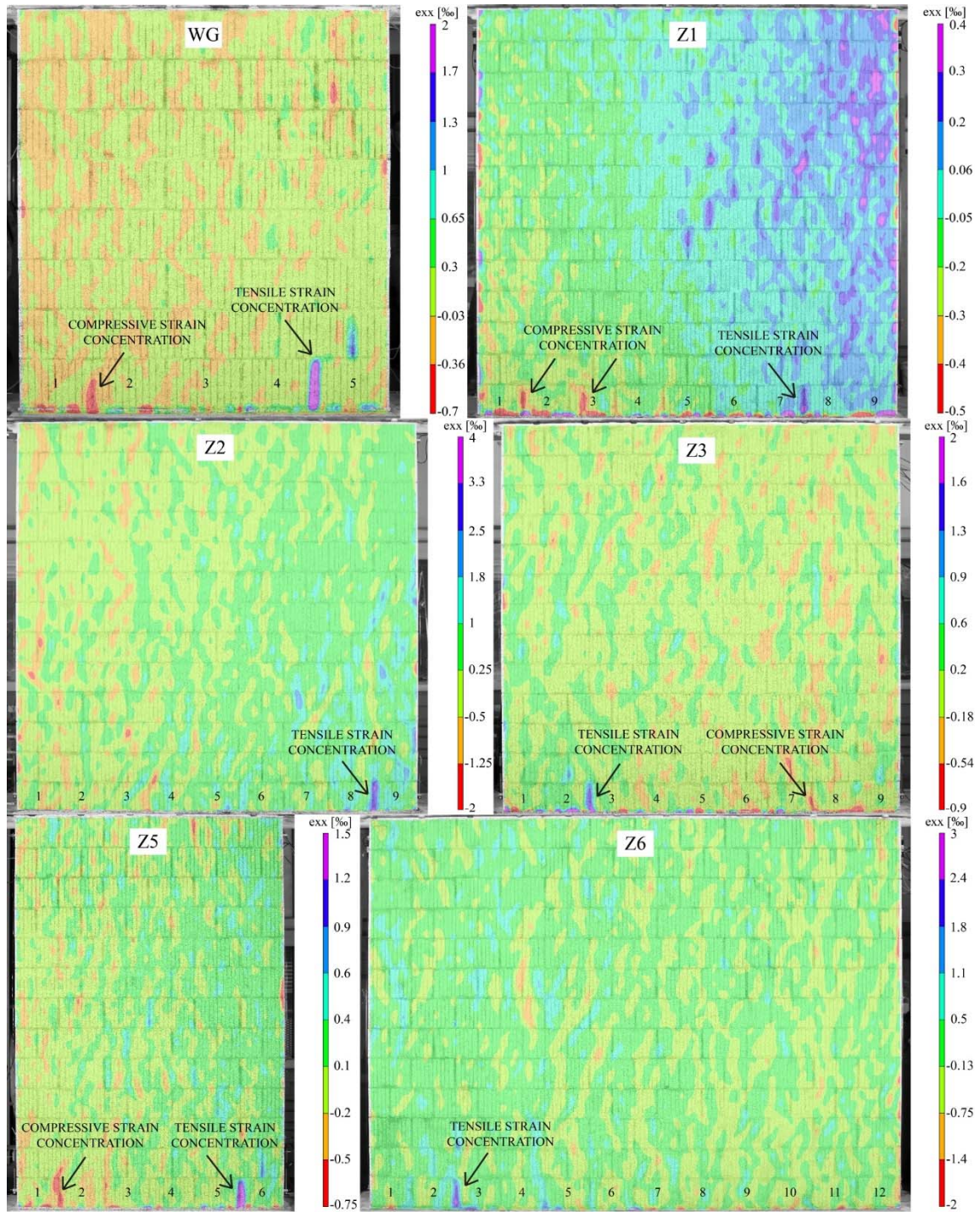
Figure 3-51. Longitudinal (horizontal) strain field on the surfaces of the walls

3.5 Monotonic in-plane shear and relaxation tests on masonry triplets with a rubber granulate core soft layer in multi-layer bed joints

A thorough analysis of the results from the test on masonry triplets and preliminary and main testing phase on URM walls with a multi-layer bed joint indicate that their shear behavior is dependent on the loading speed. Since the source of such loading speed dependent behavior is a multi-layer bed joint, there is a need for additional investigation of its shear load-deformation characteristics. The additional investigation is concentrated on the multi-layer bed joint with a rubber granulate soft layer, which was chosen as a core soft layer for the main testing phase of URM walls. A series of monotonic shear and relaxation tests were performed on masonry triplets with a rubber-granulate core soft layer to further investigate the shear load-deformation characteristics of the multi-layer bed joint and to assess the parameters needed for the theoretical investigation. The test results verify the previously revealed loading speed-dependent shear behavior of the multi-layer bed joint and indicate that the behavior of the multi-layer bed joint with a rubber granulate core soft layer can be characterized as linear elastic-viscoplastic.

3.5.1 Test programme and masonry materials

All triplets were prepared in the manner described in Section 3.2.1, at the same time as the specimens for the main testing phase of URM walls with a multi-layer bed joint and using the same soft layers and masonry components: typical Swiss perforated clay blocks, with nominal dimensions of 290x150x190 mm and void area of 42% and standard cement mortar. A mechanical characteristics of the used masonry components are reported in Section 3.4.1. Specimens were classified into three series according to the designated pre-compression level, σ_{pc}. For each series 13 different loading speed levels were foreseen and for each loading speed level one specimen was tested. The test programme is summarized in Table 3-17.

Table 3-17. URM triplets with a rubber granulate core soft layer in multi-layer bed joints: test programme

σ_{pc} [MPa]	Series	Loading speed [mm/min]												
		0.25	0.5	1	3	5	7	10	13	15	20	30	40	50
0.2	T1	T11	T12	T13	T14	T15	T16	T17	T18	T19	T110	T111	T112	T113
0.4	T2	T21	T22	T23	T24	T25	T26	T27	T28	T29	T210	T211	T212	T213
0.6	T3	T31	T32	T33	T34	T35	T36	T37	T38	T39	T310	T311	T312	T313

3.5.2 Test set-up, testing procedure and measurements

The test set-up was the same as one used for testing the URM triplets described in section 3.2.2. However, larger specimen dimensions demanded the larger universal testing machine. After the prescribed curing time, each specimen was placed in the universal testing machine between two load transmission elements and centered to avoid any bending influence, see Figure 3-52. A hydraulic jack together with the pendulum manometer was used to apply the pre-compression force and maintain it at the constant level during testing. Subsequently a specimen was subjected to the monotonic shear load by applying computer-controlled relative displacement (slip) between the middle and one of the outer blocks. The loading speed was kept at a constant level during each tests. After reaching the slip value of 0.3 mm in each test, the computer-controlled slip was stopped and kept constant until the shear load was relaxed, i.e. until there was no more change in value of the measured shear load. Then, a specimen was reloaded until reaching the maximum shear load, when the computer-controlled slip was stopped again and kept constant until the relaxation of the shear load. Finally, if there was no damage detected, a specimen was unloaded and prepared for the next loading speed level.
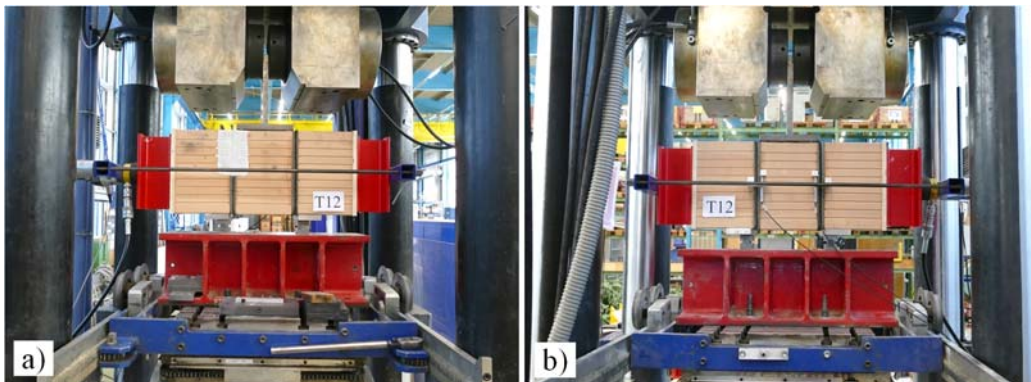
Figure 3-52. Test set-up: a) South specimen's side; b) North specimen's side

All measured data, i.e. vertical shear load, slip between the middle and outer blocks, pre-compression force, were recorded and processed in real time. A pair of load cells were used to monitor the level of the applied pre-compression force, see Figure 3-53a. Relative displacement (slip) between the middle and outer blocks were measured by means of two LVDTs on the North side of the specimen. One of those LVDTs was used for the test control purpose. All LVDTs had the measuring span of 10 mm and rested on L-shape aluminium plates, which in turn were glued to the blocks, see Figure 3-53b.

Figure 3-53. Measuring devices: a) loading cells; b) LVDTs; c) DIC system

A 2D-DIC measurement system was used to obtain the information on the displacement field on the surface of a multi-layer bed joint on the South side of the specimen, see Figure 3-53c. Only the multi-layer bed joint with the controlled slip was considered. The computer used for data acquisition triggered the DIC camera every 5 seconds. Figure 3-54 shows exemplarily the minor principal strain field and shear strain field of specimen T11, evaluated at the point of maximum pre-compression load and slip value of 0.3 mm, respectively.
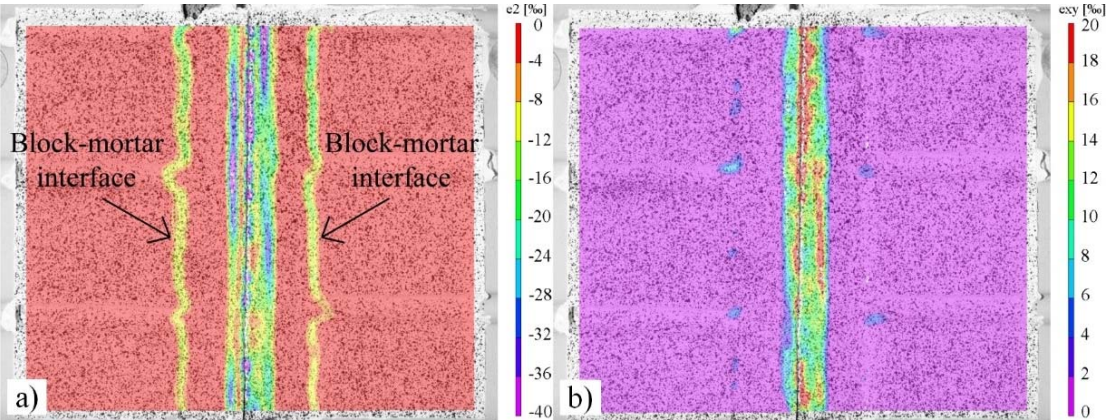
Figure 3-54. Specimen T11: a) minor principal strain field; b) shear strain field

3.5.3 Test results and specimen behavior

After applying the pre-compression load that was maintained at the constant level during the tests each specimen was subjected to the monotonic shear load. Figure 3-55 shows exemplarily the variation of the pre-compression over time. As in case of shear monotonic tests on masonry triplets with a multi-layer bed joint reported in Section 3.2, a typical shear deformation, i.e. sliding in the multi-layer bed joints between the core soft layers and elastomer layers, was observed in each test, see Figure 3-56. Values of the maximum shear force per bed joint, H, are summarized in Table 3-18. Table 3-19 shows the values of shear force after relaxation recorded after reaching the maximum shear force values.
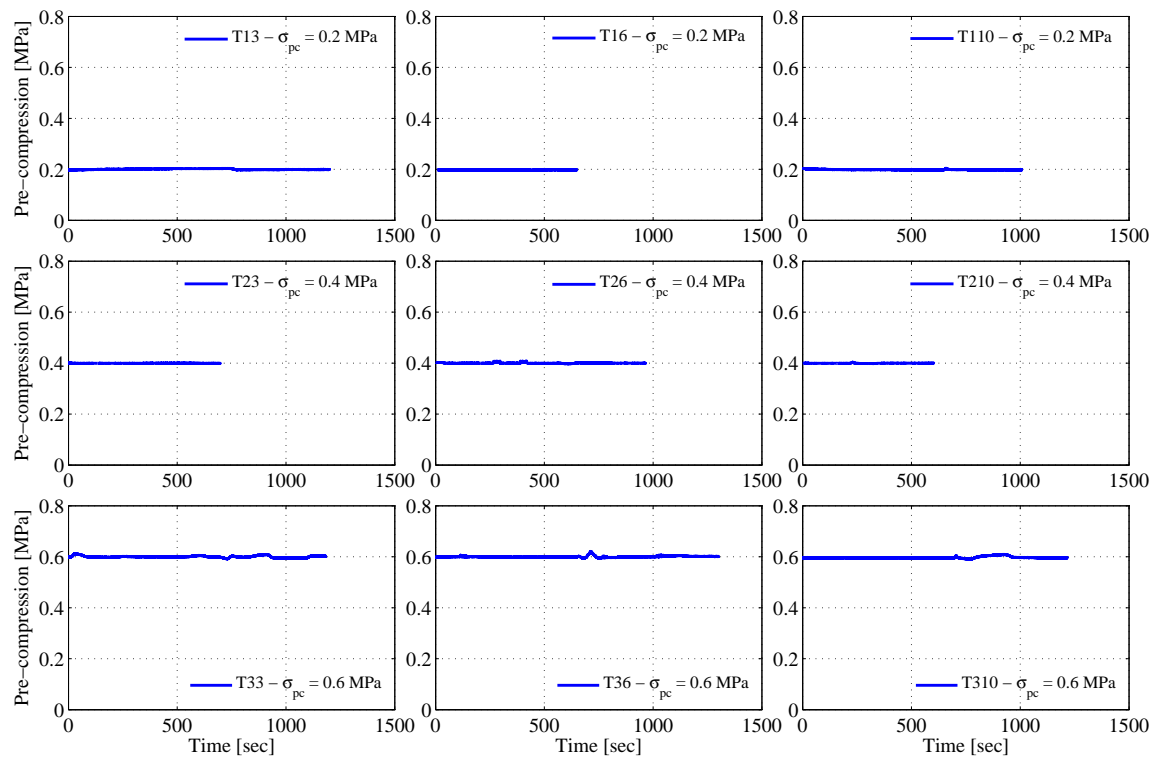
Figure 3-55. Pre-compression load vs. time
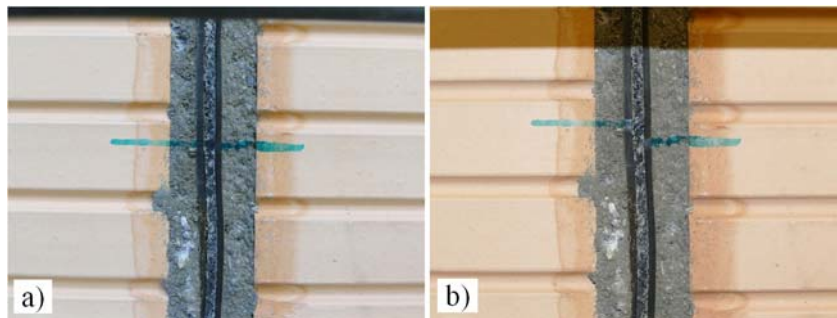
Figure 3-56. Typical shear-sliding deformation of specimens of series T1: a) before deformation; b) after deformation

Table 3-18. Monotonic tests on URM triplets with a rubber granulate core soft layer in multi-layer bed joints: values of maximum shear force [kN]

Series	Loading speed [mm/min]												
	0.25	0.5	1	3	5	7	10	13	15	20	30	40	50
T1	3.17	3.04	3.10	3.33	3.30	3.14	3.65	5.18	5.50	5.76	6.21	6.72	6.94
T2	4.22	4.93	5.51	7.01	7.77	8.48	8.86	9.47	9.70	9.99	10.82	10.98	11.68
T3	5.50	6.34	6.82	8.80	10.21	10.66	11.68	12.13	-	13.18	14.40	14.91	15.10

Table 3-19. Monotonic tests on URM triplets with a rubber granulate core soft layer in multi-layer bed joints: values of shear force after relaxation [kN]

Series	Loading speed [mm/min]												
	0.25	0.5	1	3	5	7	10	13	15	20	30	40	50
T1	2.19	1.92	1.89	1.85	1.81	1.76	1.85	1.79	1.69	1.63	1.63	1.63	1.53
T2	2.75	3.04	2.94	3.13	3.2	3.49	3.39	3.39	3.46	3.29	3.24	2.94	3.23
T3	3.4	3.4	3.6	3.68	3.74	3.68	3.65	3.58	-	3.68	3.58	3.45	3.36

Typical multi-layer bed joint shear load-deformation relationships obtained from the tests are shown in Figure 3-57. The deformation value shown in the diagram is the computer-controlled relative displacement between the middle and outer block. All specimens exhibited a non-linear behavior almost from the beginning. After reaching the maximum value of the shear force, which in turn depended on the loading speed as well on the pre-compression level, all specimens developed the plastic plateau.
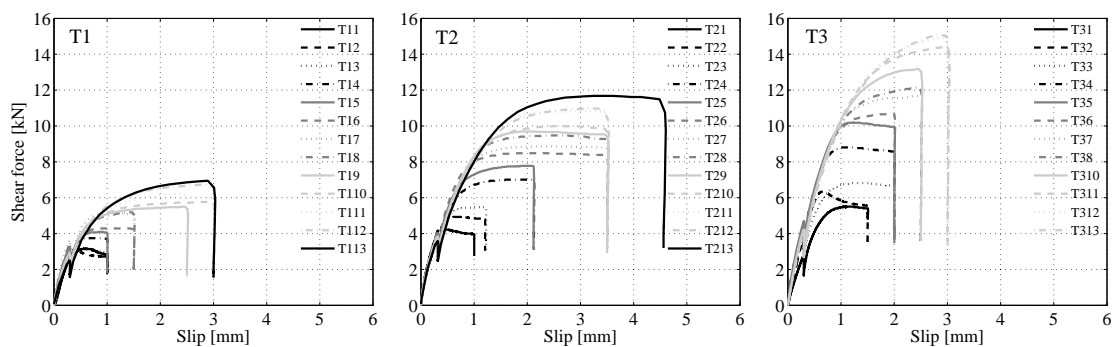
Figure 3-57. Shear force-slip relationships

All observed failure patterns were characteristic for masonry failing in a sliding mode. Sliding planes were formed along the interface between a rubber granulate core soft layer and the protective elastomer layers. In no case did shear failure occur through the units, and for none of the tests was any damage to the clay blocks observed. In addition, almost no damage of the soft layers was noticed after completion of the tests.

88

3.5.4 Discussion

The presented test results will be discussed in the following section. The influence of the applied pre-compression level and the loading speed is considered. Firstly, the shear load-deformation response of specimens is discussed. Further, the parameters of the linear relation between normal (pre-compression) and shear stress, i.e. Mohr-Coulomb's failure criterion are investigated. Finally, the deformation as well the degradation of elastomer and core soft layers is addressed.

3.5.4.1 Load-deformation characteristics

Observing the measured shear load-deformation relationships given in Figure 3-57 for each pre-compression separately, one can notice that all specimens had rather identical (initial) response up to the certain level of shear force, i.e. of slip, which did not depend on the loading speed. Thereafter, load-deformation curves defer from each other. Specimens could develop larger shear resistance with the increase of loading speed (a slight inconsistency can be noticed in measured values of maximum shear force for the first six specimens of series T1, caused by the sensitivity of the system used to keep the pre-compression load at the constant level, which was especially demanding during testing of the specimens of series T1). Such a behavior can be characterized as linear elastic-viscoplastic one. The force limit of the elastic behavior can be determined from the relaxation tests, see Table 3-19. It can be noticed that the values of shear force recorded after the relaxation depend on the level of pre-compression. Since the calculated values of COV from the sample of measured shear force after the relaxation measured in test series T1, T2 and T3 are 9.5%, 7% and 3.5%, respectively, it can be concluded that the influence of the loading speed on the value of shear force after the relaxation is small and can be neglected. When comparing the response characteristics from corresponding specimens from different test series, it can be seen that the values of maximum shear force and the initial stiffness increase with the increase of pre-compression, cf. Table 3-18 and Figure 3-57.

3.5.4.2 Shear stress-normal stress relationship

The test parameters allow us to check the applicability of Mohr-Coulomb's failure criterion to quantify the relationship between the applied pre-compression and the shear stress measured for different levels of loading speed. Note that shear stresses are calculated

using the gross cross-section area of the blocks, $A_b = 150\times290$ mm². A very good correlation between the test results and a theoretical linear relationship are obtained for each loading speed level, see Figure 3-58a.
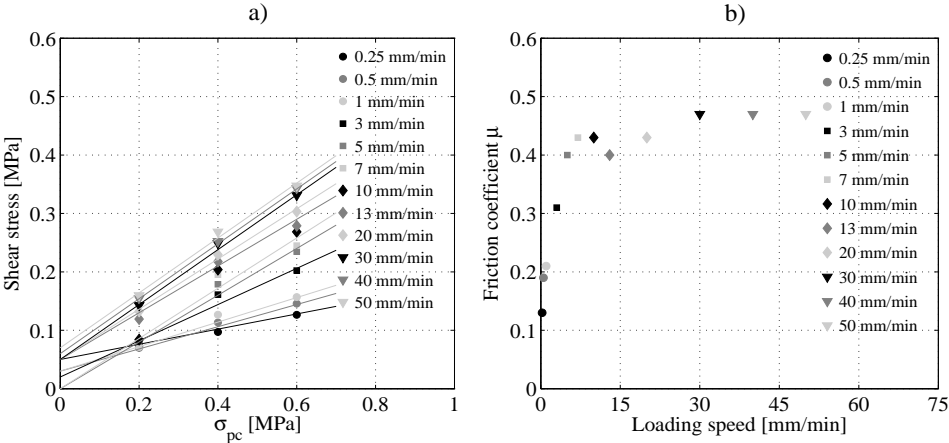
Figure 3-58. Shear strength parameters: a) pre-compression vs. nominal shear stress for different levels of loading speed; b) friction coefficient for different levels of loading speed

As can be seen from Figure 3-58b, the value of friction coefficient increases following approximately an exponential law as the loading speed increases.

The calculated values of the friction coefficient and the apparent cohesion (which can be neglected) are given in Table 3-20. The results obtained are in a very good agreement with the results on the coefficient of friction obtained from previous monotonic shear tests on masonry triplets with a rubber granulate core multi-layer bed joint, see Section 3.2.4.2. The dependence of the friction coefficient on the loading speed is strong and convergent. The upper bound of the value of friction coefficient is close to the value of friction coefficient of 0.44, which was determined from the static-cyclic shear tests on masonry triplets with a rubber granulate core soft layer in multi-layer bed joints, see Section 3.2.4.2. Further, it was observed during testing the Specimen Z2 that the increase of the horizontal force resistance, after exceeding the loading speed level of 9.5 mm/min, was negligible, see Section 3.4.3.2. The same can be considered as true here for the values of friction coefficient. Therefore, the statement that the applicability of Mohr-Coulomb's failure criterion, with zero or non-zero cohesion, to determine the shear strength of URM bed joint with incorporated soft layers, requires the friction properties to be experimentally determined for the particular soft layer material and the particular soft layer bed joint configuration using a loading protocol with varying loading magnitudes and speeds, is verified. In addition, a cyclic loading protocol is desired to account for the cyclic load-

caused degradation of friction coefficient. However, it should be kept in mind that the influence of the loading speed is convergent, and that with an increase of the length of the multi-layer bed joint, the contribution of the friction coefficient reduces, while the contribution of the apparent cohesion to the horizontal force resistance rises and cannot be neglected anymore (see Section 3.4.4.1).

Table 3-20. Values of the friction properties calculated for different levels of loading speed

Parameter	Loading speed [mm/min]											
	0.25	0.5	1	3	5	7	10	13	20	30	40	50
c [MPa]	0.05	0.03	0.03	0.02	0	0	0	0.05	0.05	0.05	0.06	0.07
μ [-]	0.13	0.19	0.21	0.31	0.4	0.43	0.43	0.4	0.43	0.47	0.47	0.47

3.5.4.3 Deformation of the multi-layer bed joint

Use of DIC measurement system allow us to determine two important parameters that describe the deformation of the multi-layer bed joint when subjected to the pre-compression and the shear load. First, values of the contraction of the thickness of the multi-layer bed joint Δt_{ml} were measured during applying the pre-compression load. The values which correspond to the maximum levels of pre-compression are given in Table 3-21. Second, using the values of relative displacement (slip) measured within the initial phase of applying the shear load, i.e. during the pre-sliding regime, where one can assume that the soft layers of the multi-layer bed joint remain connected to each other and deform in a pure shear, the values of multi-layer bed joint shear modulus, G_{ml}, can be determined. The equation (3-7) was used to determine the value of G_{ml} for each test series.

$$G_{ml} = \frac{H \cdot \left(t_{ml} - \Delta t_{ml} \right)}{A_b \cdot d} \tag{3-7}$$

The equation (3-7) is derived from the shear stress-shear strain relationship, $\tau / \gamma = G_{ml}$, while taking into account the relationship between the shear stress and the shear load

$$\tau = H / A_b \tag{3-8}$$

and that the multi-layer bed joint represents a localized zone of intense shearing with constant thickness, $t_{ml} - \Delta t_{ml}$, and relating the shear strain, γ, to the slip in the multi-layer bed joint, d

$$\gamma \cdot \left(t_{ml} - \Delta t_{ml} \right) = d \tag{3-9}$$

see Oberender and Puzrin [48]. The values of multi-layer bed joint shear modulus calculated for the measured slip value of 0.1 mm are given in Table 3-21.

Table 3-21. Contraction of the thickness and shear modulus of the multi-layer bed joint (t_{ml}=7.4 mm)

Series	σ_{pc} [MPa]	Δt_{ml} [mm]	G_{ml} [MPa]
T1	0.2	0.24	2
T2	0.4	0.27	1.95
T3	0.6	0.53	2.2

As expected, the larger values of the contraction of the thickness of the multi-layer bed joint were measured for the larger pre-compression level, see Table 3-21. However, the pre-compression did not influence the value of shear modulus of the multi-layer bed joint, which in average equals 2 MPa. As it is already mentioned, the specimens in each series had rather identical (initial) response, i.e. initial stiffness up to the certain point of shear force. Since the initial stiffness is determined by the value of G_{ml}, one can conclude that the loading speed did not affect the value of G_{ml}.

3.5.4.4   Degradation of elastomer and core soft layers

As in case of previous monotonic tests on masonry triplets with multi-layer bed joints, a modest damage of the soft layers was detected even for the highest level of pre-compression, see Figure 3-59. Only the signs of the sliding motion were visible on the surface of soft layers for each series and were more pronounced for higher levels of applied pre-compression. Once more it was confirmed that the degradation of the multi-layer bed joint soft layers during monotonic loading is not an issue of concern.
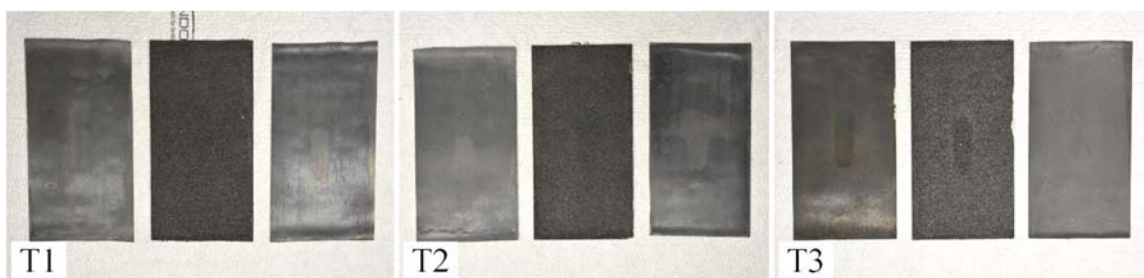
Figure 3-59. Degradation of elastomer and core soft layers

3.6 Summary and conclusions

Based on the presented analysis and discussion of the results of the material-level tests on small masonry elements with a multi-layer bed joint(s) subjected to the in-plane compression load or to the combination of in-plane pre-compression and shear load, being either monotonic or static-cyclic, and of the results of the structural element-level static-cyclic shear tests of URM walls with a multi-layer bottom bed joint, the following conclusions may be drawn.

When subjected to the in-plane compression load perpendicular to the bed joints, the behavior of URM is influenced by the multi-layer bottom bed joint in such way that: as compared to the masonry elements made without the multi-layer bed joint, only the presence of a rubber granulate core soft layer in the multi-layer bed joint leads to the somewhat lower compressive strength of masonry; the vertical deformability of masonry is influenced by any type of considered multi-layer bed joints. Although small, those influences should be taken into account in the design of URM with such multi-layer bottom bed joints.

Results from the series of monotonic and static-cyclic in-plane shear tests on small masonry elements (triplets) indicate the following. An increase of the level of the pre-compression leads to higher values of shear resistance of the multi-layer bed joint, regardless to the core soft layer and the loading protocol type. The same is true for increasing loading speed. Therefore, the applicability of Mohr-Coulomb's failure criterion to determine the shear resistance of the multi-layer bed joint, since the criterion considers the constant friction properties, i.e. the properties independent of the loading speed, requires the friction properties to be experimentally determined for the particular soft layer material and the particular soft layer bed joint configuration using a loading protocol with varying loading magnitudes and speeds. However, the maximum shear resistance can be predicted adequately using the Mohr-Coulomb's failure criterion with zero cohesion. Based on the presented results from static-cyclic tests, an friction coefficient of 0.5 is recommended to estimate the maximum shear resistance of multi-layer bed joint with a rubber granulate, cork-rubber granulate, cork or a bitumen core soft layer, while for the multi-layer bed joint with a PVC-based core soft layer, the value of friction coefficient should not be taken greater than 0.1. The intended protective role of the extruded elastomer

layers is largely fulfilled. Only for static-cyclic loading and for higher pre-compression levels, a certain degradation of bitumen and rubber-granulate core soft layers was ascertained. Based on the observed hysteretic behavior, considerable energy dissipation and quasi-ductile behavior could be expected in URM walls with a multi-layer bed joint.

Additional series of monotonic shear tests on URM triplets with a rubber granulate core soft layer in multi-layer bed joints verify the previously revealed loading speed-dependent shear behavior of such multi-layer bed joints and provide more information needed to characterize it. The behavior of the multi-layer bed joint with a rubber granulate core soft layer can be characterized as linear elastic-viscoplastic. After the initial elastic, loading speed-independent behavior, the influence of loading speed appears: an increase of the loading speed leads to higher values of shear resistance. As shown from the relaxation tests, the loading speed does not influence the value of shear load at the elastic limit (shear load after the relaxation). The value of shear load at the elastic limit is in turn dependent on the pre-compression level: higher values of pre-compression lead to higher values of shear load at the elastic limit. The same is true for the values of shear resistance as well for the values of the contraction of the multi-layer bed joint thickness. Further, the shear modulus of multi-layer bed joint is found independent of the pre-compression and the loading speed and equals 2 MPa. Finally, although convergent, the dependence of friction coefficient on the loading speed must be taken into account when applying the Mohr-Coulomb's failure criterion to determine the shear resistance of the multi-layer bed joint. The value of friction coefficient increases following approximately an exponential law as the loading speed increases.

All URM walls with a rubber granulate core soft layer, which is chosen as the best of four considered core soft layer types based on the results of the preliminary testing phase, respond in the same manner: the initial response, which primarily originates from the soft layer shear and vertical deformability, is followed by sliding along the multi-layer bed joint. The maximum horizontal force resistance of URM walls with a rubber granulate core soft layer can be predicted adequately using the Mohr-Coulomb's friction law. Based on the presented test results, a friction coefficient of 0.2 and the corresponding apparent cohesion of 0.15 MPa, are recommended to estimate the maximum horizontal force resistance of full-scale URM walls with a rubber granulate core soft layer in multi-layer bed joints. Therefore, considering the results obtained from the shear tests on masonry

triplets, it can be concluded that increasing the size of the specimen, and therefore the length of the multi-layer bed joint, the friction coefficient reduces, while the contribution of the apparent cohesion to the force resistance rises and cannot be neglected anymore. However, since the walls respond in sliding in a multi-layer bed joint, the horizontal force resistance of URM with a multi-layer bed-joint is found dependent on the loading speed. Such an issue deserves a special intention. A mechanical model for the in-plane shear response of URM walls with a rubber granulate core soft layer in the multi-layer bed joint which comprises the influence of loading speed as well the pre-compression level is developed based on the observations obtained from the shear tests on masonry small and large elements, and is presented in Chapter 4. It is also found that the increase of the level of the pre-compression leads to higher values of maximum horizontal force resistance, initial stiffness and shear span of the walls. The ultimate displacement capacity as well the failure mode of the tested walls is strongly influenced by the extent of shear cracks that develop in the wall as well as by the appearance of (vertical) tensile cracks in the head joints at the bottom block course, which further tend to reduce the effective area of the wall. It is shown that the location of such tensile crack within the bottom block course can be predicted by analyzing the bottom wall cross-section with a multi-layer bed joint "block by block" at the onset of sliding, while assuming the linear and parabolic distribution of normal and shear stresses, respectively. In loading cycles before the reduction of the effective area of the wall appears, the stiffness of all tested walls remains close to the initial stiffness until reaching the maximum horizontal force resistance. The initial stiffness of URM walls with a multi-layer bed joint can be estimated as 1.4 times the value of elastic stiffness calculated using the proposed equation, which, besides the masonry shear and flexure deformation, considers the shear deformation of the multi-layer bed joint, the rocking deformation allowed by the multi-layer vertical deformability as well the influence of the pre-compression. Further, a method to construct an idealization of the horizontal force-displacement response envelope for the tested URM walls with multi-layer bed joints is proposed. The parameters of this envelope are defined by analogy to the response envelope proposed in FEMA-356 [46] to capture the strength, stiffness and ultimate displacement capacity of the walls, as well as to model sudden drops in wall horizontal force resistance if they occur. The protective extruded elastomer layers are able to limit the deterioration of the rubber granulate core soft layer. Only local damage to the rubber granulate core soft layer, i.e. crumbling caused by normal stress concentration in

combination with the sliding motion, was detected at the location where the tensile cracks in the head joints at the bottom block course appeared. As compared to the corresponding conventional URM walls made without a multi-layer bed joint, see [43,44], the URM walls with a multi-layer bottom bed joint have: about 30% lower maximum shear resistance, 15-40% lower initial stiffness and up to six times larger displacement capacity, depending on the wall size, type of core soft layer, pre-compression level and wall aspect ratio. However, the displacement capacity should be limited to 26 mm, i.e. 1% in terms of drift ratio, due to the interaction of the wall with other structural and non-structural components of the building. In case of pre-compression load not greater than 5% of masonry compressive strength, a wall experienced essentially no damage when subjected to the static-cyclic shear load. Moreover, in case of pre-compression load of 10% of masonry compressive strength, although the wall was damaged, i.e. the wall effective area was reduced, the wall kept its integrity, had essentially no, for URM, typical diagonal shear cracks, and could further exhibit a stable response and carry the vertical load applied. The presence of the multi-layer bed joint with a rubber granulate core soft layer results in relatively soft response of URM walls, i.e. leads to an elongation of the initial fundamental vibration period of URM structures that contain such multi-layer bed joints. The multi-layer bed joints can allow for a remarkable amount of inelastic deformation (given their thickness) before the onset of shear failure (if any) of the masonry, making their response quasi-ductile and protecting the URM walls from the excessive shear-caused diagonal cracking. Given the above, it can be finally concluded that the bottom multi-layer bed joints in URM walls act to modify the seismic response of URM walls, and further to enable the URM structures with such walls to achieve the target performance goals given in Section 1.2: 1) experience essentially no damage in frequent earthquakes and under high wind loads when the structure is expected to remain elastic; 2) experience controlled damage in design-basis earthquakes through an elongation of the structural response period due to relatively low stiffness in the pre-sliding regime and the stable lateral sliding deformation; and 3) collapse prevention in beyond-design-basis earthquakes through preserving the gravity load-carrying capacity of the structural masonry walls. The exhibited displacement capacities of URM walls with multi-layer bed joints are, however, moderate, making this seismic response modification approach suitable for regions of low and moderate seismicity.

96

4   Analytical Modelling

Findings from the performed in-plane static-cyclic shear tests on masonry triplets as well the findings from the preliminary and main testing phase on URM walls with a multi-layer bed joint indicate that the load-bearing URM with a multi-layer bed joint, in spite of the prevailing sliding response, exhibit a significant shear capacity that depends on the type of core soft layer material, applied level of pre-compression as well as on the loading speed. Therefore, use of Mohr-Coulomb's failure criterion to determine the shear strength of URM with a multi-layer bed joint requires determining the friction properties experimentally for the particular core soft layer material and loading speed by using a cyclic loading protocol with varying loading magnitudes and speeds. In this Chapter, a mechanics-based analytical model of the loading speed-dependent in-plane shear behavior of the masonry multi-layer bed joint with a rubber granulate core soft layer will be presented and further extended to describe the horizontal force-displacement behavior of URM walls with rubber granulate core multi-layer bottom bed joints.

4.1   Model description

Figure 4-1 shows the mechanical behavior of the multi-layer bed joint with a rubber granulate core soft layer under monotonic shear loading, i.e. the experimentally observed relationships between the shear stress, τ, and slip, d, where shear stress is calculated by dividing the bed joint shear load with the nominal cross-section area of the brick $A_b = 150 \times 290$ mm. The results depicted in Figure 4-1 are obtained from the shear tests on specimens from T2 series, see Section 3.5. It can be seen that the initial branches of the shear stress-slip curves (up to displacement of approximately 0.3 mm) are identical and independent on the loading speed. Thereafter, shear stress-slip curves differ from each other and depend on the loading speed. As stated in Section 3.5.4.1, such behavior can be described as elastic-viscoplastic, or more precisely as elastic-perfectly viscoplastic, since the shear stress values obtained from relaxation tests, indicating the elastic limit, are found independent on the loading speed level. Further, this behavior can be schematically represented by a uniaxial model consisting of a dashpot with a parameter η^*, denoting the loading speed sensitive viscosity-related parameter, whose dimension is time, and a sliding element with a parameter τ_y, denoting the elastic shear stress limit. These two elements are placed in parallel and are further connected in series with an elastic spring

with a modulus G_{ml}, the shear modulus of the multi-layer bed joint, as shown in Figure 4-2.
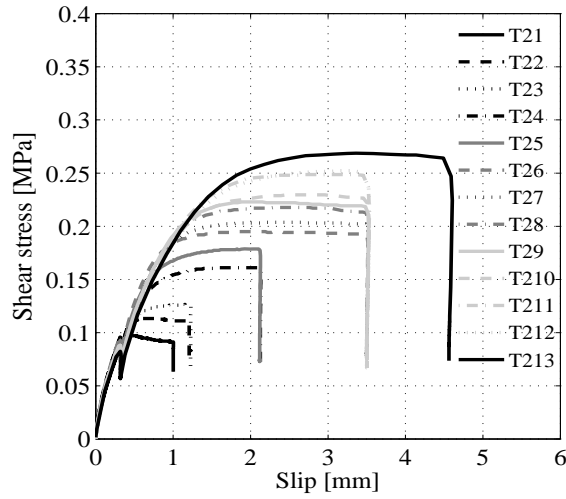
Figure 4-1. Shear stress-slip relationships for the specimens in test series T2
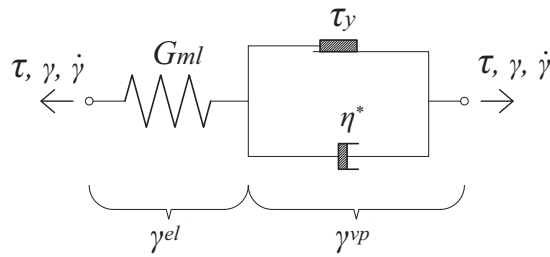
Figure 4-2. Schematic representation of the loading speed-dependent mechanical model

The mechanical behavior of the model can be defined as follows:

- A total shear strain, γ, can be decomposed into a sum of an elastic (recoverable) and viscoplastic (permanent) components:

$$\gamma = \gamma^{el} + \gamma^{vp} \tag{4-1}$$

- The elastic stress-strain relationship is:

$$\tau = G_{ml} \cdot \gamma^{el} \tag{4-2}$$

- The yield function is:

$$\Phi\left(\tau, \tau_y\right) = |\tau| - \tau_y \quad \text{where} \quad \tau_y = f\left(\sigma_{pc}\right) \tag{4-3}$$

- The viscoplastic flow rule is (adopted from de Souza Neto et al. [49]):

$$\dot{\gamma}^{vp} = \lambda \cdot \text{sign}(\tau) \tag{4-4}$$

where

$$\lambda = \begin{cases} \dfrac{1}{\eta^*} \cdot \left[\dfrac{|\tau|}{\tau_y} - 1 \right] & \text{if } \Phi(\tau, \tau_y) \geq 0 \\[2ex] 0 & \text{if } \Phi(\tau, \tau_y) < 0 \end{cases} \tag{4-5}$$

It is noteworthy that λ, as compared to the theory of plasticity, where it represents a plastic multiplier that should be determined from the consistency condition, $\dot{\Phi} \cdot \lambda = 0$ (see [49] for details), in the present theory of viscoplasticity is an explicitly given function, capable of modelling the dependence of the viscoplastic strain speed on the state of stress. As stated before, it is assumed that the multi-layer bed joint exhibits the elastic-perfectly viscoplastic behavior, i.e. the shear yield stress τ_y is constant. Let us further consider the problem in the domain of the positive shear stress and strain. After the initial pure elastic behavior, i.e. after exceeding the elastic limit (τ_y, or γ_y in terms of deformation), a multi-layer bed joint behaves viscoplastically. Starting from equation (4-1)

$$\gamma = \gamma^{el} + \gamma^{vp} \quad \text{yields} \quad \dot{\gamma} = \dot{\gamma}^{el} + \dot{\gamma}^{vp} \tag{4-6}$$

and further by considering equations (4-2), (4-4) and (4-5), one can derive

$$\dot{\gamma} = \frac{\dot{\tau}}{G_{ml}} + \frac{1}{\eta^*} \cdot \left(\frac{\tau}{\tau_y} - 1 \right) \quad \text{or} \quad \dot{\tau} + \frac{G_{ml}}{\eta^* \cdot \tau_y} \cdot \tau = \frac{G_{ml}}{\eta^*} + G_{ml} \cdot \dot{\gamma} \tag{4-7}$$

Further, applying standard methods for solving first-order ordinary linear differential equations, the equation (4-7) can be solved and the shear strain (loading) speed-dependent shear stress-shear strain response of the multi-layer bed joint can be obtained. Assuming the shear strain speed as constant and starting from the general solution of the differential equation (4-7)

$$\tau(t) = C_1 \cdot e^{-\frac{G_{ml}}{\tau_y \cdot \eta^*} \cdot t} + \tau_y \cdot \left(1 + \eta^* \cdot \dot{\gamma} \right) \tag{4-8}$$

and further substituting $t = \gamma / \dot{\gamma}$, one can obtain that

$$\tau\left(\gamma,\dot{\gamma}\right) = C_1 \cdot e^{-\frac{G_{ml}}{\tau_y \cdot \eta^*} \cdot \frac{\gamma}{\dot{\gamma}}} + \tau_y \cdot \left(1 + \eta^* \cdot \dot{\gamma}\right) \tag{4-9}$$

With known force boundary condition $\tau\left(\gamma = \gamma_y\right) = \tau_y$, the constant C_1 can be determined

$$C_1 = -\tau_y \cdot \dot{\gamma} \cdot \eta^* \cdot e^{\frac{G_{ml}}{\tau_y \cdot \eta^*} \cdot \frac{\gamma_y}{\dot{\gamma}}} \tag{4-10}$$

and finally the shear strain (loading) speed-dependent shear stress-shear strain relationship

$$\tau\left(\gamma,\dot{\gamma}\right) = \tau_y \cdot \left[1 + \dot{\gamma} \cdot \eta^* \cdot \left(1 - e^{-G_{ml} \cdot \frac{\gamma - \gamma_y}{\tau_y \cdot \eta^* \cdot \dot{\gamma}}}\right)\right] \tag{4-11}$$

Furthermore, as it is mentioned before, one can take into account that the multi-layer bed joint represents a localized zone of intense shearing with constant thickness t_{ml}, and relate the shear strain γ and shear strain speed $\dot{\gamma}$ to the slip in the multi-layer bed joint d and the slip (loading) speed $\dot{d}$, respectively, see [48]. In addition, the contraction of the thickness of multi-layer bed joint due to pre-compression, Δt_{ml}, can be considered:

$$d = \gamma \cdot \left(t_{ml} - \Delta t_{ml}\right) \text{ yields } \dot{d} = \dot{\gamma} \cdot \left(t_{ml} - \Delta t_{ml}\right) \tag{4-12}$$

This allows for formulating the shear stress-shear deformation relationship in the shear stress-displacement space:

$$\tau\left(d,\dot{d}\right) = \tau_y \cdot \left[1 + \frac{\dot{d}}{t_{ml} - \Delta t_{ml}} \cdot \eta^* \cdot \left(1 - e^{-\frac{G_{ml}}{\tau_y \cdot \eta^*} \cdot \frac{d - d_y}{\dot{d}}}\right)\right] \tag{4-13}$$

As can be seen from equation (4-13), knowing the thickness of the multi-layer bed joint, one needs a total of 4 parameters, i.e. τ_y, G_{ml}, the viscosity-related parameter η^*, and the contraction of the thickness of multi-layer bed joint due to pre-compression Δt_{ml} to fully define the shear stress dependence on the loading speed and the displacement (slip). The model behavior for constant value of η^* and different values of loading speed is shown in Figure 4-3 (black solid lines). In addition, the limits when $\dot{d} \vee \eta^* \to 0$ (denoting an infinitely small loading speed or an non-viscous material) and $\dot{d} \vee \eta^* \to \infty$ (denoting an infinitely large loading speed or an infinitely viscous material) are shown (red solid lines).

100
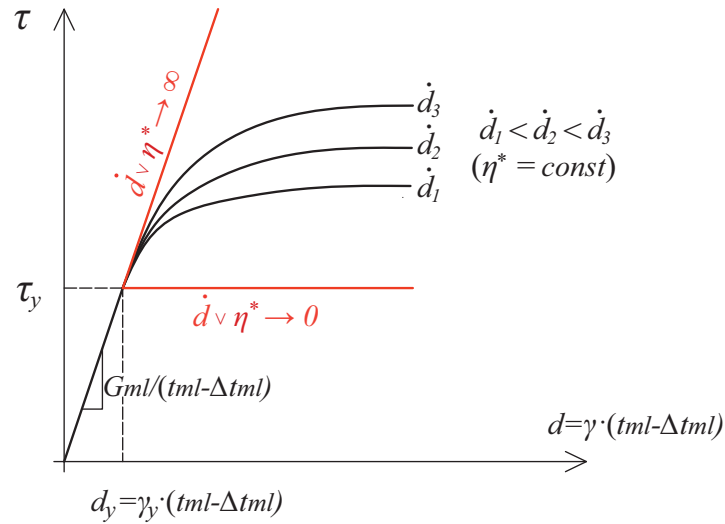
Figure 4-3. Behavior of the loading speed-dependent mechanical model

4.2 Model parameters

A multi-layer bed joint consists of a core soft layer protected with two layers of extruded elastomer that are placed in the middle of the mortar bed joint. One can assume that the soft layers of the multi-layer bed joint remain connected to each other during the pre-sliding regime and deform in shear, and that the shear deformation of the mortar layers is relatively small and therefore negligible. The performed series of monotonic shear tests on masonry triplets with a rubber granulate core soft layer in multi-layer bed joints under different levels of pre-compression and loading speeds, and use of DIC measurement system, provided the data to estimate the multi-layer bed joint shear modulus as well the relation between the thickness contraction of the multi-layer bed joint and the level of pre-compression, see Section 3.5.4.3. The results indicate that the value of the shear modulus of the multi-layer bed joint can be considered as independent of the pre-compression level and loading speed and equals 2 MPa. The dependence of the multi-layer thickness contraction, Δt_{ml}, on the level of pre-compression, estimated from the DIC results, is shown in Table 3-21. For the sake of assessing values of τ_y, the controlled bed joint slip was stopped after reaching the maximum shear force in each test and the relaxation of the shear load was recorded. The relaxation part lasted until the (bed joint) shear force, H, became constant, indicating the value of H_y, i.e. $\tau_y = H_y/A_b$. The results show that the value of τ_y depends on the level of pre-compression, but it is independent of the shear loading speed, cf. Table 3-19 for values of the shear force after the relaxation. Knowing the thickness of multi-layer bed joint $t_{ml} = 7.4$ mm, and values of τ_y, G_{ml} and Δt_{ml}, the

101

corresponding values of slip at the elastic limit, d_y, can be calculated using equation (4-14), which considers the aforementioned relationship between the shear strain and slip in the multi-layer bed joint, see Table 4-1.

$$d_y = \tau_y \cdot \left(t_{ml} - \Delta t_{ml} \right) / G_{ml}$$ (4-14)

Table 4-1. Monotonic shear tests (T specimens): elastic limit determination

Test series	Pre-compression [MPa]	[a] τ_y [MPa]	G_{ml} [MPa]	d_y [mm]
T1	0.2	0.04	2	0.15
T2	0.4	0.07	2	0.25
T3	0.6	0.08	2	0.28

[a] Average from the sample of calculated values of τ_y for different loading speeds

Table 4-2. Static-cyclic shear tests (G series): elastic limit

Test	Pre-compression [MPa]	d_y [mm]	G_{ml} [MPa]	τ_y [MPa]
G1_1 and G1_2	0.2	0.15	2	0.04
G2_1 and G2_2	0.6	0.28	2	0.08
G3_1 and G3_2	1	[a] 0.35	2	0.18

[a] Value obtained by extrapolating the measured data from Table 4-1

Values of the remaining model viscosity parameter η^* could be found by calibrating the model so as to capture the measured shear resistances from the monotonic shear tests. However, since the model should account for the cyclic loading-caused elastic (initial) shear stiffness degradation, data from the monotonic shear tests cannot be considered as appropriate to calibrate the model. For that reason, data on the shear capacity from series of static-cyclic shear tests on masonry triplets with multi-layer bed joints will be used. Those data are reported in detail in Section 3.2. Note that only the specimens with a rubber granulate core soft layer are considered, i.e. the G series. Test data are available for three levels of pre-compression, namely 0.2 MPa, 0.6 MPa and 1.0 MPa, and the loading speed range of 0.5-10 mm/min. Assuming that the values of d_y, G_{ml} and Δt_{ml} are the same as estimated for the monotonic test series, the corresponding values of τ_y can be calculated for different levels of pre-compression by using equation (4-14), see Table 4-2.

In order to account for the elastic (initial) stiffness degradation, one can assume that the cyclic loading causes degradation of the shear modulus of the multi-layer bed joint, since it is directly proportional to the shear stiffness of the multi-layer bed joint, cf.

equation (4-14). The data from the static-cyclic shear tests indicate that the evolution of the (relative) degradation of the elastic stiffness, measured at the beginning of each first pushing semi-cycle applied, with the number of performed loading cycles, *n*, is independent of the level of pre-compression and that it can be approximated quite well using a rational function, see Figure 4-4.
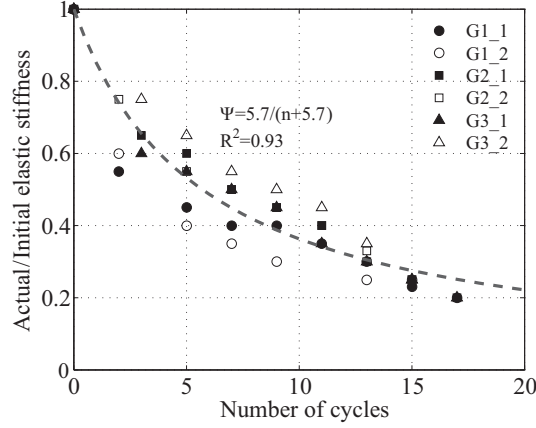
Figure 4-4. Relative degradation of the elastic stiffness with the number of performed loading cycles

Therefore, the elastic (initial) stiffness degradation with the number of loading cycles can be accounted for through degradation of the shear modulus of the multi-layer bed joint by simply multiplying it with a coefficient $\psi = 5.7/(n+5.7)$, see Figure 4-4. Now considering coefficient ψ, and the relationship between the shear stress and the shear force, $\tau = H/A_b$, the following model equation can be obtained:

$$H = H_y \cdot \left[1 + \frac{\dot{d}}{t_{ml} - \Delta t_{ml}} \cdot \eta^* \cdot \left(1 - e^{-\frac{\psi \cdot G_{ml} \cdot A_b}{H_y \cdot \eta^*} \cdot \frac{d - d_y}{\dot{d}}} \right) \right] \tag{4-15}$$

With the defined (initial) values of τ_y, d_y and the degradation of the elastic stiffness, the model can be finally calibrated for the model parameter η^*, so as to capture the values of the maximum shear force measured for each first pushing semi-cycle applied during the static-cyclic tests on masonry triplets, while considering the corresponding loading speed, the maximum displacement (slip) and the number of the performed loading cycles. The loading speed is considered as constant and equal to the average value in spite of the sinusoidal loading pattern. Values of the model parameter η^* are calculated for each level of pre-compression and for each replicate, except for the replicate G3_1 whose resistance was far below expected, indicating that the test data are not reliable. It should be noted

that values of τ_y are kept constant, while the values of d_y change as the elastic (initial) stiffness degrades with the increase of the number of loading cycles. The obtained results, as well the input values for model calibration, are summarized in Table 4-3. Figure 4-5 shows the values of the model parameter η^*, determined for each test series and plotted versus the corresponding loading speed values together with the regression curves.

Table 4-3. Input values for model calibration and the determined values of model parameter η^*

Specimen	Parameter							
G1_1	Max shear force [kN]	2.51	3.21	4.14	4.45	4.58	4.34	4.30
	Max slip [mm]	1.98	2.98	4.89	9.63	14.42	19.21	28.58
	Loading speed [mm/min]	0.5	1	3	5	10	10	10
	η^* [min]	14.26	11.18	5.5	3.64	1.89	1.76	1.73
G1_2	Max shear force [kN]	2.19	3.89	5.00	5.28	4.97	4.94	-
	Max slip [mm]	0.87	2.66	4.49	9.20	18.64	26.83	-
	Loading speed [mm/min]	0.5	1	3	5	10	10	-
	η^* [min]	10.77	15.28	7.23	4.59	2.12	2.1	-
G2_1	Max shear force [kN]	5.83	7.14	9.32	10.48	12.11	11.98	10.69
	Max slip [mm]	1.52	2.26	4.14	8.87	13.44	18.11	30.00
	Loading speed [mm/min]	0.5	1	3	5	10	10	10
	η^* [min]	45.29	31.11	10.21	5.03	2.94	2.83	2.41
G2_2	Max shear force [kN]	5.74	6.98	9.02	10.18	11.82	11.59	-
	Max slip [mm]	1.89	2.91	4.76	9.48	14.25	19.06	-
	Loading speed [mm/min]	0.5	1	3	5	10	10	-
	η^* [min]	25.47	17.22	8.01	4.73	2.81	2.69	-
G3_2	Max shear force [kN]	5.79	10.07	13.76	15.63	17.51	16.63	-
	Max slip [mm]	0.89	2.81	4.69	9.48	19.01	28.19	-
	Loading speed [mm/min]	0.5	1	3	5	10	10	-
	η^* [min]	71.22	23.88	12.24	5.79	3.02	2.78	-
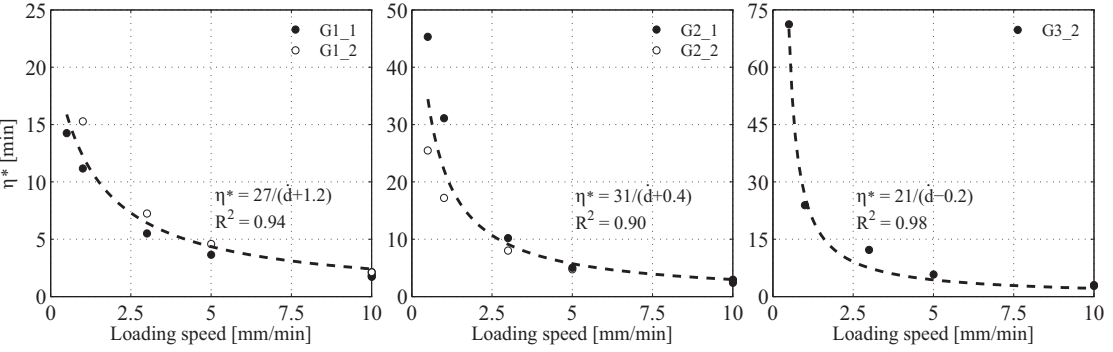
Figure 4-5. Model parameter η^* vs. loading speed

4.3 Model extension and validation

As concluded before, besides the shear deformation of the multi-layer bed joint (sliding motion during the sliding regime) and masonry deformation, another contribution to the total URM wall deformation emerges from the vertical deformability of the multi-layer bed joint, which allows the wall to rotate as a rigid body, i.e. to rock.
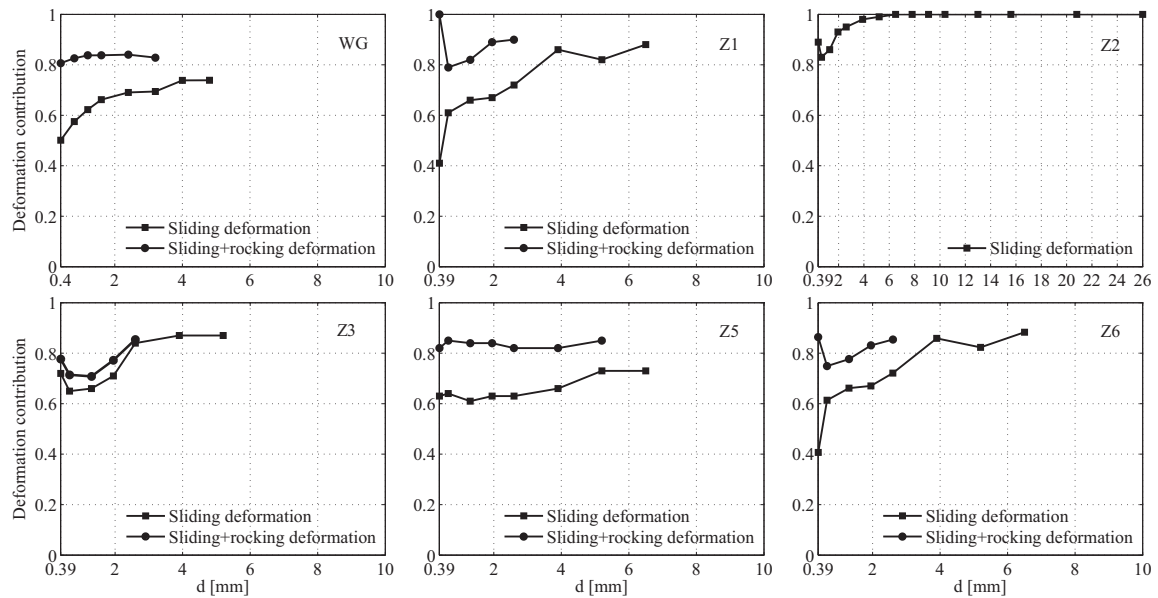
Figure 4-6. URM walls with a rubber granulate core soft layer in the multi-layer bed joint: measured deformation contribution factors

Figure 4-6 shows the deformation contribution factors quantified from the DIC measured vertical and horizontal displacements of the bottom and the top wall cross-sections, i.e. the wall top horizontal displacement components stemming from sliding and sliding+rocking motions normalized with respect to the measured wall top horizontal displacement. As mentioned in Section 3.4.4.2, vertical displacements of the wall bottom cross-section points can be transformed into the wall base rotation and further into the wall top displacement, until the assumption that the wall bottom cross-section remains plane can be considered as valid. After the appearance of the significant tensile cracks at the bottom brick course, which change the displacement distribution at the bottom cross-section, a precise quantification of the rocking deformation is no possible. The data in Figure 4-6 correspond to the first pushing semi-cycle applied, i.e. to the positive horizontal force and displacement, and are plotted vs. the corresponding target displacement. It can be seen that, for each wall, deformation of masonry do not exceed 30% of the total wall deformation, and that this percentage is becoming smaller with the increase of the target

105

wall top displacement. Such masonry deformations (in mm) are below the values of wall top displacement at the first visible/audible cracking, d_{cr}, recorded during the series of static-cyclic shear tests on corresponding URM walls made without a multi-layer bed joint, see [44]. Table 4-4 shows the measured values of d_{cr}. Only in case of Wall Z5 is the masonry deformation, determined for the pushing semi-cycle with the target displacement of 6.5 mm, higher than the value of the recorded d_{cr}. This corresponds well to the loading cycle during which the first shear cracks are observed in the test. Therefore, the assumption on the elastic behavior of masonry can be considered as justified up to the point of the appearance of the significant tensile cracks at the bottom brick course of the wall or, in case of Wall Z5, up to the point when the masonry deformation exceeds the value d_{cr}.

Table 4-4. URM walls without a multi-layer bed joint: displacement corresponding to the development of the first visible crack [44]

Wall without a multi-layer bed joint	T1(ᵃZ1)	T2(ᵃZ2)	T3(ᵃZ3)	T5(ᵃZ5)	T6(ᵃZ6)
d_{cr} [mm]	3.12	1.56	1.82	1.3	1.3

ᵃ Corresponding wall made with a rubber granulate core soft layer in the bottom multi-layer bed joint

As presented above, the source of the viscoplastic behavior is multi-layer bed joint. Before the viscoplastic behavior is triggered, a URM wall with a multi-layer bed joint, exhibit elastic behavior, which, in the horizontal force-displacement space, can be described by the initial wall stiffness, K_0. Therefore, starting from the total displacement decomposition

$$d = d^{el} + d^{vp} \text{ yields } \dot{d} = \dot{d}^{el} + \dot{d}^{vp} \tag{4-16}$$

and by including that

$$d^{el} = H \, / \, K_0 \text{ and } \dot{d}^{vp} = \left(t_{ml} - \Delta t_{ml}\right) \cdot \dot{\gamma}^{vp} = \frac{\left(t_{ml} - \Delta t_{ml}\right)}{\eta^*} \cdot \left(\frac{H}{H_y} - 1\right) \tag{4-17}$$

the model differential equation can be determined

$$\dot{H} + \frac{K_0 \cdot \left(t_{ml} - \Delta t_{ml}\right)}{\eta^* \cdot H_y} \cdot H = \frac{K_0 \cdot \left(t_{ml} - \Delta t_{ml}\right)}{\eta^*} + K_0 \cdot \dot{d} \tag{4-18}$$

Applying standard methods for solving first-order ordinary linear differential equations, while assuming the loading speed as constant, the model differential equation (4-18) can

be solved and the loading speed-dependent horizontal force-displacement relationship for a URM wall with a multi-layer bed joint can be obtained. Starting from the general differential equation solution

$$H(t) = C_1 \cdot e^{-\frac{K_0 \cdot (t_{ml} - \Delta t_{ml})}{H_y \cdot \eta^*} \cdot t} + H_y \cdot \left(1 + \frac{\eta^* \cdot \dot{d}}{t_{ml} - \Delta t_{ml}}\right) \tag{4-19}$$

and by substituting $t = d / \dot{d}$, one can obtain that

$$H(d, \dot{d}) = C_1 \cdot e^{-\frac{K_0 \cdot (t_{ml} - \Delta t_{ml})}{H_y \cdot \eta^*} \cdot \frac{d}{\dot{d}}} + H_y \cdot \left(1 + \frac{\eta^* \cdot \dot{d}}{t_{ml} - \Delta t_{ml}}\right) \tag{4-20}$$

Further, with known force boundary condition, $H(d = d_y) = H_y$, the constant C_1 can be determined

$$C_1 = -H_y \cdot \frac{\eta^* \cdot \dot{d}}{t_{ml} - \Delta t_{ml}} \cdot e^{\frac{K_0 \cdot (t_{ml} - \Delta t_{ml})}{H_y \cdot \eta^*} \cdot \frac{d_y}{\dot{d}}} \tag{4-21}$$

and finally the loading speed-dependent horizontal force-displacement relationship

$$H(d, \dot{d}) = H_y \cdot \left[1 + \frac{\eta^* \cdot \dot{d}}{t_{ml} - \Delta t_{ml}} \cdot \left(1 - e^{-\frac{K_0 \cdot (t_{ml} - \Delta t_{ml})}{H_y \cdot \eta^*} \cdot \frac{d - d_y}{\dot{d}}}\right)\right] \tag{4-22}$$

Table 4-5. URM walls with a rubber granulate core soft layer in the multi-layer bed joint: calculated deformation contribution factors

Specimen	Masonry shear deformation [%]	Masonry flexure deformation [%]	Shear deformation of the multi-layer bed joint [%]	Rocking deformation [%]
WG	14.3	11.3	56.5	17.9
Z1	21.3	13.7	51.7	13.3
Z2	21.3	16.2	52.5	10.0
Z3	21.0	9.6	49.6	19.8
Z5	15.9	23.0	38.6	22.5
Z6	24.2	8.7	58.6	8.5

As can be seen from Figure 3-43 the initial stiffness of the URM wall with a rubber granulate core soft layer in the bottom multi-layer bed joint can be approximated well using the elastic stiffness, K_{el}, calculated using equation (3-2). The ratio between K_0 and

K_{el} equals 1.4. For the sake of comparison with the initial values of the measured deformation contribution factors (given in Figure 4-6), Table 4-5 shows the deformation contribution factors calculated for each deformation component in the equation (3-2). Keeping the assumption that the values of d_y are the same as those estimated from the monotonic test series on masonry triplets, and using the values of initial stiffness estimated using equation (3-2), while considering the K_0-K_{el} correlation factor and parameters given in Table 3-13, corresponding values of H_y can be calculated for each wall, see Table 4-6.

Table 4-6. URM walls with a rubber granulate core soft layer in the multi-layer bed joint: calculated values of H_y

Test	Pre-compression [MPa]	[a] d_y [mm]	K_0 [kN/mm]	H_y [kN]
WG	0.52	0.27	53.40	14.42
Z1	0.52	0.27	86.11	23.25
Z2	0.26	0.17	85.83	14.59
Z3	1.04	0.35	83.65	29.28
Z5	0.52	0.27	44.91	12.13
Z6	0.52	0.27	127.20	34.34

[a] Values obtained by extrapolating the measured data from Table 4-1

Since the major part of the total wall deformation is in fact sliding, see Figure 4-6, degradation of the initial stiffness, i.e. of the stiffness within the elastic range, with the number of loading cycles can be accounted for through the degradation of the shear modulus of the multi-layer bed joint with the number of loading cycles. The equation (3-2) can be modified for that purpose as:

$$K_0(n) = 1.4 \cdot \cfrac{1}{\kappa \cdot \cfrac{h_w}{G_m \cdot A_w} + \cfrac{h_w^3 \cdot \left(\alpha^3 + (1-\alpha)^3\right)}{3 \cdot E_x \cdot I_w} + \cfrac{t_{ml} - \Delta t_{ml}}{\psi_1(n) \cdot G_{ml} \cdot A_w} + \alpha \cdot \cfrac{h_w^2 \cdot \Delta t_{ml}}{\sigma_{pc} \cdot I_w}} \qquad \textbf{(4-23)}$$

One can now calibrate the equation (4-23) for the parameter ψ_1, so as to capture the measured data on the degradation of the elastic response range stiffness of the tested URM walls with the number of the loading cycles.

Figure 4-7 shows the results obtained for walls WG and Z1-Z6 (data on the initial stiffness from each first applied pushing semi-cycle are considered). The results indicate that the evolution of the parameter ψ_1 with the number of loading cycles is independent of the level of pre-compression and the wall aspect ratio, and can be approximated well by using a rational function shown in Figure 4-7.
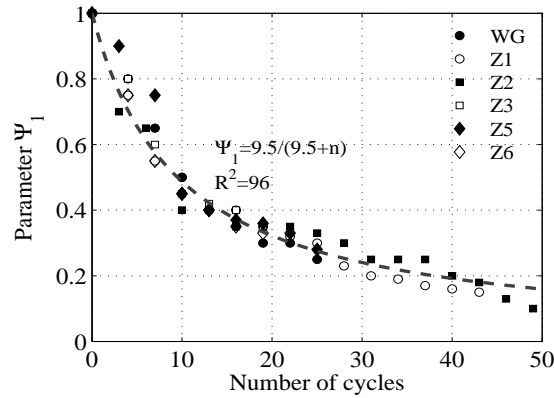
Figure 4-7. Degradation of the initial wall stiffness with the number of performed loading cycles

With the defined initial stiffness degradation function and known values of H_y, which are kept constant, meaning that the values of d_y change as the initial stiffness degrade with the increase of the number of loading cycles, and previously determined η coefficients, cf. Figure 4-5, one can calculate the force resistance of URM walls with a multi-layer bed joint for an arbitrary loading speed, $\dot{d}$, and horizontal displacement, d, using the equation (4-22).

As can be seen in Figure 4-8, the calculated values of horizontal force resistance are in very good agreement with the corresponding measured values (in case of walls Z3 and Z5 to a somewhat lower extent). Note that only the values of the horizontal force resistance measured before the appearance of the significant tensile cracks at the bottom brick course or the appearance of shear cracks are considered in case of walls WG, Z3, Z5 and Z6.

Figure 4-9 shows the model ability to describe the force-displacement relationship of the tested URM walls with multi-layer bed joints. Note that the model developed is capable to describe only the loading hysteresis branches. The unloading branches (going back to the zero force value) are in fact parallel to the initial elastic branches. The unloading parts of the measured hysteresis curves are dependent on the (un)loading speed, which can allow for certain horizontal force relaxation. In case of a sinusoidal loading pattern, a drop of the horizontal force appears in the region of peak horizontal displacement, i.e. in the region of almost zero loading speed.
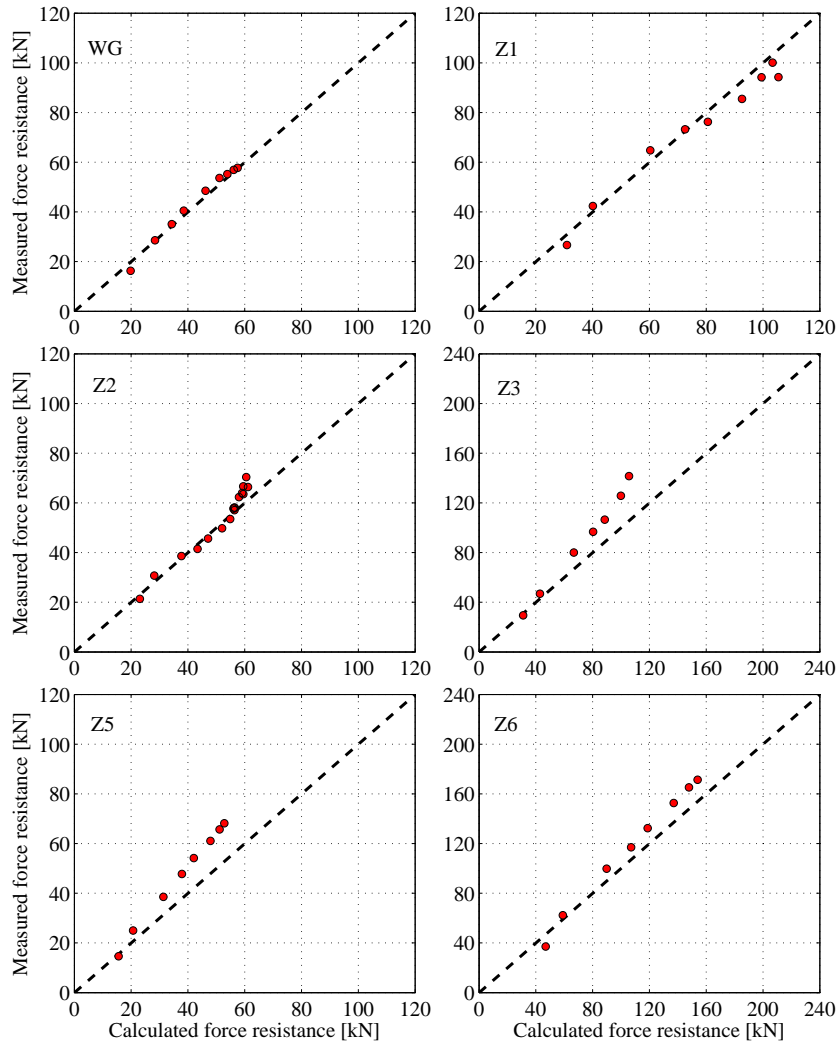
Figure 4-8. Horizontal force resistance of URM masonry walls with a rubber granulate core soft layer in the multi-layer bed joint: measured vs. calculated values
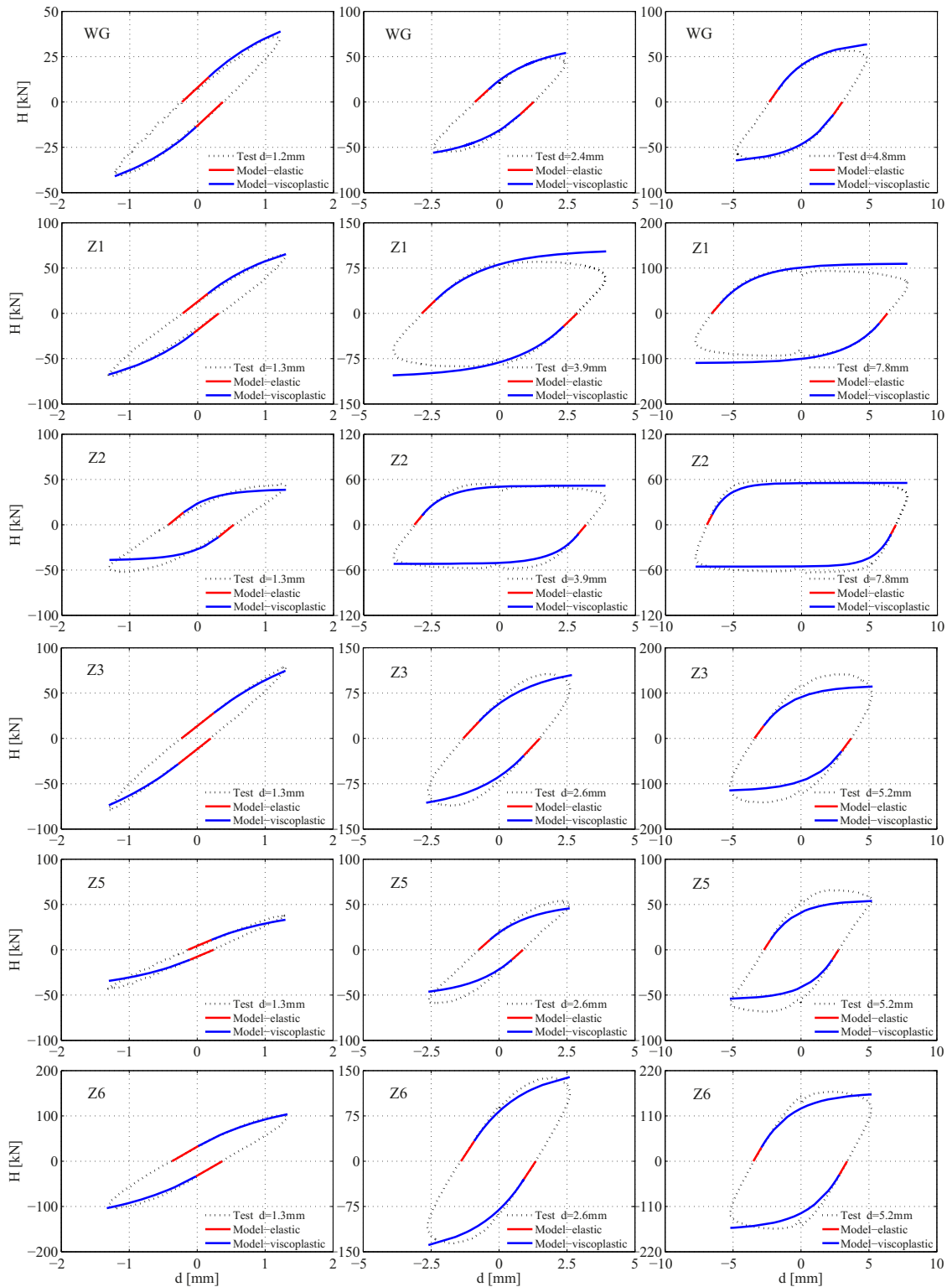
Figure 4-9. Horizontal force-displacement behavior of URM masonry walls with a rubber granulate core soft layer in the multi-layer bed joint: measured vs. calculated

4.4 Summary and conclusions

An analytical model of the loading speed-dependent in-plane shear force-slip behavior of the masonry multi-layer bed joint is presented and further calibrated for the multi-layer bed joint with a rubber granulate core soft layer. The influence of the loading speed is considered through the assumption on the elastic-perfectly viscoplastic behavior of the multi-layer bed joint. Assuming a linear elastic behavior of masonry, the model is further extended to describe the in-plane horizontal force-displacement behavior of URM walls with such multi-layer bottom bed joints and validated against the experimental results. However, possible separation of the wall into more parts, initiated by the tensile cracks in head joints at the bottom block course, which can lead to significant strength and stiffness degradation of the wall, and/or exceeding of the limit of the elastic masonry deformation, limits the model applicability. It is shown that, using the proposed model, for the given loading speed, $\dot{d}$, and horizontal displacement, d, the force resistance of URM walls with a rubber granulate core soft layer in the multi-layer bed joint can be predicted well. Moreover, using the proposed model, the in-plane horizontal force-displacement behavior of URM walls with a rubber granulate core soft layer in the multi-layer bed joint can be described with satisfactory accuracy. Somewhat conservative results are obtained in case of walls Z3 and Z5. It is noteworthy that, although the model is developed and calibrated for URM with a rubber granulate core soft layer in the multi-layer bed joint, it can be extended to the other types of core soft layer once the appropriate test data become available.

5 Supplementary investigation: I-shaped unreinforced masonry wallettes with a rubber granulate soft layer in the bottom bed joint

In the most of previously conducted studies, despite the fact that structural URM walls in buildings are intersecting each other, URM walls were considered to respond in-plane and were idealized as plane, rectangular cross-section structural elements. Interaction between the in-plane walls (webs) and the transverse walls (flanges) was disregarded. The results of experimental research performed at the structure level, reported by Paquette and Bruneau [50], Moon et al. [51], and Yi et al. [52], indicate that the effects of the flanges on the response of the in-plane structural walls, e.g., shear load and displacement capacities as well as failure mode, are significant. It was found that the presence of flanges can considerably increase the shear load capacity in all failure modes except in diagonal shear mode, where the shear load capacity can be either increased or decreased depending on the flange position. Russell et al. [53] reported the results from a series of static-cyclic tests on URM walls with flanges placed at different locations, i.e. C-shaped, T-shaped, and I-shaped walls. It was revealed that, when acting on the compression side of the walls, i.e. when positioned at the toe of the wall, the flanges increased the displacement capacity of walls. Moreover, the shear load capacity increased with flanges acting on the tension side of walls, too. It was also reported that the presence of flanges, or more precisely the length of flanges, could influence the diagonal shear crack orientation in the wall web. Khanmohammadi et al. [54] investigated the seismic performances of URM walls with flanges on both ends. The study comprised cyclic tests on four walls, two reference rectangular walls, one wall with an I-shaped and the other with a C-shaped cross-section. As compared to the reference walls, the I-shaped wall was stronger and experienced less damage, whereas the C-shaped wall exhibited a significant loss of strength because of out-of-plane distortion effects. Nevertheless, both types of the tested URM walls with flanges had similar initial stiffness, failure mode, and deformation capacity as the reference walls.

In addition to experimental work, a few analytical approaches have been aimed at quantifying the nonlinear in-plane response of URM walls with flanges, e.g [54] and [55]. These models are based on the beam theory and are validated using the results of tests on

URM walls with flanges. The comparison between the experiments and the proposed models showed that the models can be used, with some restrictions, to predict the shear force-displacement response of URM walls with flanges.

In order to extend the latest findings on the in-plane shear behavior of rectangular unreinforced masonry wallettes with soft layer bed joints, see [3], and gain insight into the possible influence of the interaction between the in-plane and transverse walls, that can be regarded as a common element of the URM structures, two series of static-cyclic shear tests on I-shaped (flanged) URM wallettes have been conducted. The results obtained from two test series on a total of eight I-shaped URM wallettes made using Swiss masonry materials and having rubber granulate soft layers in the bottom bed joint are presented and discussed in the following sections. The effects of soft layer material and its thickness, pre-compression level, and boundary conditions on the shear behavior of I-shaped URM wallettes are considered. Further, the equation for calculating the elastic stiffness of I-shaped and rectangular masonry walls built with and without a soft layer is proposed, and values of the ratio between the effective and elastic stiffness are suggested for practical application. Moreover, applying the theory of plasticity, namely the lower bound theorem, an analytical model based on discontinuous stress fields is proposed to predict the horizontal force resistance of I-shaped wallettes. The findings presented within this chapter have already been partly published in [56,57].

5.1 Test programme and masonry materials

Static-cyclic tests on two series of flanged URM wallettes with rubber granulate soft layers incorporated in the bottom bed joints have been performed at the Institute of Structural Engineering of ETH Zurich. The summary of the test programme is shown in Table 5-1. The letter I in the specimen designation scheme is because the wallettes are I-shaped. The numbers distinguishing between the specimens are not continuous because not all of the tested specimens are presented. Figure 5-1 shows the geometry of the constructed wallettes, consisting of the web (in-plane wall) and the flanges (out-of-plane or transverse walls) with nominal dimensions of 900x1200 and 600x1200 mm, respectively. The thickness of the web and the flanges was 150 mm.

Table 5-1. I-shaped URM wallettes with a soft layer bed joint: test programme [57]

Specimen	t_{sl} [mm]	Layer material	Pre-compression [MPa]	Shear span h_0 [^{a} h_w]
First test series				
I0	-	none	0.6	1.0
I1	3	rubber granulate	0.6	1.0
I2	10	rubber granulate	0.6	1.0
I3	3	rubber granulate	0.9	1.0
I4	10	rubber granulate	0.9	1.0
Second test series				
I5	3	rubber granulate	0.6	1.75
I6	10	rubber granulate	0.6	1.75
I8	10	rubber granulate	0.9	1.75

^{a} Height of the wallettes
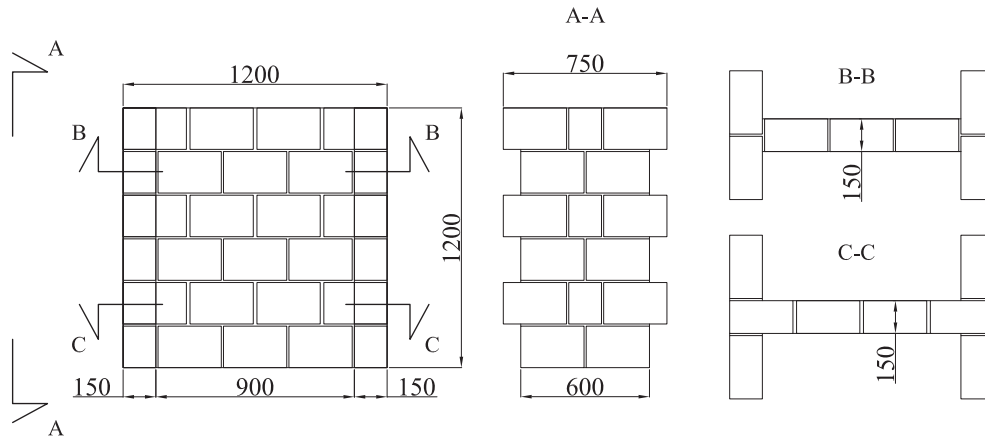
Figure 5-1. Nominal dimensions of the tested specimens [57]

The specimens of the first and second test series were built separately but with masonry units from the same batch and mortar made using the same aggregate and cement mix. As expected, a variation of the material properties from one test series to the other has been observed. All specimens were constructed in running bond using standard Swiss perforated clay blocks with nominal dimensions of 290x150x190 mm, cf. Figure 3-17. The compressive strength of the blocks was determined according to European standard EN 772-1 [30] on a sample of 10 blocks, and was equal to 31.5 MPa with the standard deviation of 2.38 MPa. A standard cement mortar was used to produce fully filled bed and head joints. The mortar compressive strength was determined for each test series by testing 40x40x160 mm mortar prisms according to EN1015-11 [29] after a curing period of at least 28 days. The mean compressive strength of mortar used to build the wallettes of the

first test series, measured for mortar specimens stored in the climatic chamber and in open air in the laboratory was 12.26 MPa with standard deviation of 0.26 MPa and 6.88MPa with standard deviation of 0.91 MPa, respectively. The measured values of mean compressive strength of mortar used to prepare the wallettes of the second test series were 17.19 MPa with standard deviation of 0.56 MPa, and 1.92 MPa with standard deviation of 0.05 MPa, for mortar specimens stored in the climatic chamber and in open air in the laboratory, respectively. Rubber granulate strips, 3 and 10 mm thick, were used as a soft layer, see Figure 5-2a. The soft layer was placed directly on a reinforced concrete pedestal, followed by the mortar bed joint, cf. Figure 5-2b. Then, the wallettes were built as usual. The total first (bottom) bed joint thicknesses were 10 and 15 mm for wallettes, with 3 mm thick and 10 mm thick rubber granulate, respectively. The goal was to produce 10 mm thick bed joints with a soft layer, consistent with the standard mortar-only bed joints. However, the mortar type used for specimen construction did not allow for layer thinner than approximately 5 mm. Therefore, the bed joints with 10 mm thick soft layers were 15 mm thick. In addition to the specimens with a soft layer, a control specimen I0 with the same nominal dimensions but without a soft layer was built. All specimens were kept in open air in the laboratory for a minimum of 28 days before testing, see Figure 5-2c.
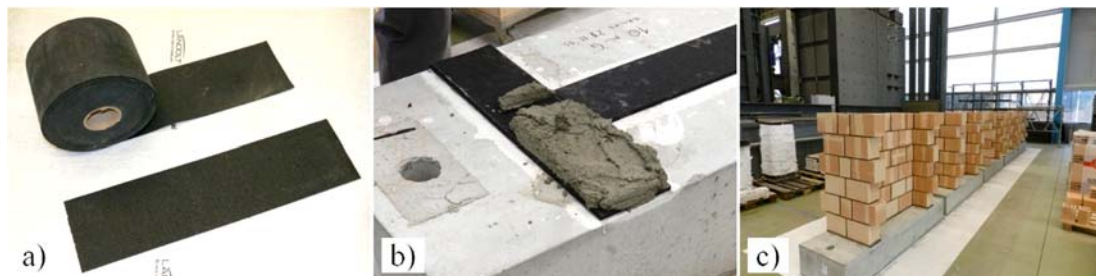
Figure 5-2. Construction and storage of the I-shaped wallettes

Masonry compressive strength perpendicular to the bed joint direction, f_x, was determined in accordance with the provisions of European Standard EN 1052-1 [34]. Three additional masonry specimens with nominal dimensions of 1000x600x150 mm were constructed at the same time as the wallettes for each test series and subsequently tested in a general-purpose testing machine, cf. Section 3.3.2 for the details of testing procedure. Mean compressive strengths of 5.97 MPa with standard deviation of 0.38 MPa, and 5.45 MPa with standard deviation of 0.43 MPa were determined for the built masonry from the first and second test series, respectively.

116

5.2 Test set-up, testing procedure and measurements

Test set-up is shown in Figure 5-3. The pre-compression load was applied by means of two vertical hydraulic jacks (9) fixed to the upper spreader beam (1) and the laboratory strong floor (8). A specimen (5) was placed between the concrete pedestal (7) and the thick steel plate (3), which was in turn fixed to the lower spreader beam (2). In order to ensure uniform vertical load distribution, a layer of mortar (4) was applied between the specimen (5) and a thick steel plate (3). As mentioned before, a soft layer (6) was placed directly on the concrete pedestal (7). The static-cyclic shear load was applied by means of the horizontal hydraulic actuator (10), which was fixed to the upper spreader beam (1) and the reaction wall (11) on the opposite side.
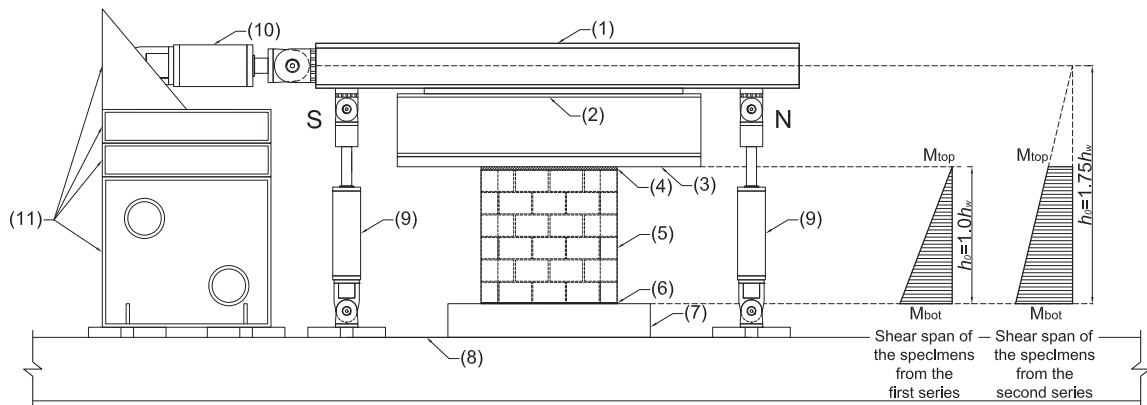
Figure 5-3. I-shaped URM wallettes with a soft layer bed joint: drawing of the test set-up [57]

After placing a specimen in the test set-up, a pre-compression load was applied first and kept constant throughout the test. Two levels of pre-compression, namely 0.6 and 0.9 MPa, corresponding to approximately 10 and 15% of the compressive strength of the built masonry, were applied to different specimens, cf. Table 5-1. These two levels of pre-compression were selected based on the typical range of the vertical pre-compression load acting on the ground floor masonry walls in the case of standard 3-story to 4-story URM buildings in Switzerland. The specimens were subsequently subjected to the quasi-cyclic horizontal shear load. The static-cyclic shear load pattern was the same for both test series and was applied in computer-controlled displacement steps. Each step comprised two identical sinusoidal cycles. The average loading speed was kept at a low value of 1 mm/min for the small displacement steps. In order to control the total duration of a test, the loading speed was gradually increased to a value of 10 mm/min for the maximum applied displacement amplitude of 40 mm. Table 5-2 shows the used loading history, i.e.

117

the amplitude, average loading speed, and duration of loading cycles. Using this procedure, the test duration varied from 70 to 140 min. All tests started with a push cycle (positive horizontal displacement and horizontal force).

Table 5-2. Loading history for static-cyclic shear tests [57]

Target displacement [mm]	Loading speed [mm/min]	Duration [min]
0.2	1	1.6
0.5	1	4
1	1	8
1.5	1	12
2	3	5.3
5	3	13.3
10	3	26.7
15	10	12
20	10	16
30	10	24
40	10	32

For the first test series, cantilever boundary conditions were simulated. In order to achieve this, the vertical hydraulic jacks have been coupled to the force measured by the horizontal actuator to keep the shear span constant and equal to the height of the wallette, i.e. to maintain a zero moment at the top of the wallette during the tests. The wallettes of the second test series were tested without keeping the moment zero at the top of the wallette. The shear span extended to the line of action of the horizontal actuator and was equal to 1.75 times the wallette height, see Figure 5-3.

The actions applied by the hydraulic jacks, i.e. forces and displacements, were measured by means of the actuator load cells and displacement transducers. Additional measurements included vertical, horizontal, and diagonal deformations of the specimen, as well as monitoring of the important elements of the test setup, see Figure 5-4. Horizontal and vertical deformations of the wallette web were measured by means of two pairs of potentiometers, WHT and WHB, and WVN and WVS, respectively. Potentiometers FVN and FVS were used to measure vertical deformation of the North and South flanges, respectively. Further, diagonal deformations of the web were measured using another two potentiometers, WD1 and WD2. Potentiometers WBN and WBS were

used to measure the sliding displacement of the specimen along the bottom bed joint with respect to the strong floor. The uplift displacement of the bottom web corners was measured by means of potentiometers WUN and WUS, whereas potentiometers FUN and FUS were used to capture the uplift of the flanges. Horizontal displacement of the top of the specimen was measured both on the South (potentiometer WTS) and North sides (WTLaser). Another laser measuring device (CTRLaser) was used to measure and control the horizontal displacement of the thick steel plate. Potentiometers SN and SS measured the slip between the thick steel plate and the specimen. Finally, potentiometer CS was installed for tracking the horizontal displacement of the concrete pedestal, which in turn was fixed to the strong floor with a pair of pre-stressed steel rods.
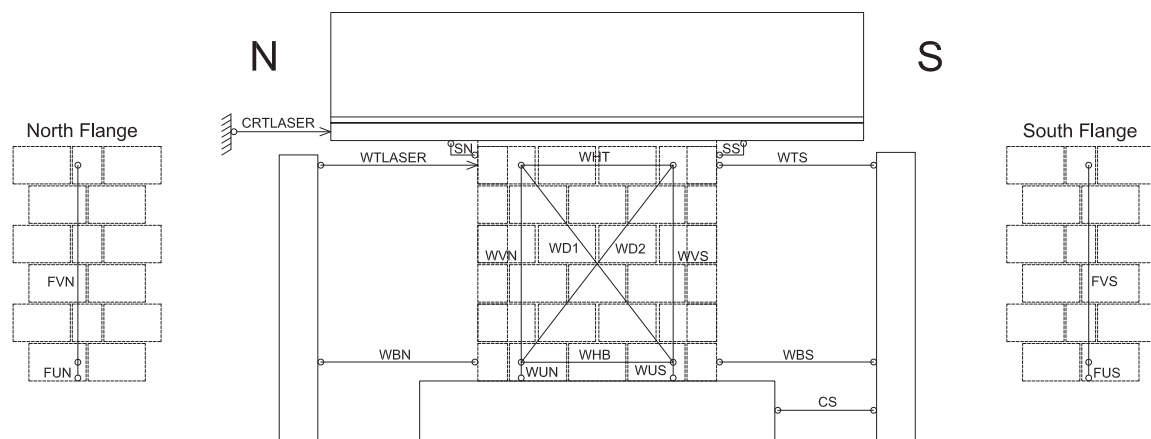
Figure 5-4. Plan of measuring devices [57]

All measuring devices were connected to the data acquisition system and the computer, which processed the data in real time. In addition to the use of a conventional measuring system, a 2D-DIC measurement system was used in order to get a complete view of the specimen deformation state, see Figure 5-5. The computer used for processing the data during the test triggered the DIC camera, ensuring the pictures were taken at the predefined points within the load cycles. Figure 5-6a depicts an approximately 140x180 mm portion of the random pattern, comprising 1.5 mm diameter circles, applied on the wallette surface. The major principal strain field in the web of Specimen I2 after applying the cycles with target displacement of 5 mm as well as the minor principal strain field in the web of Specimen I2 after applying the vertical pre-compression load are shown in Figures 5-6b and 5-6c, respectively.

Figure 5-5. Implemented 2D-DIC measurement system [57]
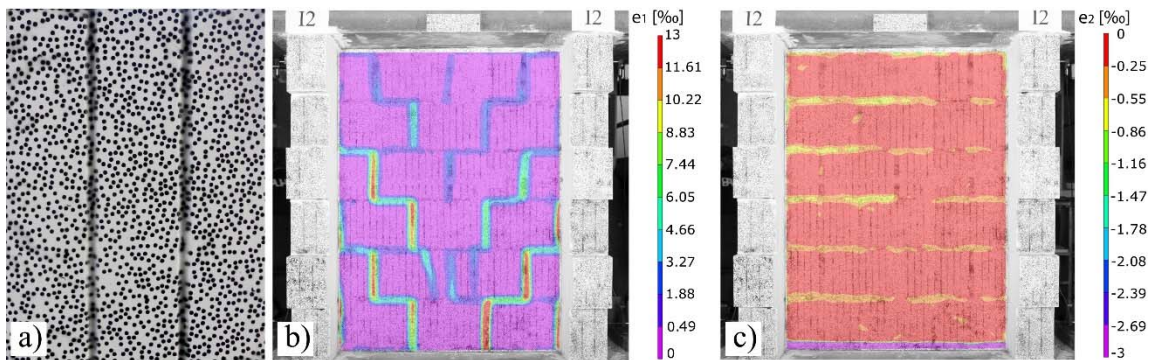
Figure 5-6. Wallette I2: a) applied pattern for DIC measurements; b) DIC measured major principal strain field in the web after applying the loading step with the target displacement of 5 mm; c) DIC measured minor principal strain field in the web after applying the vertical load [57]

5.3 Test results and specimen behavior

Table 5-3 shows the extreme values of the horizontal force H_{max} and H_{min} and the maximum horizontal displacement d_{max} recorded during the tests. The values of the horizontal displacements at the first visible or audible cracking, d_{cr}, as well the level of the target horizontal displacement of the cycle when the maximum horizontal force developed, d_{Hmax}, are also presented. Furthermore, the total number of completed load cycles, the applied level of pre-compression σ_{pc}, and the failure mode are listed. Four conventional failure mechanisms were classified as: flexural failure (F), denoting rocking behavior of the wall with subsequent tensile flexural cracking and crushing of the toes; shear failure mechanism (S), denoting a diagonal tensile failure of the wall with (diagonal) cracks going through the blocks or the mortar joints or combined; and sliding failure,

separated into sliding along a horizontal bed joint containing a soft layer (SLH) and sliding along the diagonal of the wall (SLD). In addition, a fifth failure mechanism, i.e. a punching of the wallette web through the flanges (P), was defined, see Table 5-3. Punching of the wallette web through the flanges has a considerable impact on the degradation of the shear load resistance of the wallets in the plane of the web as well as the shear load resistance of the flanges in their own plane, orthogonal to the web. Figure 5-7 shows the values of the equivalent viscous damping ratio, ξ_{eq}, obtained from the recorded horizontal force-deformation response hysteresis loops, see Section 3.4.3 for the calculation procedure. However, it should be noted that the horizontal force values that correspond to the maximum applied displacement were used herein to calculate the strain energy. The values given are calculated for each tested wallette and for each first cycle applied and are plotted against the corresponding target displacement. In addition to all previously mentioned parameters, and for the sake of discerning the influence of the flanges, the results from the corresponding tests performed on the rectangular URM wallettes of the same dimensions, position, and type of soft layer, but constructed without flanges, presented in [3] , are given in Table 5-3 as well.
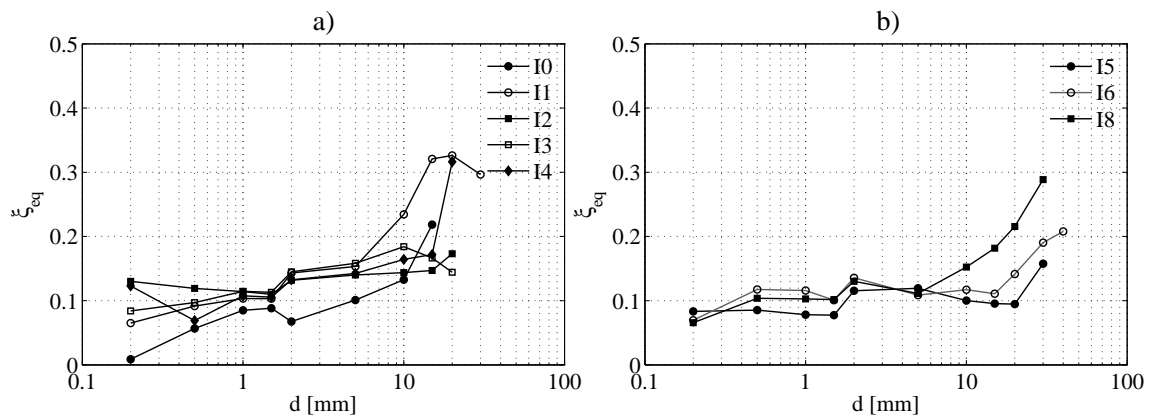
Figure 5-7. Equivalent viscous damping ratio: (a) first test series; (b) second test series [57]

Table 5-3. Static-cyclic tests on I-shaped URM wallettes: test results

Specimen	σ_{pc} [MPa]	No.of cycles	d_{max} [mm]	d_{Hmax} [mm]	d_{cr} [mm]	H_{max} [kN]	H_{min} [kN]	d_y [mm]	d_u [mm]	δ_u [%]	H_u [kN]	d_u/d_y [-]	Failure mode	K_{eff} [kN/mm]	K_0 [kN/mm]	K_{el} [kN/mm]
I0	0.60	16	15	15	1.0	115.4	-72.07	1.59	15.00	1.3	105.99	9.45	S/F	66.54	94.78	127.08
I1	0.60	20	30	15	1.5	96.36	-81.09	3.43	14.76	1.2	85.86	4.30	S/SLD/P	25.00	61.61	42.5
I2	0.60	18	30	15	2.0	84.02	-77.23	6.85	21.52	1.8	76.79	3.14	S/P	11.21	35.71	13.19
I3	0.90	17	20	10	2.0	114.64	-103.39	3.10	15.89	1.3	102.57	5.13	S/P	33.08	73.96	42.91
I4	0.90	37	20	10	1.5	115.29	-87.90	7.65	17.05	1.4	104.90	2.23	S/F/P	13.70	46.75	13.38
I5	0.60	19	30	20	5.0	56.61	-51.23	2.33	30	2.5	53.76	12.88	F	23.62	41.66	24.4
I6	0.60	21	40	15	5.0	50.38	-49.68	5.93	40	3.3	47.41	6.75	F/S	7.99	25.36	7.97
I8	0.90	19	30	20	5.0	70.30	-71.11	5.66	30	2.5	66.51	5.30	F/S	11.75	36.39	8.04
*W0.10	0.60	33	15	10	2.0	47.59	-52.46	1.7	12.4	1.0	42.10	7.25	SLD/F	24.6	28.6	60.47
*WG3.10	0.60	36	20	10	2.0	50.81	-48.73	3.1	20.3	1.7	47.60	6.64	F/SLD	15.6	19.6	18.15
*WG10.10	0.60	41	30	15	1.0	46.09	-46.77	7.7	32.1	2.7	39.60	4.15	F	5.1	11.0	5.3
*WG3.15	0.90	31	15	10	1.5	66.50	-74.56	3.3	14.8	1.2	62.00	4.51	S	18.9	29.2	18.28
*WG10.15	0.90	37	20	15	0.5	58.42	-60.58	7.7	27.6	2.3	53.20	3.57	S	6.9	13.8	5.35

* Rectangular URM wallettes, Vögeli et al. [3]

5.3.1 First test series (I-shaped wallettes with soft layers tested under cantilever boundary conditions)

It can be seen from Table 5-3 that the wallettes with a thinner rubber granulate soft layer (I1 and I3) developed a higher horizontal force resistance and initial stiffness than those with a thicker layer (I2 and I4). Moreover, as compared to the control Specimen I0, the specimens with a built-in soft layer had lower horizontal force resistance and initial stiffness. However, wallettes with soft layers were able to develop larger horizontal displacement prior to failure (designated as the maximum horizontal displacement).

Horizontal force-displacement characteristics of the specimens tested within the first test series are shown in Figure 5-8 (see Appendix A3 for details), together with the horizontal force-displacement characteristics of the corresponding rectangular URM wallettes without flanges reported in [3]. The deformation value shown in the diagrams is the laser-measured horizontal displacement of the thick steel plate above the wallettes [item (3) in Figure 5-3, and the beam in case of rectangular wallettes], except for Specimen W0.10, where the shown value is the displacement of the wallette top measured by LVDT device. Because the measured values of the slip between the steel plate or beam and the top of the wallettes were negligible in all cases, the laser and LVDT displacement measurements can be considered consistent and used to represent the displacements of the top of the wallettes.

The measured responses of specimens with soft layers were fairly similar, i.e. elastic-plastic from the beginning, becoming significantly nonlinear when the lateral displacement exceeded 2 mm. Subsequently, the specimens exhibited moderate energy dissipation (Wallette I1 to a somewhat larger extent), see Figure 5-7a, and developed more deformation than the comparable wallette without a soft layer, i.e. behaved in a quasi-ductile manner. The changes in values of the equivalent viscous damping ratio, and thus the slope of the lines given in Figure 5-7a, correspond to the change in response mechanism of the wallettes and therefore the change in energy dissipation mechanism (e.g. during the cycle with the target displacement of 2 mm, the appearance of diagonal shear cracks in Wallettes I1-I4 caused an increase of values of the equivalent viscous damping ratio).
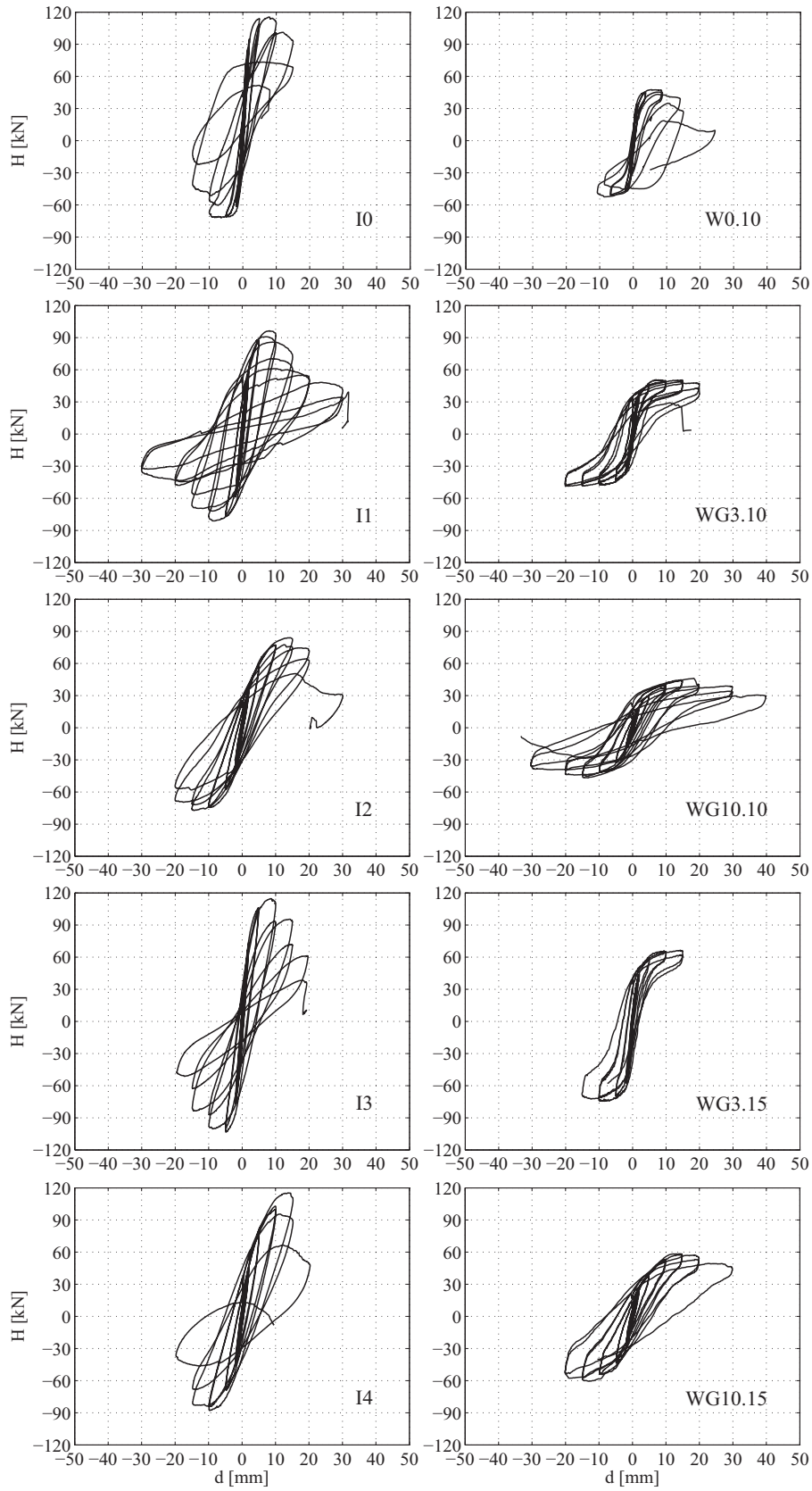
Figure 5-8. Horizontal force–displacement response hysteresis for the I-shaped wallettes of the first test series and corresponding rectangular wallettes

124

A control specimen I0 started developing diagonal shear cracks along the bed and head joints early into the test, during the pushing semi-cycle with the target displacement of 1 mm. Forming of diagonal shear cracks, which subsequently extended through the clay units, was followed by flexural tensile cracks in the middle height of the wallette (cycles with the target displacement of 5 mm). By further increasing the amplitude of the applied displacement, in addition to the progression of the diagonal cracks, compression-induced cracks developed in the bottom area of the South flange and further extended up to the middle of the flange. Subsequently, crushing of the South toe region appeared, see Figure 5-9a. The degradation of the wallette web because of diagonal cracking was significant and caused a sudden compression failure.
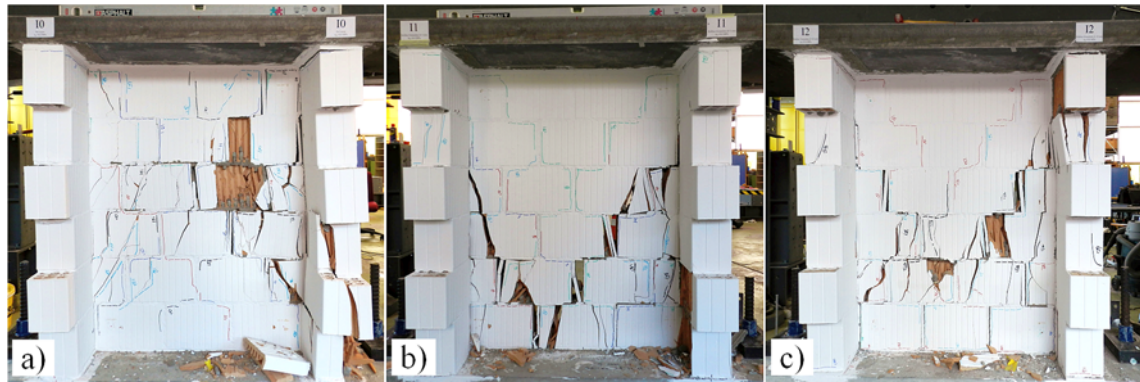
Figure 5-9. Crack patterns observed on the I-shaped wallettes of the first test series: a) Wallette I0; b) Wallette I1; c) Wallette I2 [57]

The initial response of the wallettes with a soft layer bed joint originates from the layer deformability, i.e. shear deformation of the soft layer and rotation allowed by the soft layer's vertical deformability. It was followed by diagonal shear cracks forming along the bed and head joints, i.e. step-wise cracking with subsequent extension through the clay units. Combined sliding along the layer bed joint and the diagonal cracks system started as the connection between the web and flanges deteriorated. A significant deterioration of the connection between the web and flanges commenced during the 5 mm cycle as a consequence of shear stress concentration. Sliding motion further caused vertical (punching) cracks in the flanges, which were observed during the testing of each wallette with a soft layer, see Figure 5-10a. This behavior was more pronounced for the wallettes subjected to the lower level of pre-compression (0.6 MPa), especially for Wallette I1, which exhibited the largest sliding motion, see Figures 5-9b and 5-10b. Wallettes I3 and I4, tested under the higher pre-compression level (0.9 MPa), developed severe diagonal

shear cracks and were not able to develop significant sliding motion, see Figure 5-11. In addition to the diagonal cracks, compression-induced cracks appeared in the bottom area of the North flange of Wallette I4. Subsequently, the North toe region was crushed, see Figure 5-10c. As for the control specimen I0, a significant degradation due to diagonal cracking caused a sudden compression failure of Wallettes I3 and I4.
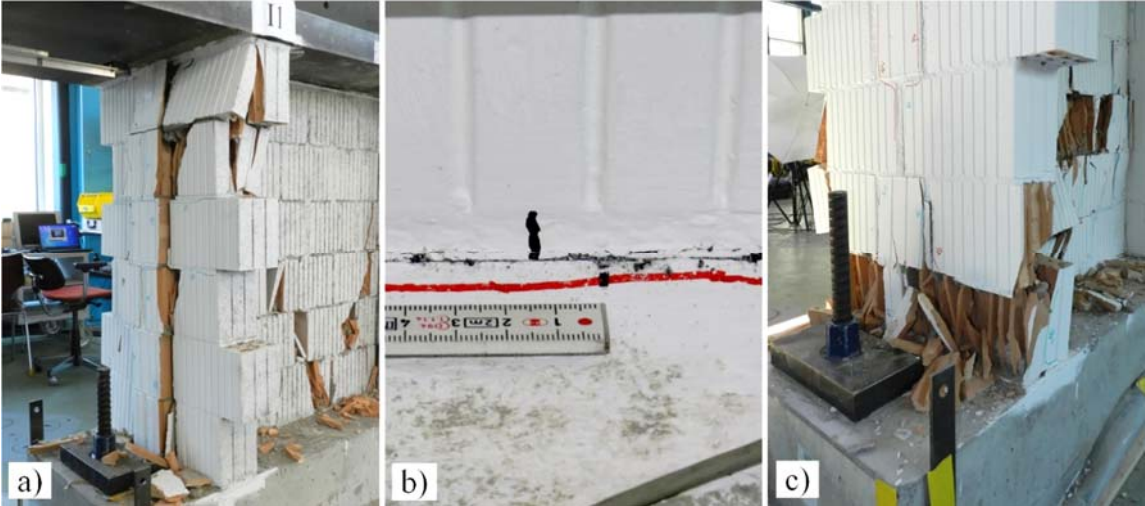
Figure 5-10. Failure modes of the selected wallettes of the first test series: a) punching of the web through the flange of Wallette I1; b) sliding in the bottom bed joint of Wallette I1; c) northern toe crushing of Wallette I4 [57]
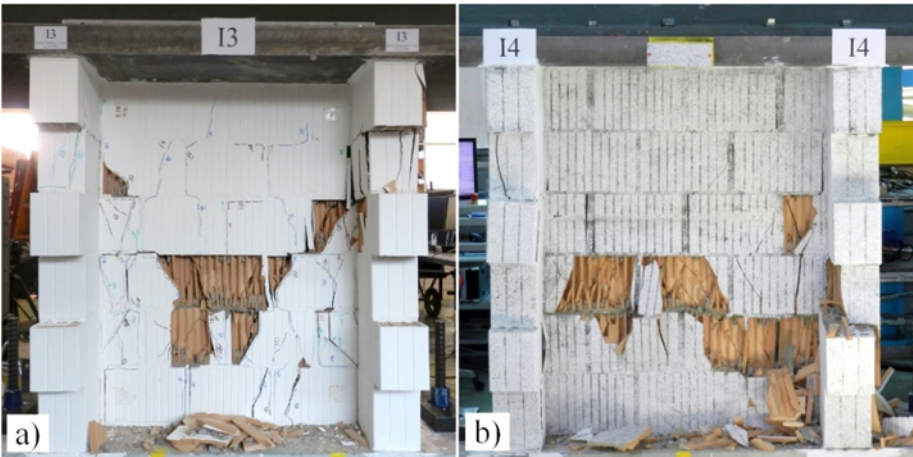
Figure 5-11. Crack patterns observed on the I-shaped wallettes of the first test series: a) Wallette I3; b) Wallette I4 [57]

126

5.3.2 Second test series (I-shaped wallettes with soft layers with the shear span of 1.75 h_w)

Figure 5-12 shows the horizontal force-displacement response of the second-series specimens (see Appendix A3 for details). The deformation value shown in the diagrams is the laser-measured horizontal displacement of the thick steel plate [item (3) in Figure 5-3]. Specimens of the second series exhibited pronounced flexural behavior (rocking) from the beginning. Such behavior is characterized by the narrow, S-shaped hysteresis and low strength and stiffness degradation. A rocking motion was followed by diagonal shear cracks forming along the bed and head joints, sliding motion along the layer bed joint and formed diagonal cracks, and gradual degradation of the connection between the web and the flanges, see Figure 5-13.
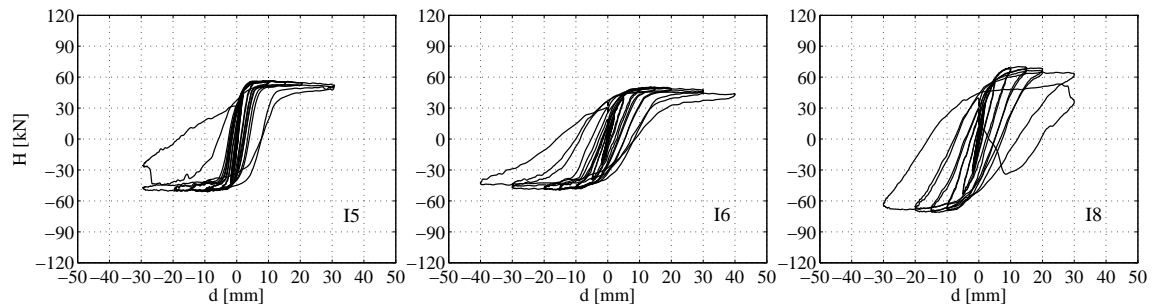
Figure 5-12. Horizontal force–displacement response hysteresis for the I-shaped wallettes of the second test series [57]
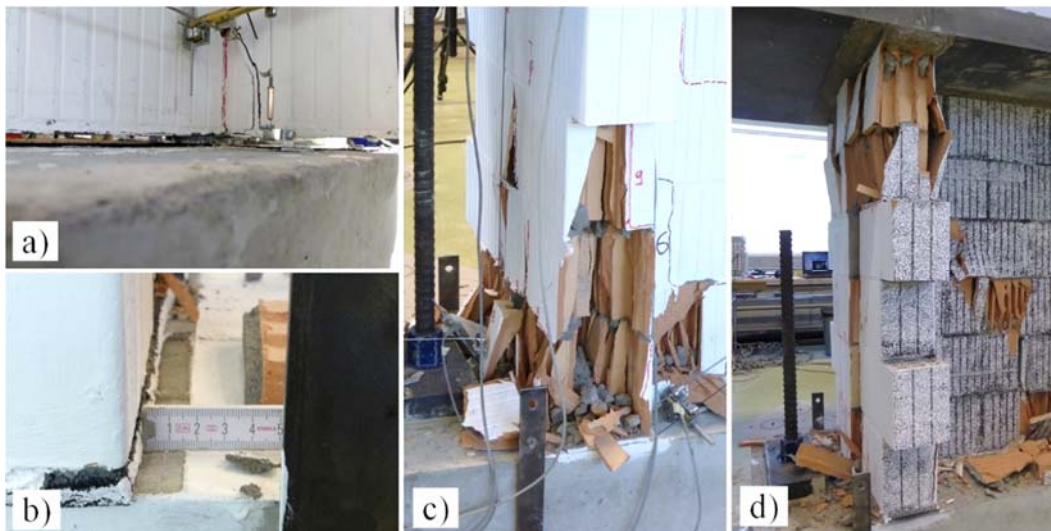
Figure 5-13. Failure modes of the selected wallettes of the second test series: a) uplift motion of Wallette I5; b) sliding in the bottom bed joint of Wallette I8; c) northern toe crushing of Wallette I8; d) punching of the web through the flange of Wallette I8 [57]

127

Because the specimens responded by rocking, the energy dissipation capacity of specimens from the second series was moderate, see Figure 5-7b. As the tests propagated, forming of new diagonal shear cracks in the wallette web, sliding motion, and gradual degradation of the connection between the web and flanges, which started to be pronounced during the cycle with the target displacement of 10 mm in each test, increased the hysteretic energy dissipation, see Figure 5-7b. As compared to Wallettes I5 and I6, Wallette I8 experienced more significant diagonal shear cracks, see Figure 5-14, and therefore exhibited larger energy dissipation capacity (see the values of the equivalent viscous damping ratio for target displacements of 10 mm or more in Figure 5-7b). In case of Wallette I8, sliding motion allowed the web to punch through the flanges and thus completely disassemble wallette parts, see Figure 5-13d. Prior to failure, compression-induced cracks in the bottom area of the flanges were developed in each test. Those cracks further evolved into vertical splitting cracks and extended up to the middle of the flange height, see Figure 5-13c. Failure of the wallettes from second series occurred through crushing of the toe regions, in some cases in combination with diagonal shear cracks (Wallettes I6 and I8), see Figure 5-14.
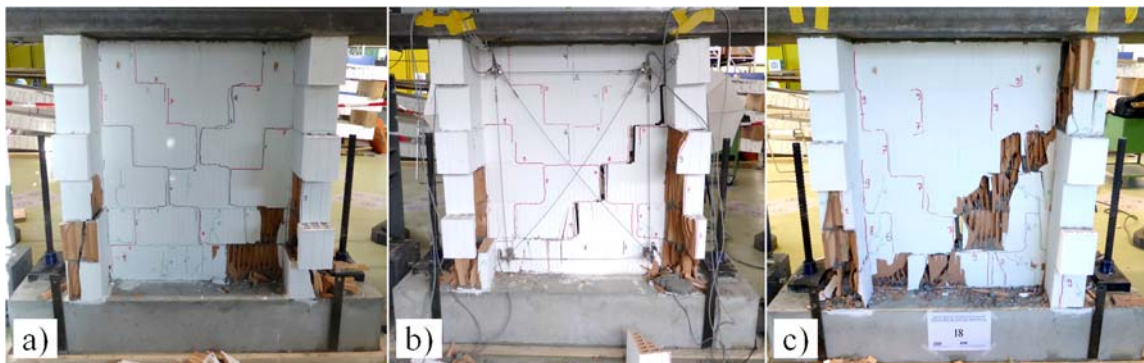
Figure 5-14. Crack patterns observed on the I-shaped wallettes of the second test series: a) Wallette I5; b) Wallette I6; c) Wallette I8 [57]

5.4 Horizontal force-displacement response characterization and discussion

Test data on strength, deformation capacity, hysteretic energy dissipation, and overall behavior of the flanged URM wallettes with built-in rubber granulate soft layers subjected to static-cyclic loading have been presented previously. Behavior of the rectangular masonry wallettes with a layer bed joint under static-cyclic loading is presented in [3] and

is referred to when comparing the behavior of the tested specimens with masonry wallettes built without flanges. In the following sections, the characteristics of the behavior of the tested specimens are discussed in general, and further in terms of the influence of the pre-compression level, side boundary conditions, shear span, and soft layer presence, as well the thickness of the soft layer. Furthermore, soft layer degradation during cycling is addressed.

5.4.1 Load-deformation response characteristics and their idealization

In general, the response of URM walls subjected to cyclic shear loading is nonlinear and depends on several parameters, such as the pre-compression level, the wall aspect ratio, and the boundary conditions. Moreover, cyclic loading causes gradual reduction of the strength and stiffness of URM walls. The backbone curve of the horizontal force-displacement response hysteresis, such as the one shown in Figure 5-15 for Wallette I1, can be chosen as representative of load-deformation characteristics for the evaluation of the deformation capacity of masonry. This backbone curve is constructed from the hysteresis curve according to ASCE/SEI [58] by connecting the peak displacement points of the first cycles of each displacement step. For practical applications, the backbone curve can be idealized using a bilinear linear-elastic perfectly-plastic relation, see Figure 5-15.
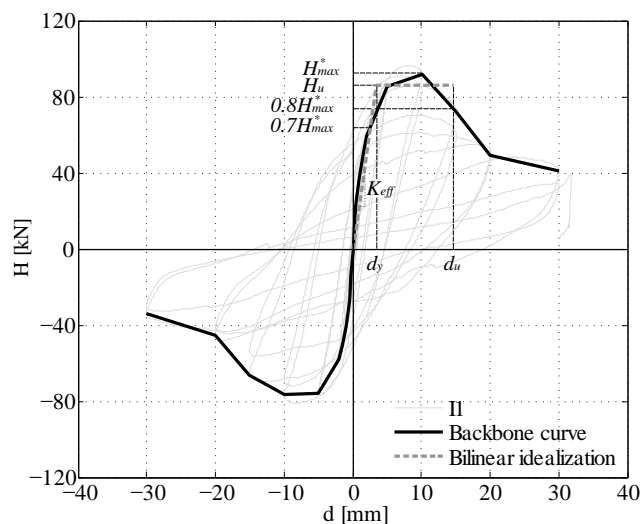
Figure 5-15. Wallette I1: horizontal force-displacement response hysteresis, backbone curve, and its bilinear idealization [57]

Several different approaches to determine this bilinear idealization are available in the literature. In this paper, the approach based on the condition that the area under the actual backbone and its idealization are the same, i.e. the energy equality as proposed in

[45], was used. The bilinear idealization is described by three parameters: the effective stiffness K_{eff}, the ultimate displacement d_u, and the ultimate horizontal force resistance H_u. The effective stiffness is defined as the secant of the backbone curve at 70% of the maximum horizontal force. The ultimate displacement corresponds to the horizontal force at the 20% post-peak strength degradation level. The ultimate horizontal force resistance is calculated based on the aforementioned equal energy condition. The backbone curves and bilinear idealizations of the force-displacement responses measured in the present tests are shown in Figures 5-16 and 5-17, respectively. The resulting bilinear idealization parameter values, including the yield displacement $d_y = H_u/K_{eff}$ and the ductility ratio d_u/d_y, are given in Table 5-3.
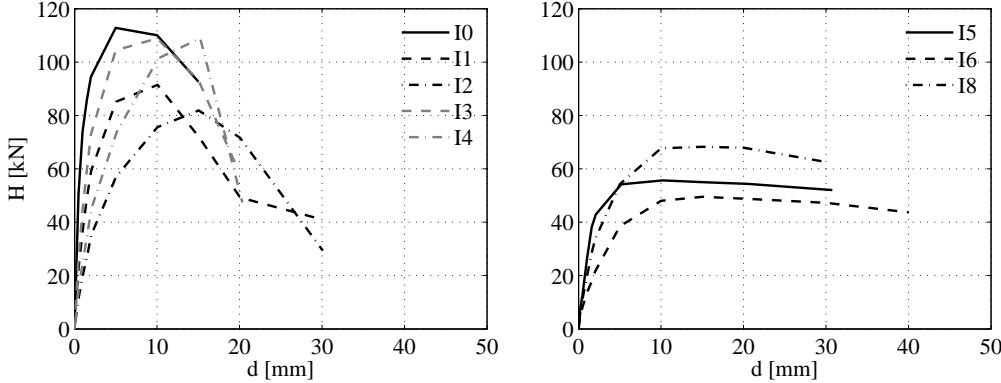
Figure 5-16. Backbone curves for the tested specimens (first quadrant-positive horizontal force and displacement) [57]
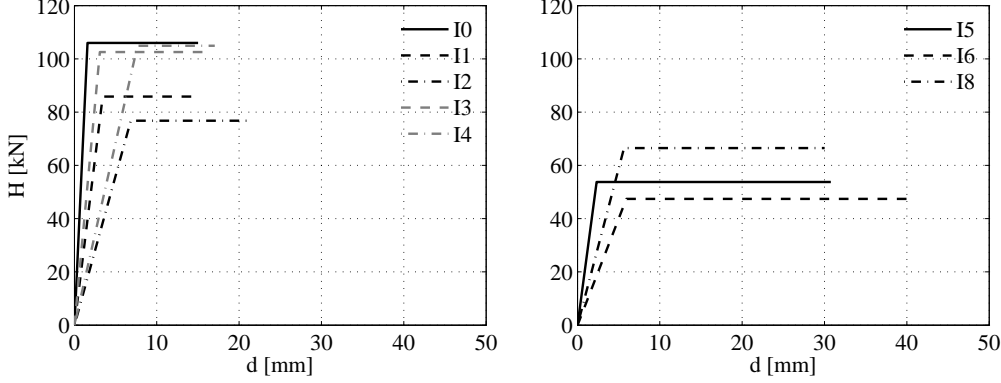
Figure 5-17. Bilinear force-deformation response idealization curves for the tested specimens [57]

The effective stiffness K_{eff} is lower than the initial tangent stiffness of masonry K_0 because of its nonlinear behavior. The initial stiffness represents the slope of the initial part of the horizontal force-deformation response curve. Because it is generally difficult to determine

130

the values of K_0 and K_{eff}, they are usually approximated using the elastic stiffness K_{el}. As mentioned before, the elastic stiffness of the masonry wall can be calculated according to the elastic beam theory incorporating both shear and flexure deformation, see [45]. The equation for K_{el} for URM walls with a soft layer, where the additional soft layer shear deformation was considered, was proposed in [3], however, the influence of the pre-compression level and the contribution of the wallette base rotation because of the vertical deformability of the soft layer were not included. As it was shown in Section 3.4.4.2, vertical deformability of the soft layer in the bed joint allows the wall to rotate, i.e. allows for rocking deformation, and therefore has a significant influence on the initial stiffness of the walls.
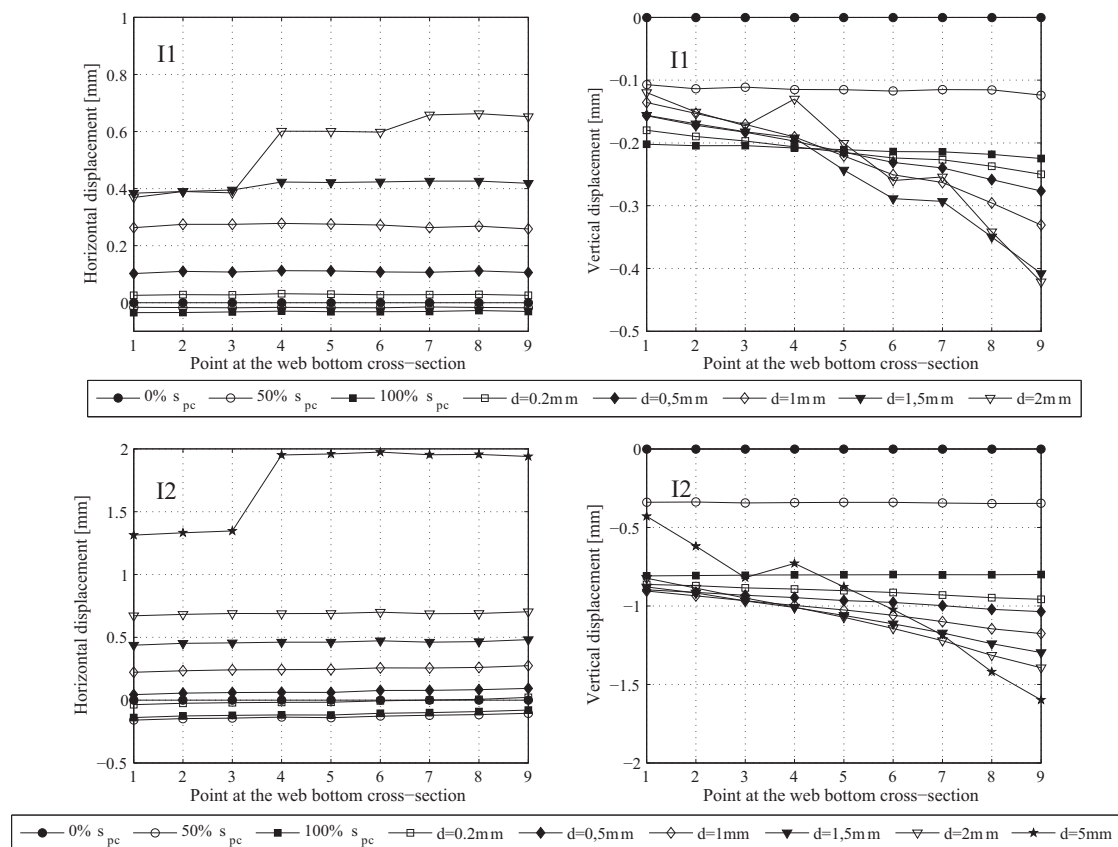
Figure 5-18. DIC-obtained horizontal and vertical displacement at the web bottom cross-section level of Specimens I1 and I2 [57]

Figure 5-18 shows the horizontal and the vertical displacements at the level of the bottom cross-section for the webs of Specimens I1 and I2. Points 1 and 9, shown on the horizontal axis of graphs in Figure 5-18, correspond to the very end points of the bottom wall web cross-section. All consecutive points have the same mutual distance (around 110 mm).The

131

vertical displacements were obtained by DIC for different levels of the pre-compression load (0, 50, and 100% of the total applied load). The horizontal displacements were measured (also using DIC) for different positive peak horizontal displacements in the subsequent horizontal load cycles. The obtained vertical displacements can be transformed into base rotation and further to the wallette top displacement, whereas assuming that the deformation of the bed joint mortar is relatively small as compared to the layer deformation and thus negligible, the bottom cross-section of the wallette remains plane. The first assumption, as it was already stated, can be justified by comparing the values of the deformation moduli of the mortar and the rubber granulate soft layers: the elastic and shear moduli of the soft layer are three orders of magnitude less than the typical values for mortar. As can be seen in Figure 5-18, the latter assumption is justifiable up to a certain peak horizontal displacement (1.5-2 mm, depending on the specimen). Finally, as in case of URM walls with a multi-layer bed joint, a decomposition of the measured wallette top displacements indicates that the displacement components derived from the layer horizontal (shear) and vertical (axial) deformability are the governing ones. For example, calculated for the first loading cycle with the target displacement of 0.2 mm, those components amount to 75 to 95% of the total wallette top displacement, depending on the soft layer thickness.

$$
K_{el} = \frac{1}{\kappa \cdot \dfrac{h_w}{G_m \cdot A_w} + \dfrac{h_w{}^3}{\alpha' \cdot E_x \cdot I_w} + \dfrac{\left(t_{sl} - \Delta t_{sl}\right)}{G_{sl} \cdot A_w} + \alpha \cdot \dfrac{h_w{}^2 \cdot \Delta t_{sl}}{\sigma_{pc} \cdot I_w}}
\tag{5-1}
$$

Based on these observations, and similar to the equation (3-2), equation (5-1) is proposed to calculate the elastic stiffness K_{el} of flanged URM walls with a soft layer that has a thickness t_{sl} and shear modulus G_{sl}. In equation (5-1), A_w and I_w denote the area and moment of inertia of the wall horizontal cross-section, respectively, and G_m and E_x correspond to the shear and elastic moduli of masonry. Here the level of pre-compression σ_{pc} is included through the influence on the thickness of the soft layer Δt_{sl}. Although the influence of pre-compression on the elastic stiffness is not significant, it is considered here for completeness. Coefficient κ is the shear coefficient, defined as the ratio of the area of the wall horizontal cross-section to the shear area of the section [59]. Herein κ can be estimated as 2 while assuming the shear area of the cross-section equal to 1050x150 mm^2, cf. Figure 5-1. Coefficients α' and α account for the influence of boundary conditions on

132

the value of masonry flexure deformation and for the influence of the position of the zero bending moment (inflection) point, i.e. the shear span, h_0, on the value of rocking deformation, respectively. Coefficient α' equals 3 for the cantilever boundary conditions of the first test series and 1.41 for the boundary conditions of the second test series. The latter value of coefficient α' considers the influence of the additional bending moment at the top of the wallette on its flexural deformation. Coefficient α equals 1 for the cantilever boundary conditions of the first test series and 1.75 for the boundary conditions of the second test series. Note that the equation (5-1) is written in such manner to distinguish between the components which contribute to the total wallette deformation. Looking from left to right, the following deformation components are given: masonry shear deformation, masonry flexure deformation, soft layer shear deformation and rocking deformation, respectively.
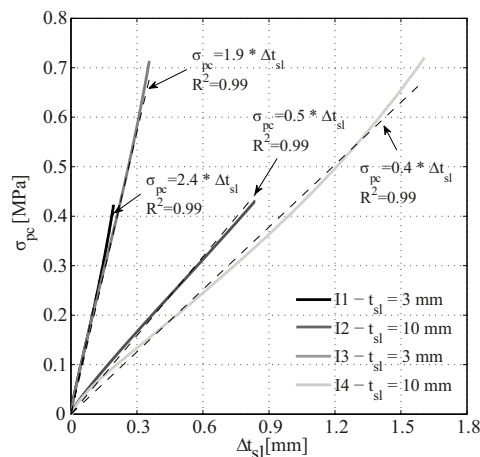
Figure 5-19. Contraction of the rubber granulate soft layer thickness vs. pre-compression

The contribution of the wall rotation due to soft layer vertical deformability is considered as follows. Assuming a linear normal stress distribution at the bottom cross-section of the wallette and knowing the σ_{pc}-Δt_{sl} relationship, the wallette base rotation caused by the bending moment can be estimated and further transformed to the wallette top displacement. Here too, the first intention was to derive the values of elastic moduli of rubber granulate soft layer from the values of Δt_{sl} and implement it into equation (5-1). However, as it is mentioned in Section 3.4.4.2, the values of the soft layer thickness contraction, measured from the tests on URM walls with a soft layer in the bottom bed joint, are not appropriate for assessing the soft layer elastic modulus. Figure 5-19 shows the measured values of the of soft layer thickness contraction (an average from N and S uplift sensors shown in Figure 5-4) with respect to the pre-compression load for wallettes

of the first test series. All the parameters used for calculating the elastic stiffness of the I-shaped masonry wallettes with a soft layer are summarized in Table 5-4. Values of the computed elastic and initial tangent stiffness, K_{el} and K_0, of the tested specimens are given in Table 5-3.

Table 5-4. Parameters used in the equation (5-1)

Specimen	E_x [MPa]	G_m [MPa]	[a]$\sigma_{pc}/\Delta t_{sl}$ [MPa/mm]		[b]G_{sl} [MPa]	A_w [mm^2]	I_w [mm^4]	α [-]	α' [-]	κ [-]
			t_{sl}=3 [mm]	t_{sl}=10 [mm]						
First test series	3660	1464	2.15	0.45	2	$3.15 \cdot 10^5$	$59.06 \cdot 10^9$	1	3	2
Second test series	2364	945.6	2.15	0.45	2	$3.15 \cdot 10^5$	$59.06 \cdot 10^9$	1.75	1.41	2
Rectangular walls	2821.9	1128.8	2.15	0.45	2	$1.80 \cdot 10^5$	$21.60 \cdot 10^9$	1	3	1.2

[a] Estimated from measurements (average from corresponding values given in Figure 5-19)
[b] Experimentally obtained value adopted from [3]

The ratio between the measured effective stiffness and the elastic stiffness calculated using equation (5-1), as well as the ratio between the measured effective stiffness and the initial stiffness for the tested I-shaped wallettes with a soft layer, is given in Figure 5-20a. The K_{eff}/K_{el} ratio is estimated to be 0.75 with $R^2 = 0.75$. For the rectangular wallettes built with a soft layer, the data in Figure 5-20b indicate that the estimated K_{eff}/K_{el} ratio is 1.0 with $R^2 = 0.95$.
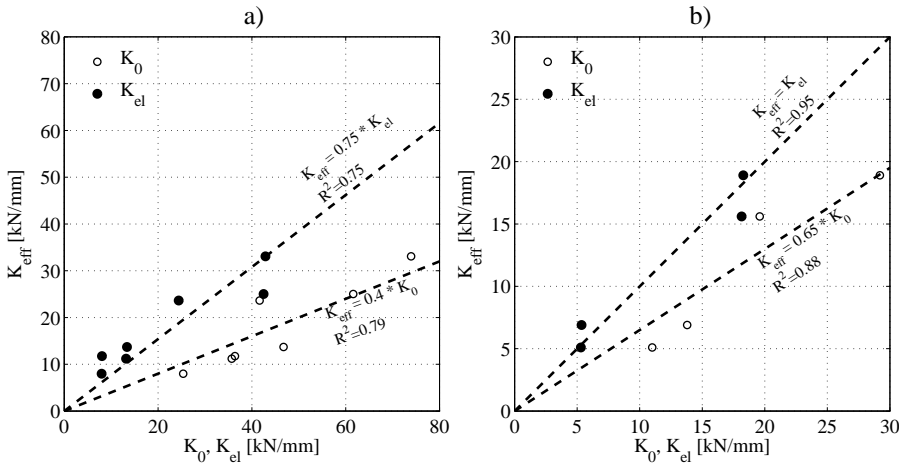
Figure 5-20. Comparison of the initial stiffness and the calculated elastic stiffness to the effective stiffness: a) I-shaped wallettes with a soft layer; b) rectangular wallettes with a soft layer

The calculated ultimate shear resistances H_u, shown in Figure 5-17, are equal to approximately 90% of the maximum recorded horizontal shear force values, see also Table 5-3. This compares well to the results of previous investigations of the shear behavior of the URM walls with a soft layer, e.g. [3,26]. Recommendations for the values of ultimate horizontal displacement available in the literature, e.g. [38,46,60–62], depend on the failure mode, aspect ratio, shear span, and pre-compression level. However, those empirical recommendations are given for rectangular URM walls.

As presented in previous sections, I-shaped wallettes developed drift ratios prior to failure as large as 3.3%. However, appreciable degradation of the post peak horizontal force resistance of the wallettes from the first test series, related to the extent of the induced damage in the wallette web and flanges, limits the useful range of the displacement capacity of these walls. On the other hand, the wallettes from the second series, which responded in a rocking mode, developed significant horizontal displacements with almost no strength degradation, and thus the maximum horizontal displacement is the ultimate horizontal displacement, see Table 5-3. Based on the results and observations from the first test series, where cantilever I-shaped wallettes failed in a shear-dominated failure mode, setting a limit of the ultimate drift ratio $\delta_u = d_u / h_w$ to 1.3% is reasonable and on the safe side. According to the test results from the second test series (Wallettes I5–I8), the displacement limit could be set to a slightly higher drift ratio of 1.67%. These drift ratio limits hold regardless of the presence of a soft layer and pre-compression level. Nevertheless, for pre-compression levels higher than 20% of the masonry compressive strength, the amount of plastic deformation should be set to zero, and an elastic brittle response of the cantilever I-shaped masonry walls should be assumed. This suggested limits of the drift ratio could be reformulated to take the pre-compression level into account once more test data becomes available.

Values of the ultimate drift ratio δ_u obtained from the presented tests that include specimens with different levels of pre-compression and shear span allow for calibration of the empirical model for estimating the ultimate drift ratio capacity of URM walls proposed by Salmanpour et al. in [43]:

$$\delta_u = \delta_0 \cdot \left(1 - 2.4 \cdot \frac{\sigma_{pc}}{f_x} \right) \cdot \frac{h_0}{h_w} \tag{5-2}$$

135

For the given pre-compression, masonry compressive strength, shear span and wallette height, the model can be calibrated for the value of the so-called base drift ratio δ_0 so as to capture the measured values of δ_u. Table 5-5 reports the values of δ_0 calculated from the tests on I-shaped wallettes. The mean value of δ_0 equals 2%, with a small variation over the data set (coefficient of variation COV = 14%), and can be proposed for practical applications when considering the typical Swiss clay I-shaped masonry walls with a soft layer.

Table 5-5. Calculated values of the base drift ratio δ_0 [57]

Wallette	h_0/h_w [-]	σ_{pc}/f_x [-]	δ_{u_test} [%]	δ_0 [%]
I0	1	0.1	1.3	1.71
I1	1	0.1	1.2	1.58
I2	1	0.1	1.8	2.37
I3	1	0.15	1.3	2.03
I4	1	0.15	1.4	2.19
I5	1.75	0.1	2.5	1.88
I6	1.75	0.1	3.3	2.48
I8	1.75	0.15	2.5	2.23
Mean	-	-	-	2.06
COV	-	-	-	14.42
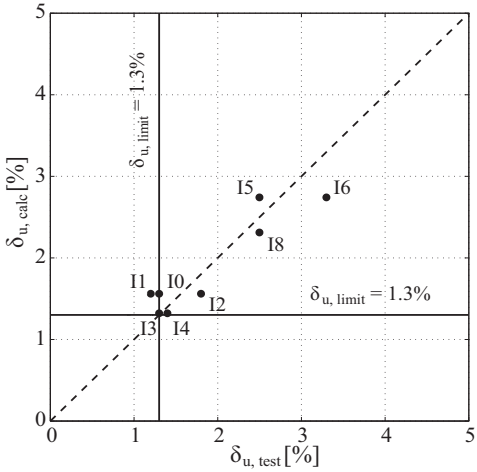
Figure 5-21. Ultimate drift ratio of the I-shaped masonry wallettes: test versus calculated values [57]

Figure 5-21 shows the correlation between the values of ultimate drift ratio of I-shaped masonry wallettes obtained from the tests and the values calculated using equation (5-2) and calculated mean value of δ_0, together with a conservative limit of 1.3%.

136

5.4.2 Influence of the pre-compression level

Two levels of pre-compression were selected for this experimental investigation, 0.6 and 0.9 MPa, namely 10 and 15% of the masonry compressive strength. The effects of the pre-compression level can be seen by comparing the backbone curves of Wallettes I1 and I3, I2 and I4, and I6 and I8 given in Figure 5-16. It is clear that as the level of pre-compression increases, the stiffness as well the horizontal force resistance of the wallettes increases, whereas their displacement capacity decreases. The values of K_0, H_{max}, and d_{max}, given in Table 5-3, indicate that in specimens from the first test series with 3 mm thick rubber granulate, an increase of the pre-compression level by 50% led to the increase of the stiffness and the horizontal force resistance by 20-40%, whereas the displacement capacity decreased by approximately 30%.

The level of pre-compression affected the behavior of the specimens from the first test series. The specimens tested under higher pre-compression (I3 and I4) developed less sliding along the layer bed joint and less penetration of the wallette web through the flanges than the specimens with lower pre-compression. However, degradation of Wallettes I3 and I4 caused by diagonal cracking was significant and led to a sudden compression failure of the wallettes (see the postpeak response of Wallettes I3 and I4 in Figure 5-8). On the other hand, the level of pre-compression did not have a significant influence on the behavior of the specimens from the second series (Specimens I6 and I8). In fact, increasing the level of pre-compression exacerbated the extent of diagonal shear cracks, i.e. shear cracks formed along the head and bed joints and subsequently extended through the clay units, see Figure 5-14.

5.4.3 Influence of the flanges

Influence of the flanges can be discerned by comparing the results of the first test series presented herein with the corresponding tests performed on the rectangular URM wallettes of the same dimensions, position, and type of soft layer, but constructed without flanges, see [3] for more details. The corresponding specimen pairs are W0.10 versus I0, WG3.10 versus I1, WG10.10 versus I2, WG3.15 versus I3, and WG10.15 versus I4. A significant increase of the horizontal force resistance and the initial stiffness of the wallettes with flanges is evident. These observations are consistent with those made in previous studies on the effect of flanges in I-shaped masonry walls without soft layers, e.g. [53,54].

However, there are no significant differences in the displacement capacities of the wallettes. The rectangular wallettes with a lower pre-compression, i.e. 10% of their axial load capacity, developed deformations through rocking and sliding along the layer bed joint or the diagonal stepwise crack system along the masonry bed joints of the wallettes. On the other hand, the wallettes pre-compressed to 15% of their axial load capacity deformed primarily in shear with some sliding along the layer bed joint and the diagonal stepwise cracks regardless of their geometry.

Observations also indicate that development of the sliding deformation mechanism in I-shaped wallettes tested under cantilever boundary conditions requires the failure of the connection between the wallette web and the flanges. This increases the resistance of the I-shaped wallettes, delays the onset of sliding, and eventually induces a shear-dominated failure of I-shaped wallettes. In this sense, the presence of flanges was somewhat detrimental to realizing the intended seismic response modification purpose of the layer bed joints.
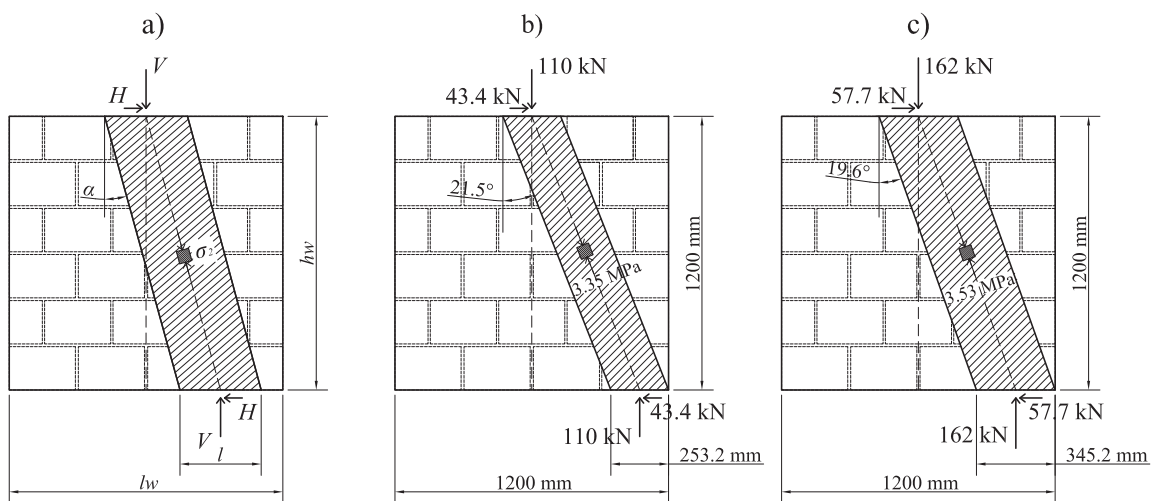
Figure 5-22. Stress field in rectangular masonry wall subjected to the combined action of centric in-plane vertical and shear loads: a) general case; b) case with the vertical load of 110 kN; c) case with the vertical load of 162 kN [57]

A significant increase of the horizontal force resistance of the wallettes with flanges can be described by applying the methods of the theory of plasticity, namely the lower bound limit theorem. This modeling approach is based on discontinuous stress fields, which rely on the ideal-plastic behavior of the material. In general, as formulated by Muttoni et al. [63], in a plastic design, a stress field is chosen such that the equilibrium conditions and the static (force) boundary conditions are fulfilled (statically admissible

138

stress field). The dimensions of the cross-section have to be proportioned such that the resistances everywhere are greater than or equal to the corresponding internal forces. Considering the cantilever rectangular masonry wall subjected to in-plane loads, i.e. to an axial force V and a shear force H, as given in Figure 5-22a, it is assumed that the loads could be transmitted through the wall by means of one uniaxially compressed stress field of length l. As stated by Mojsilović [64], a model with a single uniaxial stress field (strut) is the simplest model that could be developed based on the theory of plasticity, i.e. load transfer through the masonry wall could also be achieved by means of several struts or combined struts and fans. The dimensions and the inclination of the stress field, α, are determined by the geometry of the wall, applied loads, and static boundary conditions. Starting from the moment and force equilibrium equation

$$M_{bot} = H \cdot h_w = 0.5 \cdot V \cdot \left(l_w - l\right) \tag{5-3}$$

and including that $H/V = \tan\alpha$, the length of the stress field can be expressed as a function of the inclination angle α

$$l = l_w - 2 \cdot \frac{H \cdot h_w}{V} = l_w - 2 \cdot h_w \cdot \tan\alpha \tag{5-4}$$

Further, the failure criterion must be satisfied; i.e. the resulting principal compressive stress in the field σ_2 may not be greater than the masonry uniaxial strength f_α, which in turn depends on the strut inclination angle:

$$\sigma_2 = \frac{V}{l \cdot t_w \cdot \cos^2\alpha} \leq f_\alpha \tag{5-5}$$

Variation of the masonry uniaxial strength f_α with respect to the strut inclination shown in Figure 5-23 was recently reported within a research project on the behavior of masonry under reversal biaxial stress states, where the same materials as in presented tests were used, see Salmanpour et al. [65]. The stress field inclination angle is limited to the value of 45.8°, the value when bed joint sliding failure occurs. Given the previous, it is clear that for the known value of a vertical load V, the horizontal force resistance of cantilever rectangular masonry walls is governed by the maximum allowable value of angle α.
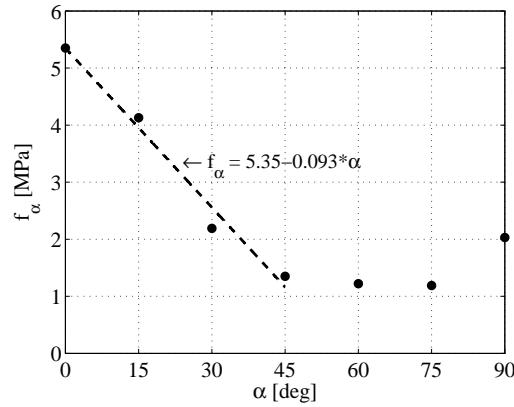
Figure 5-23. Variation of the masonry uniaxial strength with the angle α [57]

Using the equations (5-4) and (5-5) and the variation of the masonry uniaxial strength with the angle of inclination of the bed joints shown in Figure 5-23, one can obtain that

$$\left(l_w - 2 \cdot h_w \cdot \tan \alpha\right) \cdot f_\alpha \cdot t_w \cdot \cos^2 \alpha \geq V \tag{5-6}$$

and, with the known wallette dimensions, calculate the corresponding angle α, and thus the maximum horizontal force resistance, $H_{max,\ calc} = V \cdot \tan\alpha$, and length of the compression struts of the rectangular wallette, see equation (5-4). Therefore, considering the wallettes tested by Vögeli et al. [3], with nominal dimensions of dimensions of 1200x1200x150 mm, subjected to pre-compression of 0.6 and 0.9 MPa, corresponding to vertical forces of 110 and 162 kN, respectively, the following can be calculated. For the wallette with V=110 kN, a maximum allowable angle α=21.5° can be calculated, that further gives an maximum horizontal force resistance of 43.4 kN and l=253.2 mm. In case of the wallette with V=162 kN, a maximum allowable angle α=19.6° and corresponding maximum horizontal force resistance of 57.7 kN and l=345.2 mm can be calculated. The resulting stress fields, shown in Figures 5-22b and 5-22c, also fulfill the geometrical condition; i.e. they can be accommodated within the area of the considered wallettes. As can be seen from Table 5-6, the predicted values of the horizontal force resistance are in good agreement with the experimental results.

Table 5-6. Comparison of the values of measured and calculated horizontal force resistance

Parameter	Specimen									
	W0.10	WG3.10	WG10.10	WG3.15	WG10.15	I0	I1	I2	I3	I4
H_{max} [kN]	47.59	50.81	46.09	66.5	58.42	115.4	96.36	84.02	114.64	115.29
$H_{max,\ calc}$ [kN]	43.4	43.4	43.4	57.7	57.7	84	84	84	112.3	112.3
$H_{max}/H_{max,\ calc}$ [-]	1.09	1.17	1.06	1.15	1.01	1.37	1.15	1.00	1.02	1.02
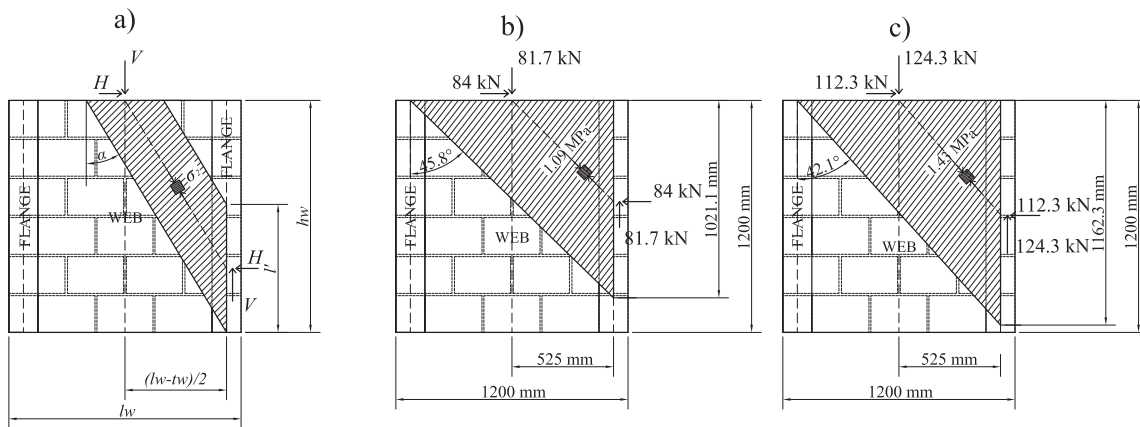
Figure 5-24. Stress field in I-shaped masonry wall subjected to the combined action of centric in-plane vertical and shear loads: a) general case; b) case with the web tributary vertical load of 81.7 kN; c) case with the web tributary vertical load of 124.3 kN

When considering the stress field in I-shaped masonry walls, the presence of flanges (adequately strong and competently connected to the wall web) may allow for a more inclined stress field, i.e. larger stress field inclination angle α (up to the limit of 45.8°). As shown in Figure 5-24a, a larger horizontal force resistance, compared to the rectangular wall with the same level of vertical load, could then be developed. A larger angle α, however, demands a stress field partly or even fully supported by the flange. Vertical cracks at the connection between the wallette web and flanges, observed during the tests, clearly indicate that the flanges could support the wallette webs and restrain their deformation until stepwise cracks along the web masonry joints occurred. Thus, the connection between the web and flanges appears as another parameter that governs the resistance of the I-shaped wall. As a result, the horizontal force resistance of the walls is not only limited by the largest allowable value of angle α, but is also limited by the resistance of the connection between the wallette web and flanges. The stress field must fulfill the equilibrium condition

$$M_{bot} = H \cdot h_w = V \cdot 0.5 \cdot \left(l_w - t_w\right) + H \cdot (h_w - 0.5 \cdot \frac{l_w - t_w}{\tan \alpha}) \tag{5-7}$$

as well as the following geometric condition

$$l' \leq \frac{l_w - t_w}{\tan \alpha} \tag{5-8}$$

In addition, the stress field must satisfy the failure criterion

141

$$\sigma_2 = \frac{V}{l' \cdot t_w \cdot \sin\alpha \cdot \cos\alpha} \leq f_\alpha \tag{5-9}$$

If one assumes that the connection between the web and flanges of an I-shaped wallette is sufficiently strong to support the stress field, the largest allowable value of angle α can be calculated using equations (5-8) and (5-9) while considering the variation of the masonry uniaxial strength with the angle of inclination of the bed joints shown in Figure 5-23. With known value of α, the maximum wallette horizontal force resistance and strut length are determined. It can be assumed that the applied vertical load is distributed among the wallette web and the flanges according to their nominal horizontal cross-section area. This means that, according to the wallette nominal dimensions given in Figure 5-1, 57% of a total vertical load is carried by the flanges, while the web carries 43% of a total vertical load. For the wallettes I0, I1 and I2 that have a total vertical load of 190 kN, i.e. the web tributary vertical load of 81.7 kN, one can calculate the value maximum allowable angle α=45.96° that exceeds the limit value of 45.8°. Thus, the maximum horizontal force resistance of the wallettes I0-I2 is $H_{max,\ calc}$ = 81.7kN·tan(45.8°) = 84kN, while the strut length is l'=1021.1 mm. Similarly, in case of wallettes I3 and I4, with a total vertical load of 290 kN, i.e. with the web tributary vertical load of 124.3 kN, the value of maximum allowable angle α=42.1°, and further the maximum wallette horizontal force resistances, $H_{max,\ calc}$ = 124.3kN·tan(42.1°) = 112.3 kN, and the strut length, l'=1162.3 mm, can be calculated. According to the test observations, the tested I-shaped wallettes developed the maximum horizontal force before the failure of the connection between the wallette web and the flanges. Therefore, the assumption that the connection between the web and flanges is sufficiently strong is justified. The resulting stress fields are shown in Figures 5-24b and 5-24c. A fair correlation, acceptable for practical application, between the experimentally obtained and the calculated values of the horizontal force resistances is obtained, cf. Table 5-6.

The model developed based on the discontinuous stress fields considers only the uniaxial stress field (strut) that develops in masonry. Therefore, the failure criterion depends on the masonry uniaxial compressive strength f_α. The soft layer is a separate entity whose influence can be taken into account through the force boundary condition: sliding limits the horizontal force that can be transferred from the wall to its base.

5.4.4 Influence of the shear span

A higher shear span caused a pronounced rocking of the specimens in the second test series. As compared to the specimens from the first test series, specimens from the second test series did not develop pronounced shear cracks, except Specimen I8, tested under a higher level of pre-compression. The developed step-wise cracks followed the head and bed joints of the web and did not influence the failure mode, cf. Figure 5-14. Further, it can be seen from Table 5-3 that the wallettes tested within the second test series (with $h_0 = 1.75h_w$) developed a significantly lower horizontal force resistance and initial stiffness as compared to the corresponding specimens of the first series (with $h_0 = h_w$). On average, the horizontal force resistance and initial stiffness decreased by 40 and 28%, respectively. Moreover, it can be noticed that the second-series wallettes with a thicker soft layer developed larger maximum horizontal displacements (up to 50% for the specimens tested under higher levels of pre-compression), whereas the maximum horizontal displacements for wallettes with a thinner layer are approximately the same.

5.4.5 Influence of the soft layer and its thickness

The influence of the soft layer can be seen in Figure 5-16 by comparing the backbone curves of the I-shaped wallettes tested within the first test series under the pre-compression level of 0.6 MPa. First, as compared to the control specimen I0, Specimens I1 and I2 developed somewhat less horizontal force resistance and were significantly softer. Second, a significant increase of the displacement capacity of the wallettes with layer bed joints is clearly noticeable. At the start of the test, more wallette deformation originates from the soft layer deformability (shear and vertical deformation of the soft layer), whereas the contribution of the masonry deformation is relatively small. However, as the wallette top displacement demand increases, the contribution of the deformation components changes such that the rocking motion resulting from the vertical deformation of the soft layer contributes less, whereas the sliding motion along the soft layer and the deformation of the masonry dominate. This delay of significant masonry deformation as compared to the wallettes built without a soft layer postpones the occurrence of maximum wall shear resistance to a larger horizontal displacement level and increases the deformation capacity of I-shaped wallettes with soft layers.

The influence of layer thickness on the specimen response can also be seen by comparing the backbone response curves of Wallettes I1 and I2, I3 and I4, and I5 and I6, shown in Figure 5-16. The effect of layer thickness on the horizontal force resistance of the wallettes with soft layers is negligible. However, the initial backbone curve stiffness is significantly affected: a thinner layer results in a higher initial stiffness. It can be seen from Table 5-3 that the specimens with thinner soft layers had, on average, 65% higher initial stiffness K_0. This is because the deformability of the soft layer increases with increasing its thickness, and a more deformable soft layer allows for more shear deformations as well for more significant rocking motion during the initial stages of the tests. However, wallettes with soft layer can benefit from the vertical deformability of the soft layer until they stop acting as a rigid rocking body, i.e. until the induced wallette deformation does not cause significant damage in the masonry (e.g. diagonal shear cracks in the wallette web). Specimens from the second test series responded predominantly in rocking mode. They could preserve web integrity longer than the comparable specimens from the first test series and benefited more from the deformability of the soft layer. Therefore, the effect of soft layer thickness on the displacement capacity of the wallettes from the first test series is small, whereas an increase of soft layer thickness increased the deformation capacity of the wallettes from the second test series by 30%.

5.4.6 Soft layer degradation

Figures 5-25 and 5-26 show the state of the rubber granulate soft layers after completing the tests and disassembling the wallettes of the first and the second test series, respectively. It can be seen from Figure 5-25 that, as a consequence of the pronounced sliding in case of Wallette I1, the soft layer placed under the web of this wallette experienced multiple tension cracks. Further, crumbling of the 3-mm-thick layer (Wallettes I1 and I3) at the outer edges is visible. This is because a soft layer allows the wallette to exhibit a certain amount of rocking motion and therefore induces normal stress concentrations in the soft layer that, in combination with sliding, can produce such damage. The layers beneath the flanges experienced some damage due to punching of the wallette web through the flanges toward the end of the tests. In the case of Specimens I1 and I3, the layer was torn up, as shown in Figure 5-25. In general, thicker soft layers and higher pre-compression led to less damage. Thicker soft layers are more resilient because they experience less shear strain at the same displacement demand levels than thinner soft layers. Higher pre-

compression makes the soft layer more compact and constrains the rubber granulate. The increase of the pre-compression load also decreases the extent of the sliding motion and thus reduces soft-layer degradation.
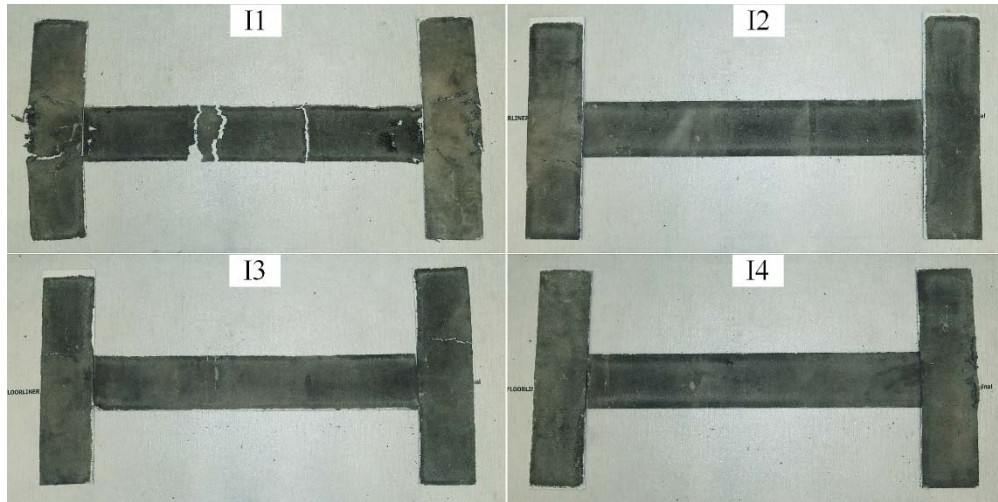
Figure 5-25. Wallettes from the first series: soft layer degradation after testing [57]
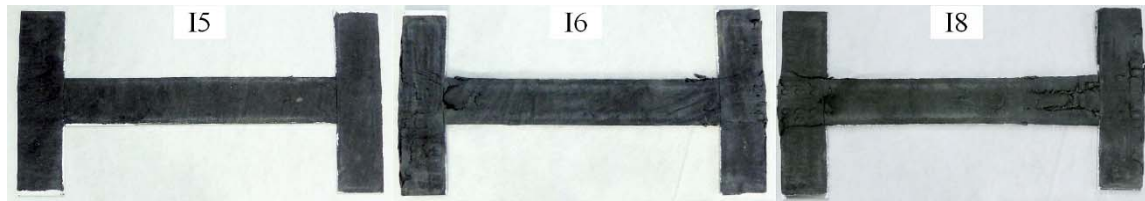
Figure 5-26. Wallettes from the second series: soft layer degradation after testing [57]

Regarding the specimens from the second test series, which responded by rocking, only the thicker layers experienced some visible damage, as can be seen from Figure 5-26. The damage is mainly concentrated at the rocking (pivot) edges, where the normal stress concentrations together with the sliding motion crumble the rubber granulate soft layer. Further, as for the specimens from the first test series, the damage caused by punching of the wallette web through the flanges is visible on the layers placed beneath the flanges. Such damage was most pronounced in Specimen I8, where the largest amount of sliding was recorded.

5.5 Summary and conclusions

The presented analysis and discussion of the results of the tests on I-shaped URM wallettes with and without a rubber granulate soft layer, conducted to investigate the interaction

between the in-plane and transverse walls (flanges) that can be regarded as a common element of the URM structures, allow for several conclusions. The flanges considerably increase the horizontal force resistance and initial stiffness of I-shaped wallettes. However, the presence of flanges is somewhat detrimental to realizing the intended seismic response modification purpose of the soft-layer bed joints. Full development of the sliding deformation mechanism in I-shaped wallettes requires the failure of the connection between the wallette web and the flanges.

An analytical model, based on discontinuous stress fields, is proposed to predict the horizontal force resistance of the I-shaped walls with soft-layer bed joints failing in shear and validated using the experimental results. Further, an equation for calculating the elastic stiffness of I-shaped URM walls with a soft layer is proposed. The effective stiffness of I-shaped URM walls with a soft layer, which characterize the bilinear idealization of the horizontal force-displacement response, can be estimated as 0.75 of the elastic stiffness value computed using the proposed equation. Thanks to the relatively large deformability of the soft layer, I-shaped wallettes with soft-layer bed joints have a lower initial stiffness, higher energy dissipation capacity, and, importantly, significantly larger displacement capacity as compared to conventional I-shaped wallettes. However, the displacement capacity should be limited to the level at which the extent of damage induced in the flanges is not significant. According to the test results and observations, those limitations correspond to drift ratios of 1.3 and 1.67% for I-shaped wallettes with shear spans equal to 1.0 and 1.75 times the wallette height, respectively.

The presence of soft layers can provide for significant seismic response modification by elongating the initial fundamental vibration period of the URM structure with such soft layers and by allowing for more deformation before the onset of brittle shear or toe crushing failure. Because the deformation capacities of URM walls with soft layers are moderate, this response modification technique is applicable to URM structures in regions of low and moderate seismicity.

Traditional connections between the wall web and the flanges made through interlocking of the masonry units with a header unit in every second course accumulates damage with increasing horizontal displacement demand and negatively affects the performance of intersecting URM walls. Alternatives include strengthening of these connections or avoiding any connection between the in-plane and out-of-plane walls.

146

Priestley et al. [66] stated that there is no reason for connecting the perpendicular walls in new URM buildings with stiff and strong, mainly reinforced concrete, floor slabs that distribute the horizontal forces among the bearing walls. Avoiding connections between in-plane and out-of-plane bearing walls would fully utilize the deformation capacity of the soft layers and is thus the preferred solution.

6 Summary and recommendations for future research

6.1 Summary

The present thesis is subdivided into three parts. The first part, comprising Chapters 2 and 3, summarizes the previous experimental and theoretical work on the response of masonry walls that develop sliding, as well the extensive experimental work conducted in the scope of this project, on the in-plane compressive and shear behavior of URM elements with a multi-layer bed joint. The second part, i.e. Chapter 4, provides a mechanics-based analytical model capable of predicting the loading speed-dependent seismic in-plane response of URM walls with a rubber granulate core soft layer in the multi-layer bottom bed joint. The third part, i.e. Chapter 5, considers the seismic in-plane behavior of I-shaped URM wallettes with a soft layer in the bottom bed joint.

The first part of the thesis presents a state-of the art review and discussion of the experimental and theoretical work on the response of masonry walls that develop sliding, with a special attention on studies on the shear behavior of URM with incorporated soft layers and summarizes the main results of the experiments conducted in the scope of this research project. The majority of the previous investigations has been focused on the investigation of the shear behavior of bed joints containing various types of soft layer at different pre-compression levels, i.e. on the assessment of the shear parameters as well the overall performance of bed joints containing soft layers by conducting static, static-cyclic and dynamic tests on small URM elements (mostly triplets). The experimental investigation conducted in this research project, summarized in Figure 3-1, comprises the following: 57 monotonic and static-cyclic material-level shear tests on URM triplets with multi-layer bed joints having five different core soft layers; 15 material-level compression tests on URM wallettes made with or without a multi-layer bottom bed joint; additional 39 material-level monotonic shear and relaxation tests on URM triplets with a rubber granulate core soft layer in multi-layer bed joints; and 9 structural element-level tests on URM walls with a multi-layer bottom bed joint subjected to the combined action of the in-plane compressive and static-cyclic shear load. The test results indicate that the vertical deformability of masonry is influenced by any type of the considered multi-layer bed joints, while only the rubber granulate core soft layer in the multi-layer bed joint induces a somewhat lower compressive strength of masonry. The shear resistance of the multi-

layer bed joint is found to depend on the level of the pre-compression as well as on the loading speed, regardless to the core soft layer type. Therefore, the applicability of Mohr-Coulomb's failure criterion to determine the shear resistance of the multi-layer bed joint requires the friction properties to be experimentally determined for the particular soft layer material and the particular soft layer bed joint configuration using a loading protocol with varying loading magnitudes and speeds. Further, it is found that the in-plane shear behavior of the multi-layer bed joint with a rubber granulate core soft layer can be characterized as linear elastic-viscoplastic: after the initial elastic, loading speed-independent behavior, the influence of loading speed appears. Findings from the performed structural element-level investigation indicate that the load-bearing URM walls with a multi-layer bottom bed joint, in spite of the prevailing sliding response, could exhibit a significant shear capacity that depends on the type of core soft layer material, applied level of pre-compression as well as on the loading speed. The ultimate displacement capacity as well the failure mode of the URM walls with a multi-layer bottom bed joint is strongly influenced by the extent of shear cracks that develop in the URM wall as well as by the appearance of tensile cracks in the head joints at the bottom block course. As compared to the corresponding conventional URM walls made without a multi-layer bed joint, the URM walls with a multi-layer bottom bed joint have: about 30% lower maximum shear resistance, 15-40% lower initial stiffness, and up to six times larger displacement capacity, depending on the wall size, type of core soft layer, pre-compression level and wall aspect ratio. However, due to the interaction of the wall with other structural and non-structural components of the building, the displacement demand should be limited to an drift ratio of 1%. This problem is further examined in the third part of the thesis, by testing half-size I-shaped URM wallettes and with a rubber granulate soft layer in the bottom bed joint.

The intended durability-improving role of the extruded elastomer layers is largely fulfilled. Except in the case of bitumen-based core soft layer, only a local damage to the core soft layer was detected, primarily at the location where the tensile cracks in the head joints at the bottom block course appeared.

A method to construct an idealization of the horizontal force-displacement response envelope for the URM walls with multi-layer bed joints is proposed. The ultimate

horizontal force resistance of URM walls with a multi-layer soft bed joint can be estimated using:

$$H_u = 0.9 \cdot H_{max,\,calc} = 0.9 \cdot A_w \cdot (c + \sigma_{pc} \cdot \tan\varphi)$$

and the initial stiffness of these walls can be computed as (according to the equation (3-2)):

$$K_0 = 1.4 \cdot K_{el} = 1.4 \cdot \cfrac{1}{\kappa \cdot \cfrac{h_w}{G_m \cdot A_w} + \cfrac{h_w^3 \cdot \left(\alpha^3 + (1-\alpha)^3\right)}{3 \cdot E_x \cdot I_w} + \cfrac{(t_{ml} - \Delta t_{ml})}{G_{ml} \cdot A_w} + \alpha \cdot \cfrac{h_w^2 \cdot \Delta t_{ml}}{\sigma_{pc} \cdot I_w}}$$

These estimates allow for computing the apparent yield displacement d_y of an URM wall with a multi-layer bottom bed joint. In addition, the experimentally obtained values of ultimate displacement, d_u, the displacement when a sudden drop of horizontal force resistance occurs, d_t, and the remaining horizontal force resistance, H_r, are listed in Chapter 3.

A mechanics-based analytical model of the elastic-viscoplastic in-plane shear behavior of the masonry multi-layer bed joint with a rubber granulate core soft layer is also presented. The model viscoplastic branch is defined as (according to the equation (4-15)):

$$H = H_y \cdot \left[1 + \frac{\dot{d}}{t_{ml} - \Delta t_{ml}} \cdot \eta^* \cdot \left(1 - e^{-\frac{\psi \cdot G_{ml} \cdot A_b}{H_y \cdot \eta^*} \cdot \frac{d - d_y}{\dot{d}}} \right) \right]$$

This model is further extended to describe the in-plane horizontal force-displacement behavior of URM walls with a rubber granulate core soft layer in the multi-layer bottom bed joint. The model elastic branch is:

$$H = K_0 \cdot d$$

while the model viscoplastic branch, which follows after exceeding the elastic limit (d_y, H_y), is (according to the equation (4-22)):

$$H(d, \dot{d}) = H_y \cdot \left[1 + \frac{\eta^* \cdot \dot{d}}{t_{ml} - \Delta t_{ml}} \cdot \left(1 - e^{-\frac{K_0 \cdot (t_{ml} - \Delta t_{ml})}{H_y \cdot \eta^*} \cdot \frac{d - d_y}{\dot{d}}} \right) \right]$$

The accuracy of the model is verified by comparisons with own tests on URM walls with a multi-layer bottom bed joint. However, possible separation of the wall into more parts, initiated by the tensile cracks in head joints at the bottom block course, which can lead to significant strength and stiffness degradation of the wall, and/or exceeding of the limit of the elastic masonry deformation, limits the model applicability.

The presence of the multi-layer bed joint with a rubber granulate core soft layer results in relatively soft response of URM walls, i.e. leads to an elongation of the initial fundamental vibration period of URM structures that contain such multi-layer bed joints. The multi-layer bed joints can allow for a remarkable amount of inelastic deformation before the onset of shear failure (if any) of the masonry, while protecting the URM walls from the excessive shear-caused diagonal cracking and preserving their gravity load-carrying capacity. Therefore, it can be concluded that the bottom multi-layer bed joints in URM walls act to modify the seismic response of URM walls, and further to enable the URM structures with such walls to achieve the target performance goals in regions of low and moderate seismicity: 1) experience essentially no damage in frequent earthquakes and under high wind loads when the structure is expected to remain elastic; 2) experience controlled damage in design-basis earthquakes through an elongation of the structural response period due to relatively low stiffness in the pre-sliding regime and the stable lateral sliding deformation; and 3) collapse prevention in beyond-design-basis earthquakes through preserving the gravity load-carrying capacity of the structural masonry walls.

Test results from series of static-cyclic shear tests on I-shaped URM wallettes with a rubber granulate soft layer in the bottom bed joint are presented and discussed in the third part of the thesis. Even though the presence of flanges leads to considerably higher horizontal force resistance and initial stiffness of URM wallettes, it is detrimental to realizing the intended seismic response modification purpose of the soft layer in bottom bed joints. The extent of damage induced in the flanges through the interaction with the wallette web limits the useful displacement capacity of the orthogonal system of URM walls with soft layer bed joints.

Note that the obtained research results and the conclusions are only briefly summarized within this Chapter. A detailed summary of the obtained results as well arising conclusions can be found at the end of each Chapter of this thesis.

6.2 Recommendations for future research

The presented research project represents an initial step towards developing the sliding-based response modification method for the seismic in-plane behavior of structural URM walls using soft layers. Even though the research outcomes provide valuable insights into the seismic in-plane response of URM walls with a multi-layer bottom bed joint, further investigation is required along the following lines:

– More tests should be done to obtain an insight into the influence of wall boundary conditions (other than fixed-end) on the seismic in plane response of URM walls with a multi-layer bottom bed joint, and further on the applicability of the proposed mechanical model to predict the seismic in-plane response of such URM walls.

– The author believes that by preventing the opening of the vertical tensile cracks between the blocks at the bottom block course of the wall the potential reduction of the wall effective area can be avoided and its seismic performance significantly improved. One way to achieve this may be by constructing a shallow RC bond beam between the multi-layer bed joint and the first block course, cf. Figure 2-2. In this case, the intended seismic response modification purpose of the soft layer in bottom bed joints could be fully realized for vertical (pre-compression) loads of up to 20% of the masonry compressive strength.

– Another important issue deserving further research is the behavior of full-size, story-high I-shaped URM walls with a multi-layer bottom bed joint and the behavior of the connection between the walls web and flanges at such size level. This should establish the limits of detrimental/beneficial influence of transverse walls on response quantities of the in-plane structural URM walls with a multi-layer bottom bed joint, especially on the displacement capacity, and better define a usable drift ratio capacity of stories with such URM walls.

– The last but not the least important issue is the lack of the system-, i.e. structural-level shaking table tests. It is of utmost importance to get an insight into the dynamics of URM structures containing multi-layer bottom bed joints. Moreover, such tests must be performed to find out how the sliding in the multi-layer bottom bed joints is distributed along the structure height, as well as to identify the coupling effects, i.e. the influence of the out-of-plane on the in-plane response of URM walls with a multi-layer bottom bed joint.

Appendix A1   Monotonic and static cyclic shear tests on masonry triplets with multi-layer bed joints

This appendix provides for the details of shear force-slip relationships measured during the monotonic and static-cyclic shear tests on masonry triplets with a multi-layer bed joints. In addition, the details of the graphs on the comparison of the measured shear force-slip relationships and corresponding backbone and capacity curves depicted in Figure 3-12, are provided.
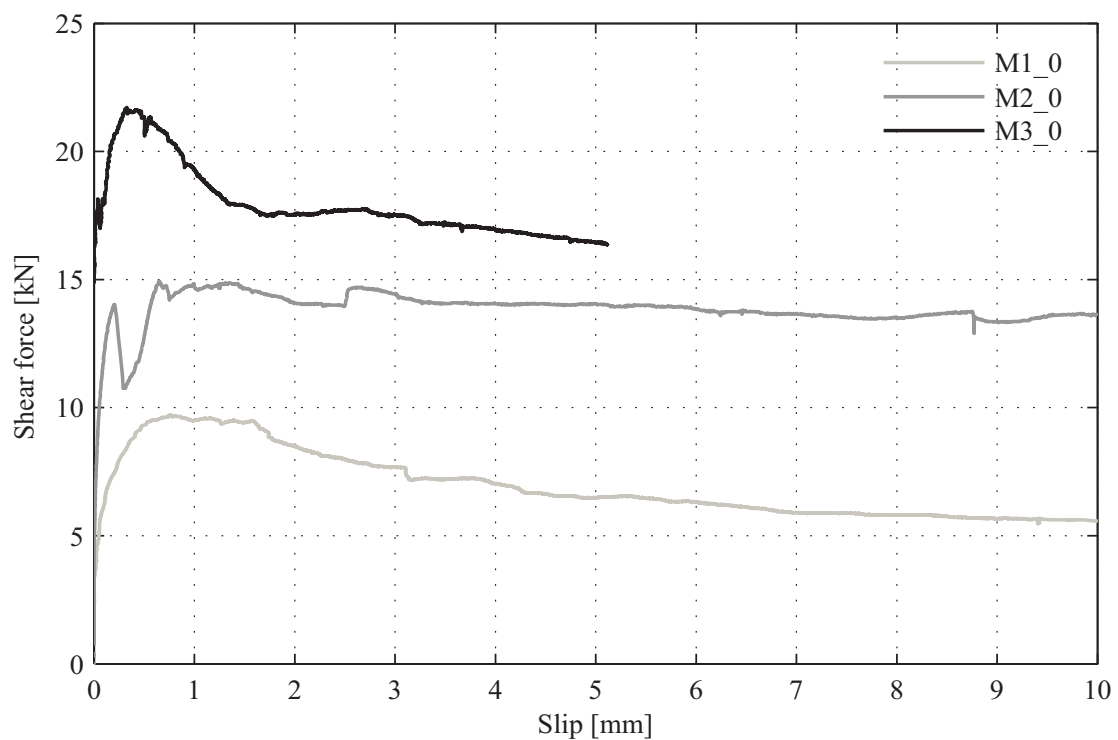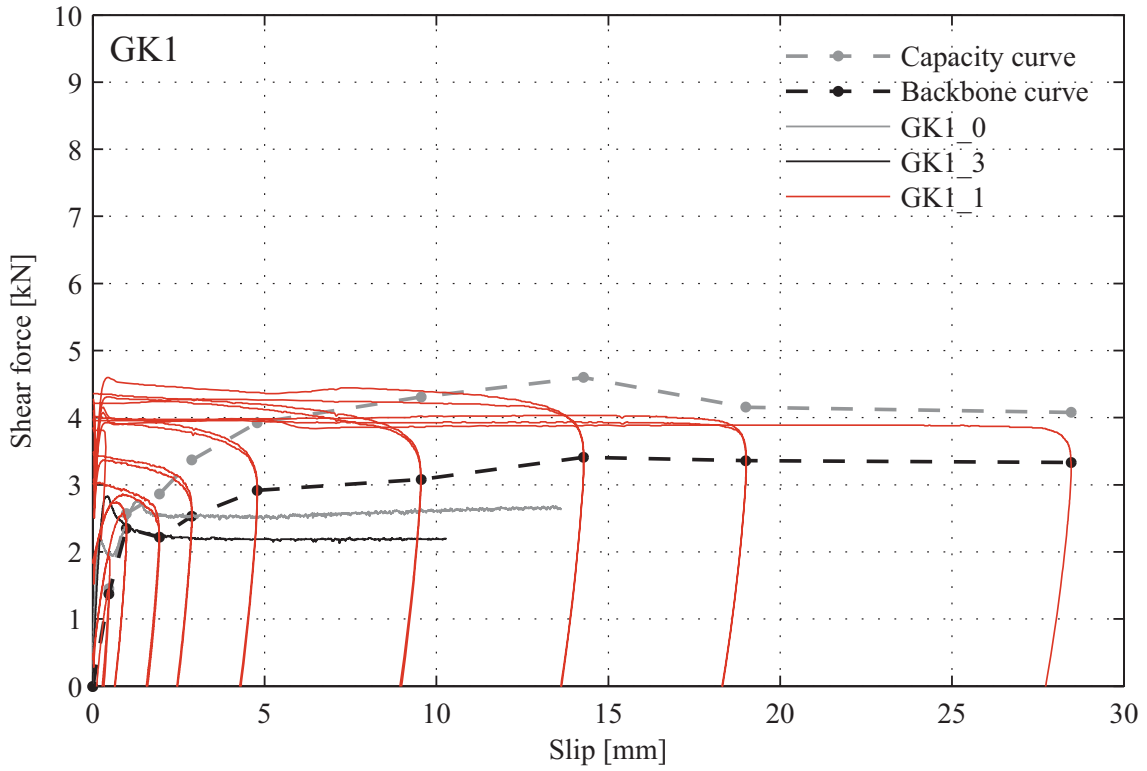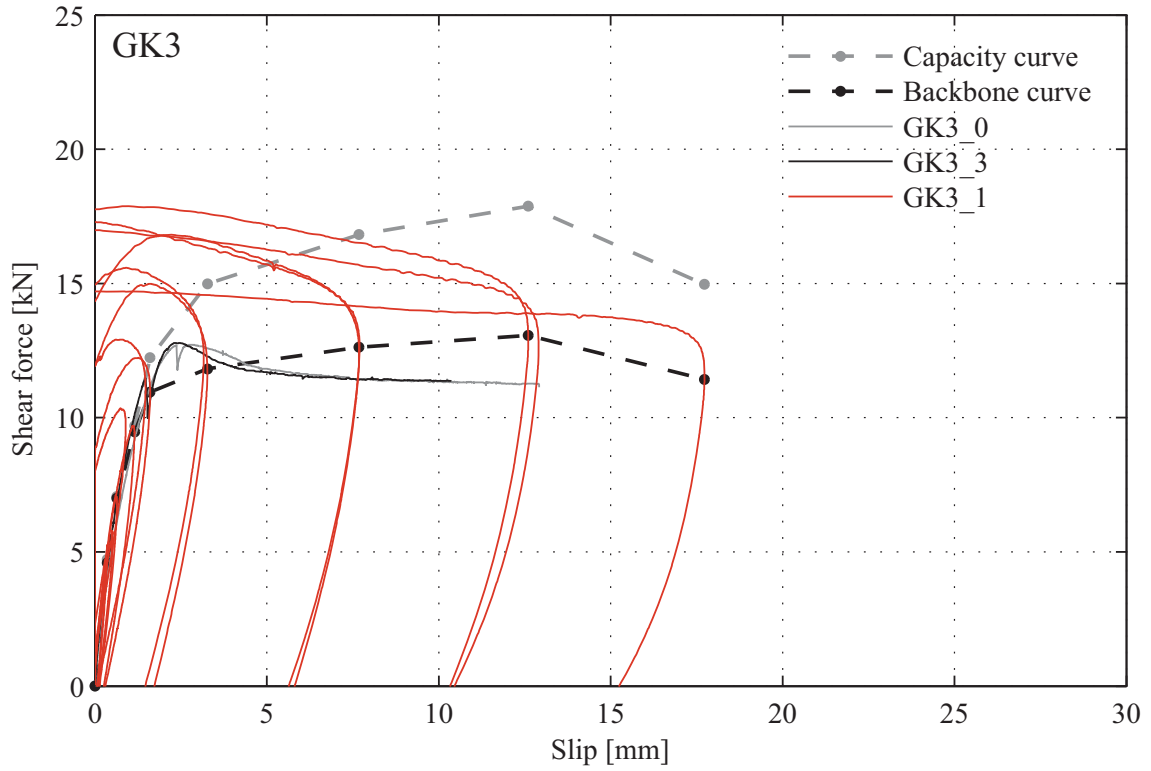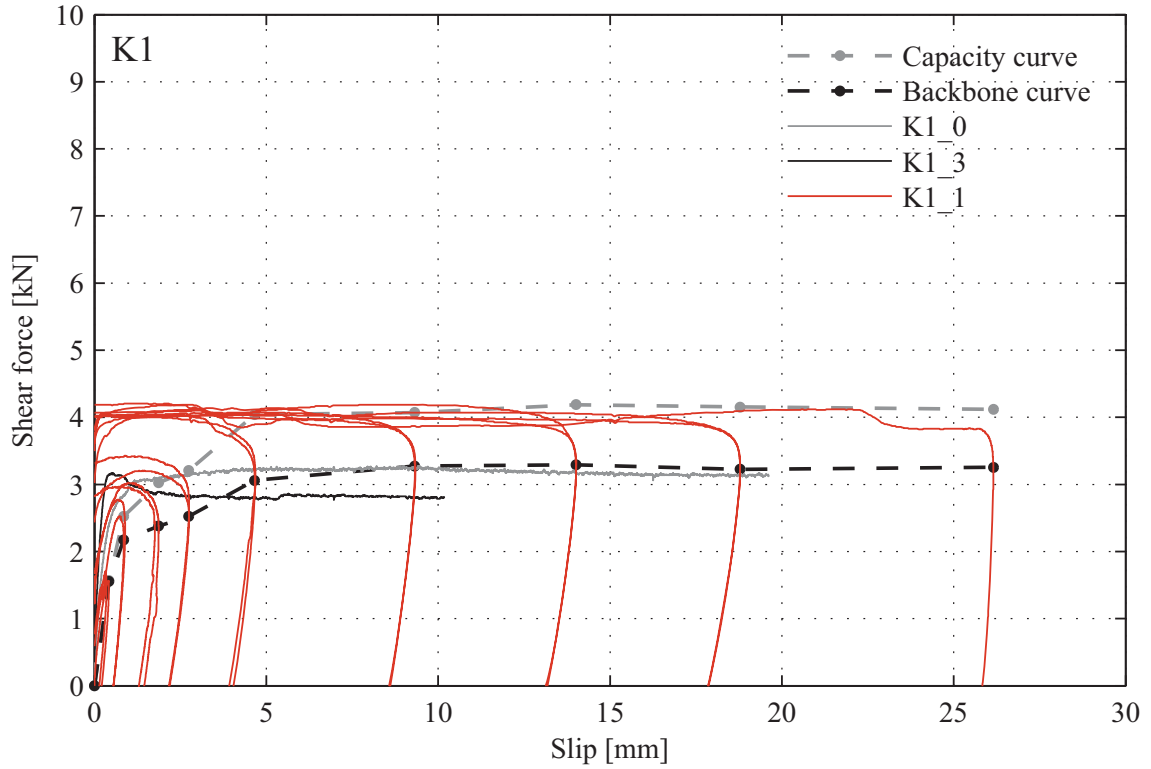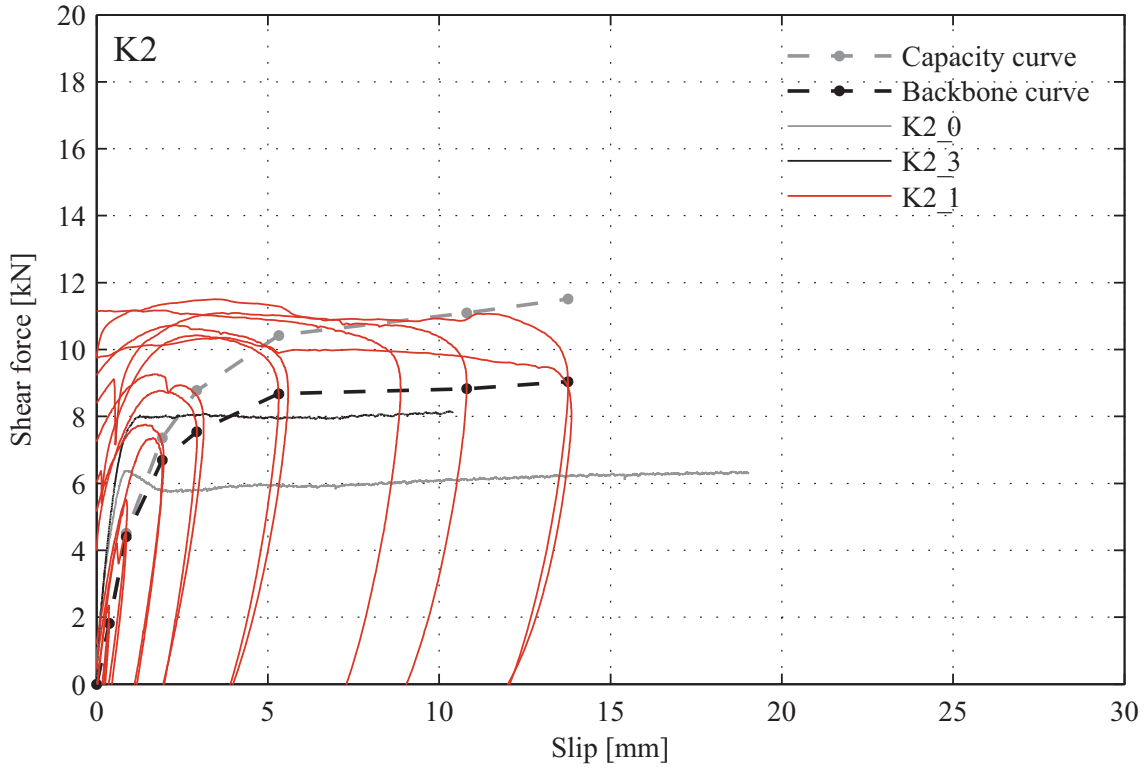

Figure A1-1. Shear force-slip relationships: Specimens M1_0, M2_0 and M3_0
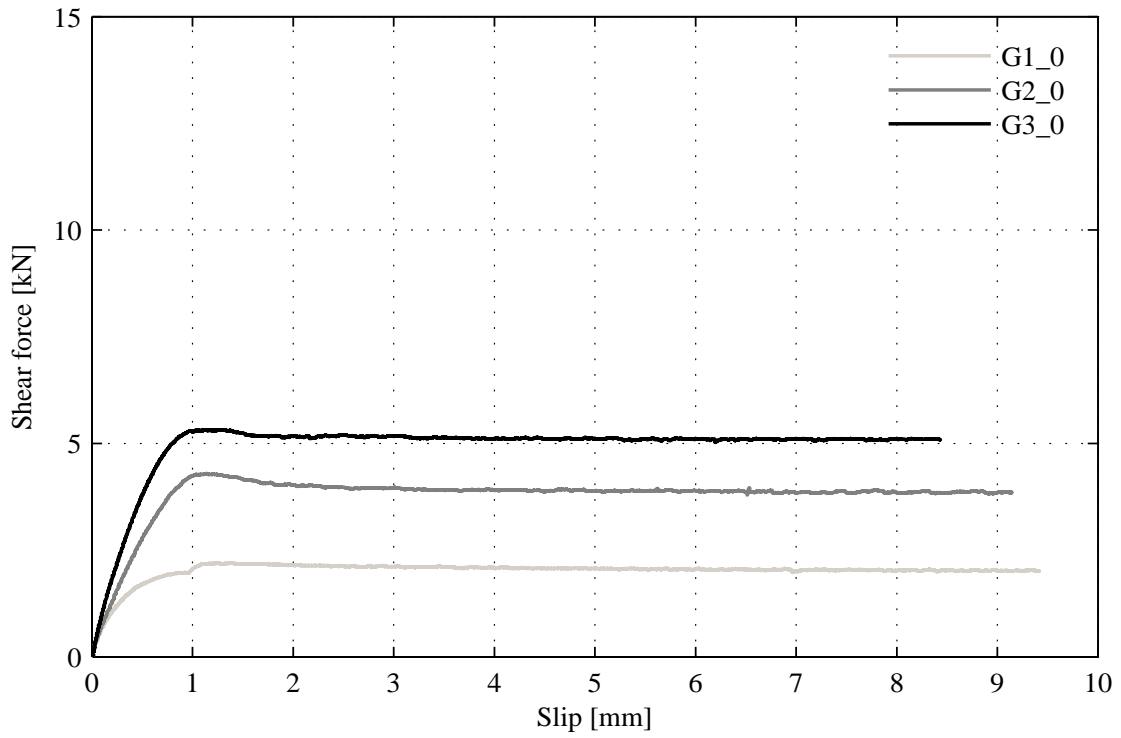
Figure A1-2. Shear force-slip relationships: Specimens G1_0, G2_0 and G3_0
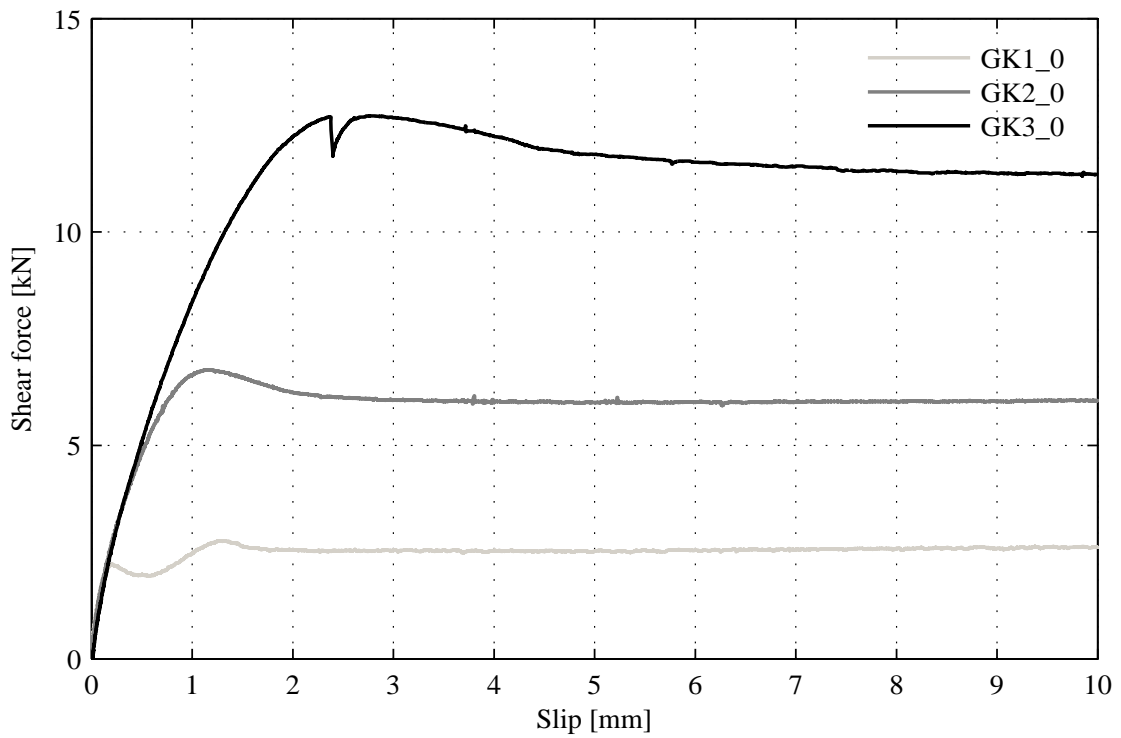
Figure A1-3. Shear force-slip relationships: Specimens GK1_0, GK2_0 and GK3_0

154
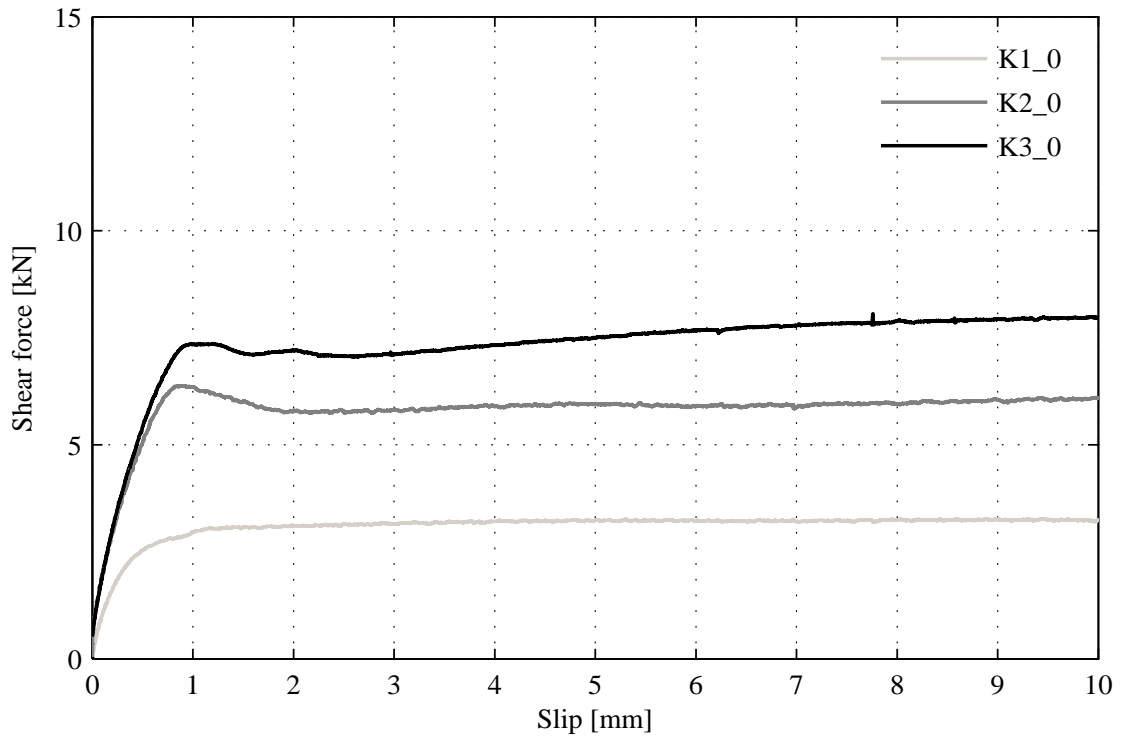
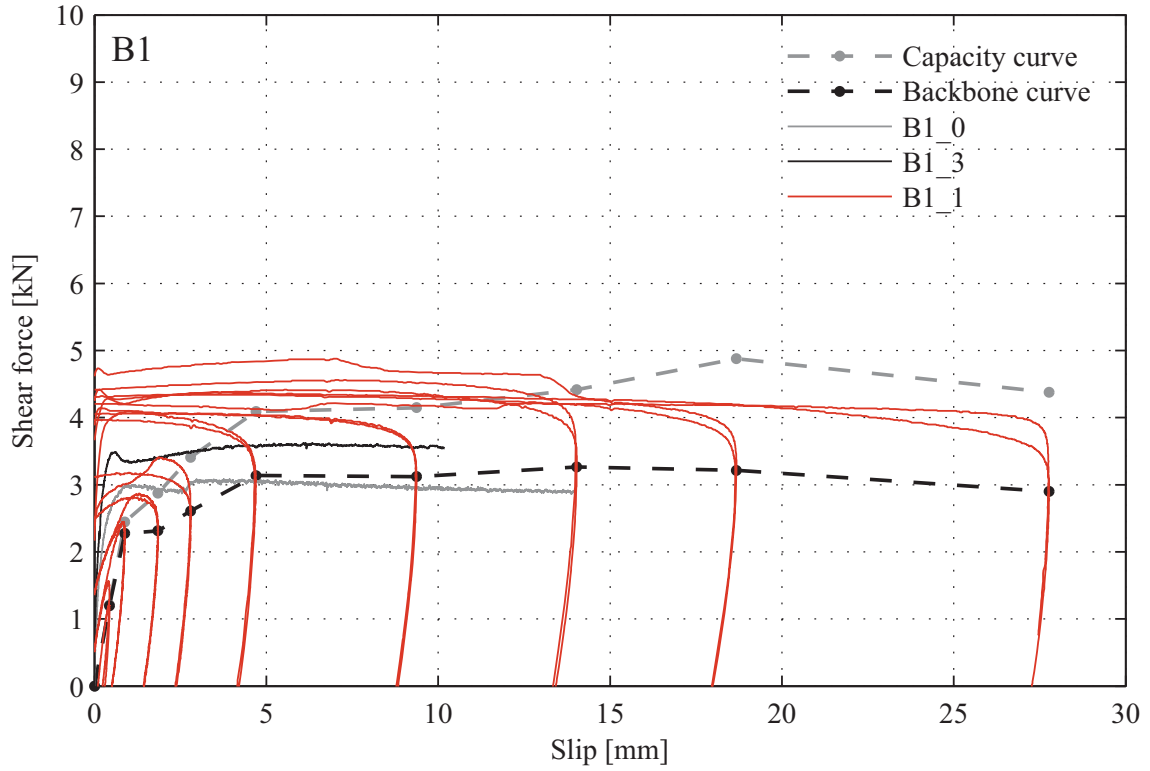**Figure A1-4. Shear force-slip relationships: Specimens K1_0, K2_0 and K3_0**
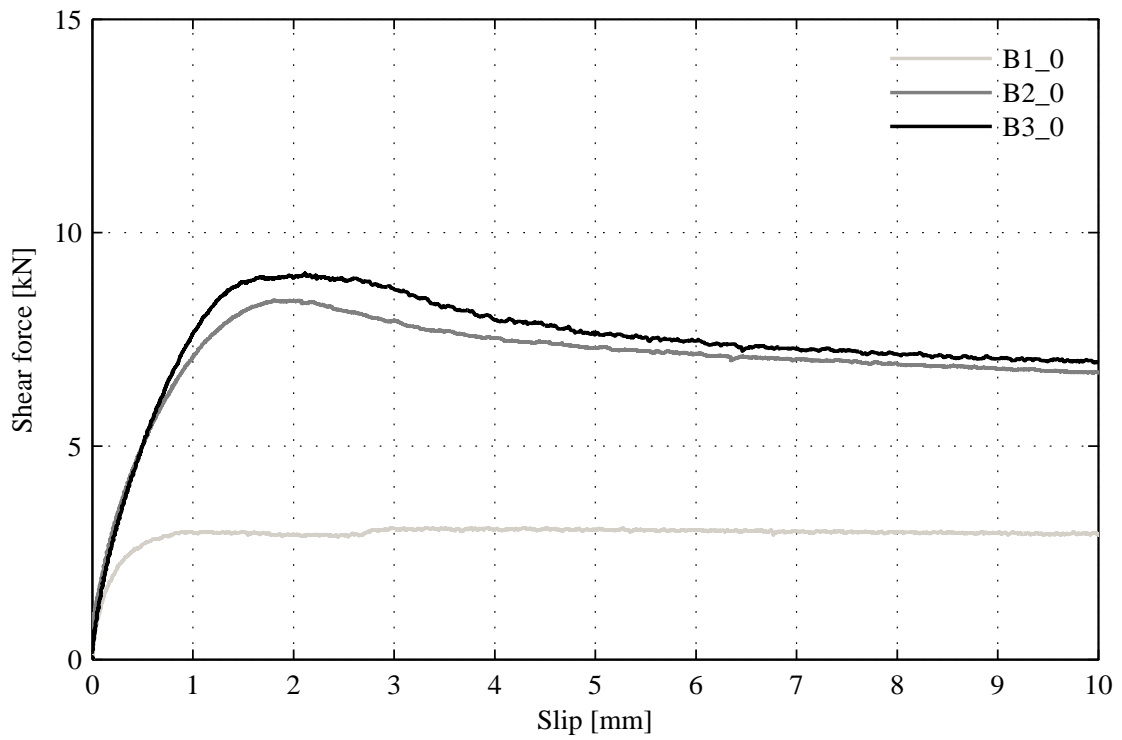
Figure A1-5. Shear force-slip relationships: Specimens B1_0, B2_0 and B3_0
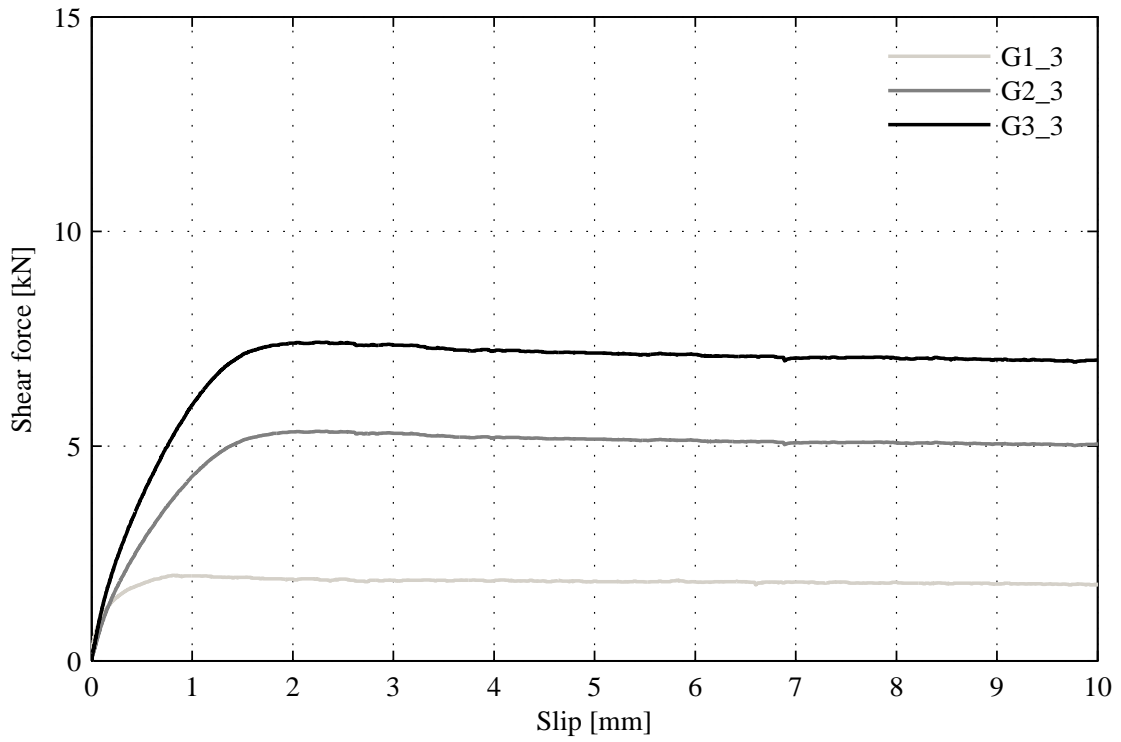
Figure A1-6. Shear force-slip relationships: Specimens G1_3, G2_3 and G3_3
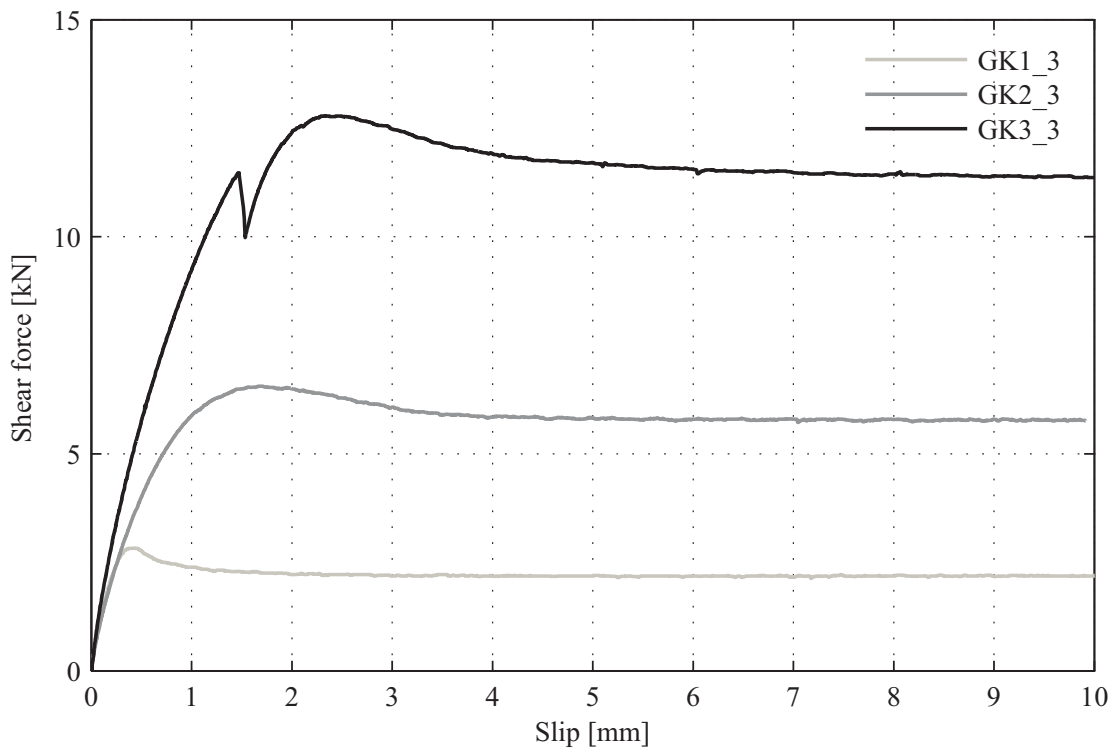
Figure A1-7. Shear force-slip relationships: Specimens GK1_3, GK2_3 and GK3_3
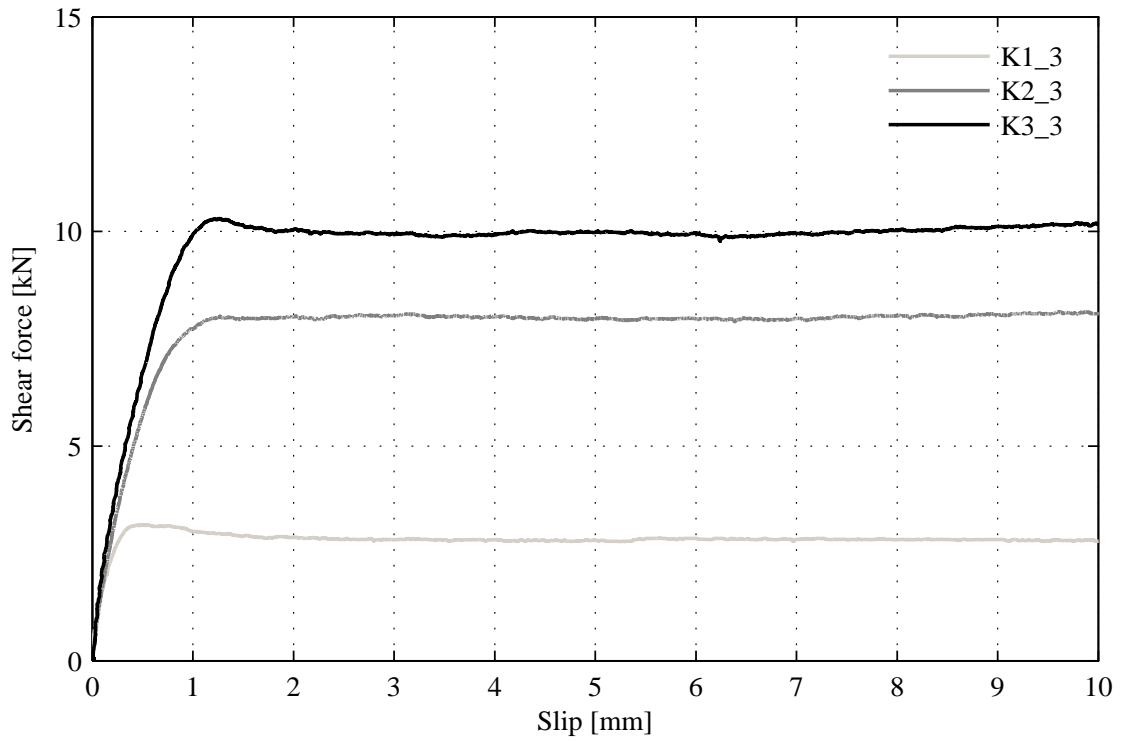
Figure A1-8. Shear force-slip relationships: Specimens K1_3, K2_3 and K3_3
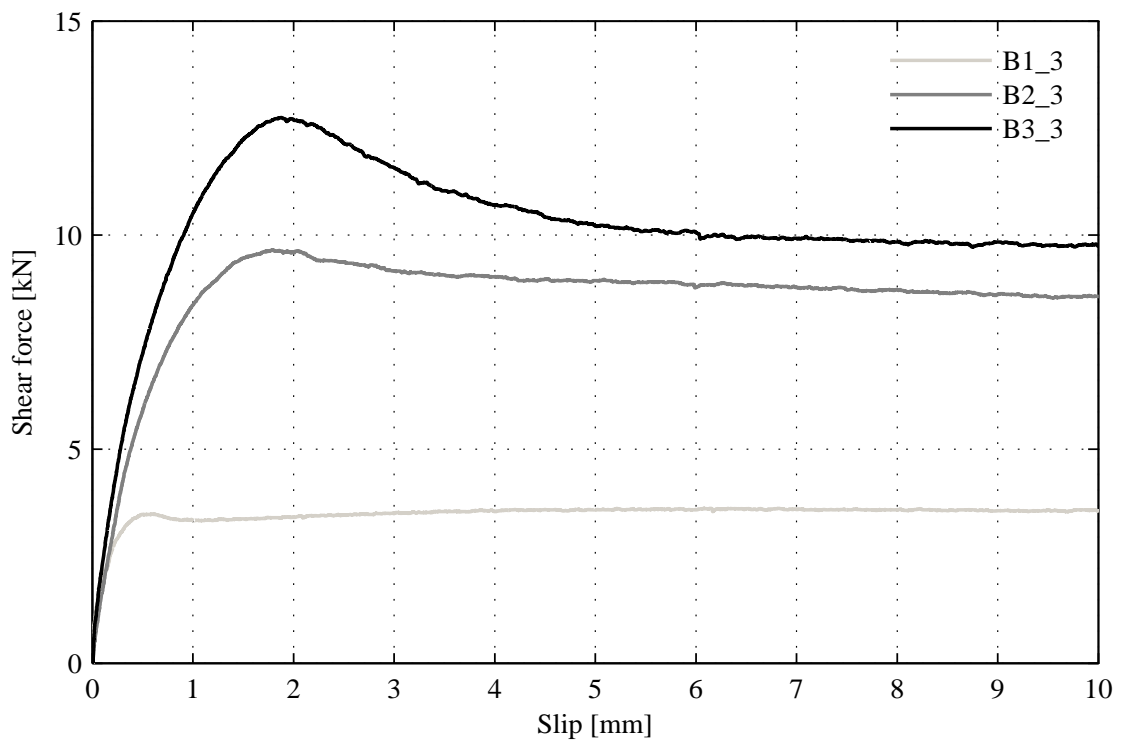
Figure A1-9. Shear force-slip relationships: Specimens B1_3, B2_3 and B3_3
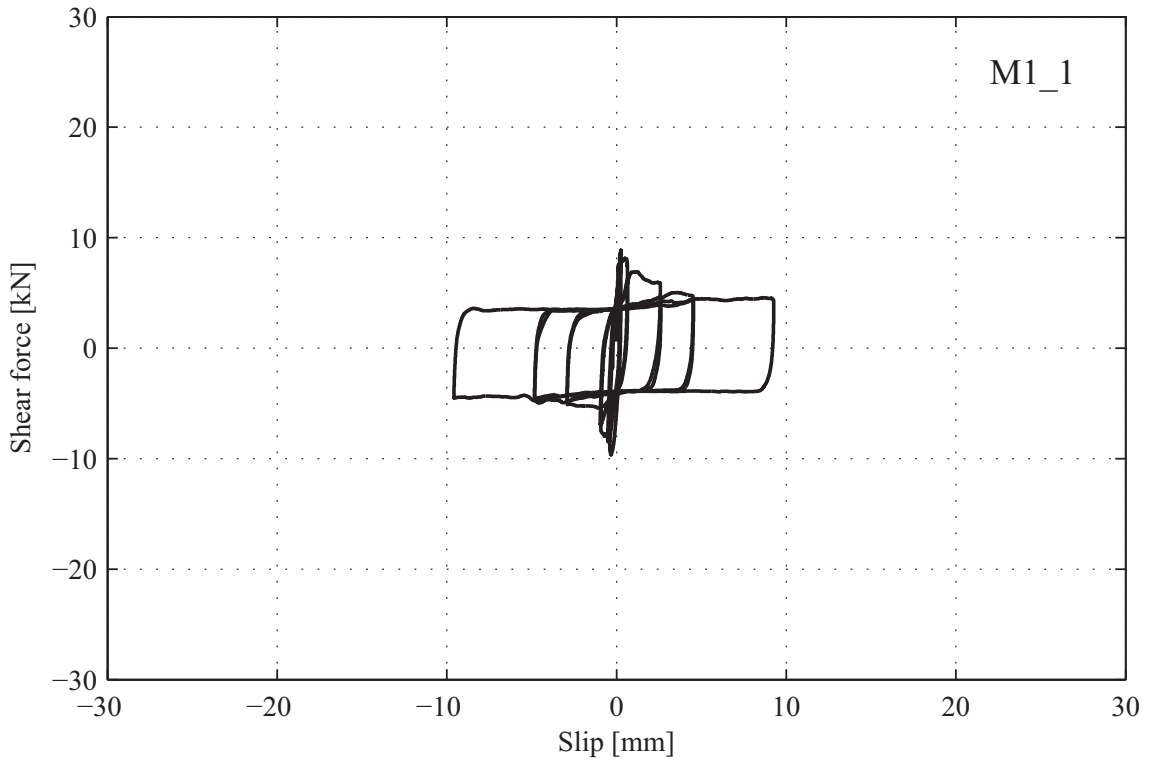
Figure A1-10. Shear force-slip relationship: Specimen M1_1
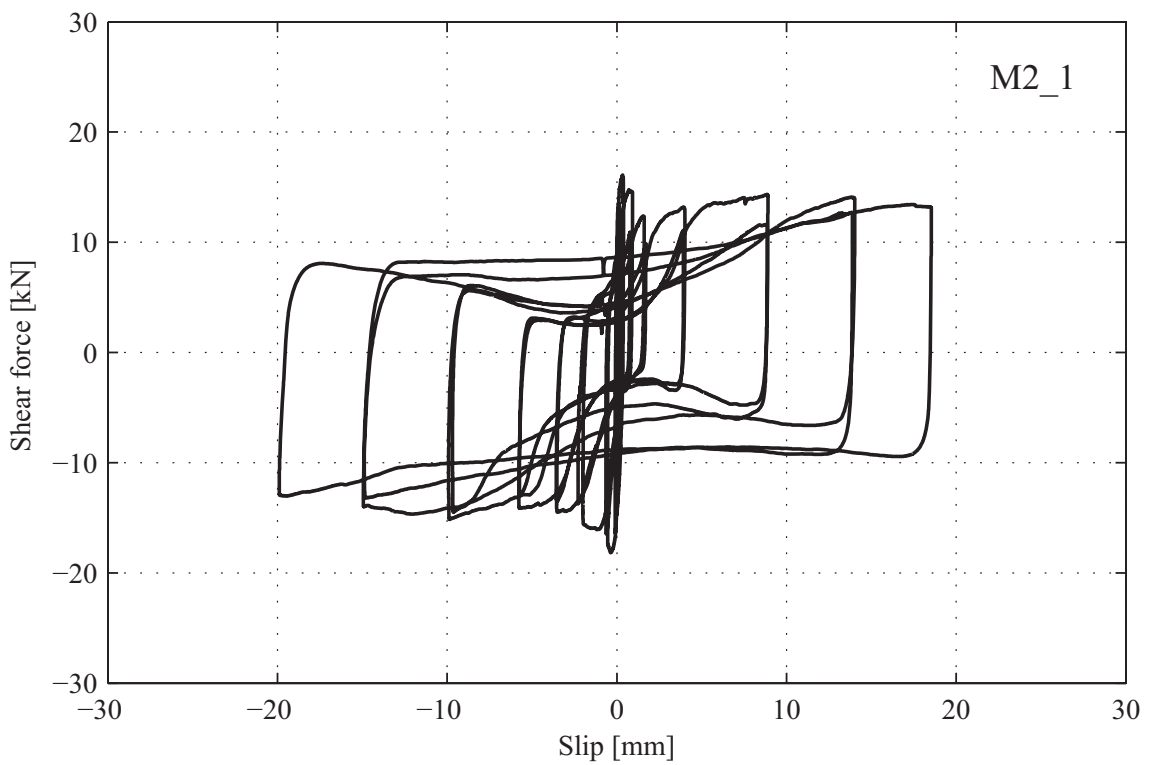
Figure A1-11. Shear force-slip relationship: Specimen M1_2

158
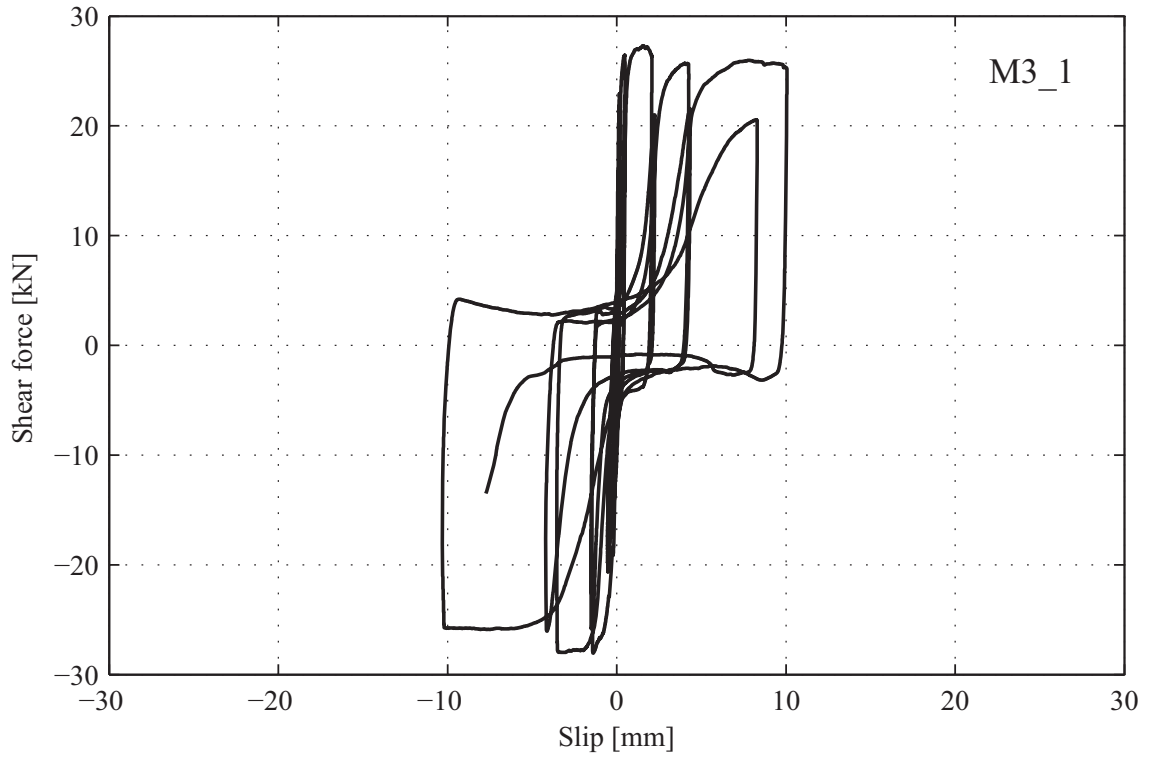
Figure A1-12. Shear force-slip relationship: Specimen M3_1
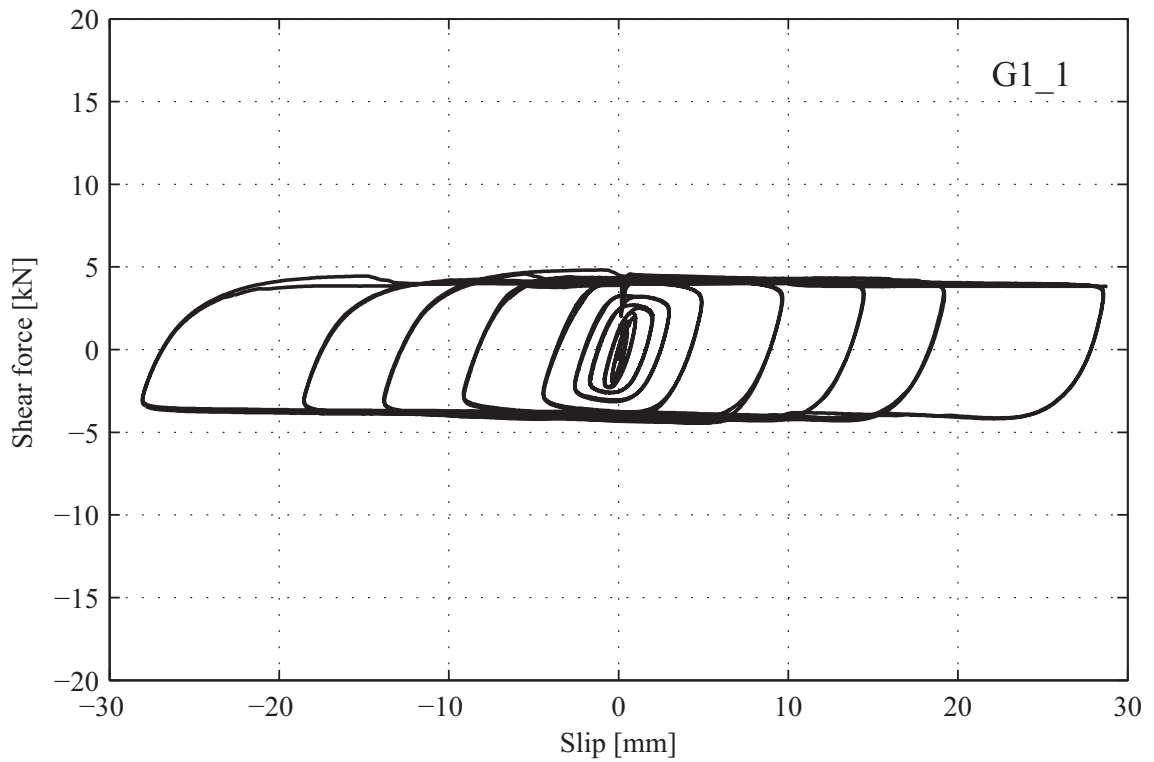
Figure A1-13. Shear force-slip relationship: Specimen G1_1
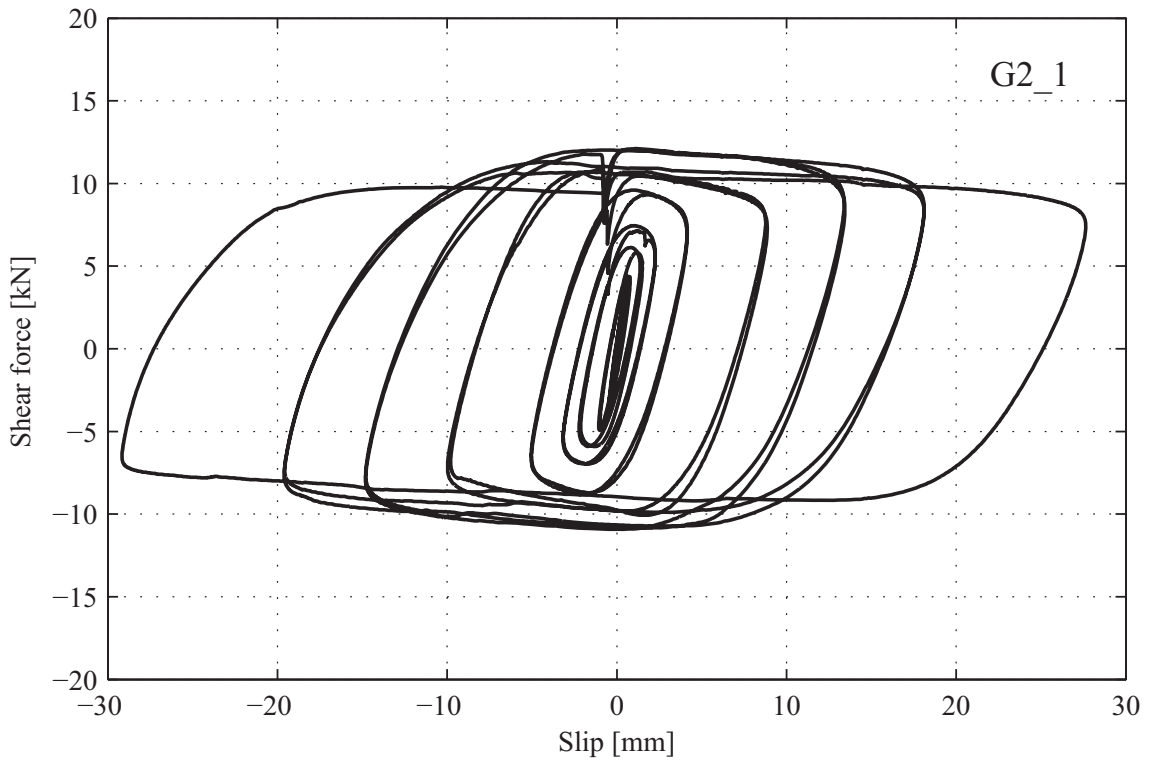
Figure A1-14. Shear force-slip relationship: Specimen G2_1
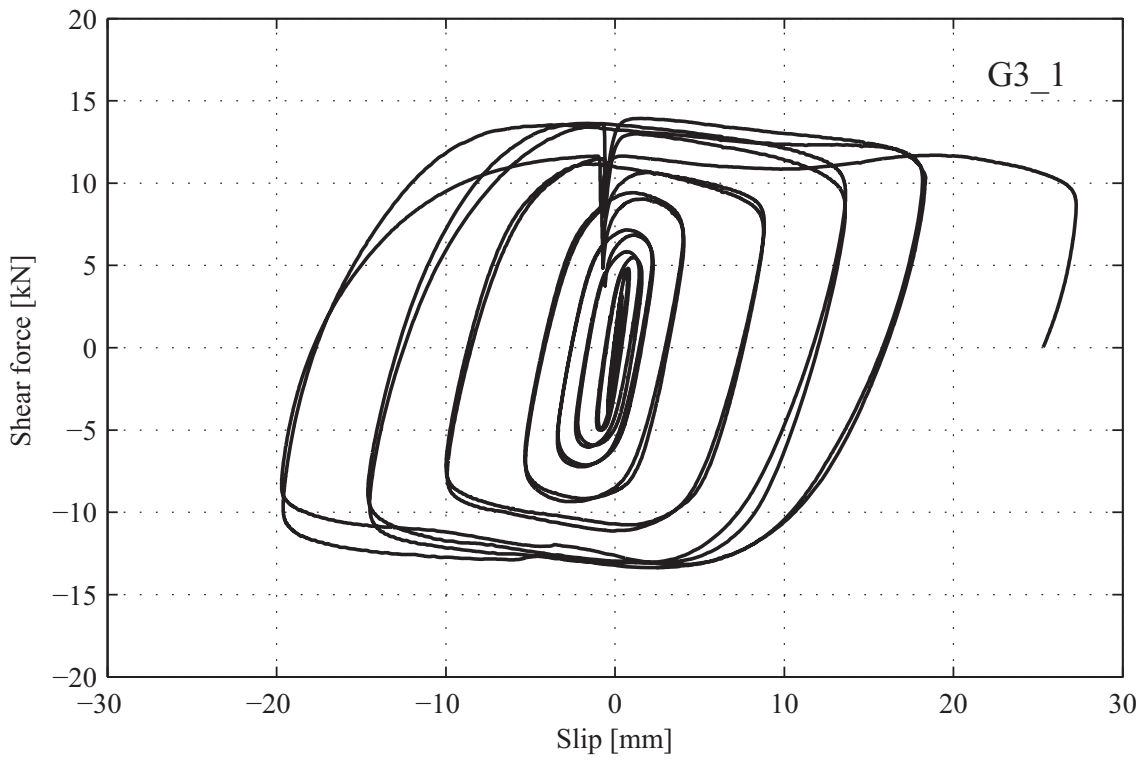
Figure A1-15. Shear force-slip relationship: Specimen G3_1

160
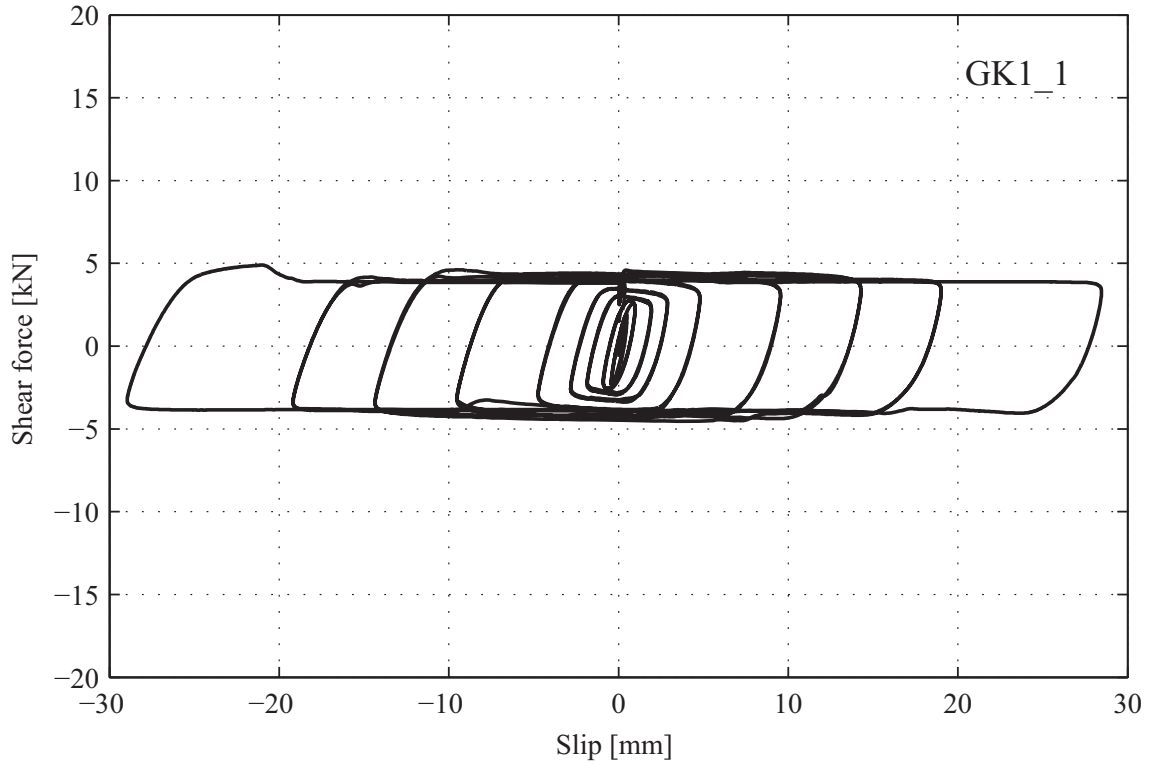
Figure A1-16. Shear force-slip relationship: Specimen GK1_1
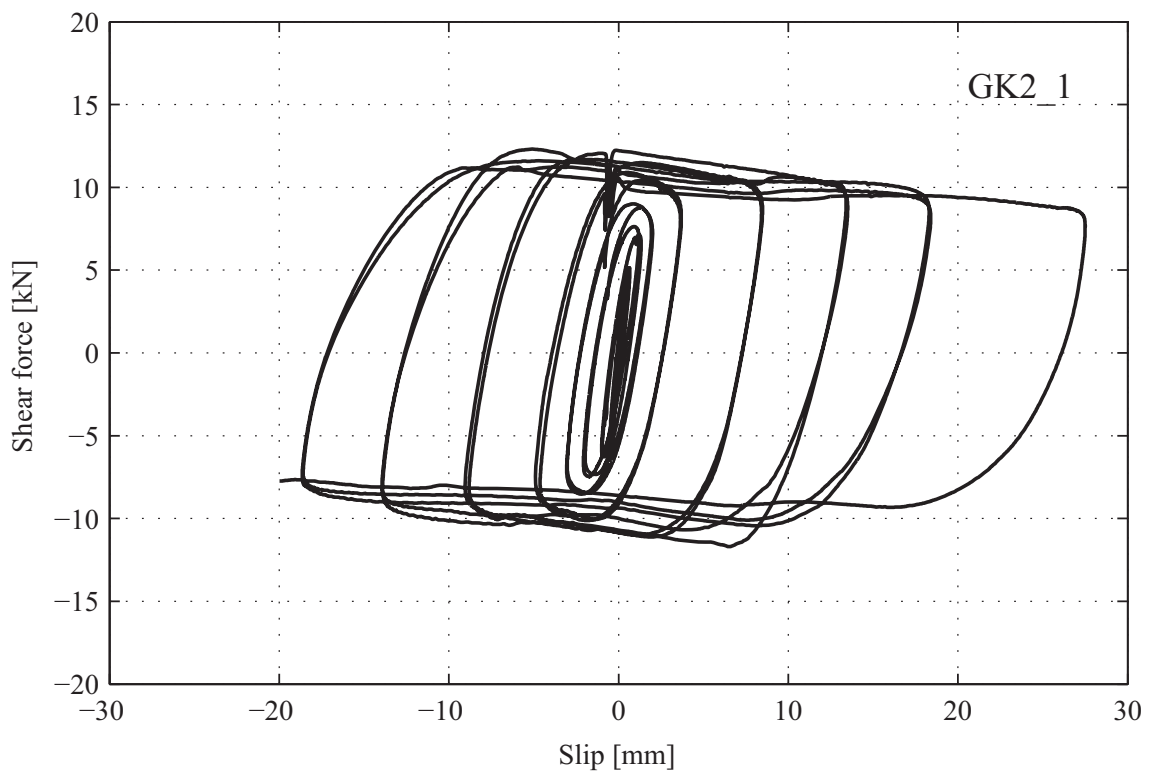
Figure A1-17. Shear force-slip relationship: Specimen GK2_1
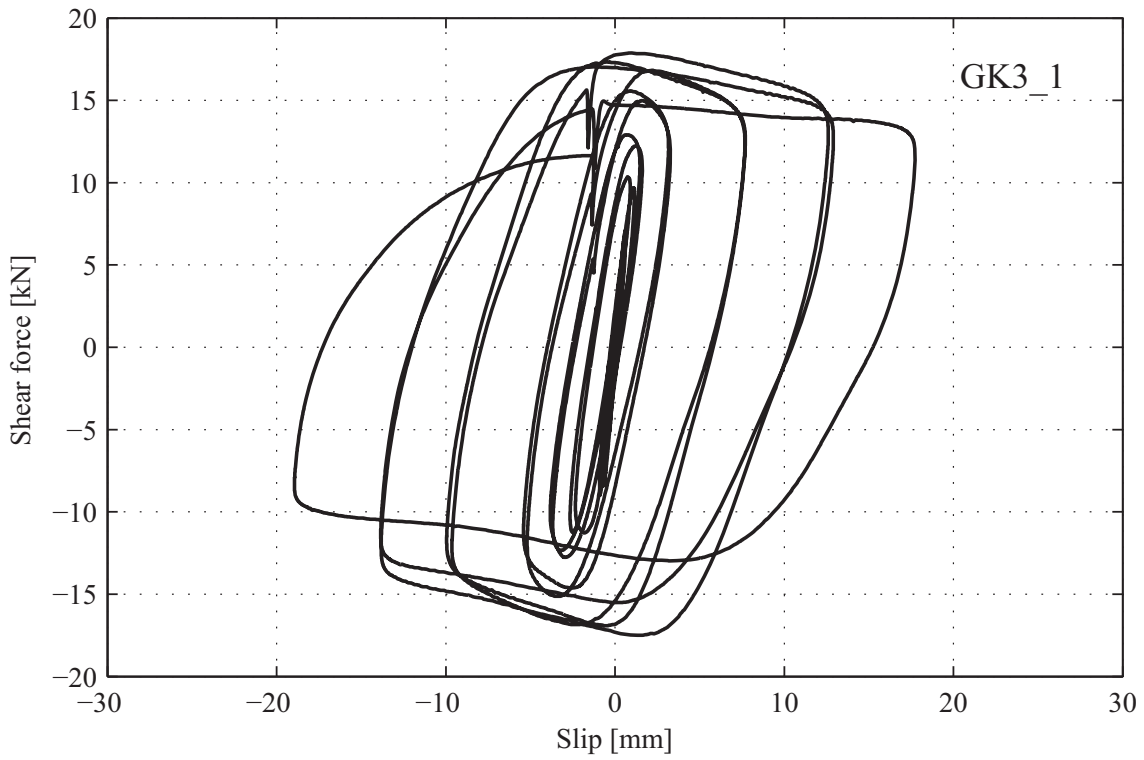
Figure A1-18. Shear force-slip relationship: Specimen GK3_1
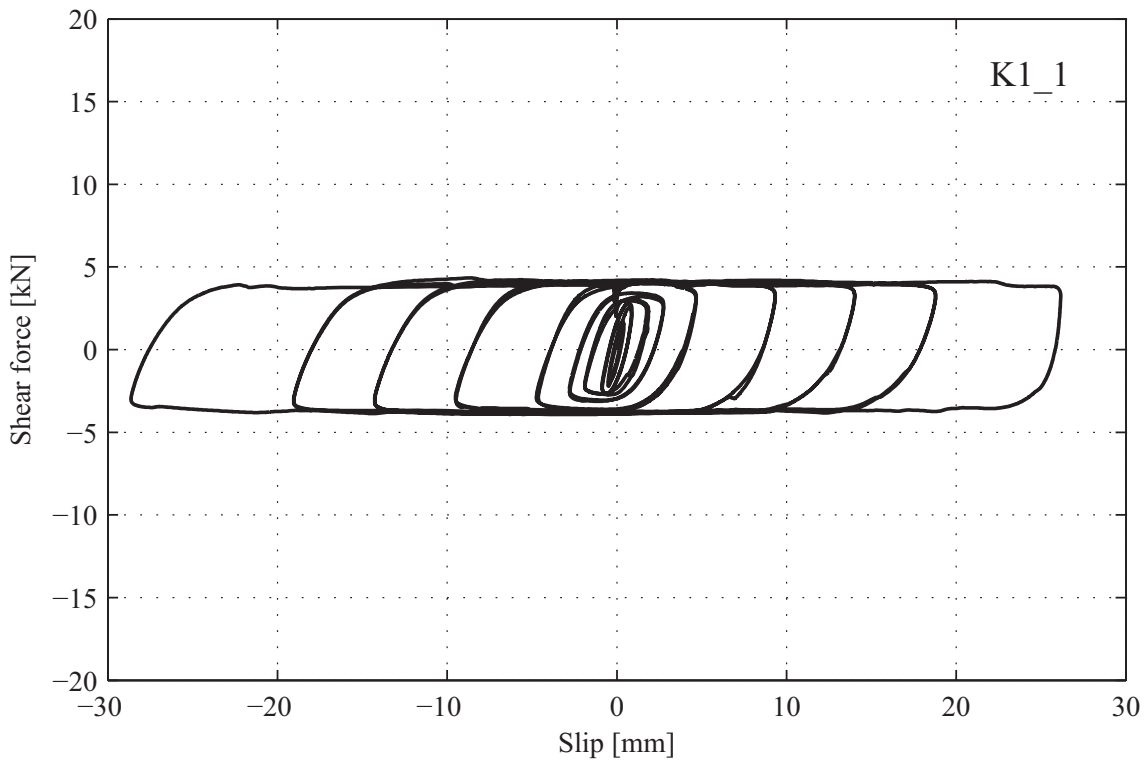
Figure A1-19. Shear force-slip relationship: Specimen K1_1

162
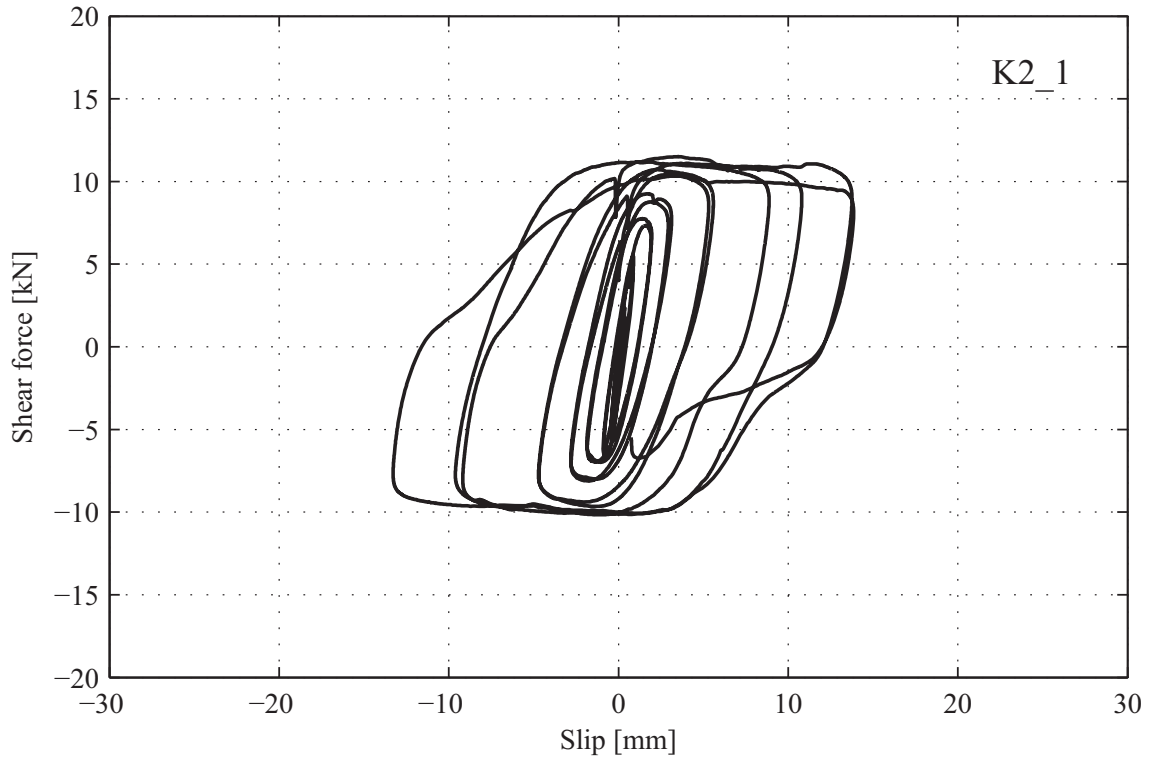
Figure A1-20. Shear force-slip relationship: Specimen K2_1
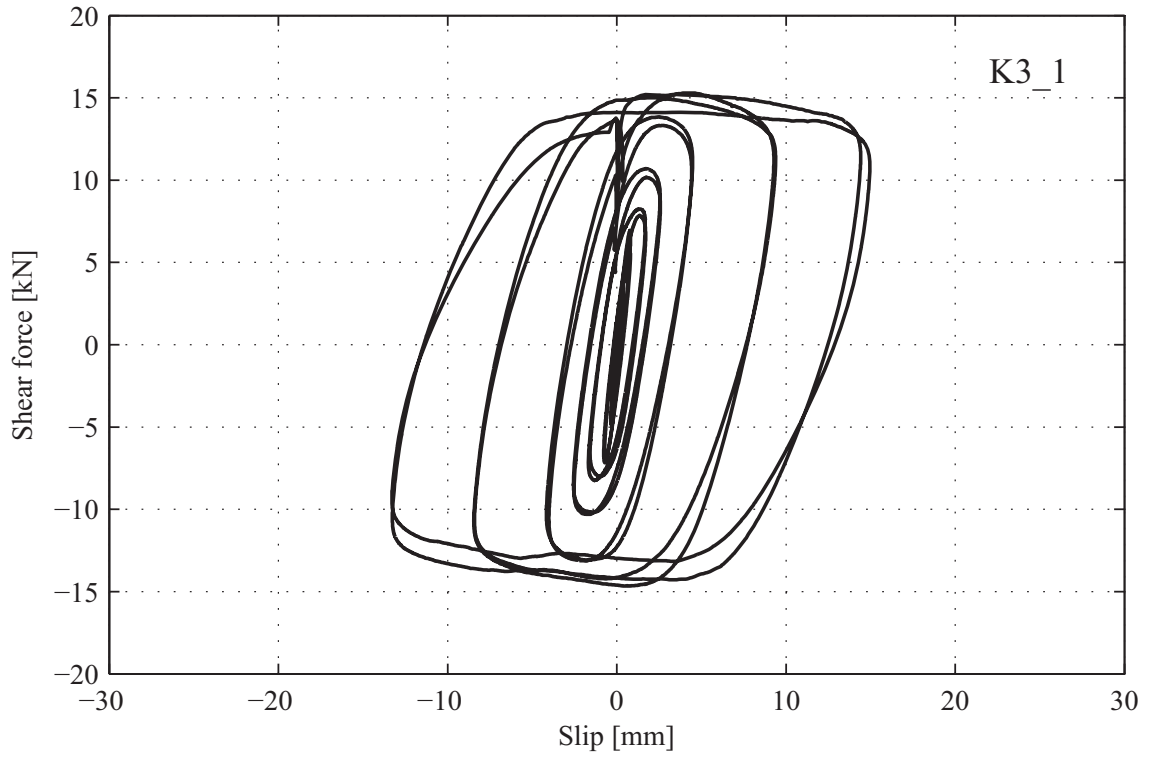
Figure A1-21. Shear force-slip relationship: Specimen K3_1
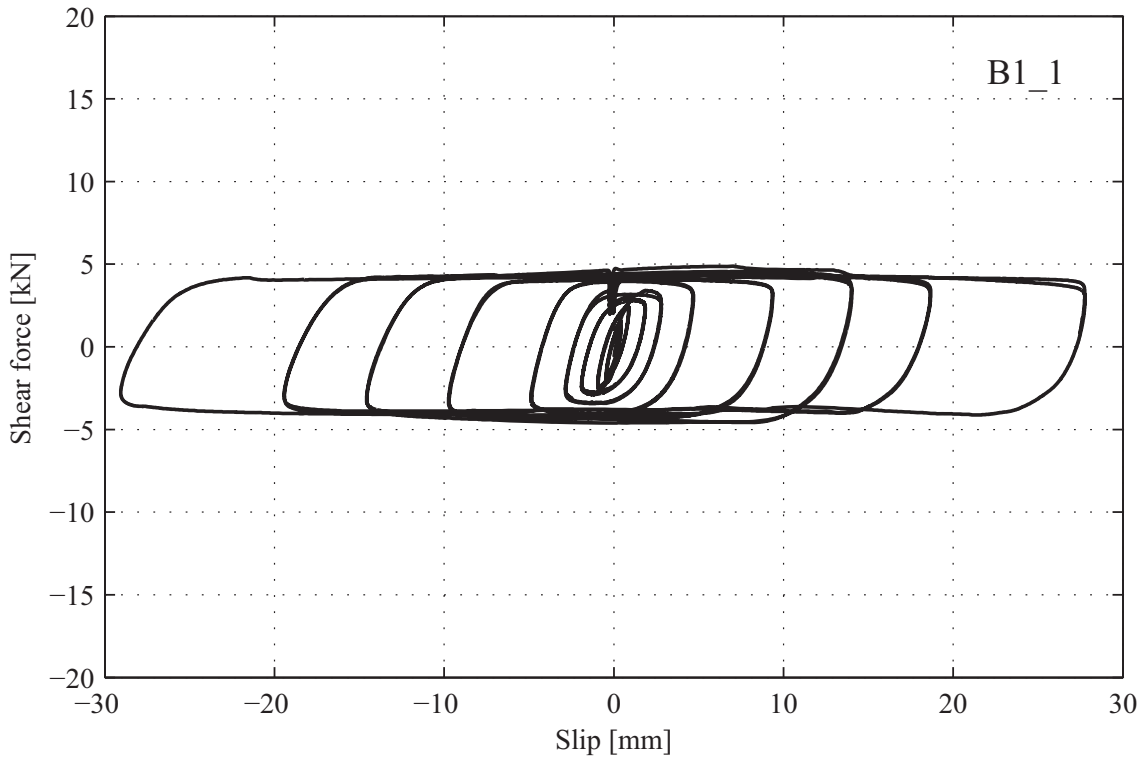
Figure A1-22. Shear force-slip relationship: Specimen B1_1
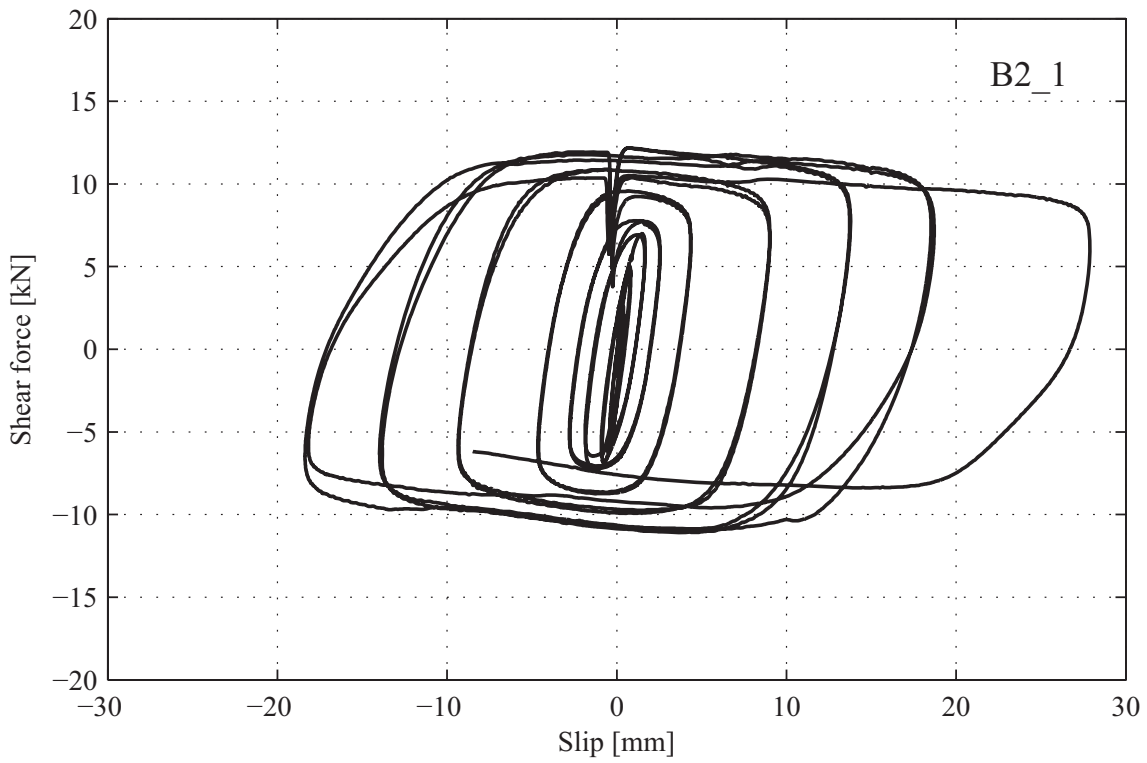
Figure A1-23. Shear force-slip relationship: Specimen B2_1

164
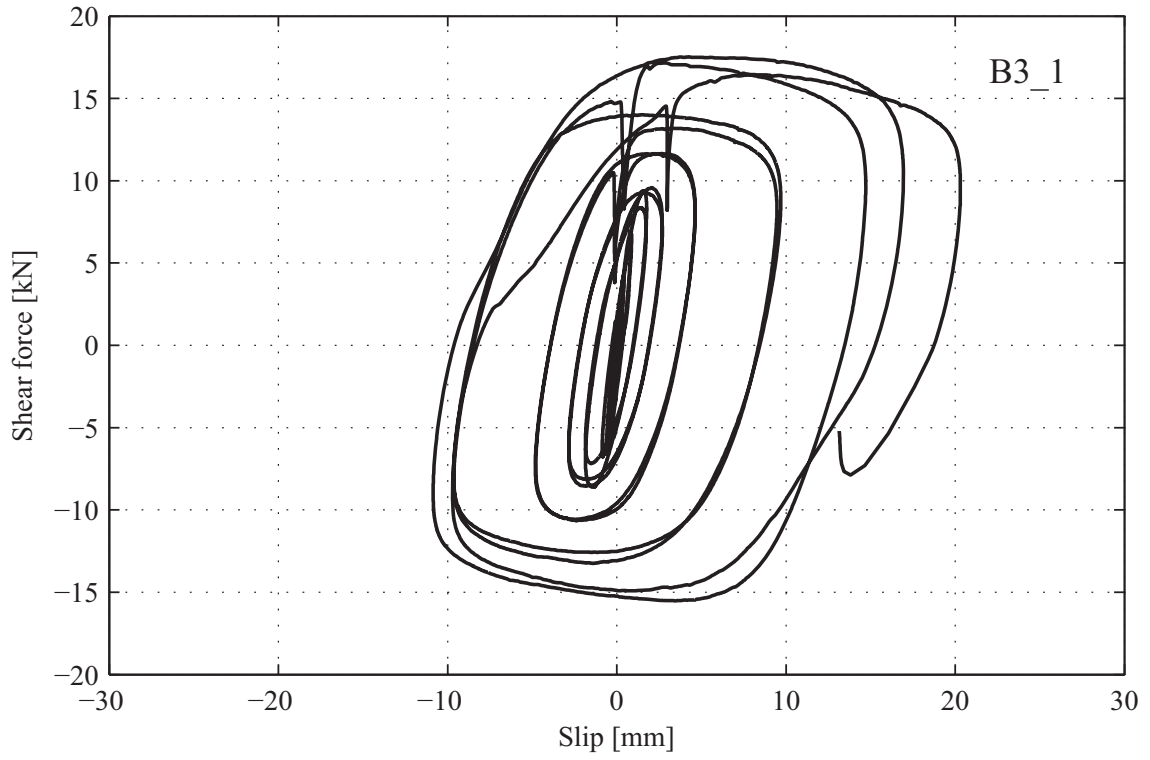
Figure A1-24. Shear force-slip relationship: Specimen B3_1
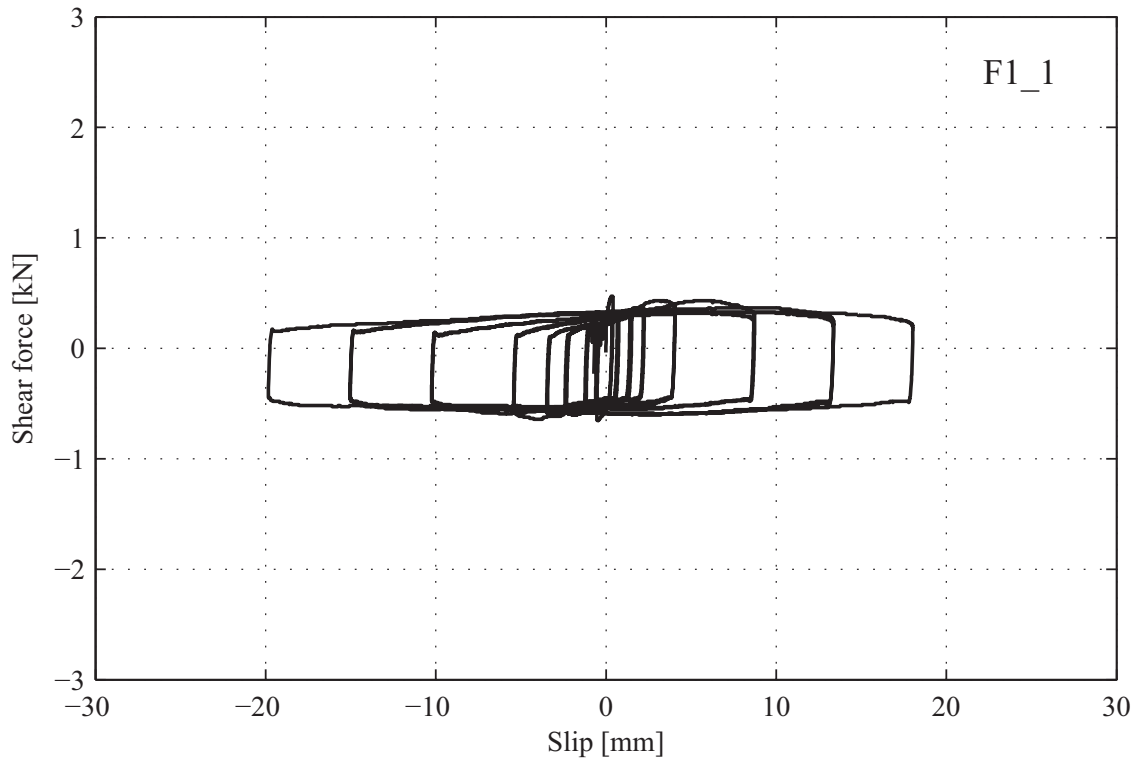
Figure A1-25. Shear force-slip relationship: Specimen F1_1
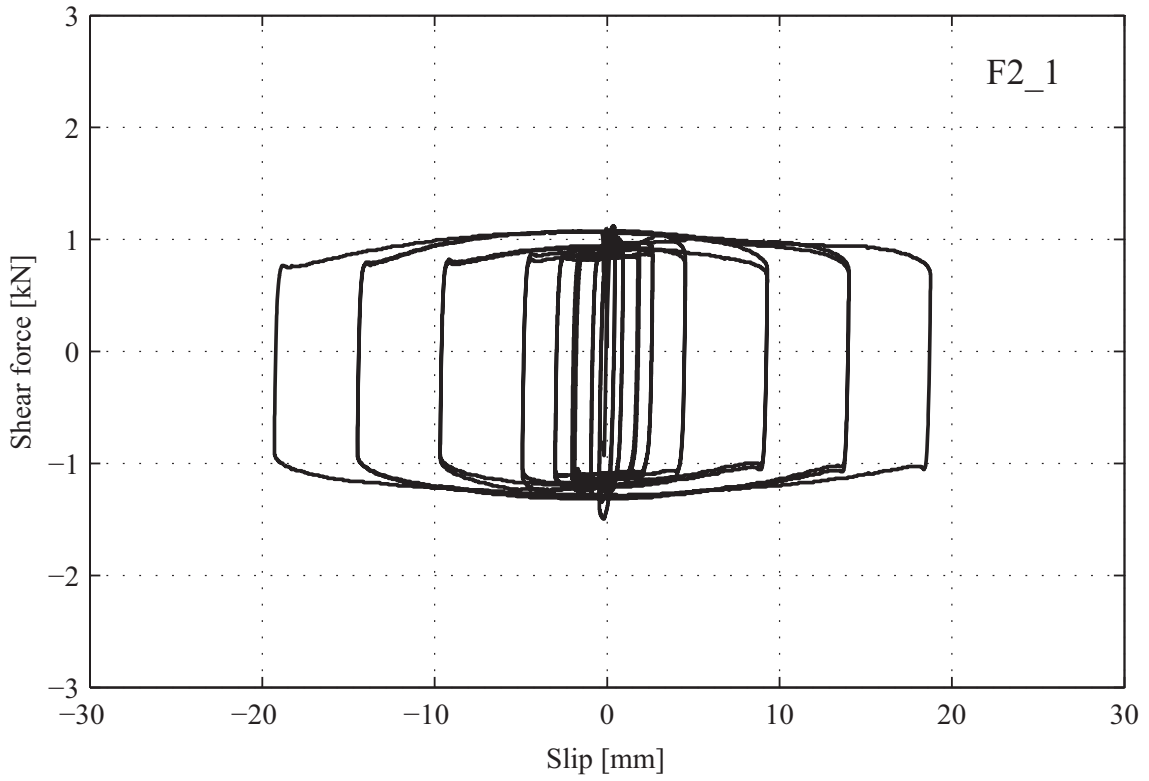
Figure A1-26. Shear force-slip relationship: Specimen F2_1
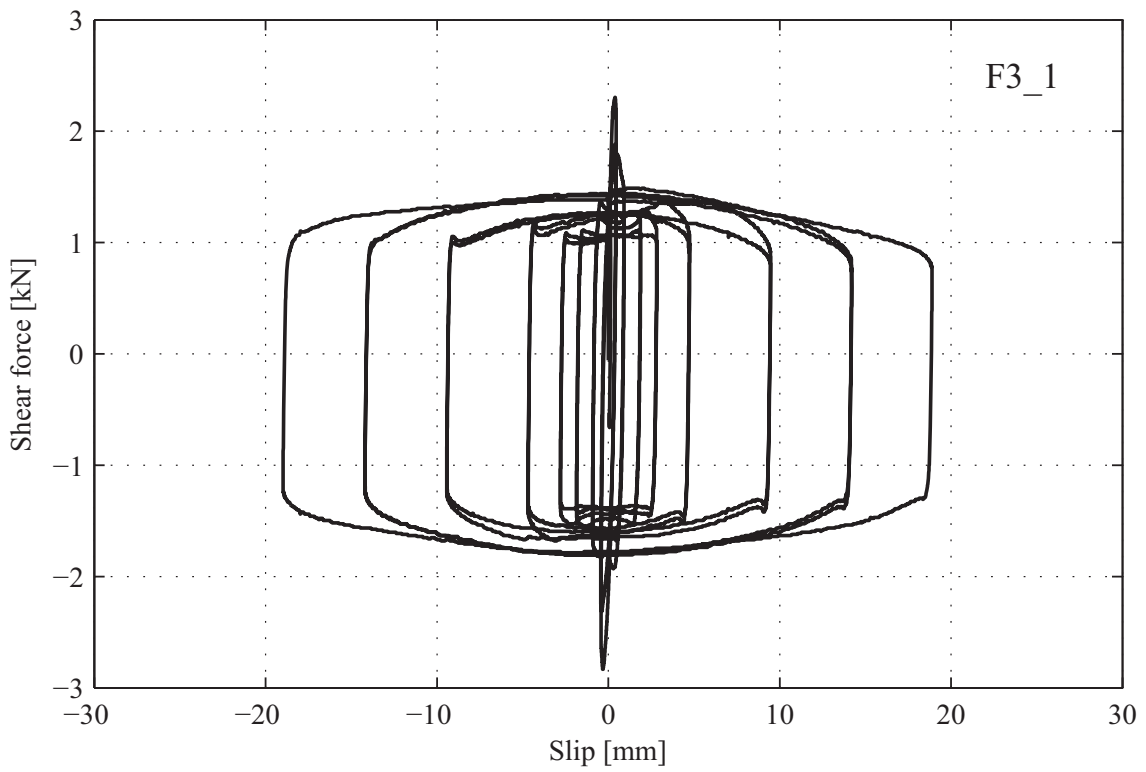
Figure A1-27. Shear force-slip relationship: Specimen F3_1

166
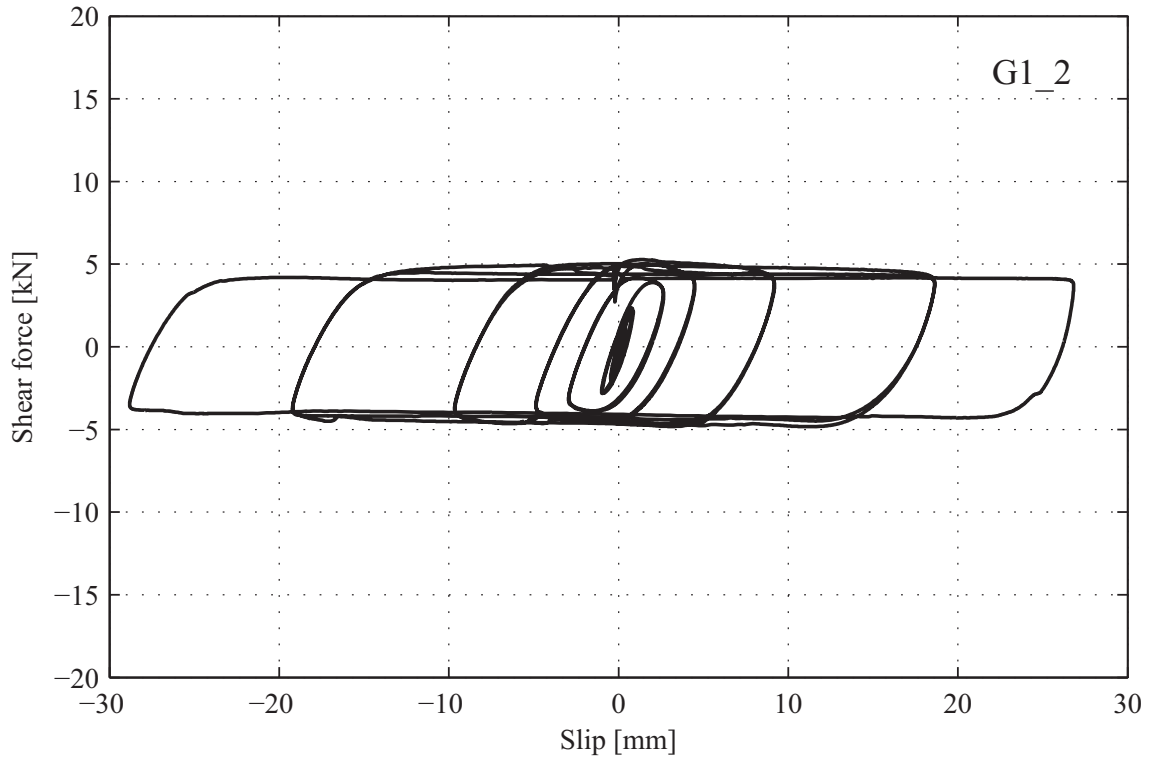
Figure A1-28. Shear force-slip relationship: Specimen G1_2
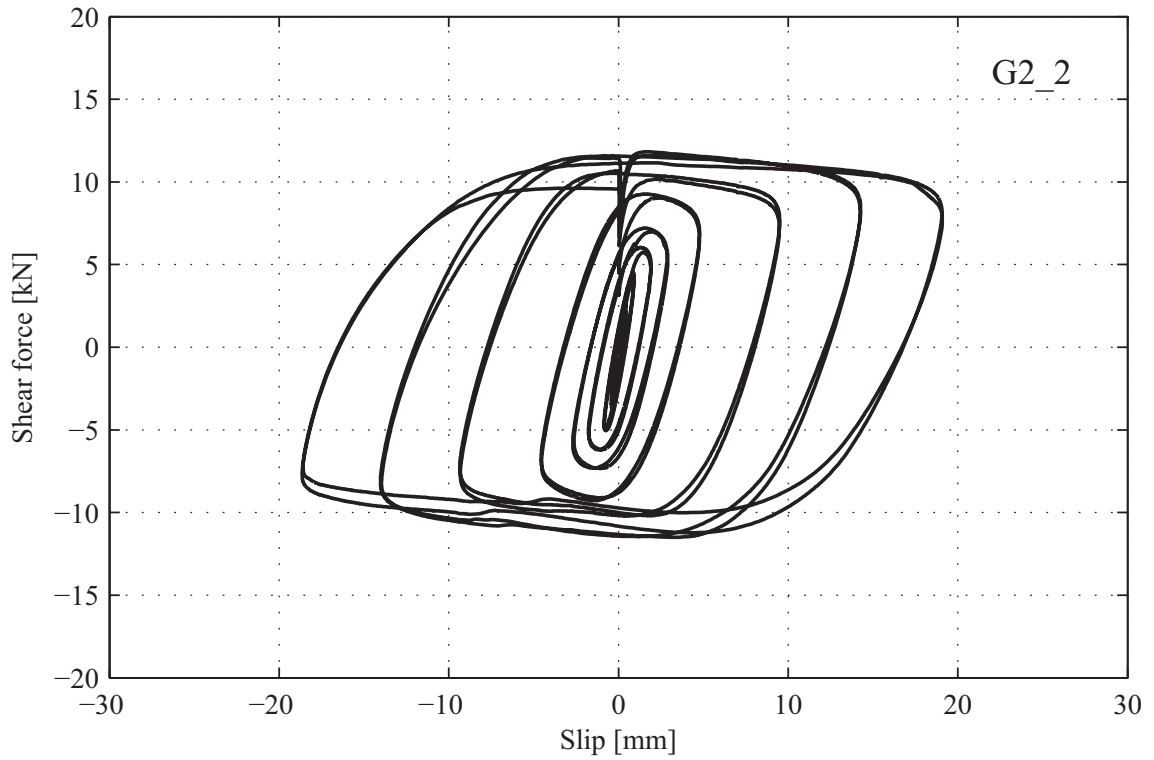
Figure A1-29. Shear force-slip relationship: Specimen G2_2
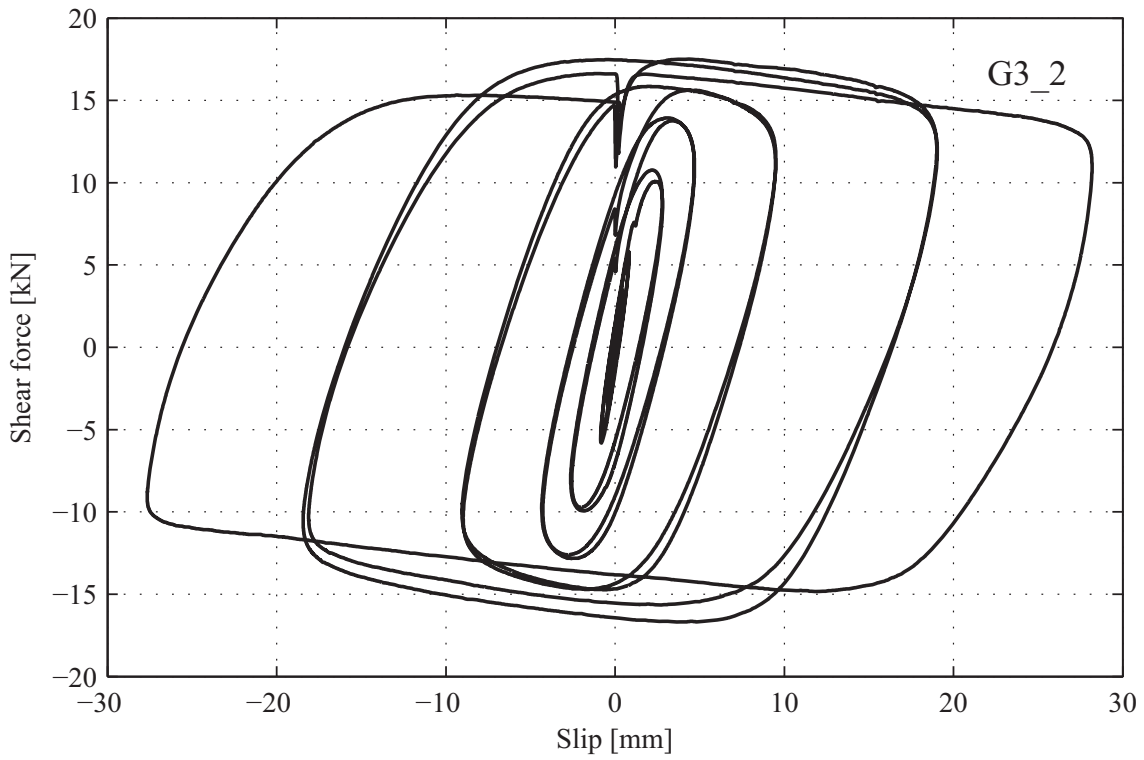
Figure A1-30. Shear force-slip relationship: Specimen G3_2
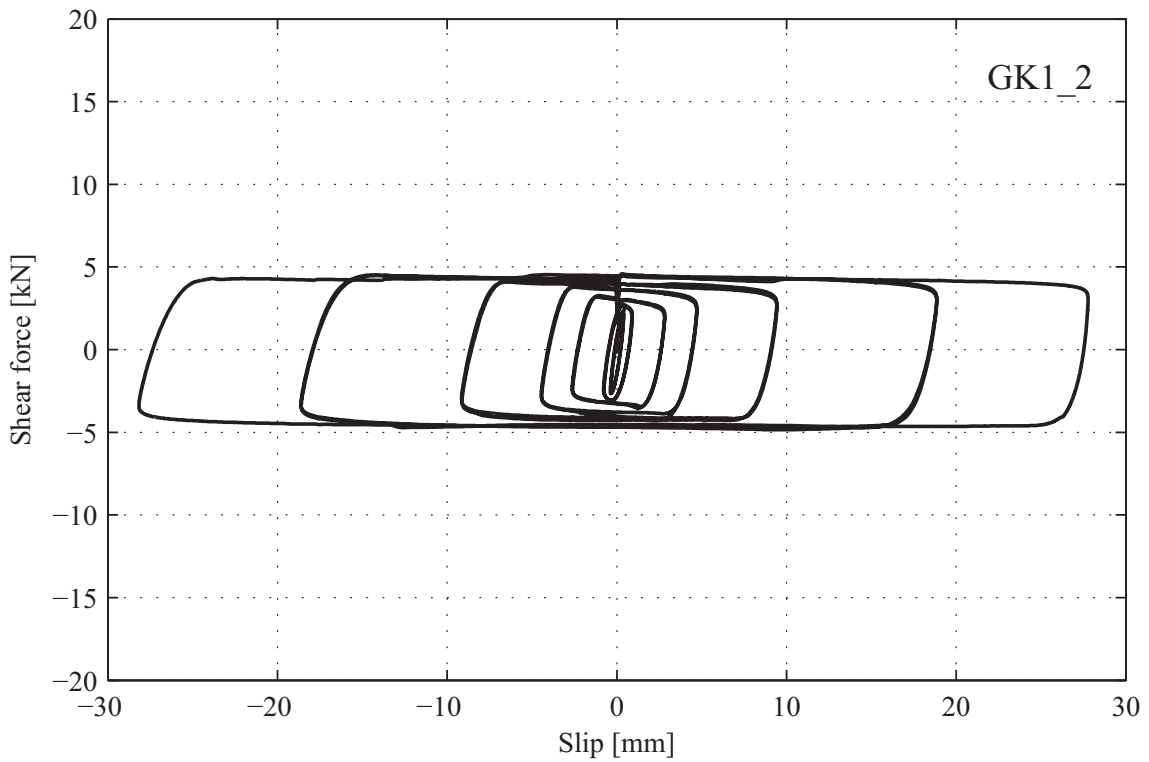
Figure A1-31. Shear force-slip relationship: Specimen GK1_2

168
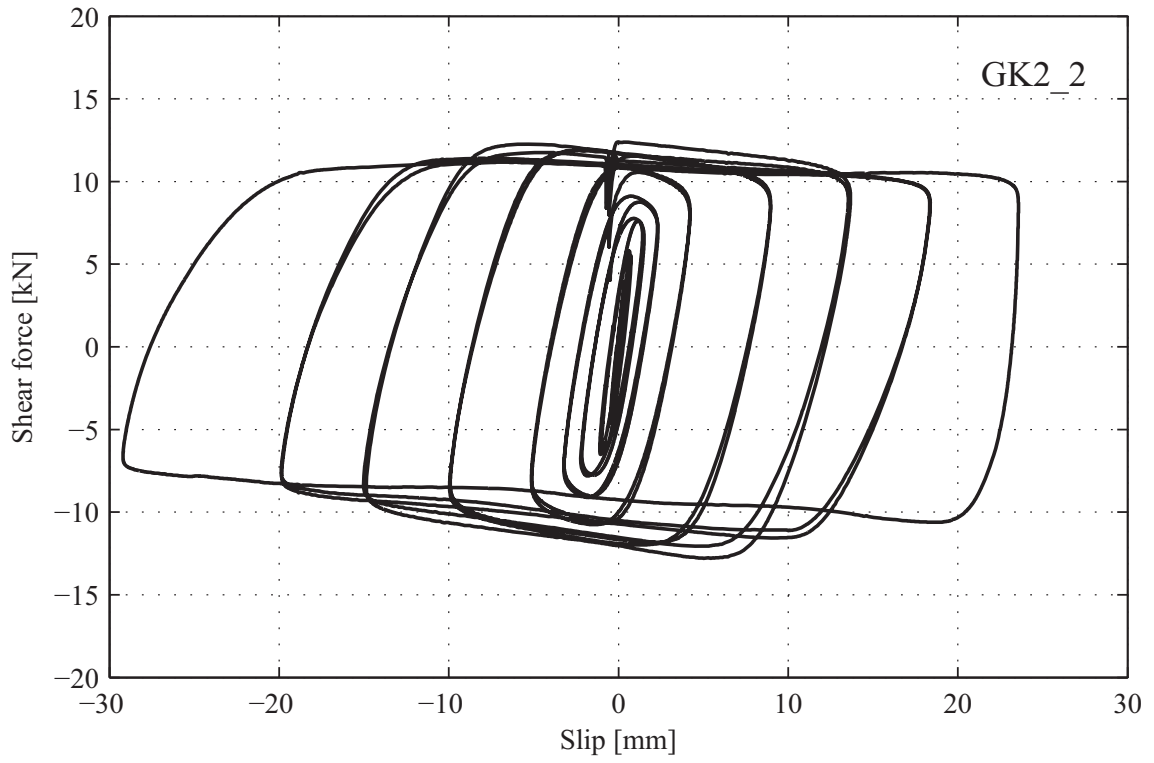
Figure A1-32. Shear force-slip relationship: Specimen GK2_2
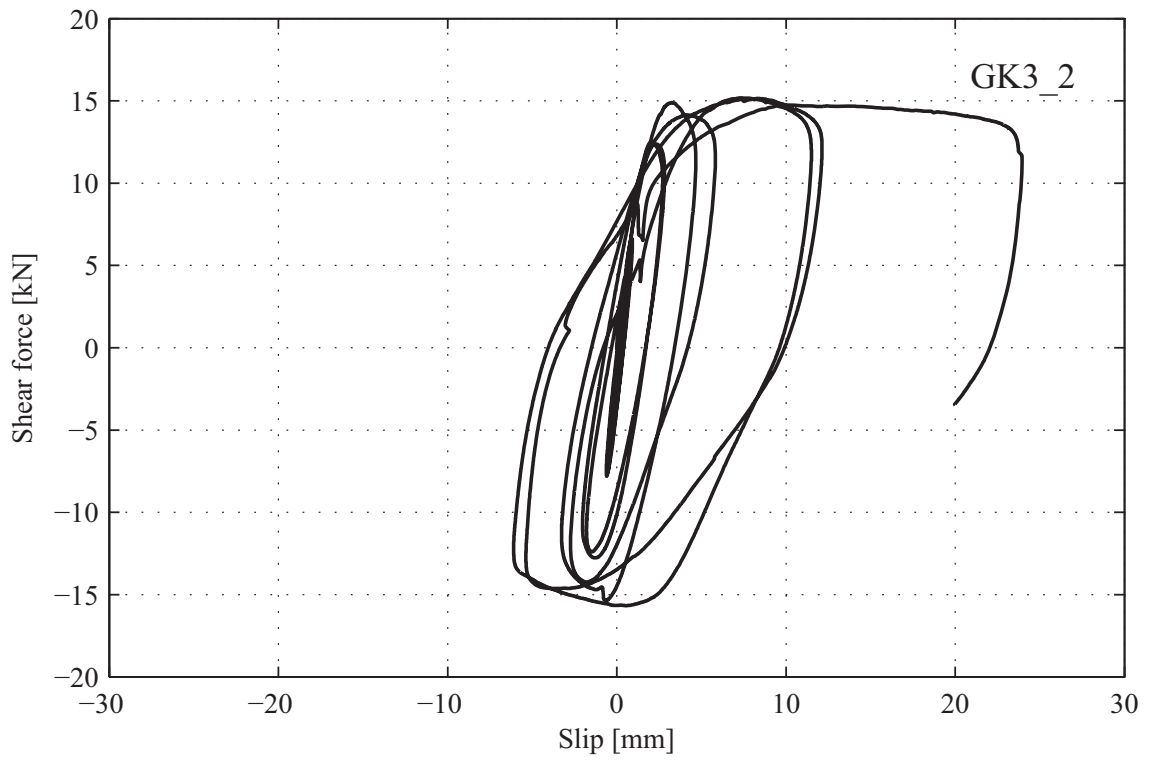
Figure A1-33. Shear force-slip relationship: Specimen GK3_2
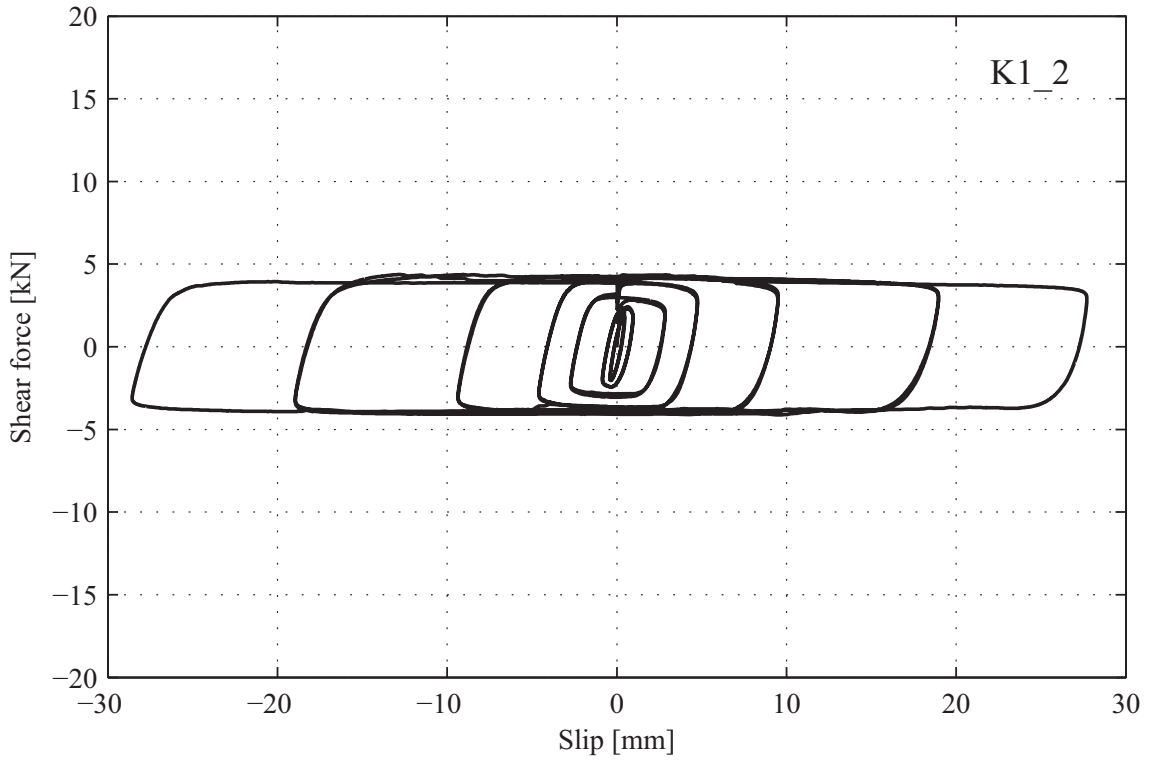
Figure A1-34. Shear force-slip relationship: Specimen K1_2
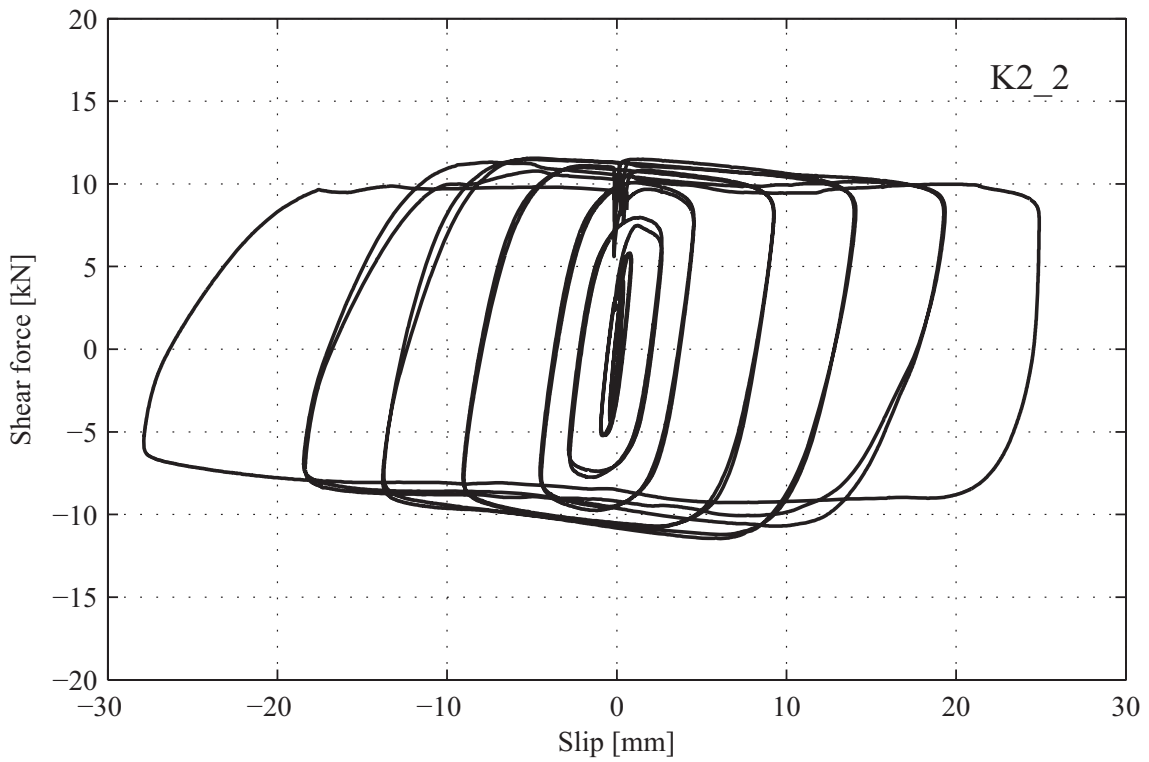
Figure A1-35. Shear force-slip relationship: Specimen K2_2

170
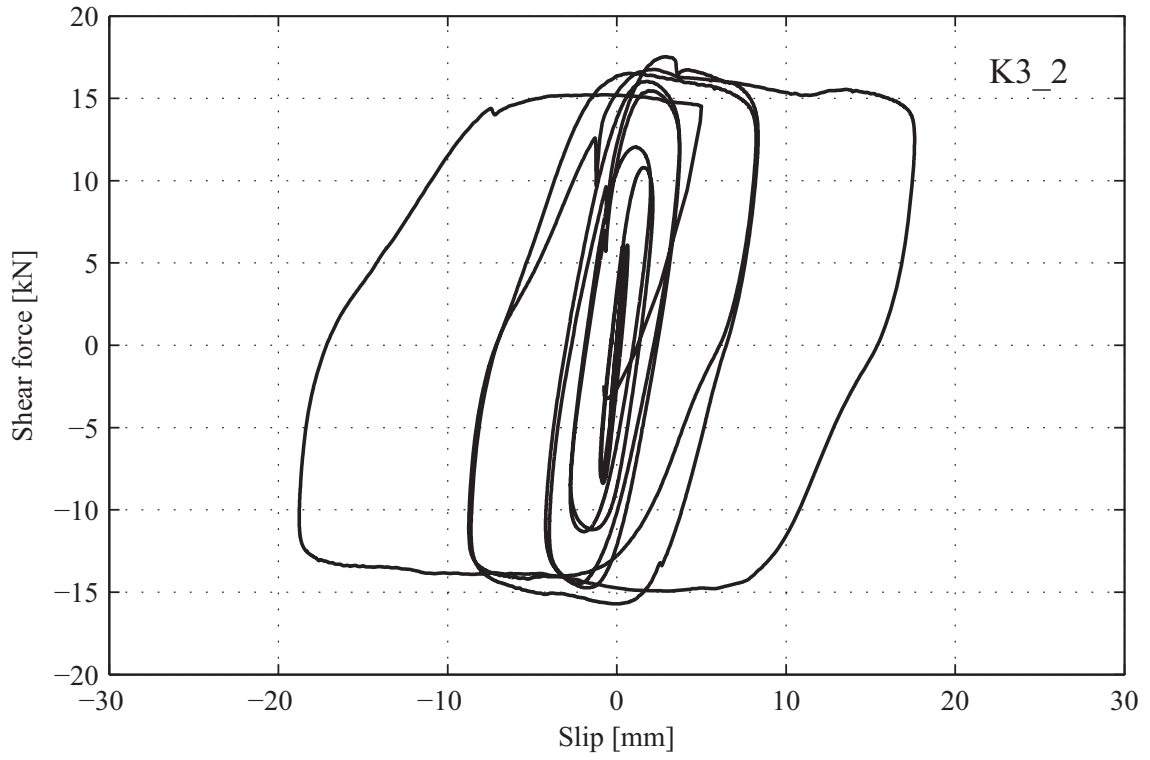
Figure A1-36. Shear force-slip relationship: Specimen K3_2
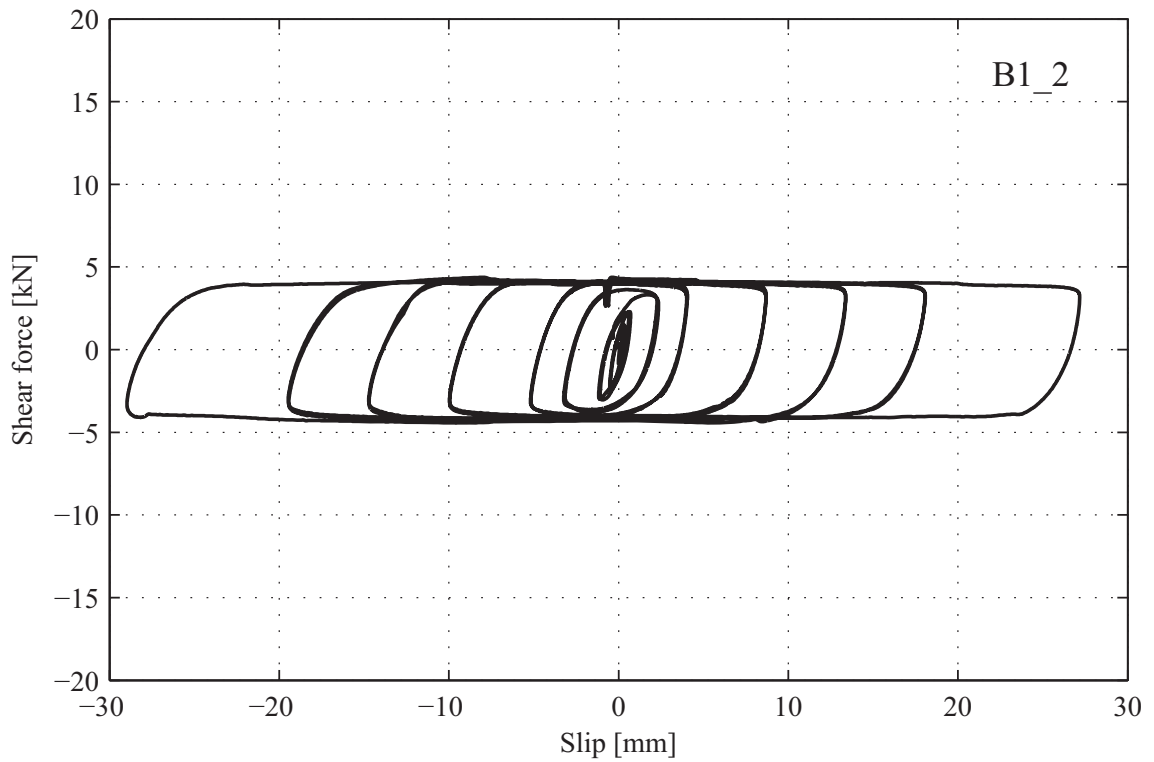
Figure A1-37. Shear force-slip relationship: Specimen B1_2

171
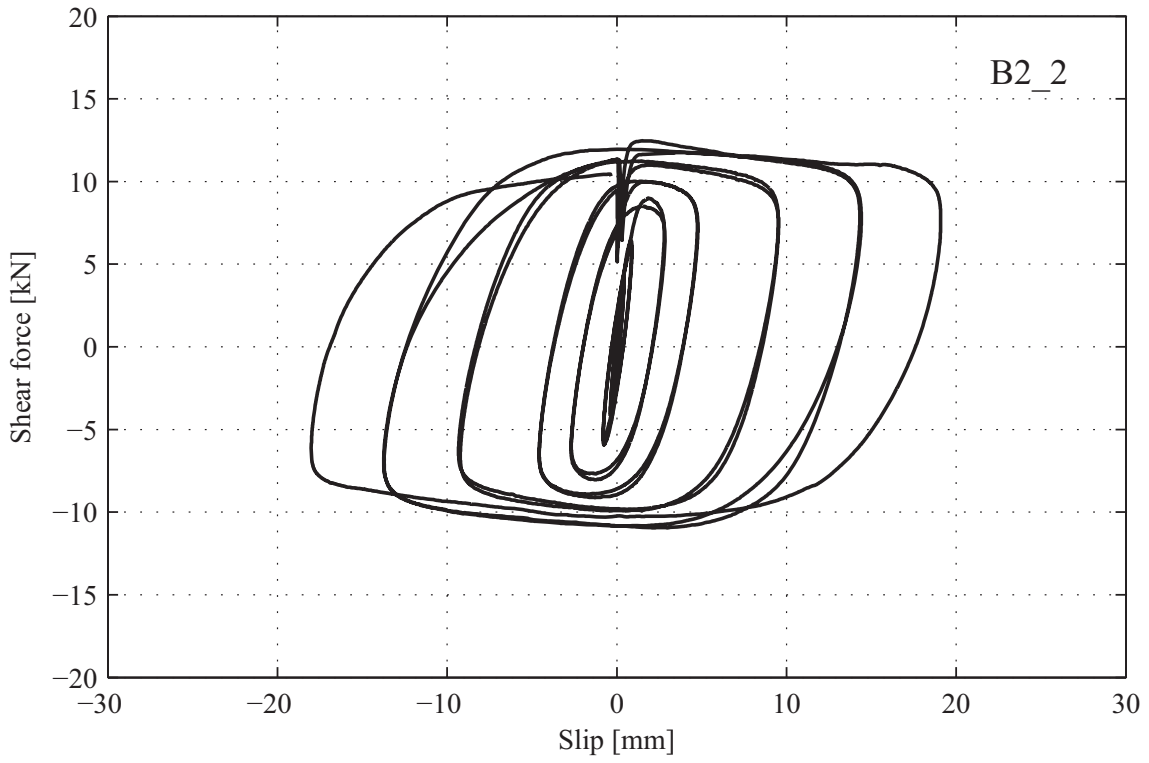
Figure A1-38. Shear force-slip relationship: Specimen B2_2
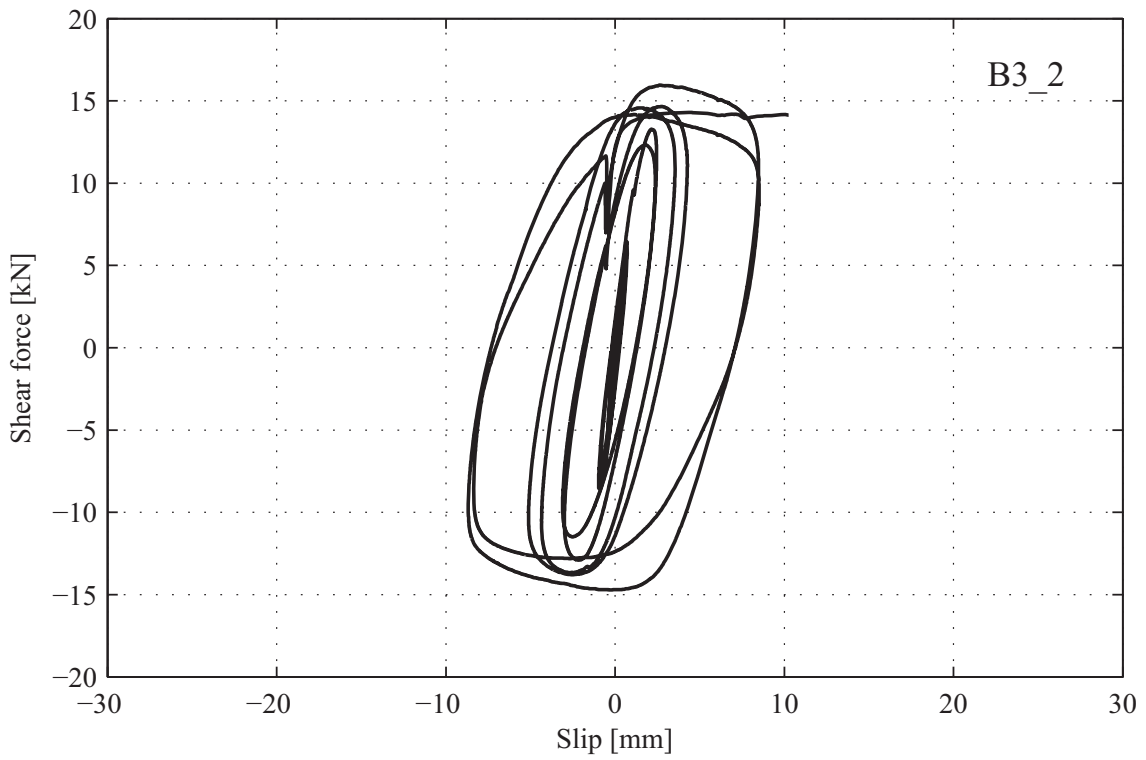
Figure A1-39. Shear force-slip relationship: Specimen B3_2

172
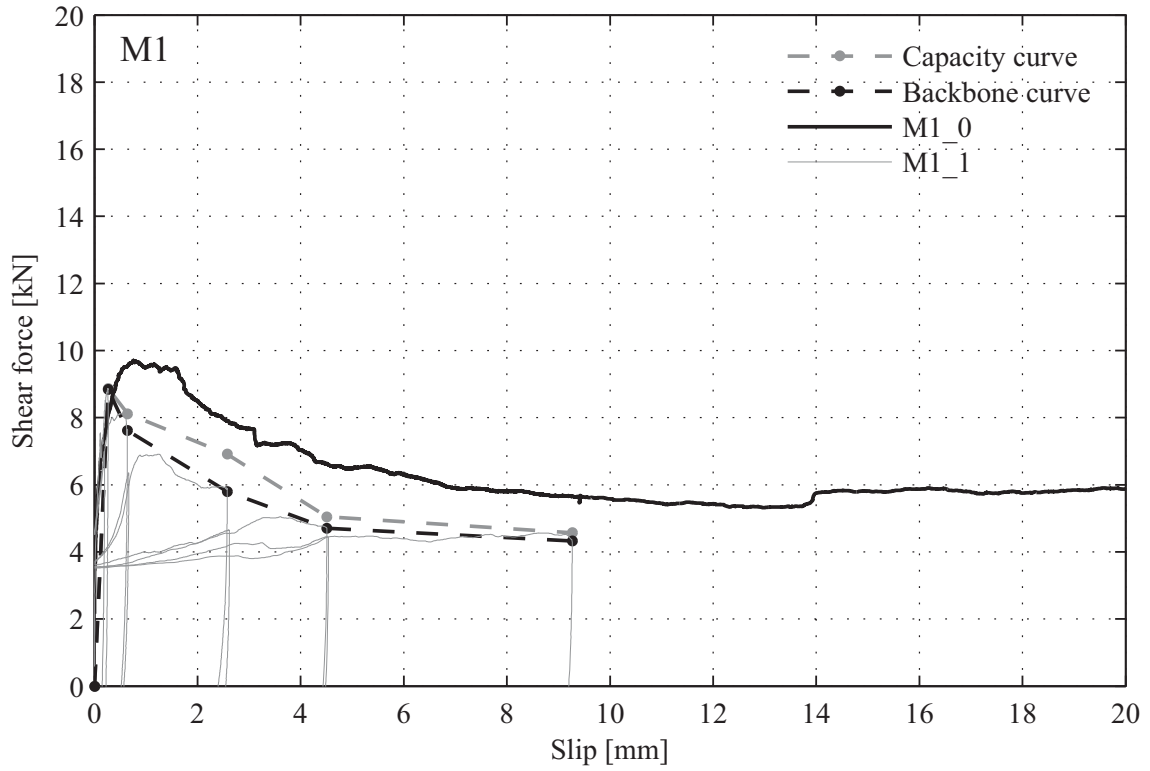
Figure A1-40. Shear force-slip relationships and corresponding backbone and capacity curves: M1 Series
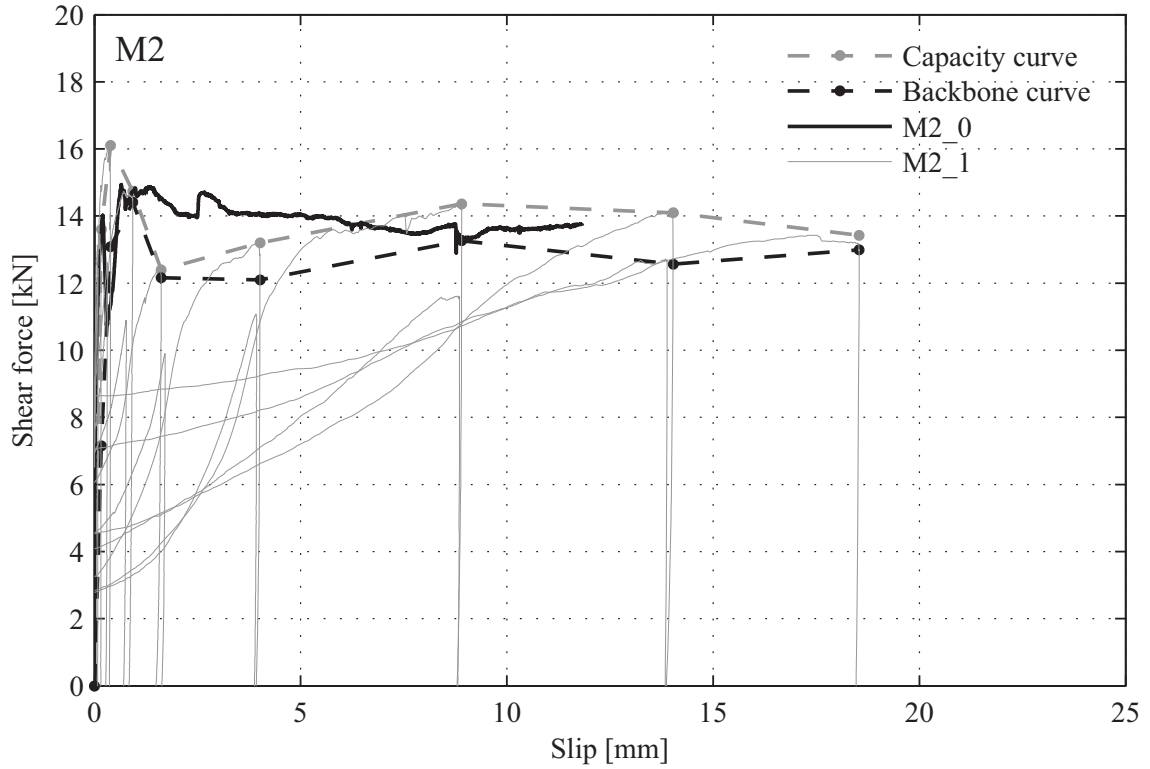
Figure A1-41. Shear force-slip relationships and corresponding backbone and capacity curves: M2 Series
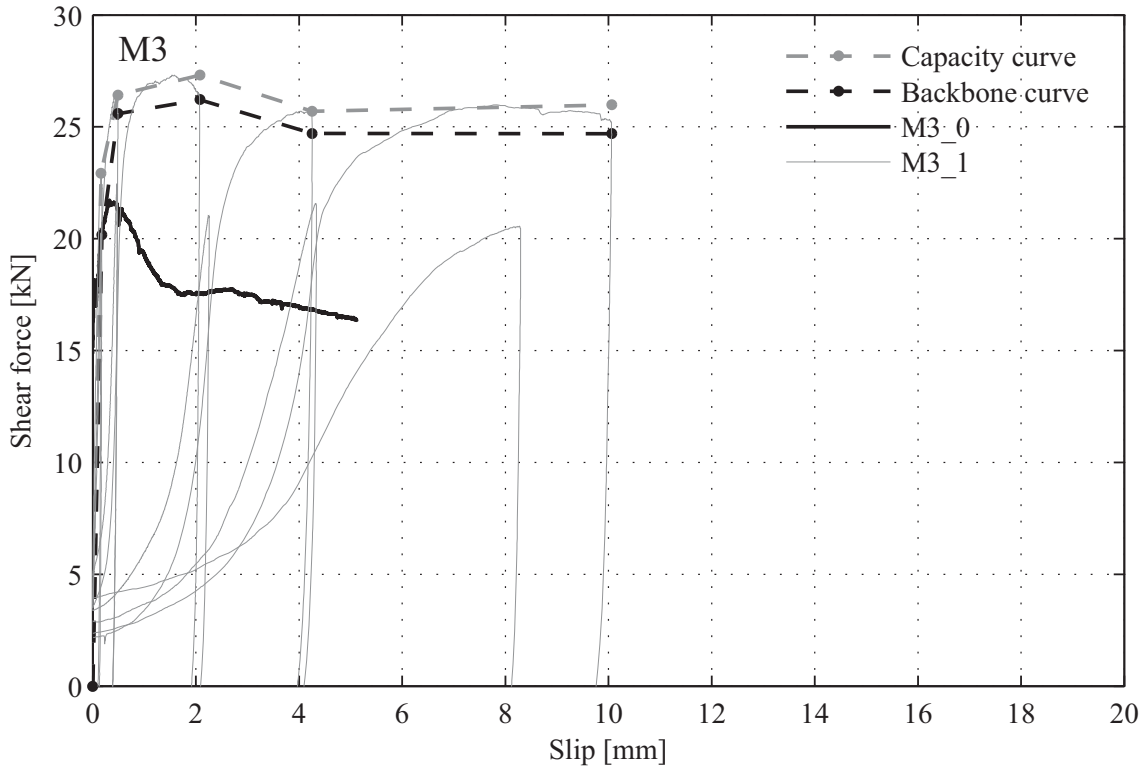
Figure A1-42. Shear force-slip relationships and corresponding backbone and capacity curves: M3 Series
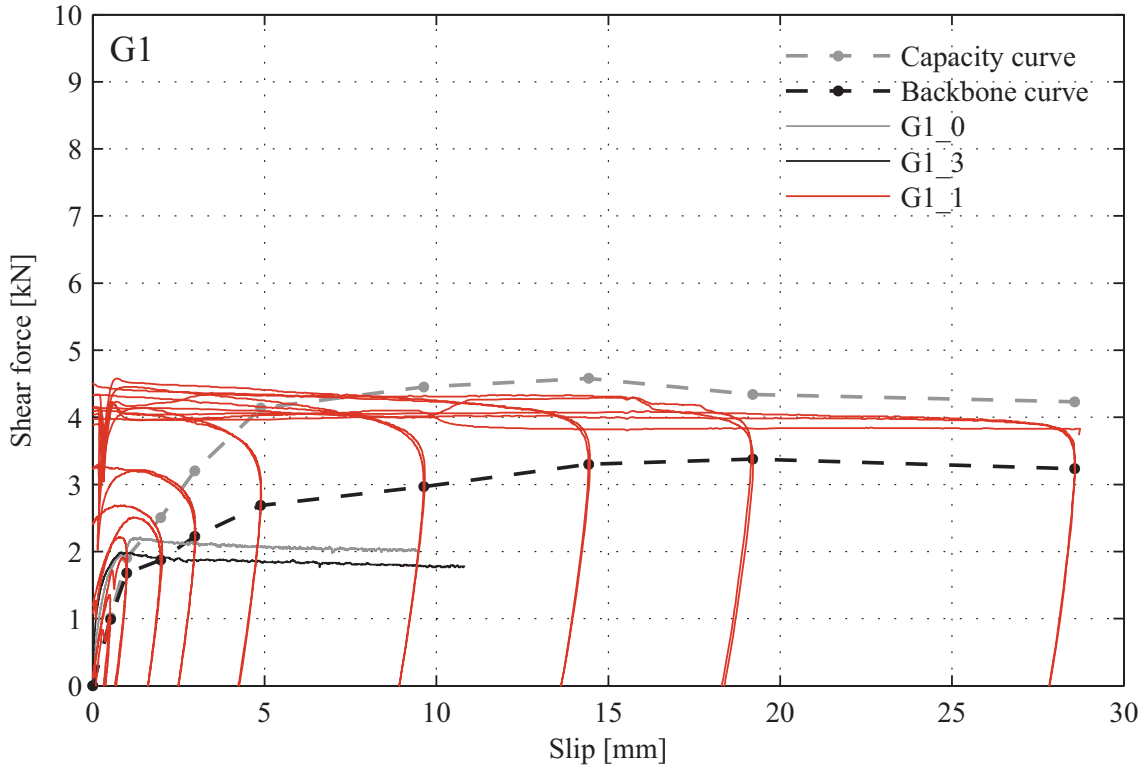
Figure A1-43. Shear force-slip relationships and corresponding backbone and capacity curves: G1 Series

174
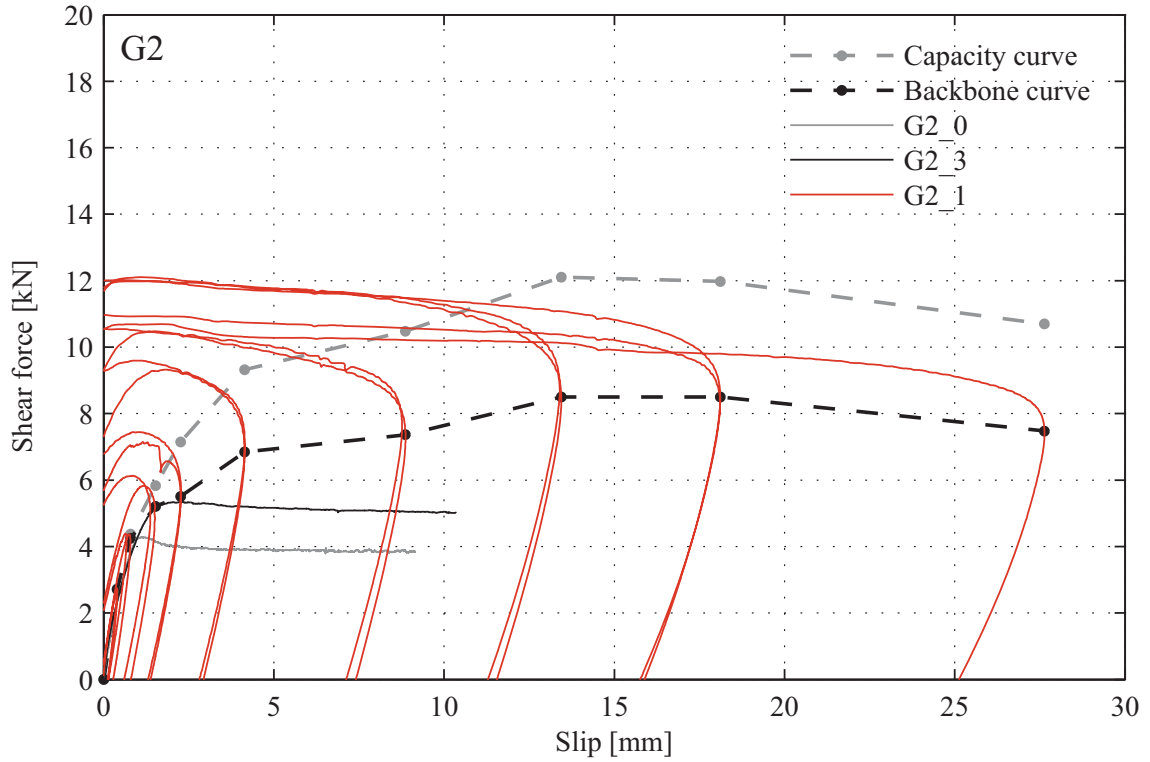
Figure A1-44. Shear force-slip relationships and corresponding backbone and capacity curves: G2 Series
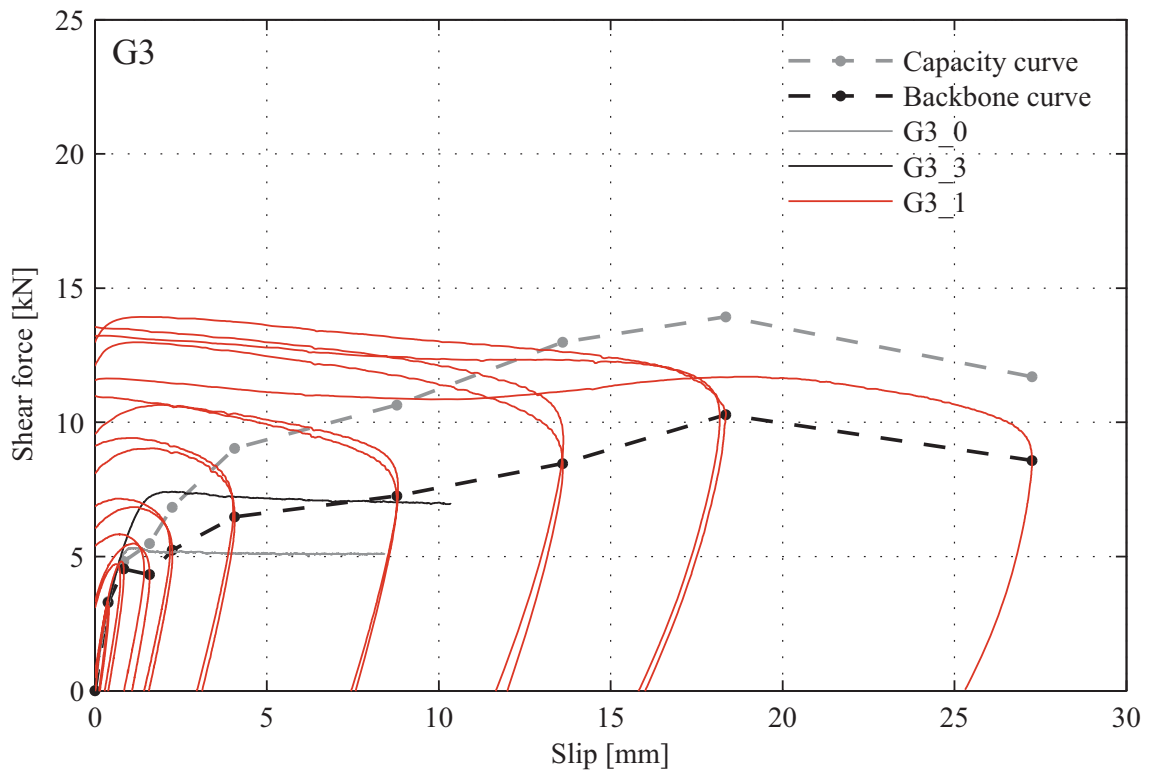
Figure A1-45. Shear force-slip relationships and corresponding backbone and capacity curves: G3 Series

Figure A1-46. Shear force-slip relationships and corresponding backbone and capacity curves: GK1 Series
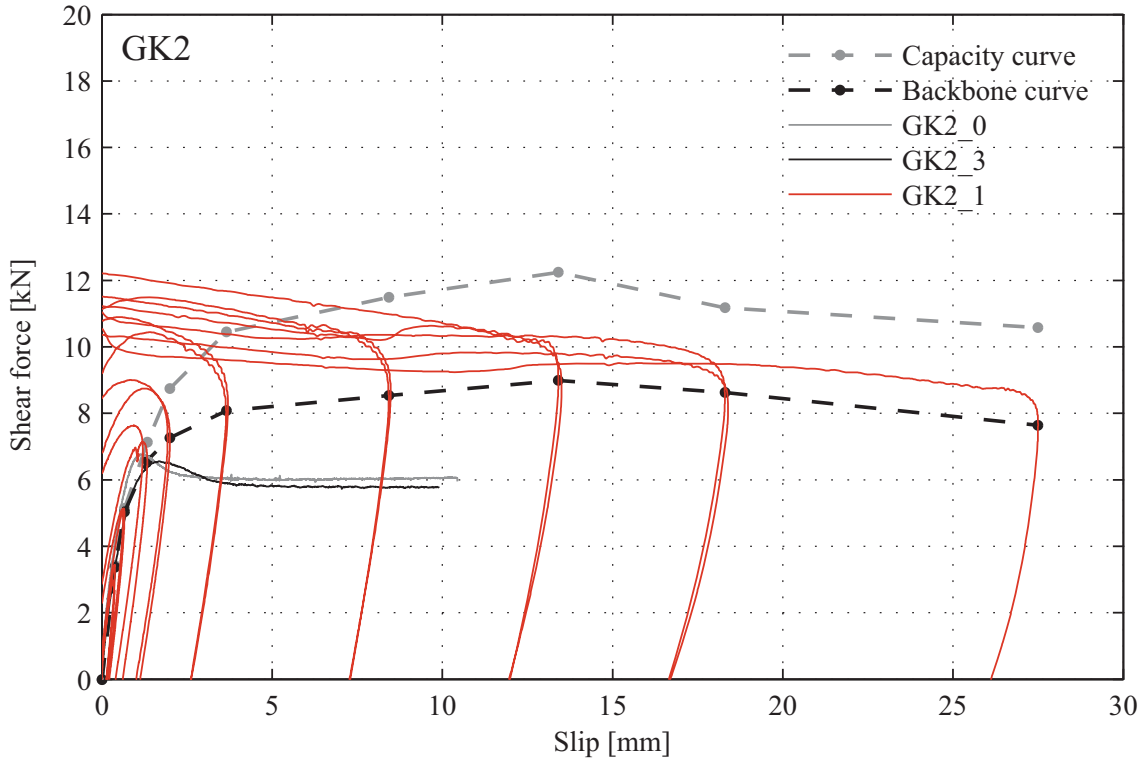
Figure A1-47. Shear force-slip relationships and corresponding backbone and capacity curves: GK2 Series

Figure A1-48. Shear force-slip relationships and corresponding backbone and capacity curves: GK3 Series

Figure A1-49. Shear force-slip relationships and corresponding backbone and capacity curves: K1 Series

Figure A1-50. Shear force-slip relationships and corresponding backbone and capacity curves: K2 Series
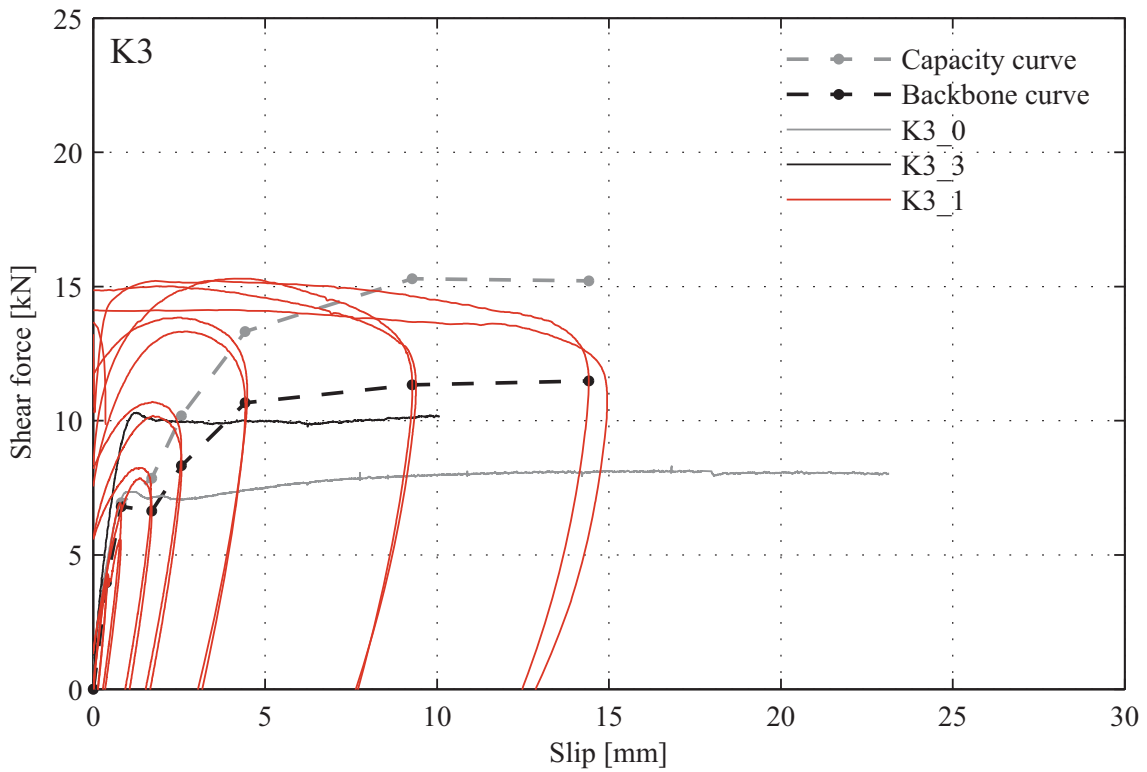
Figure A1-51. Shear force-slip relationships and corresponding backbone and capacity curves: K3 Series

178

Figure A1-52. Shear force-slip relationships and corresponding backbone and capacity curves: B1 Series
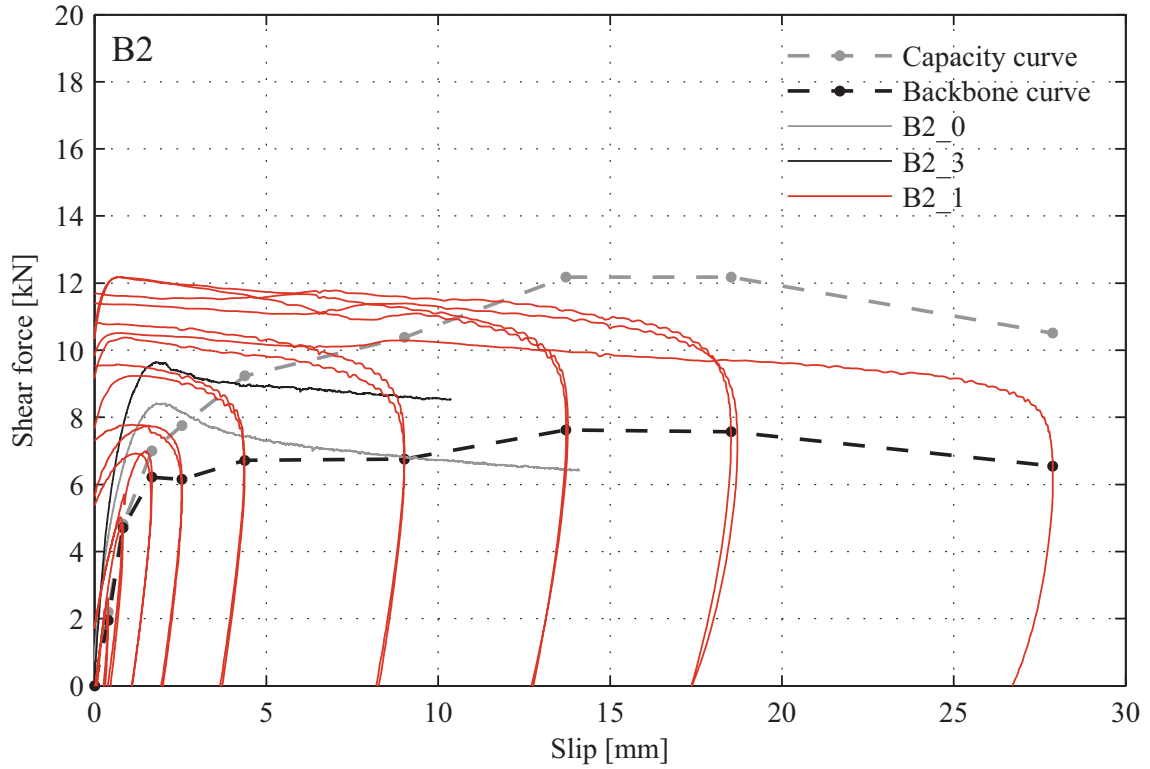
Figure A1-53. Shear force-slip relationships and corresponding backbone and capacity curves: B2 Series

179
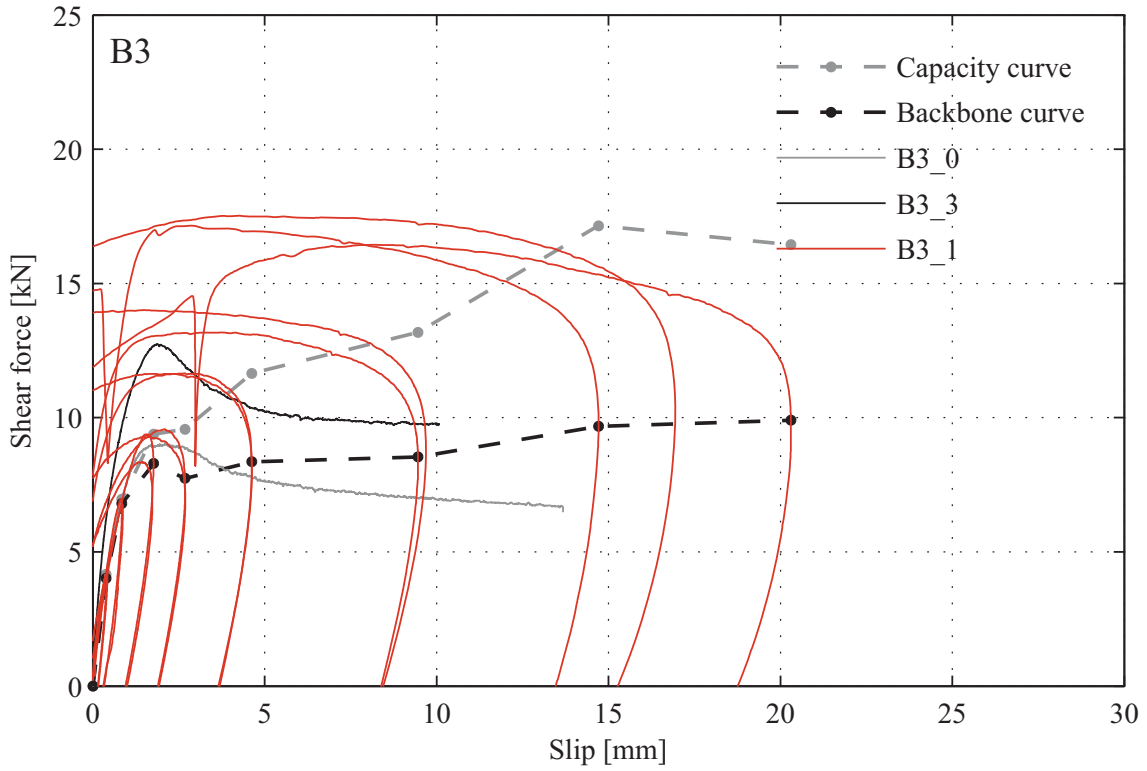
Figure A1-54. Shear force-slip relationships and corresponding backbone and capacity curves: B3 Series
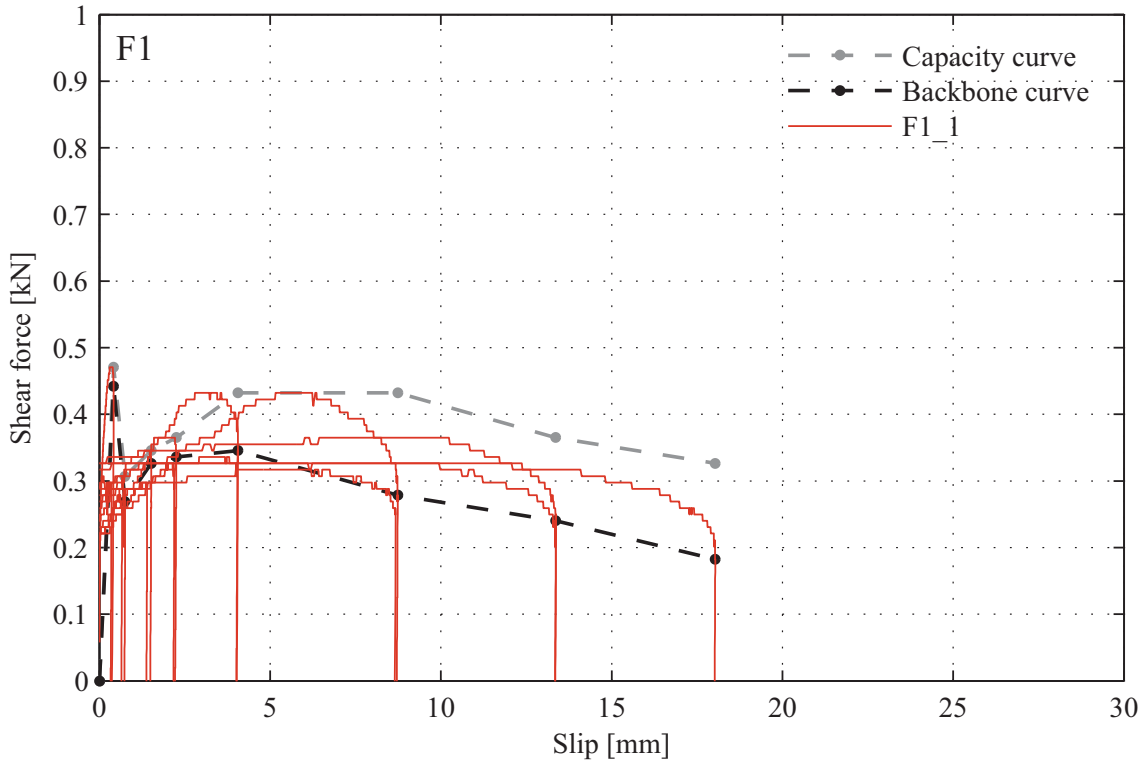
Figure A1-55. Shear force-slip relationships and corresponding backbone and capacity curves: F1 Series

180
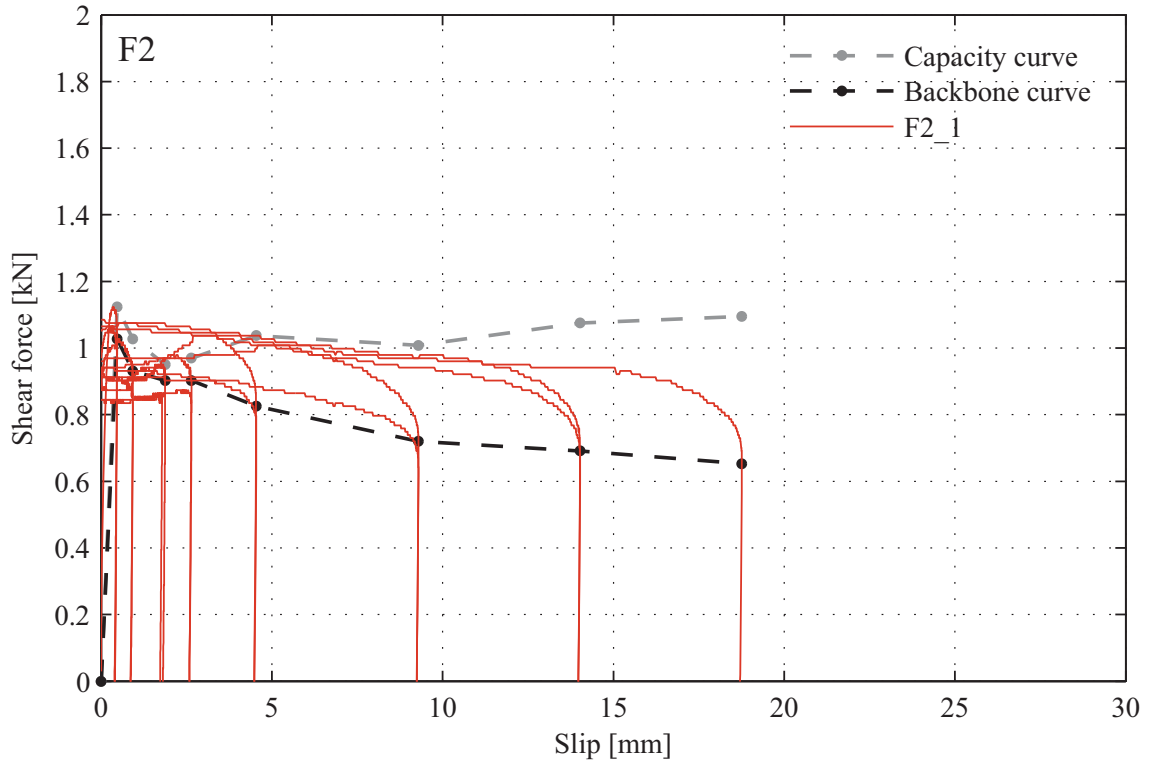
Figure A1-56. Shear force-slip relationships and corresponding backbone and capacity curves: F2 Series
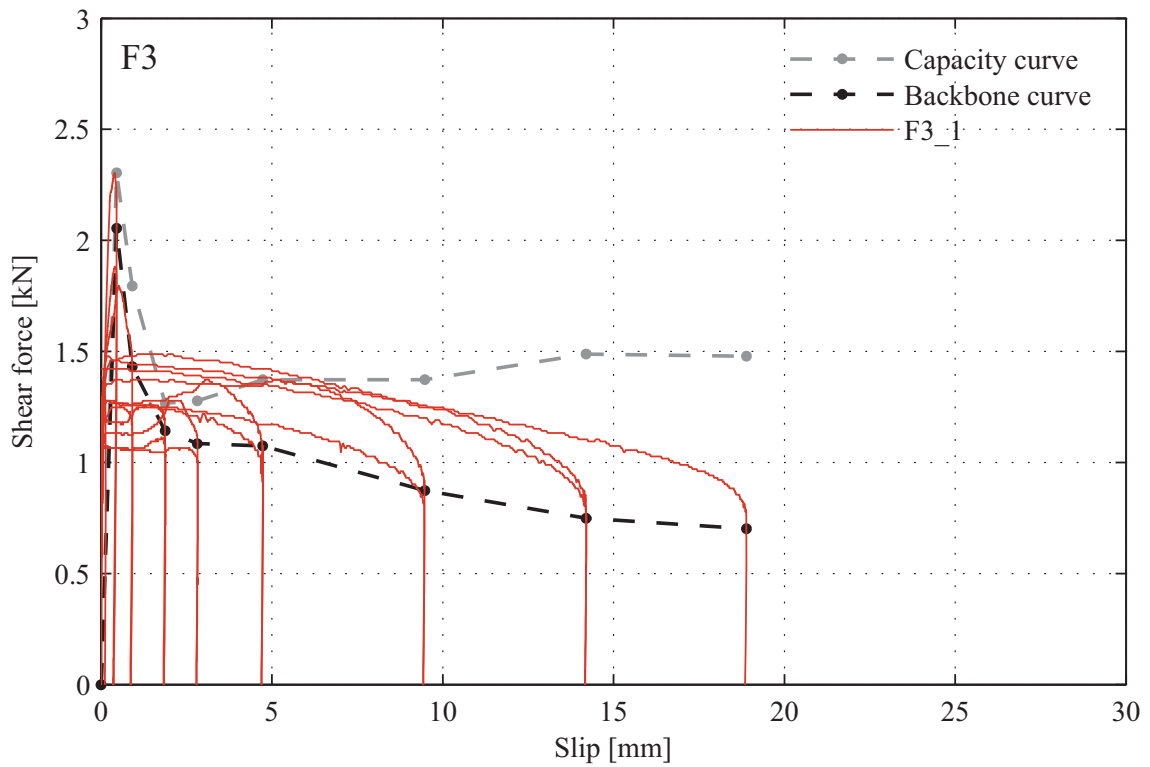
Figure A1-57. Shear force-slip relationships and corresponding backbone and capacity curves: F3 Series

Appendix A2   Static cyclic shear tests on URM walls with a multi-layer bottom bed joint

This appendix provides for the details of horizontal force-displacement relationships measured during the static-cyclic shear tests on URM walls with a multi-layer bottom bed joints. In addition, the details of the graphs on the comparison of the measured and idealized horizontal force-displacement hysteretic response depicted in Figure 3-45, are provided.
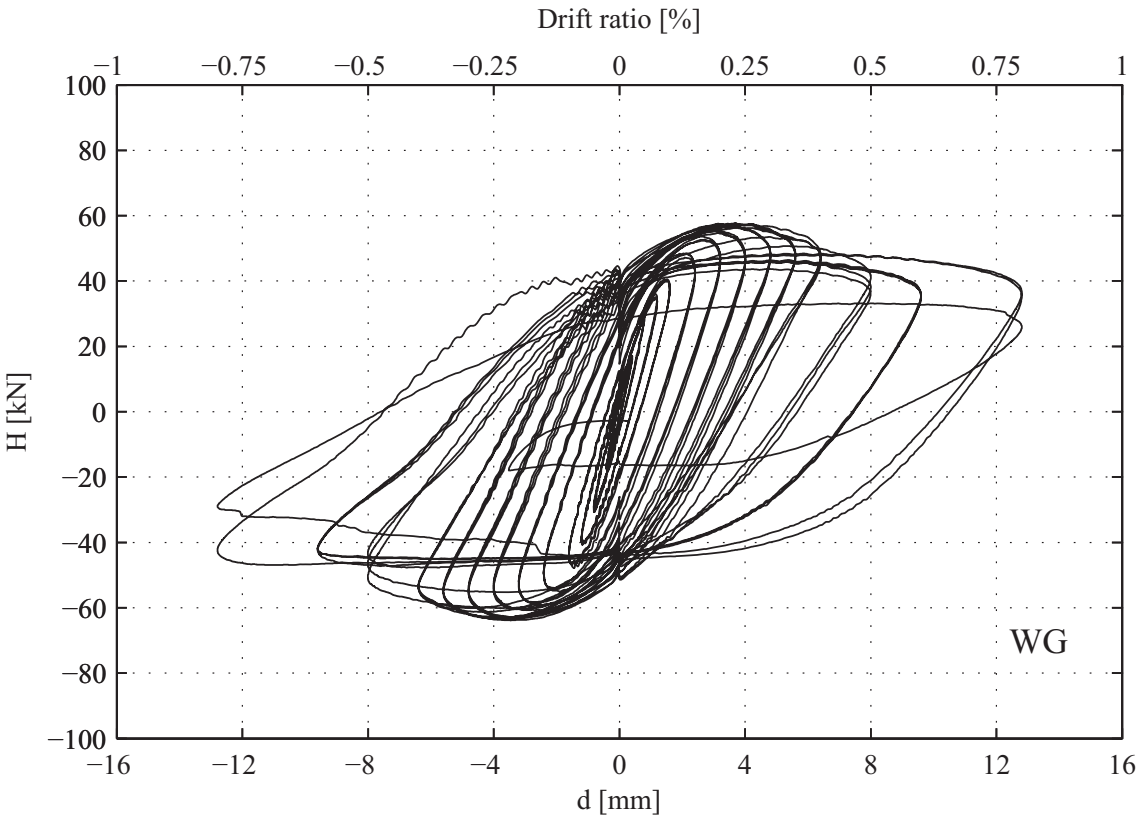
Figure A2-1. Horizontal force-displacement response hysteresis curve: Wall WG
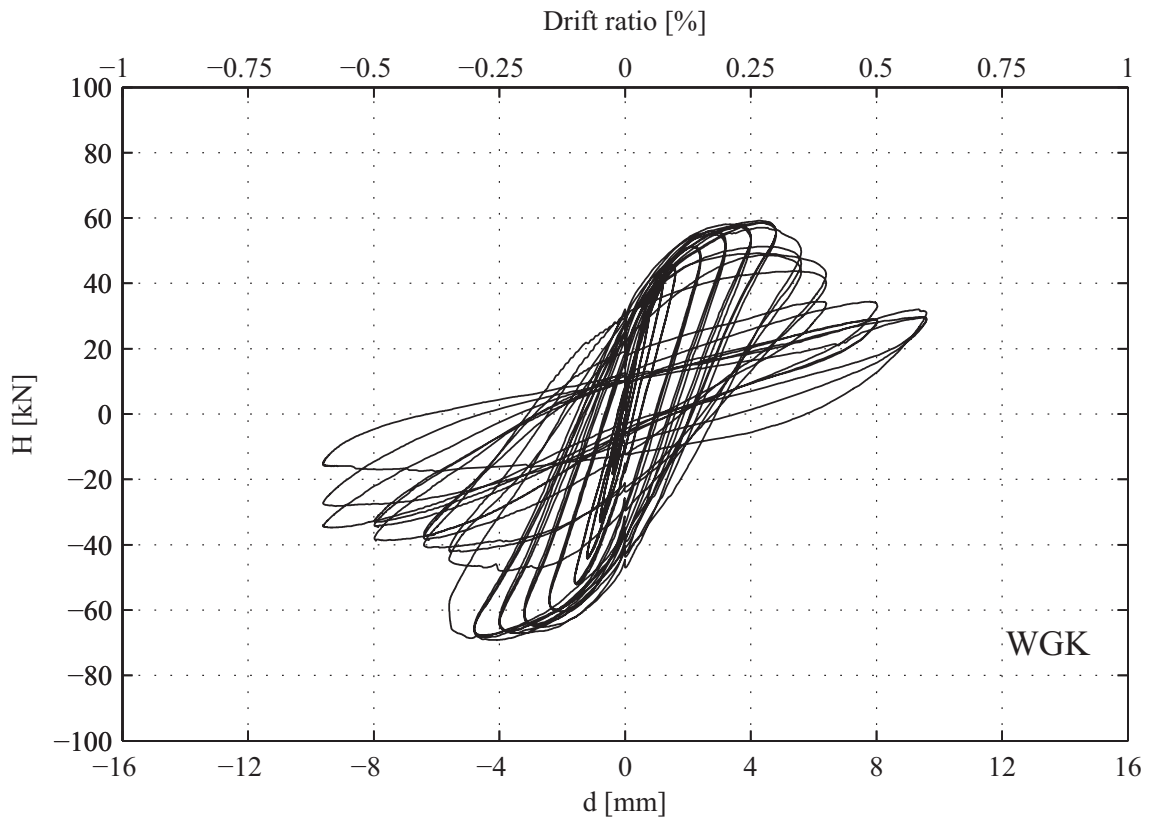
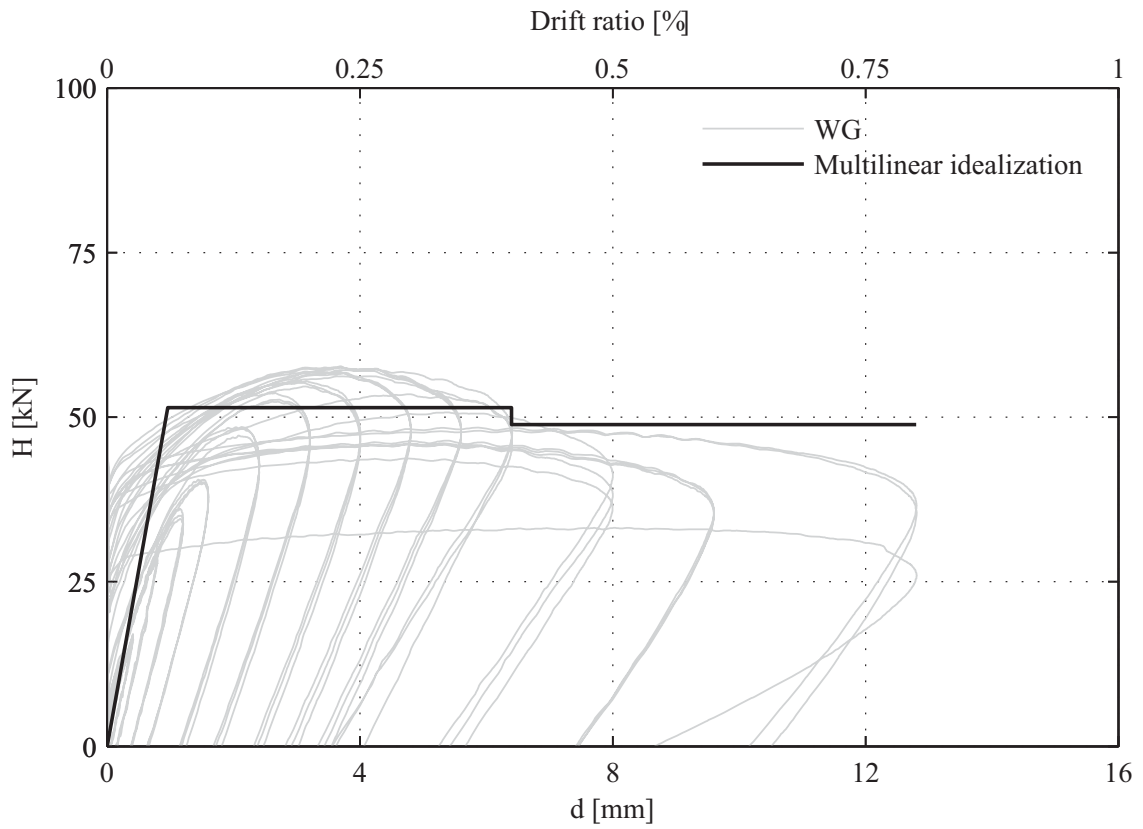**Figure A2-2. Horizontal force-displacement response hysteresis curve: Wall WGK**
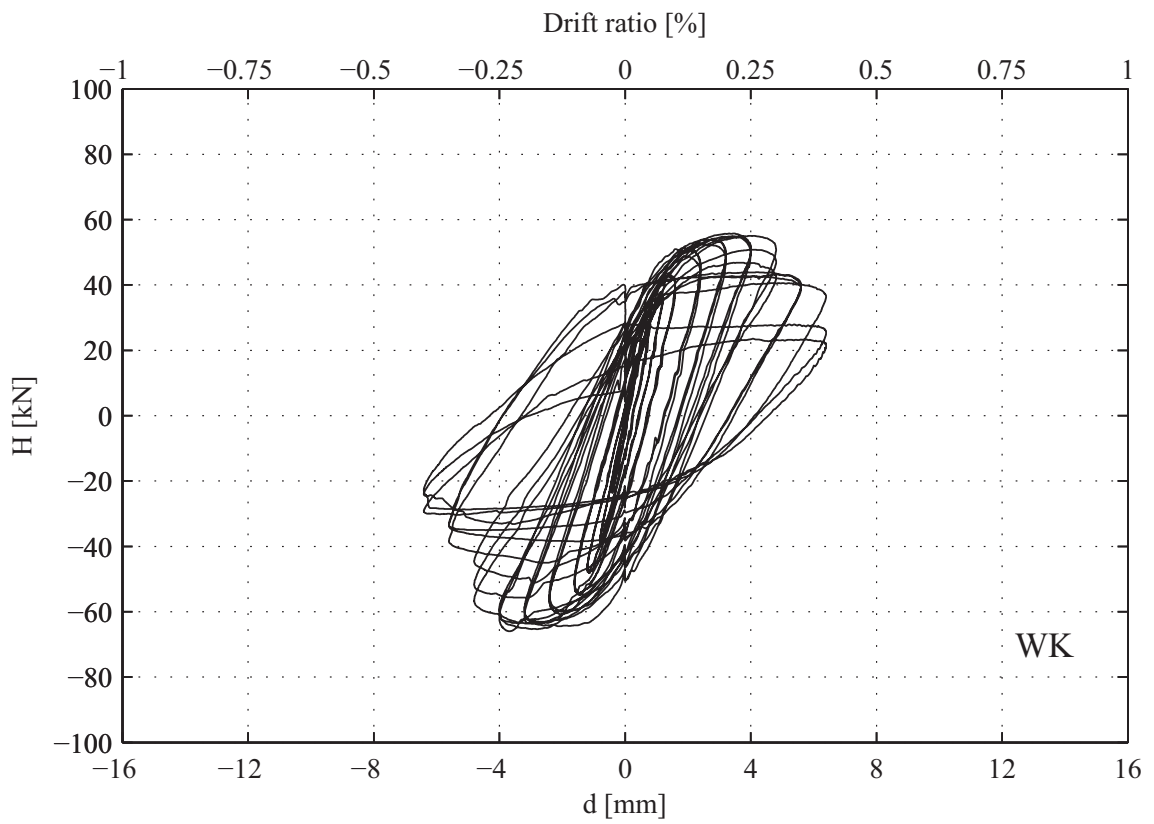
Figure A2-3. Horizontal force-displacement response hysteresis curve: Wall WK
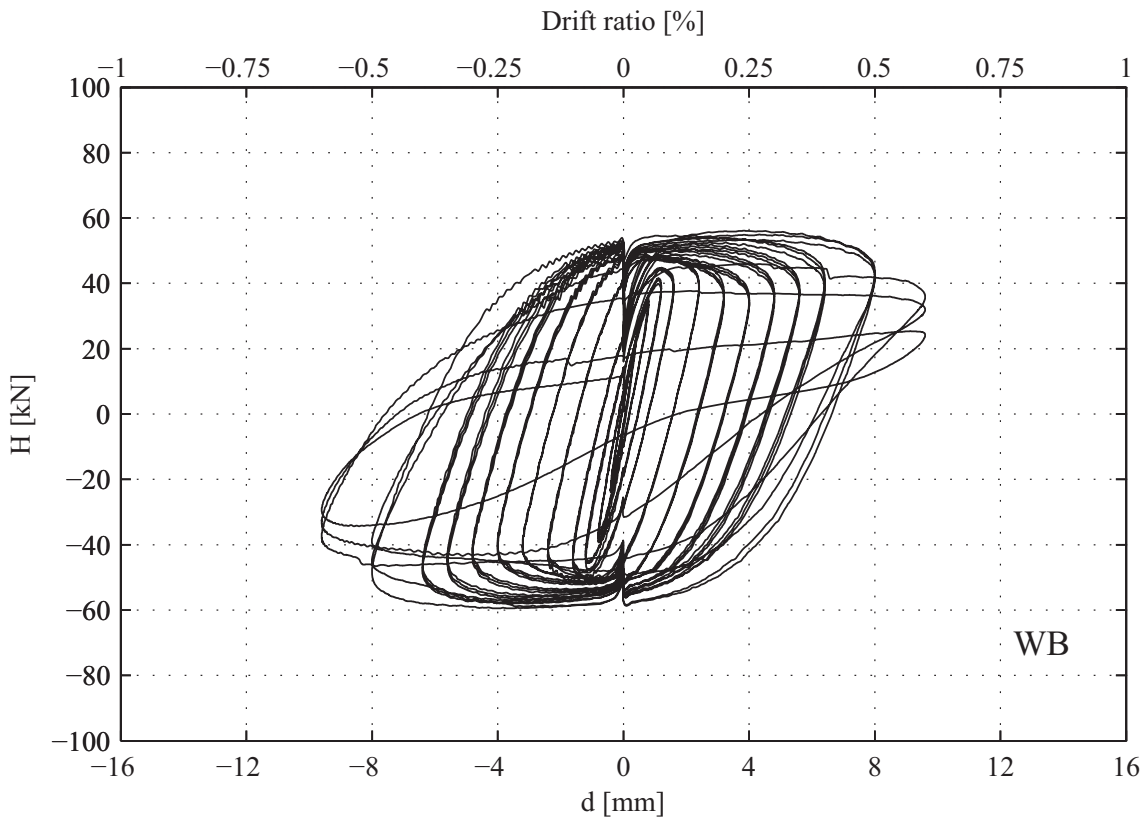
Figure A2-4. Horizontal force-displacement response hysteresis curve: Wall WB
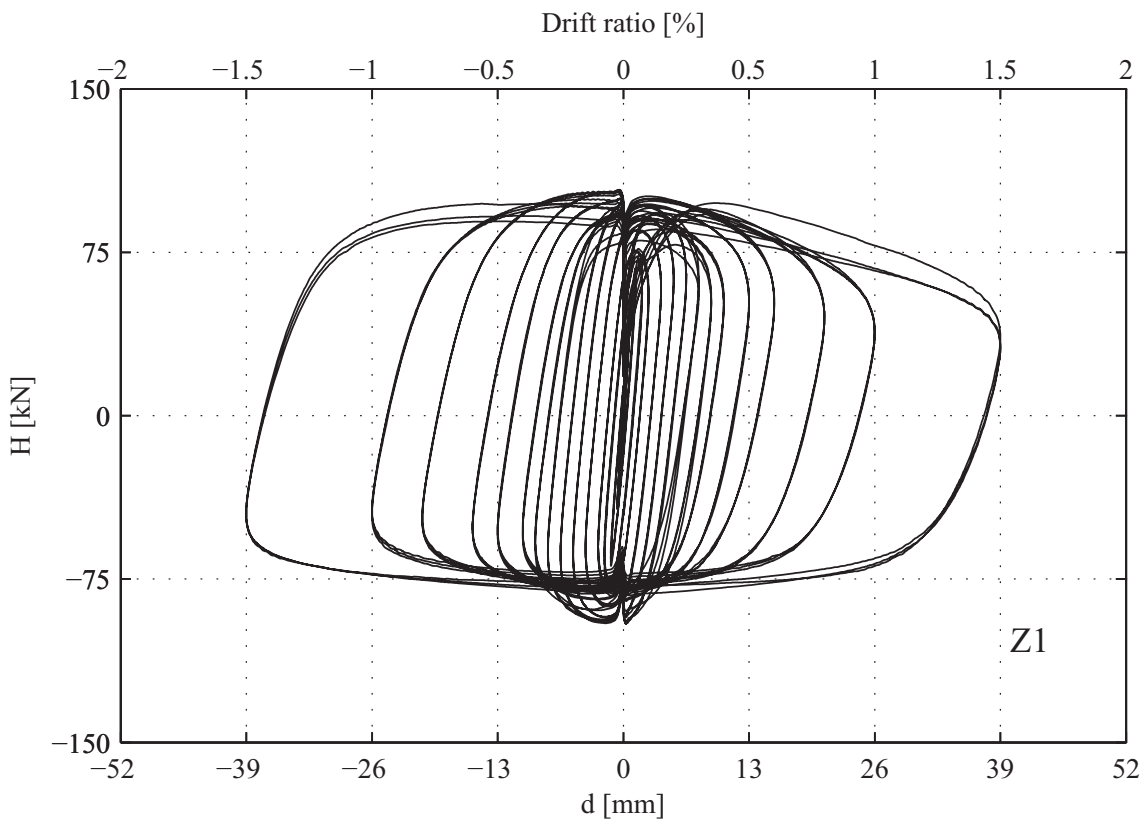
Figure A2-5. Horizontal force-displacement response hysteresis curve: Wall Z1

184
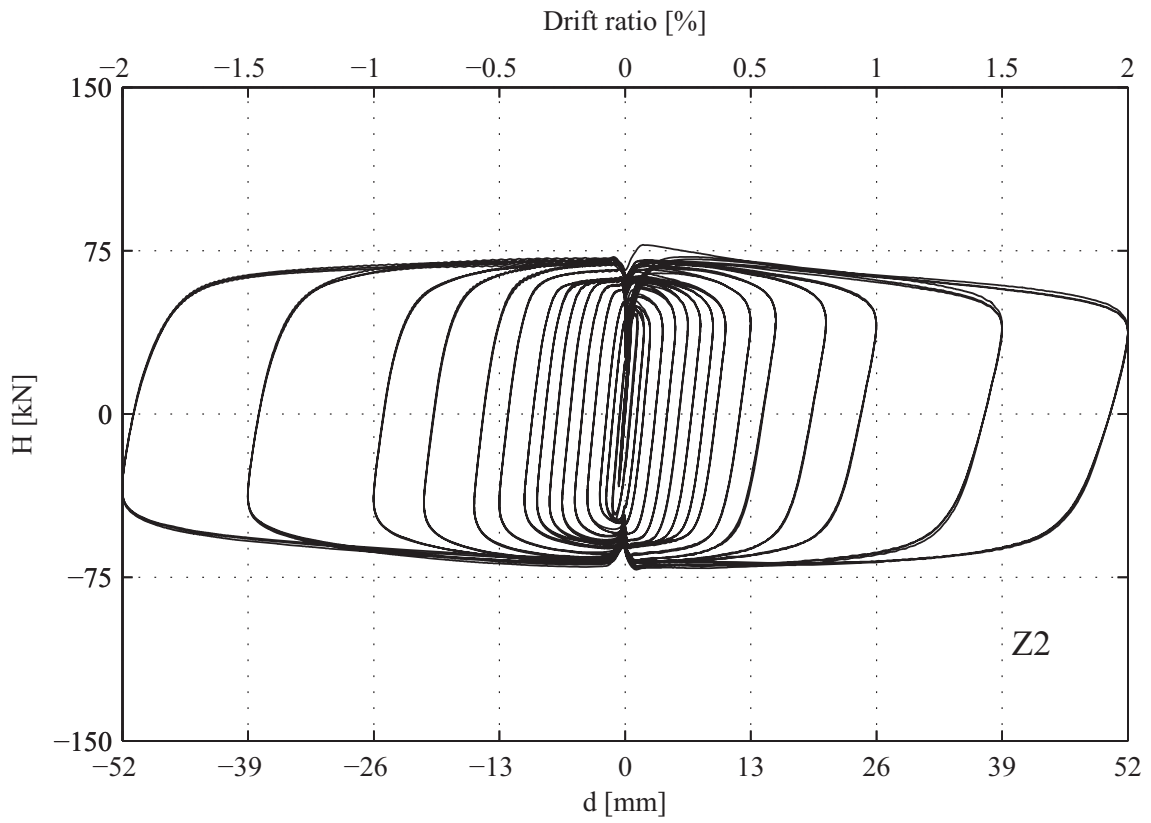
Figure A2-6. Horizontal force-displacement response hysteresis curve: Wall Z2
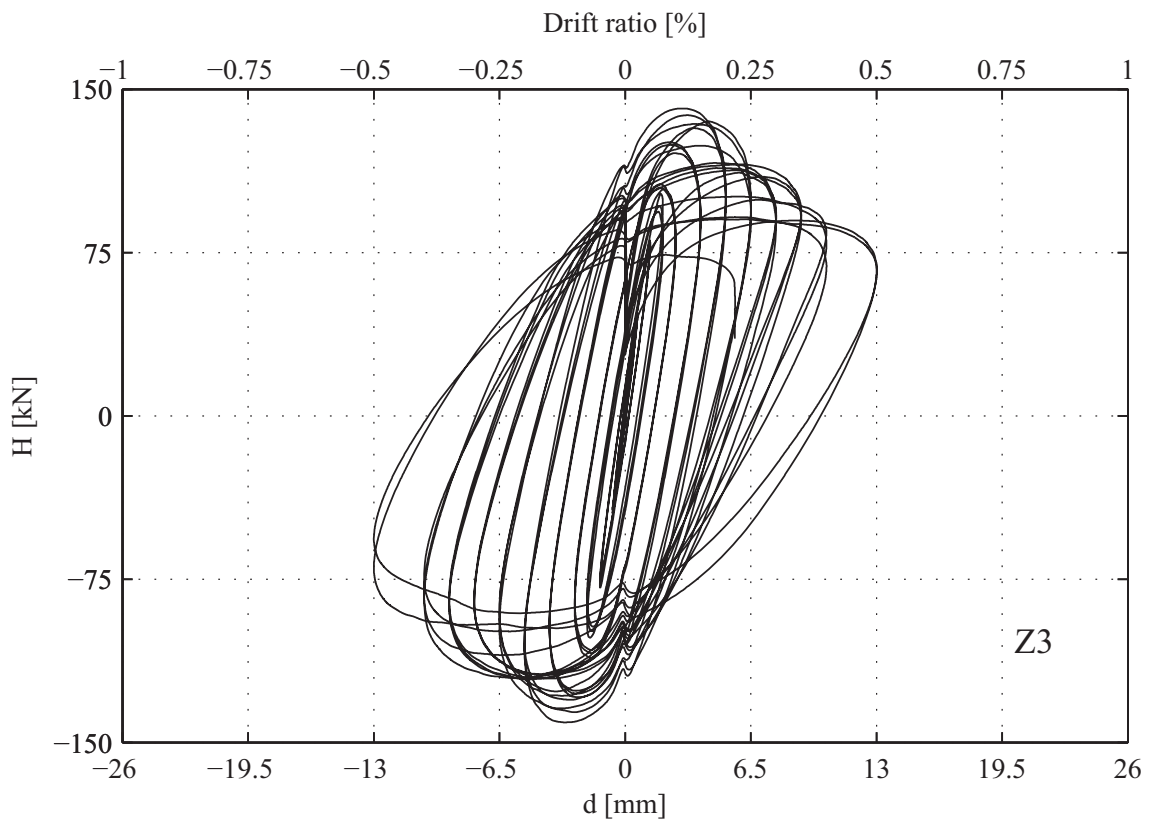
Figure A2-7. Horizontal force-displacement response hysteresis curve: Wall Z3

185
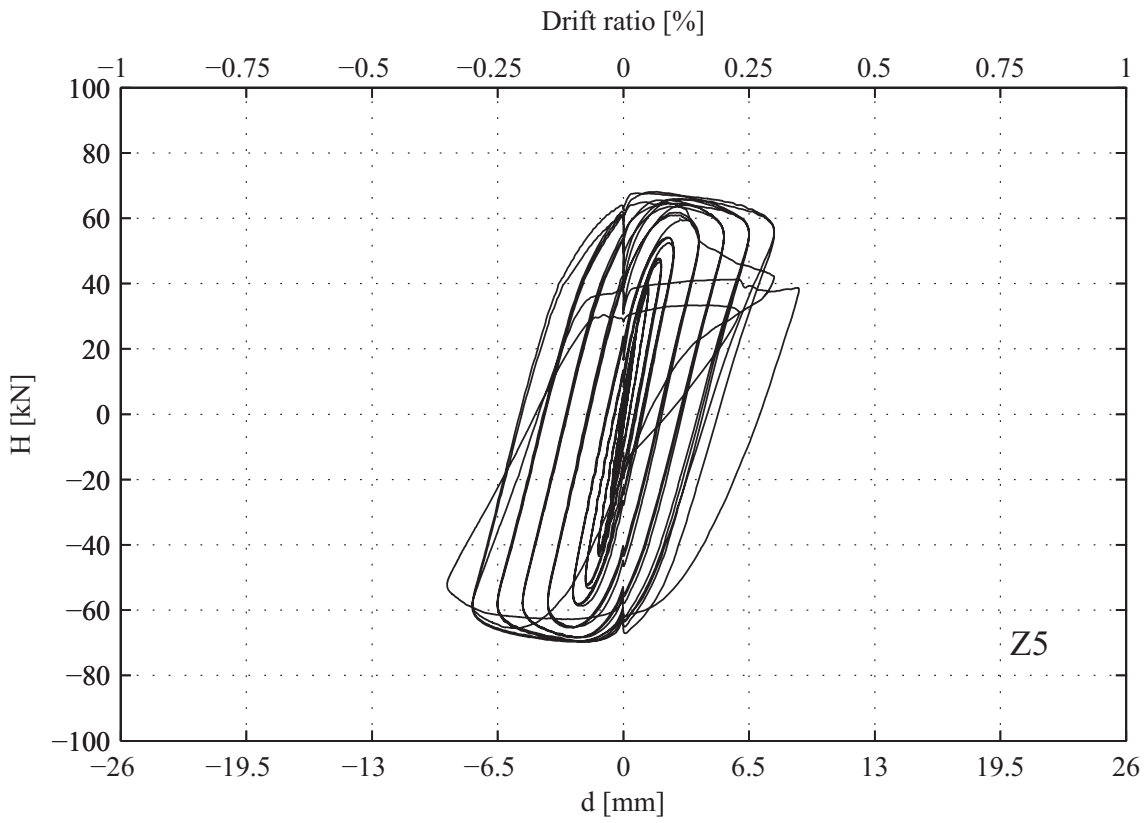
Figure A2-8. Horizontal force-displacement response hysteresis curve: Wall Z5
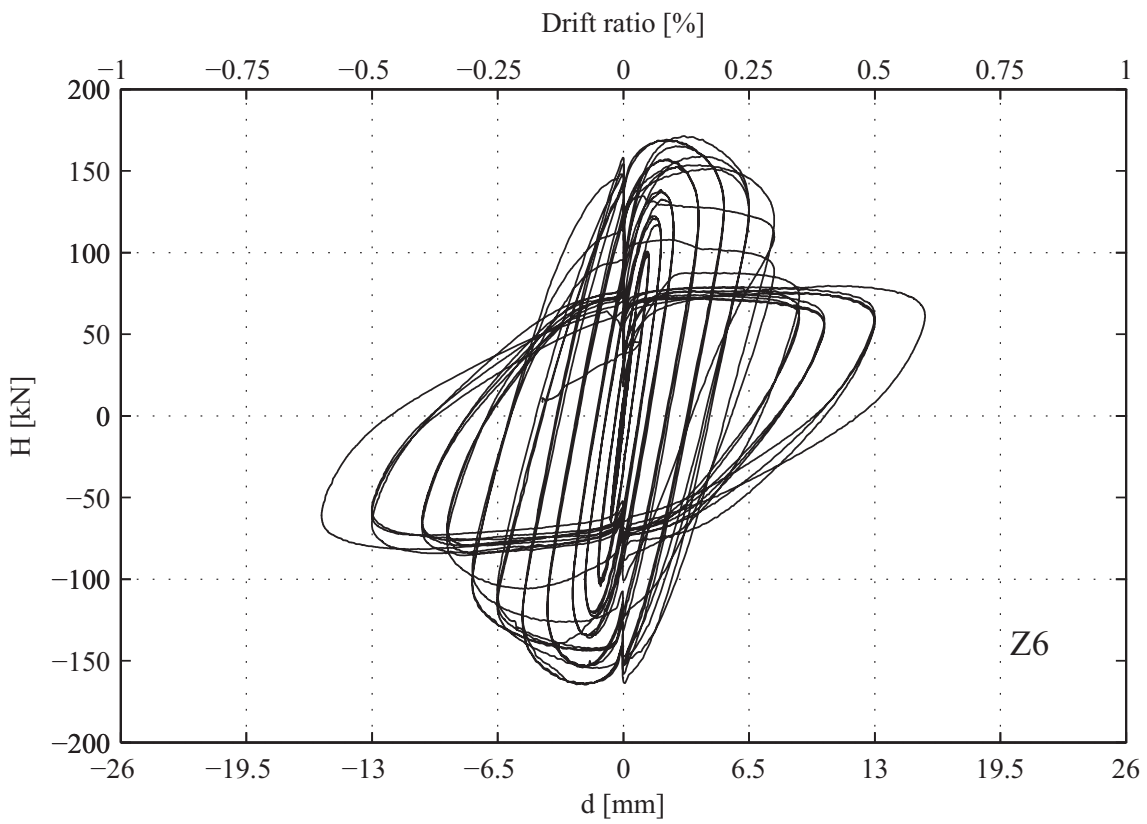
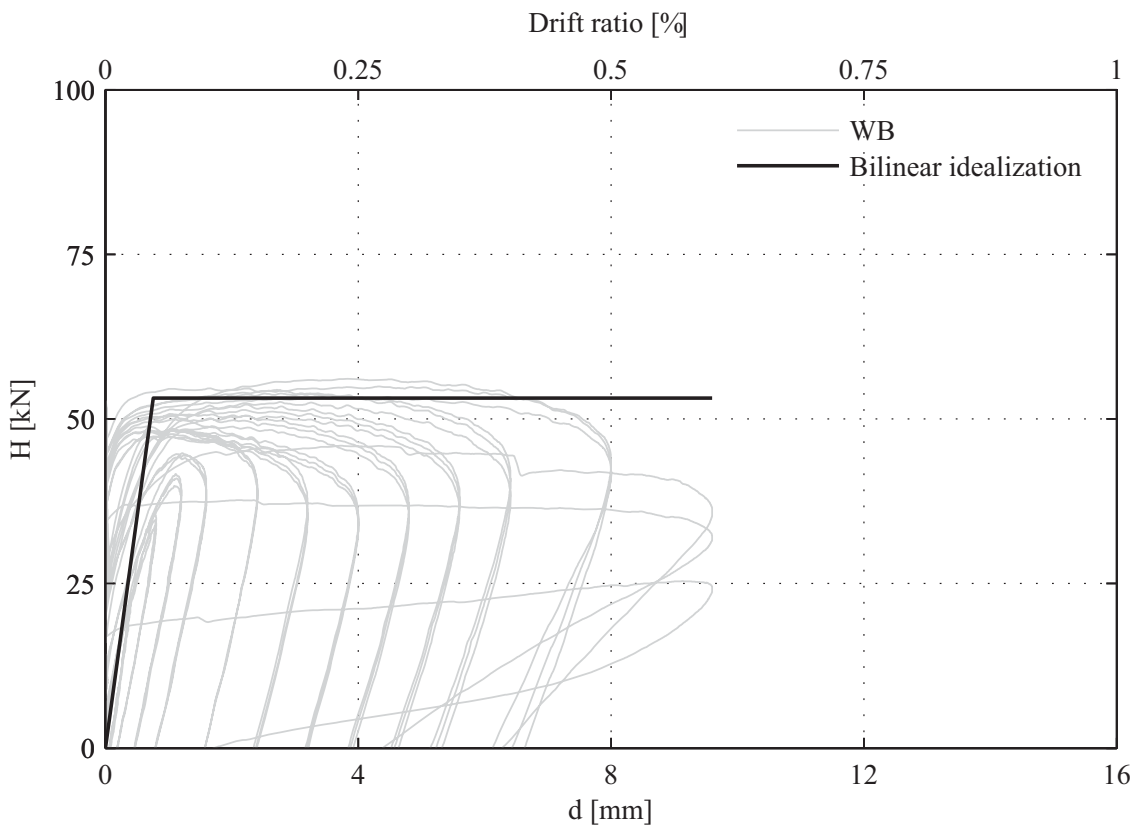**Figure A2-9. Horizontal force-displacement response hysteresis curve: Wall Z6**

Figure A2-10. Measured vs. idealized horizontal force-displacement hysteretic response: Wall WG
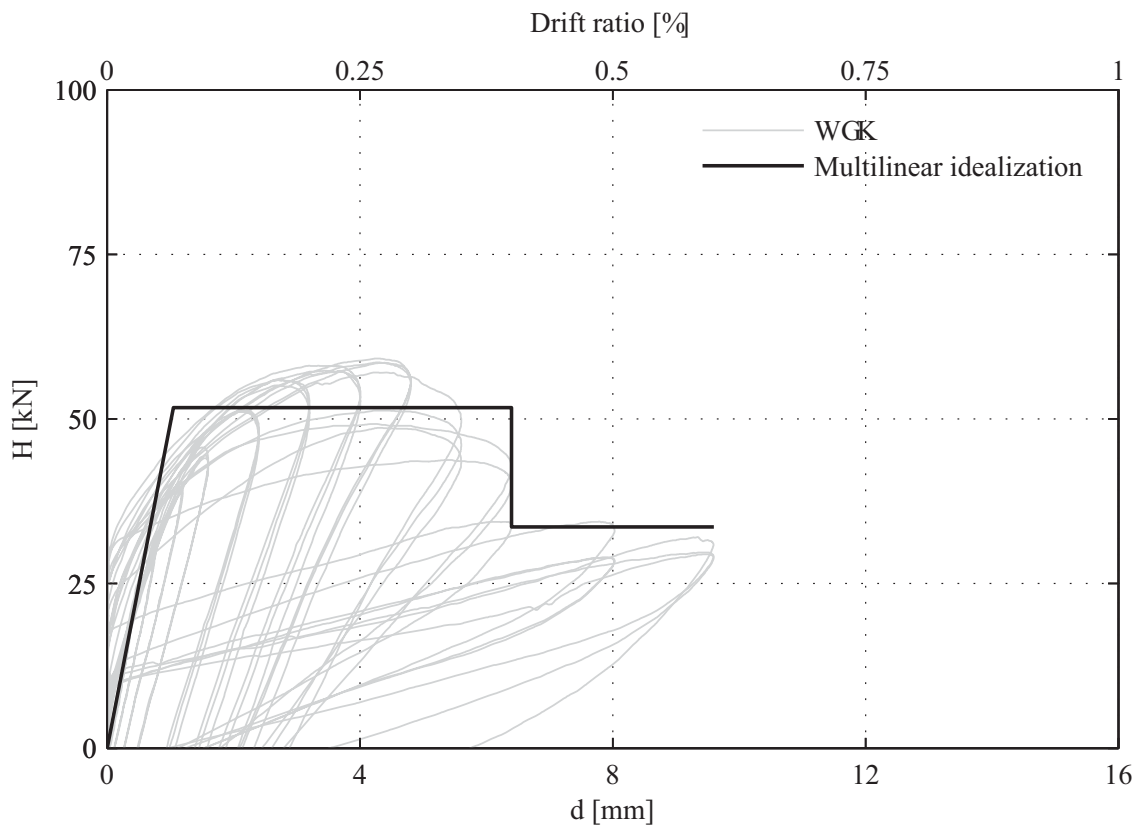
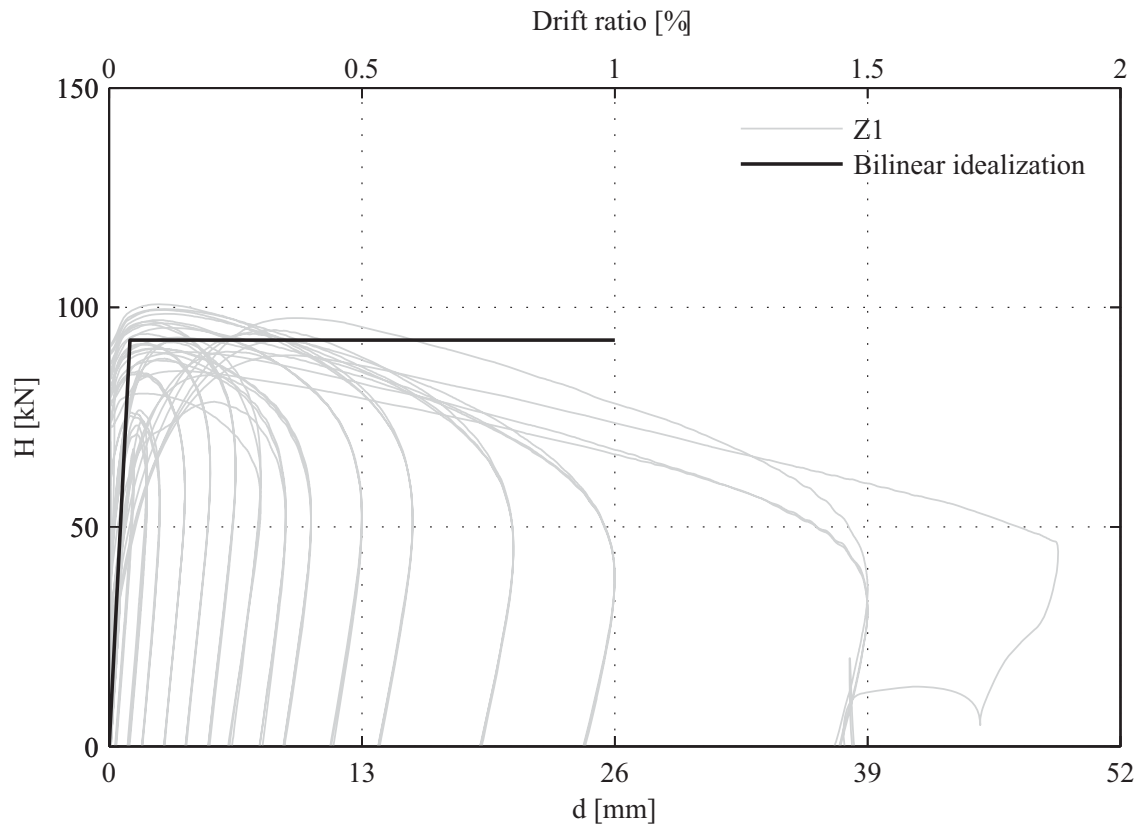**Figure A2-11. Measured vs. idealized horizontal force-displacement hysteretic response: Wall WGK**
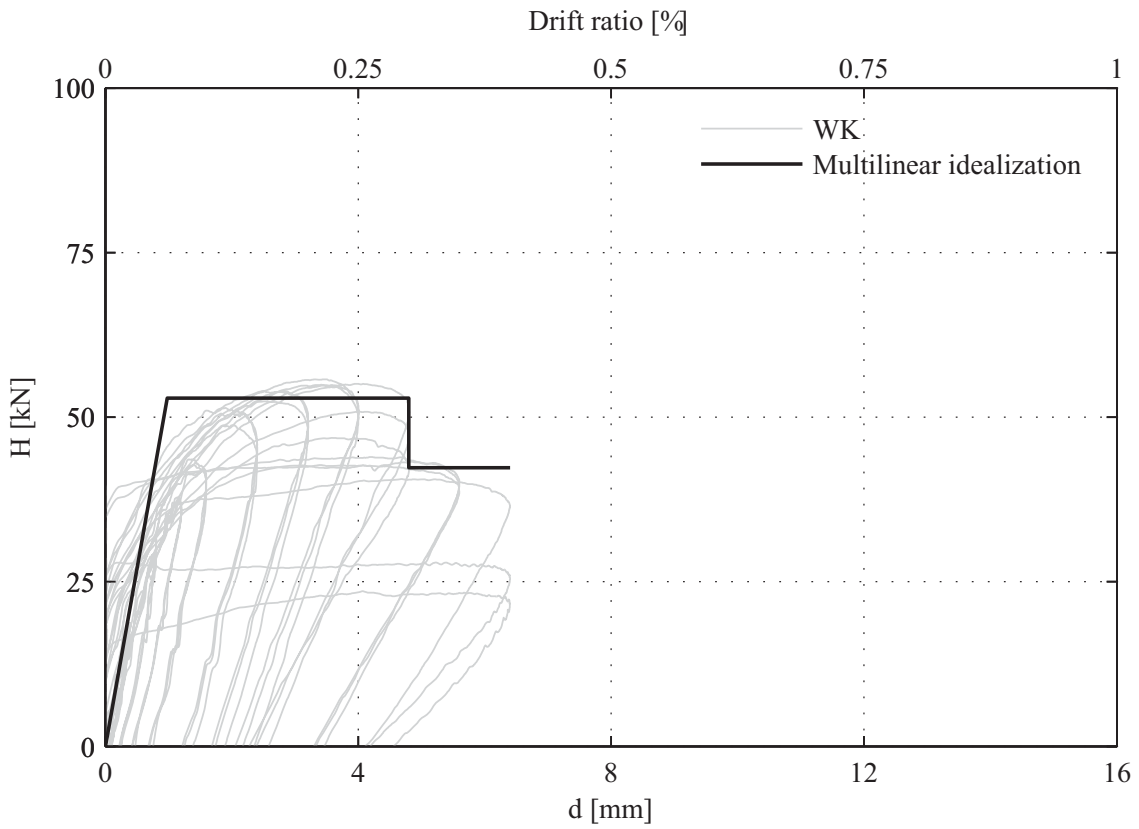
Figure A2-12. Measured vs. idealized horizontal force-displacement hysteretic response: Wall WK

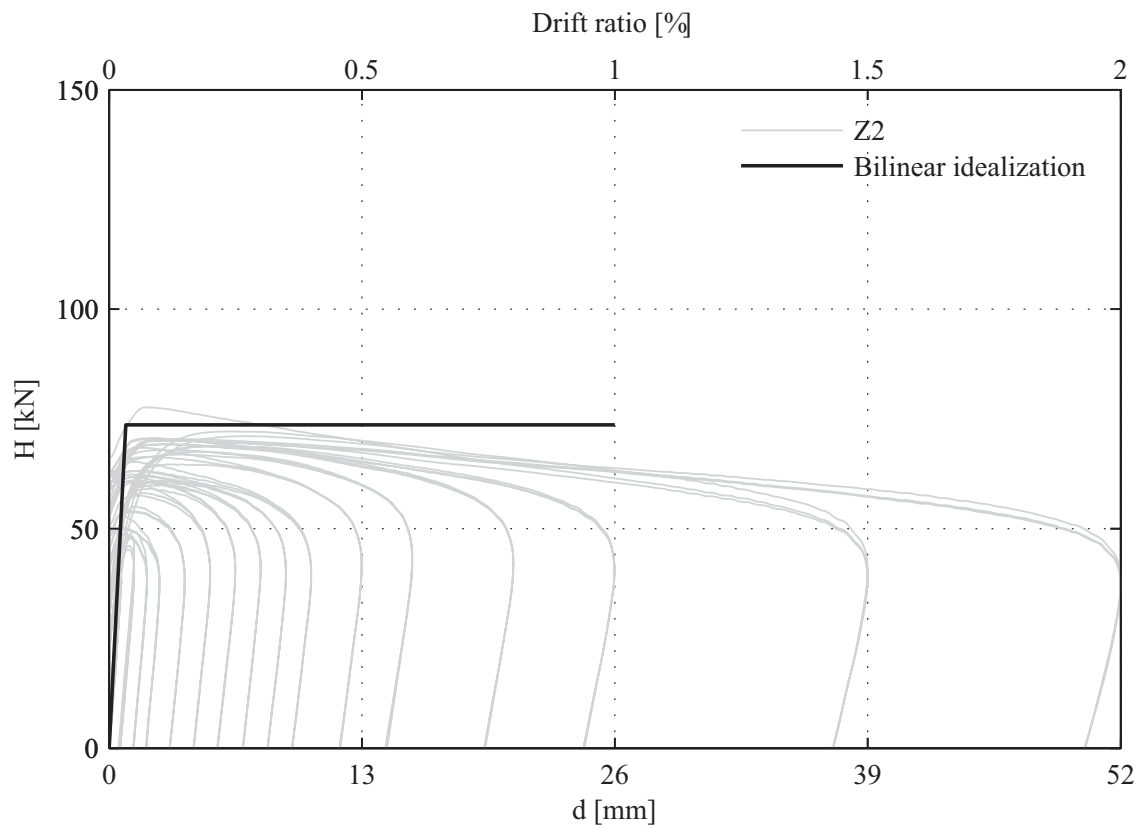**Figure A2-13. Measured vs. idealized horizontal force-displacement hysteretic response: Wall WB**

188

Figure A2-14. Measured vs. idealized horizontal force-displacement hysteretic response: Wall Z1

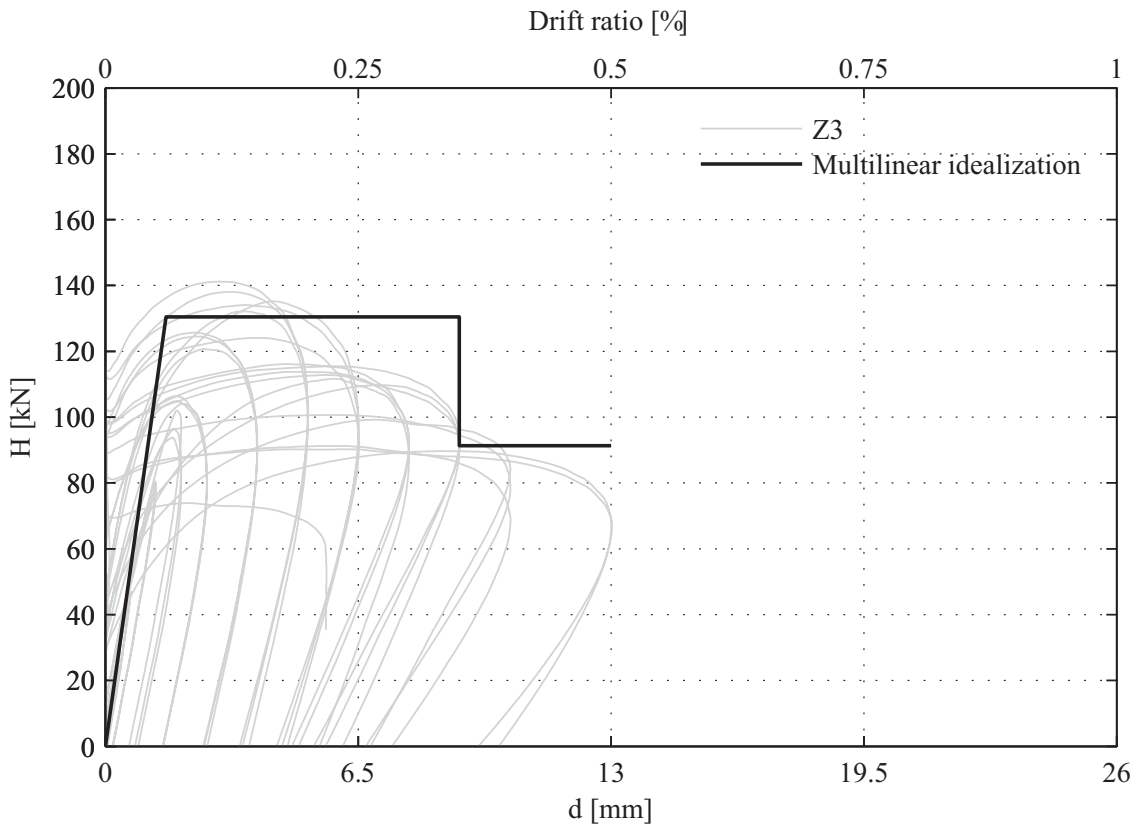**Figure A2-15. Measured vs. idealized horizontal force-displacement hysteretic response: Wall Z2**

189

Figure A2-16. Measured vs. idealized horizontal force-displacement hysteretic response: Wall Z3

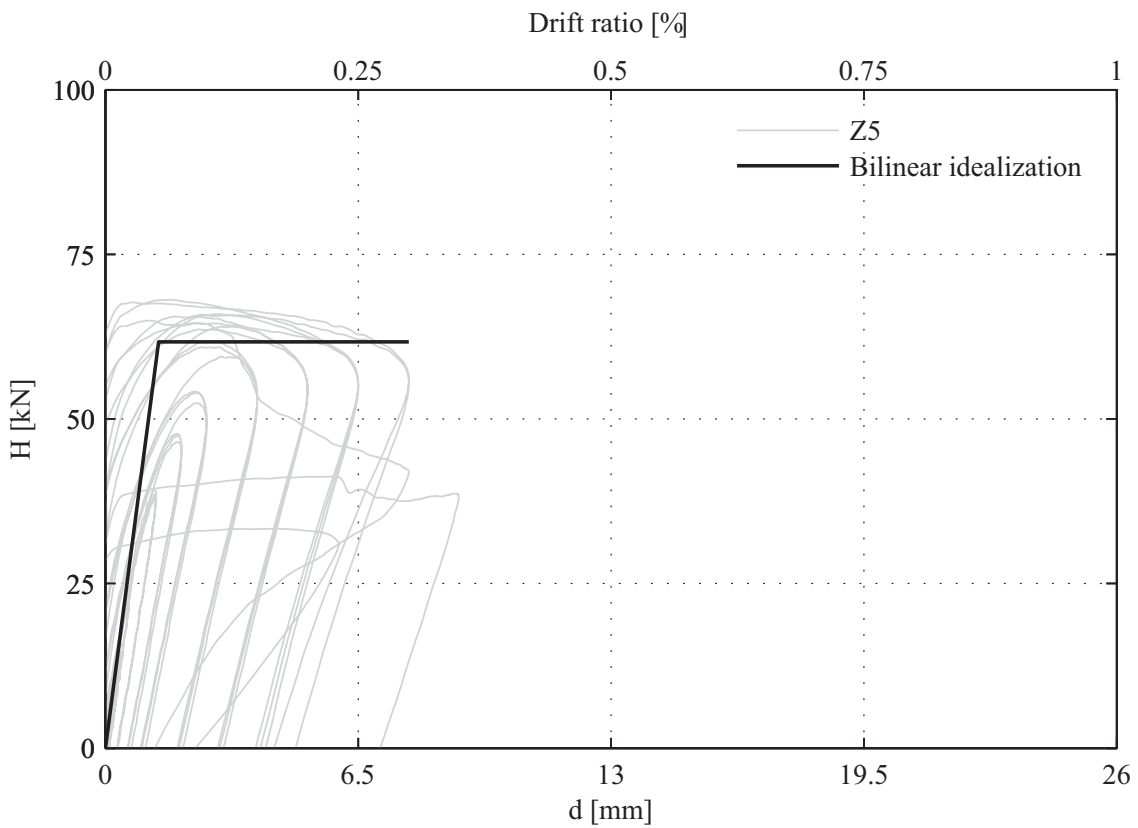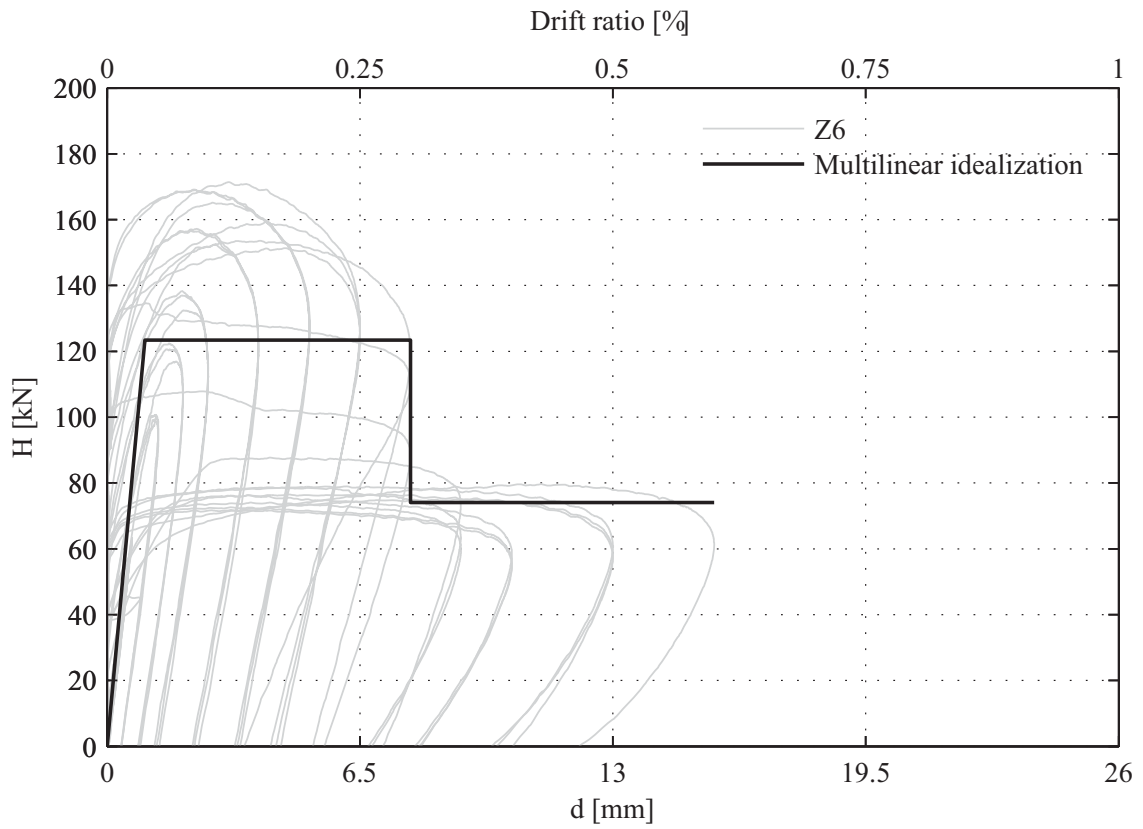**Figure A2-17. Measured vs. idealized horizontal force-displacement hysteretic response: Wall Z5**

190

Figure A2-18. Measured vs. idealized horizontal force-displacement hysteretic response: Wall Z6

Appendix A3 Static cyclic shear tests on I-shaped URM wallettes with a rubber granulate soft layer in the bottom bed joint

This appendix provides for the details of horizontal force-displacement relationships measured during the static-cyclic shear tests on I-shaped URM wallettes with a rubber granulate in the bottom bed joint shown in Figures 5-8 and 5-12. In addition, the details of horizontal force-displacement relationships of the corresponding rectangular URM wallettes with a rubber granulate in the bottom bed joint, depicted in Figure 5-8, are provided.
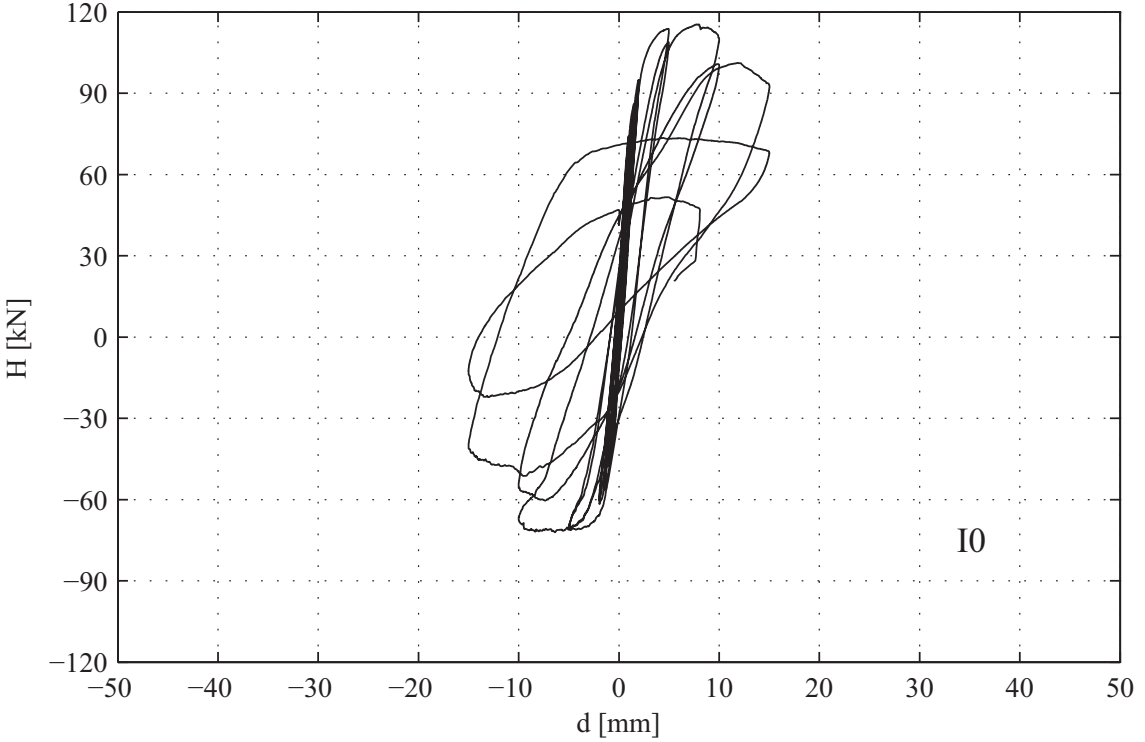

Figure A3-1. Horizontal force-displacement response hysteresis curve: Wallette I0
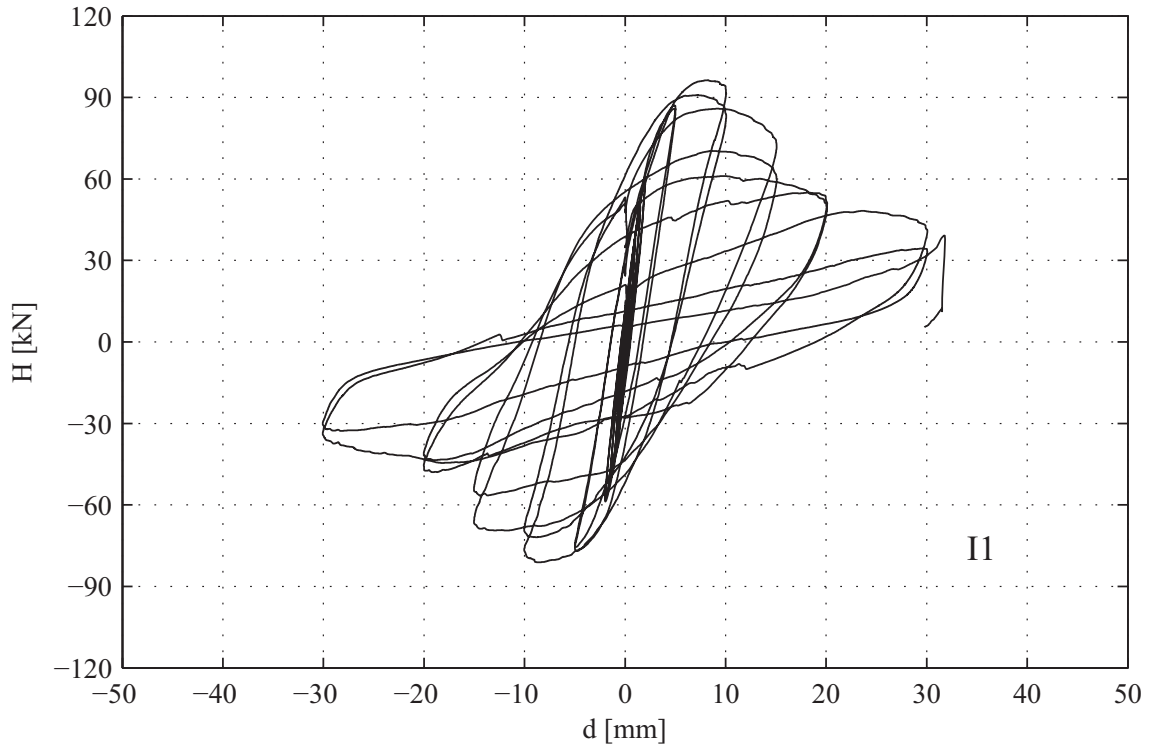
Figure A3-2. Horizontal force-displacement response hysteresis curve: Wallette I1

Figure A3-3. Horizontal force-displacement response hysteresis curve: Wallette I2

Figure A3-4. Horizontal force-displacement response hysteresis curve: Wallette I3

Figure A3-5. Horizontal force-displacement response hysteresis curve: Wallette I4
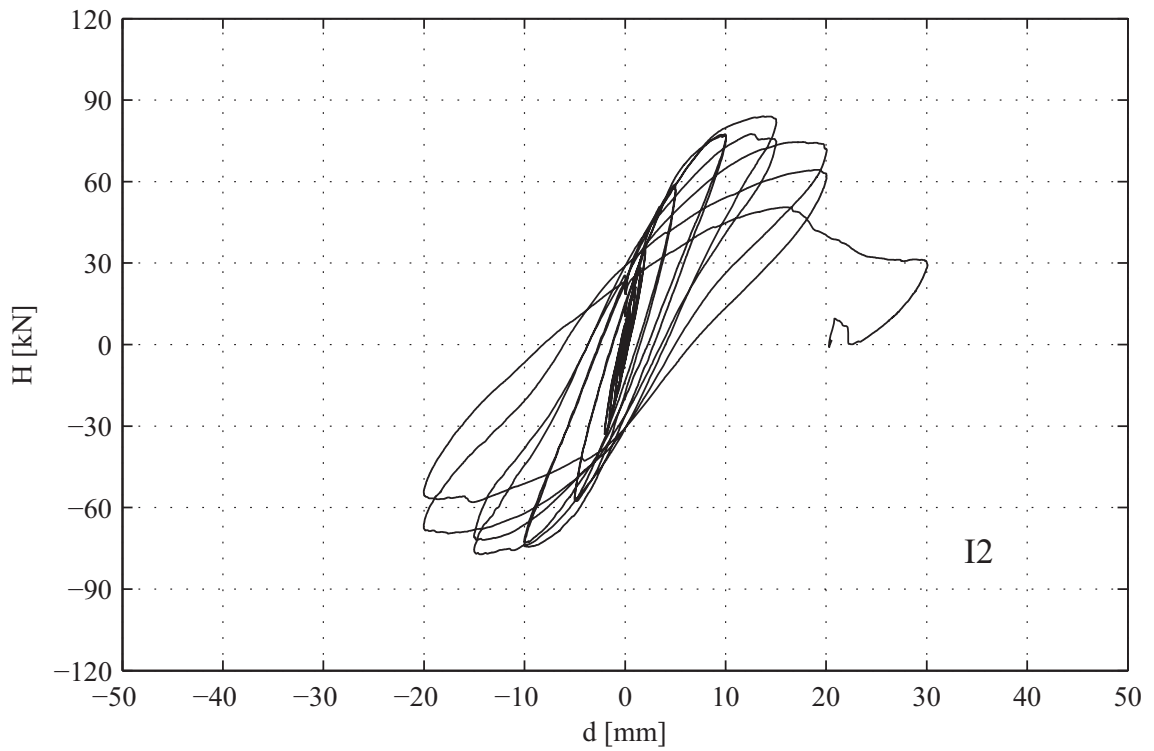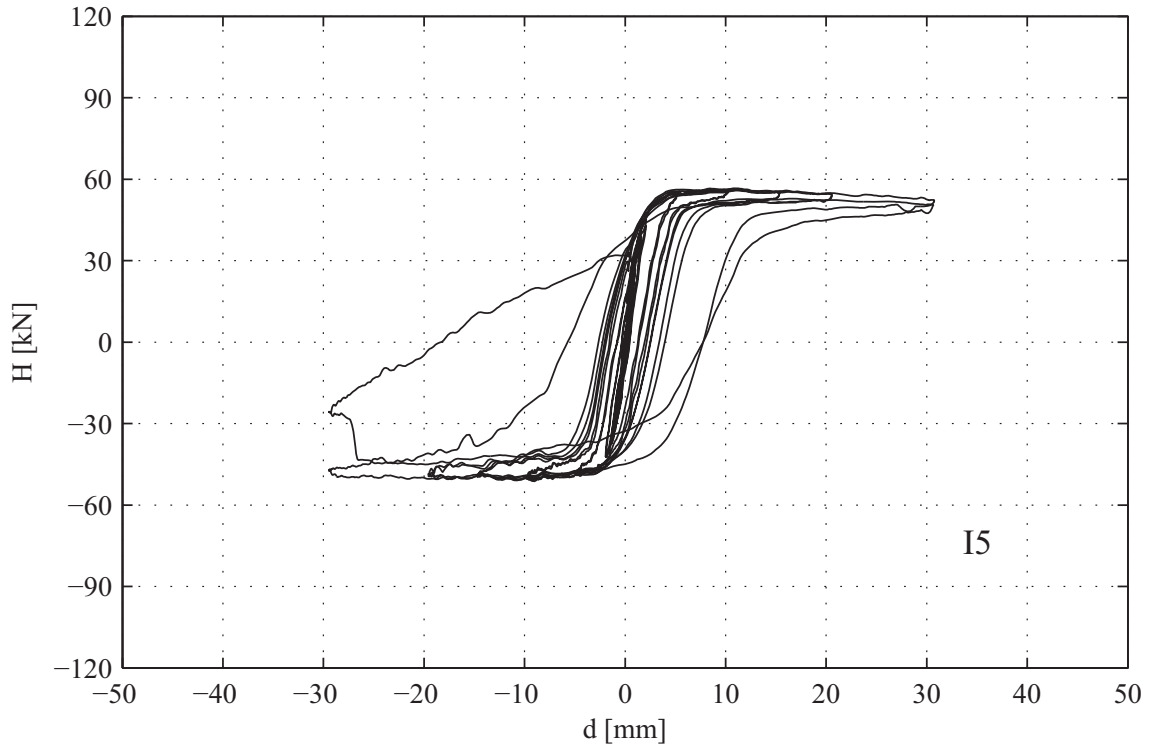
Figure A3-6. Horizontal force-displacement response hysteresis curve: Wallette I5
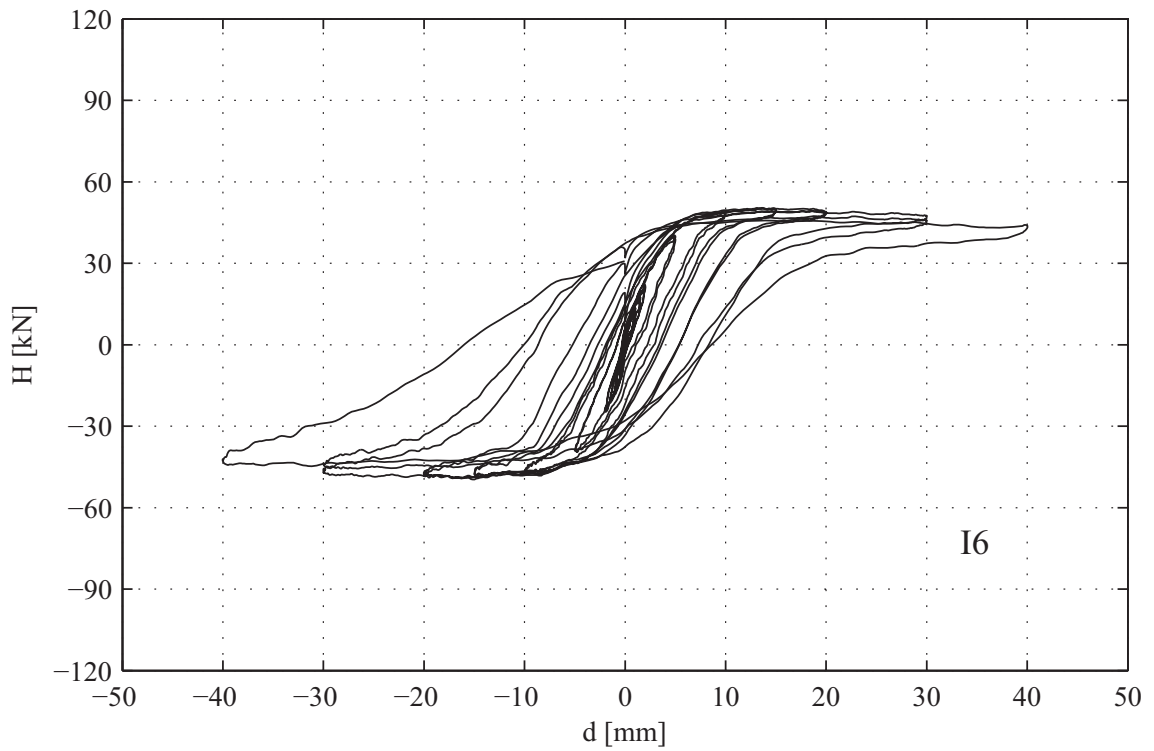
Figure A3-7. Horizontal force-displacement response hysteresis curve: Wallette I6
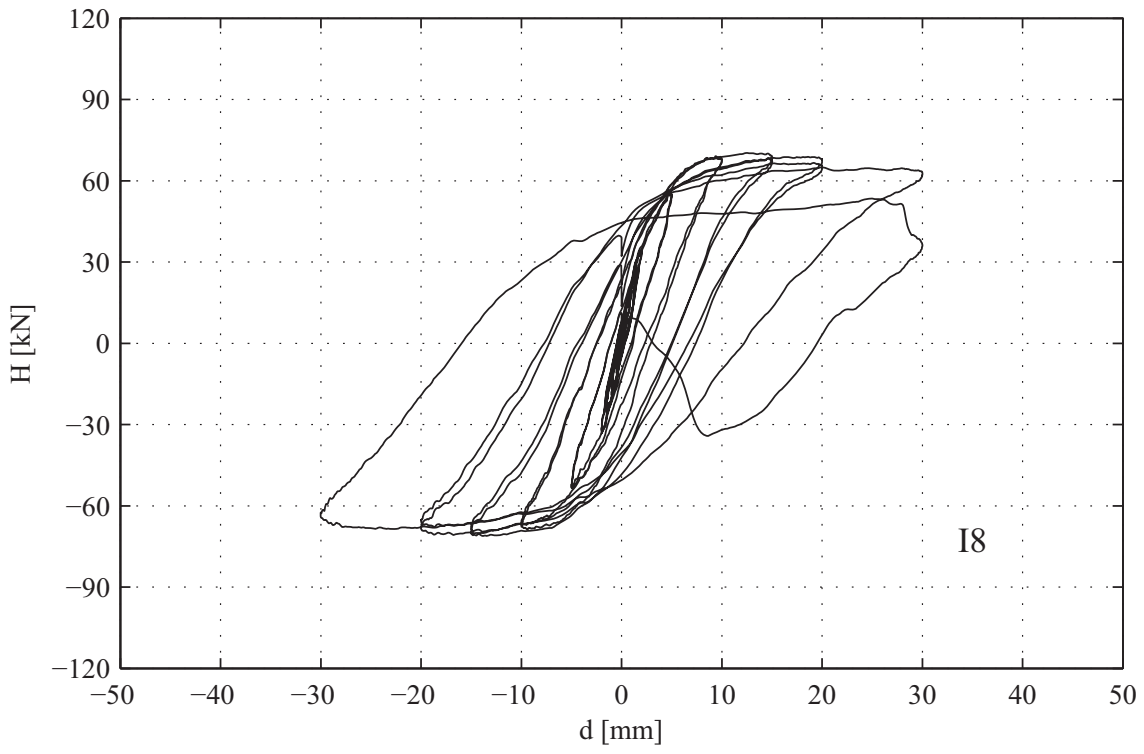
Figure A3-8. Horizontal force-displacement response hysteresis curve: Wallette I8
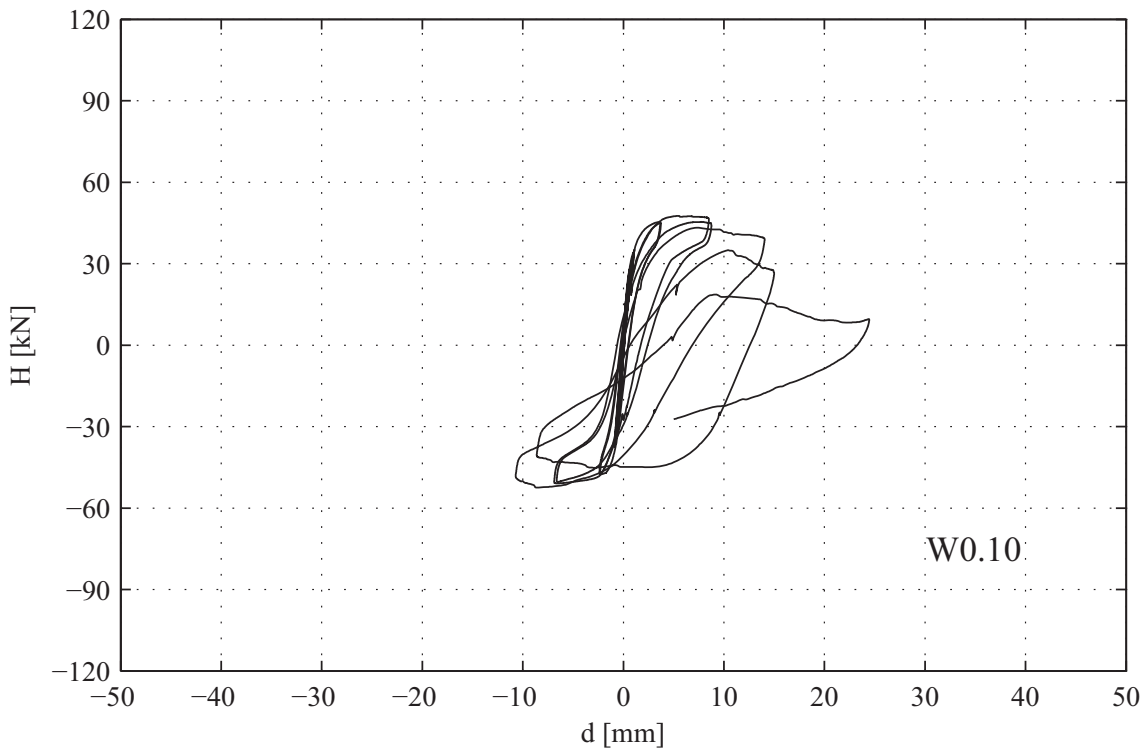
Figure A3-9. Horizontal force-displacement response hysteresis curve: Wallette W0.10

196

Figure A3-10. Horizontal force-displacement response hysteresis curve: Wallette WG3.10

Figure A3-11. Horizontal force-displacement response hysteresis curve: Wallette WG10.10
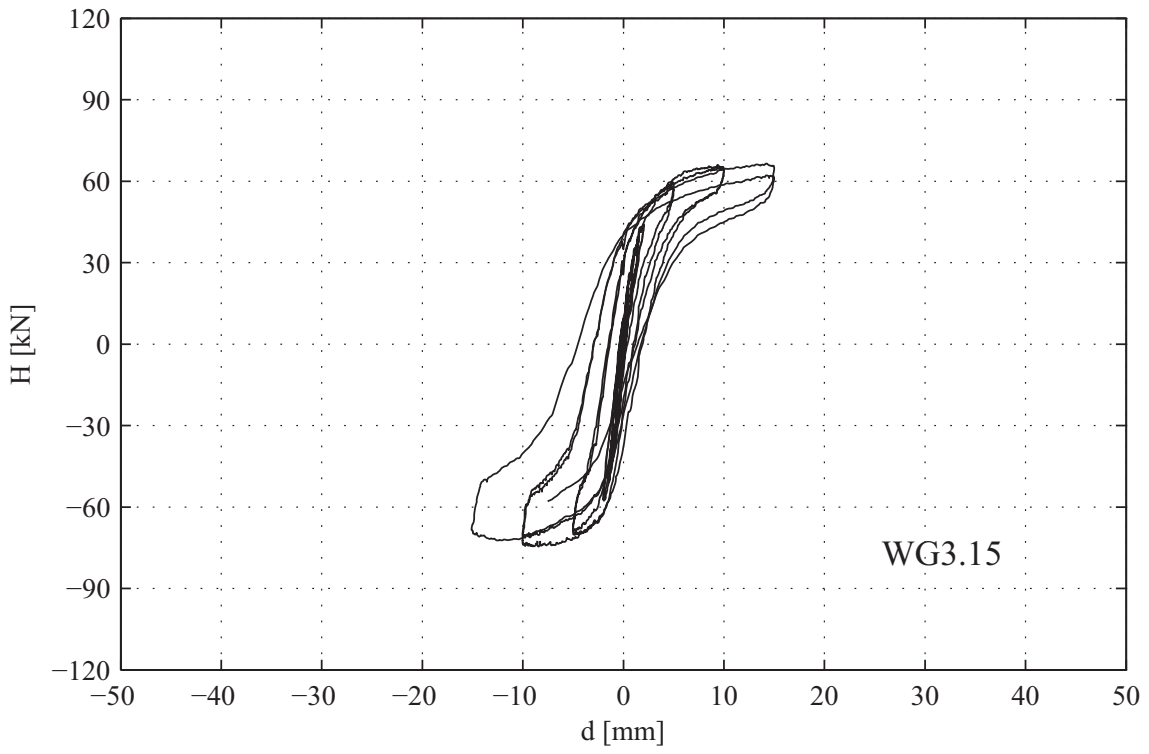
Figure A3-12. Horizontal force-displacement response hysteresis curve: Wallette WG3.15
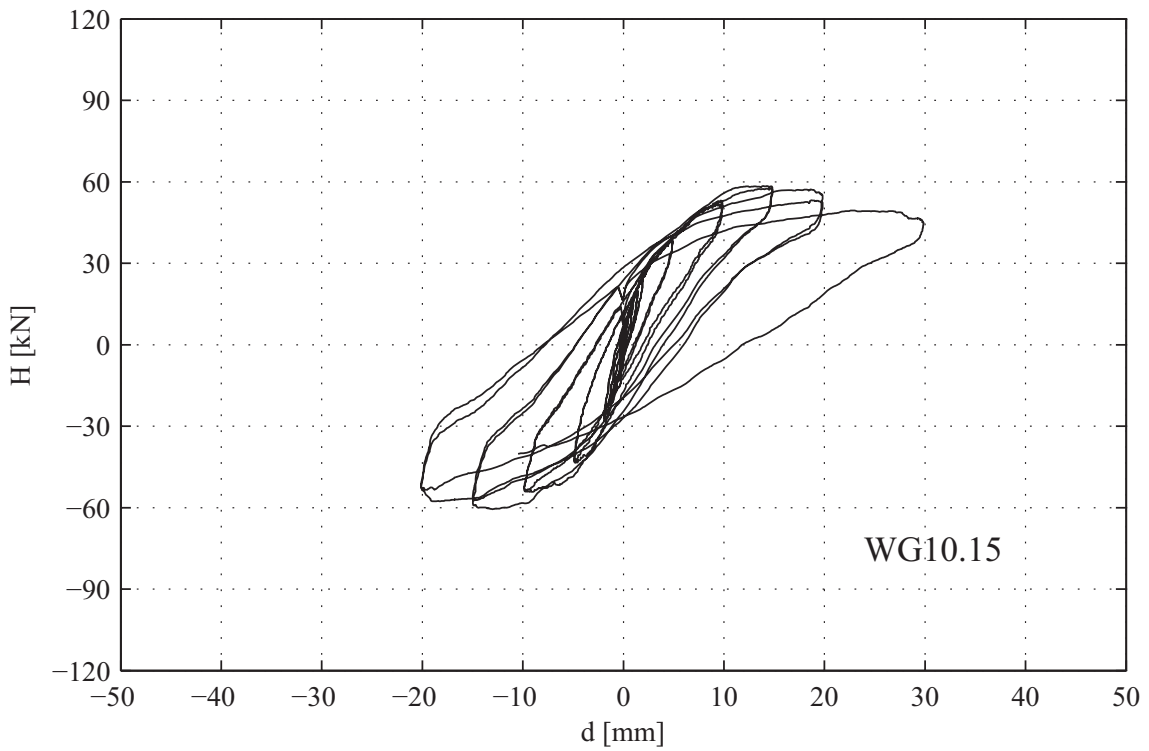
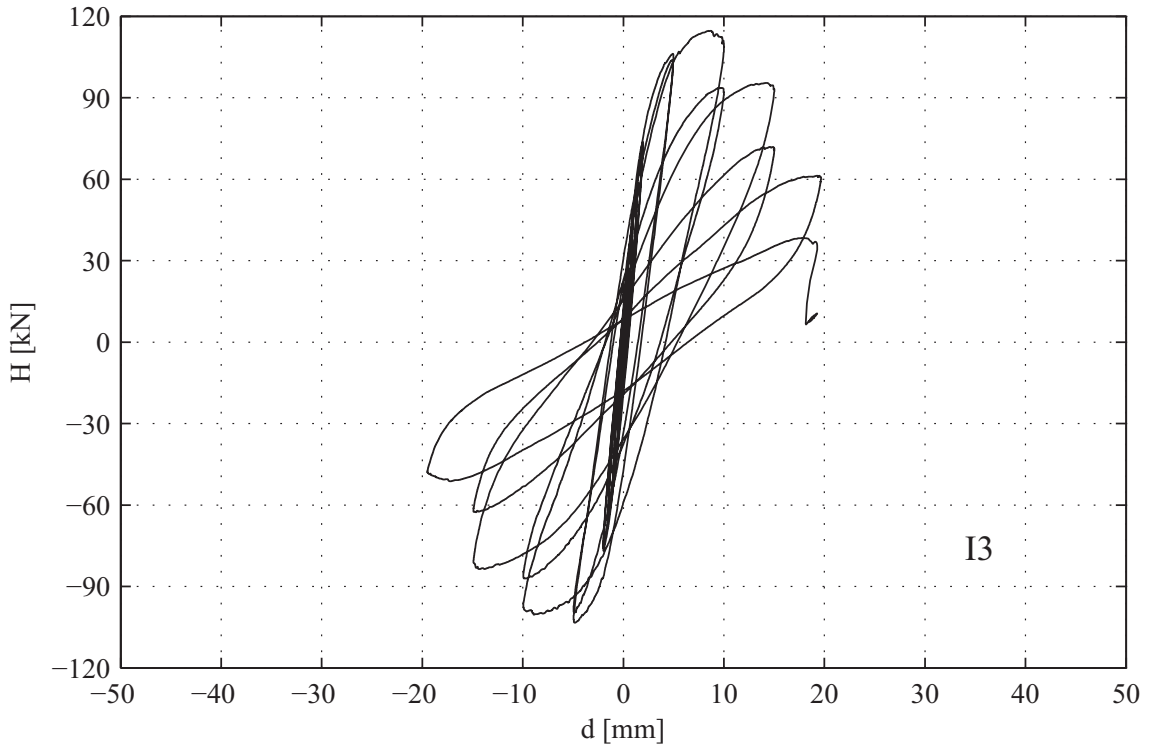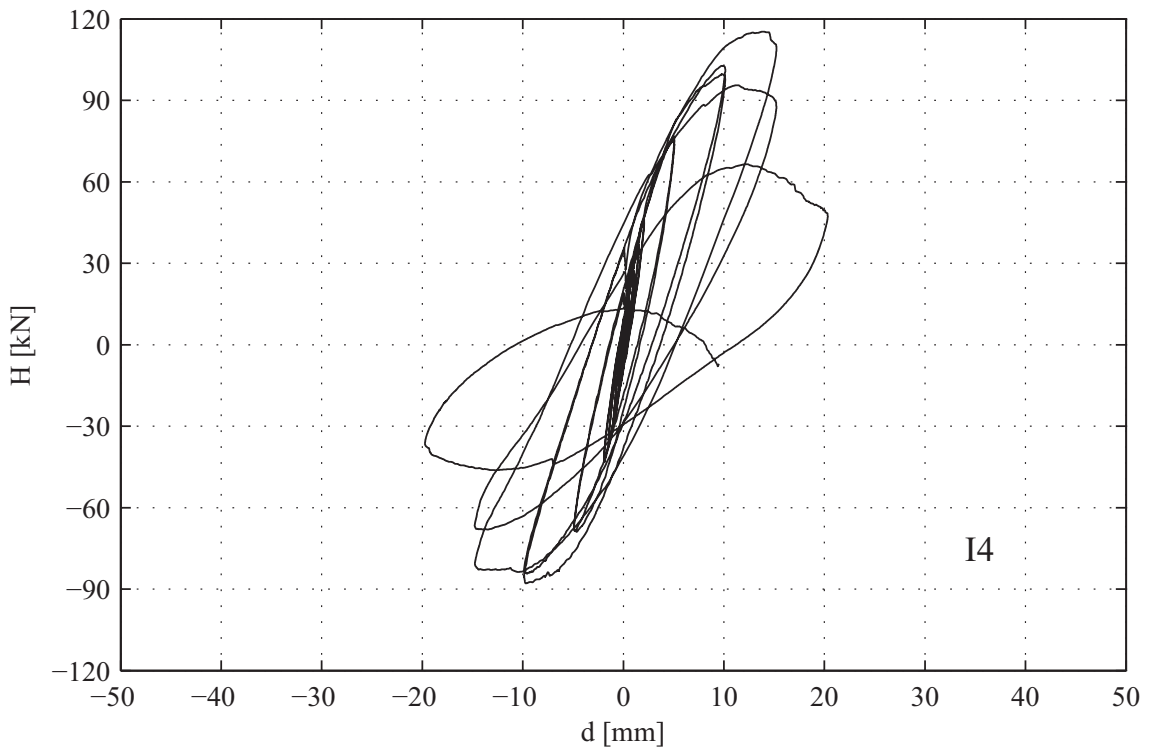**Figure A3-13. Horizontal force-displacement response hysteresis curve: Wallette WG10.15**
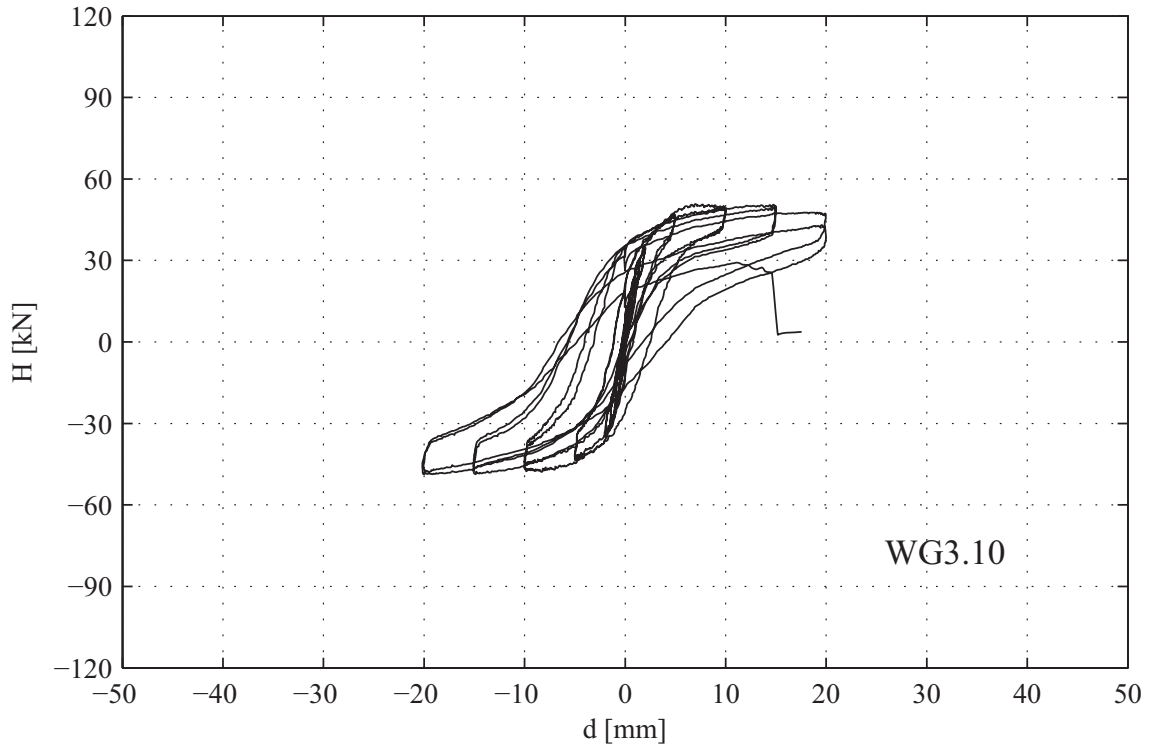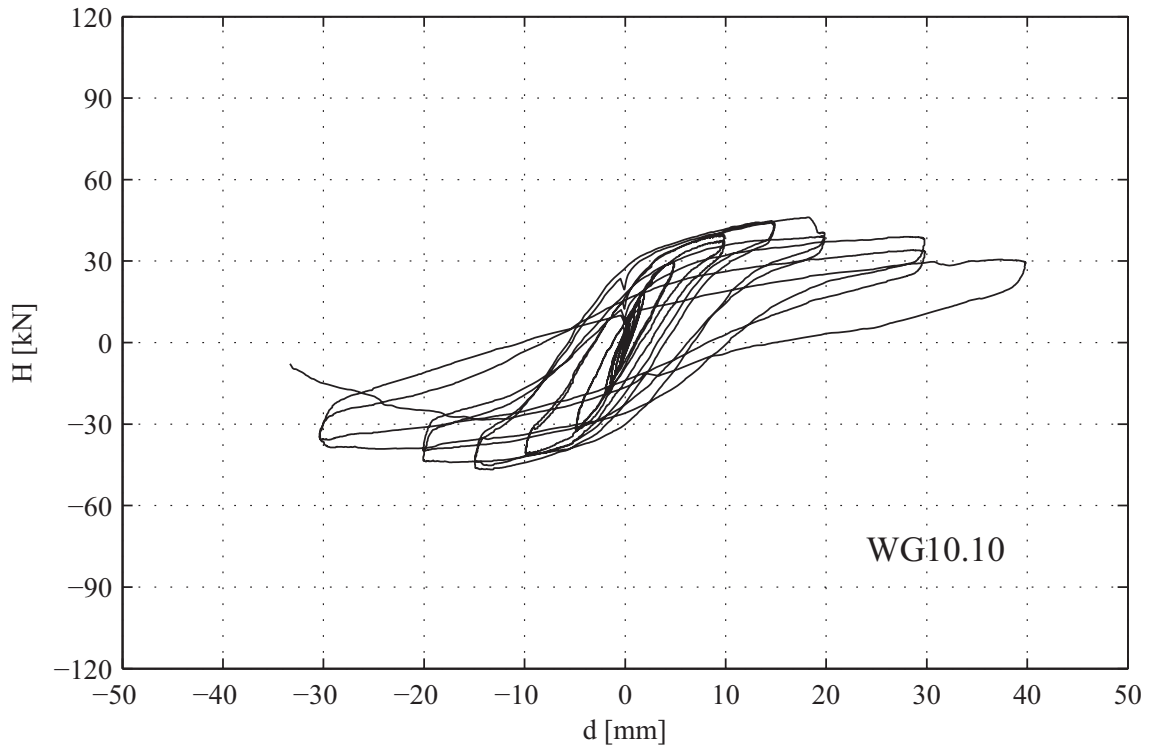
198

List of symbols

A_b gross horizontal cross-section area of the clay block

A_w gross horizontal cross-section area of the wall

COV coefficient of variation

C_l integration constant

c (apparent) cohesion

c_{sl} (apparent) cohesion at the onset of sliding

D demand force

d relative displacement (slip), horizontal displacement

d_{cr} horizontal displacement at the first visible/audible cracking

d^{el} elastic horizontal displacement component

d_{Hmax} target horizontal displacement of the cycle when the maximum horizontal force is developed

d_{max} maximum horizontal displacement

d_{min} minimum horizontal displacement

d_t horizontal displacement at the occurrence of significant loss of wall horizontal force resistance

$d_{t,\ max}$ maximum horizontal displacement at the occurrence of significant loss of wall horizontal force resistance

$d_{t,\ min}$ minimum horizontal displacement at the occurrence of significant loss of wall horizontal force resistance

d_u ultimate horizontal displacement

d^{vp} viscoplastic horizontal displacement component

d_y displacement at the elastic limit (yield displacement)

$\dot{d}$ displacement (loading) speed

$\dot{d}^{el}$ elastic displacement component speed

$\dot{d}^{vp}$	viscoplastic displacement component speed
E_x	masonry elastic modulus
E_{xm}	mean value of masonry elastic modulus
f_x	masonry compressive strength perpendicular to the bed joints
f_{xm}	mean value of masonry compressive strength perpendicular to the bed joints
f_α	uniaxial masonry compressive strength
G_m	masonry shear modulus
G_{ml}	shear modulus of the multi-layer bed joint
G_{sl}	shear modulus of the soft layer
H	shear force, horizontal force resistance, horizontal load
H_{max}	maximum horizontal force resistance
$H_{max,\,calc}$	maximum calculated horizontal force resistance
H_{min}	minimum horizontal force resistance
H_r	remaining horizontal force resistance
H_{sl}	horizontal force resistance at the onset of sliding
H_u	ultimate horizontal force resistance
H_y	ultimate horizontal force resistance
H^*_{max}	maximum horizontal force on backbone curve
$\dot{H}$	horizontal force resistance speed
h_s	position of the zero bending moment with respect to the bottom cross-section of the wall
h_w	height of the wall
h_0	shear span of the wall
I_w	moment of inertia of the wall horizontal cross-section
K_{el}	elastic horizontal stiffness of the wall

K_{eff}	effective horizontal stiffness of the wall
K_0	initial horizontal stiffness of the wall
l	length of the stress field (rectangular masonry wallettes)
l_w	length of the wall
l'	length of the stress field (I-shaped masonry wallettes)
M_{bot}	bending moment acting at bottom of the wall (normal to wall plane)
M_{top}	bending moment acting at top of the wall (normal to the wall plane)
n	number of the performed loading cycles
R	resistance force
R_{sl}	total resistance force to be exceeded in order to initiate sliding
t	time
t_{csl}	thickness of the core soft layer
t_{ml}	thickness of the multi-layer bed joint
t_{sl}	thickness of the soft layer
t_w	thickness of the wall
Δt_{ml}	vertical deformation of the multi-layer bed joint due to the pre-compression load
Δt_{sl}	vertical deformation of the rubber granulate soft layer due to the pre-compression load
V	vertical (pre-compression) load
W_w	resistance moment of the wall horizontal cross section
α	inclination of the stress field, coefficient to account for the influence of the position of the zero bending moment point on the value of masonry flexure and rocking deformation
α'	coefficient to account for the influence of boundary conditions on the value of masonry flexure deformation

γ	shear strain
γ^{el}	elastic shear strain component
γ^{vp}	viscoplastic shear strain component
$\dot{\gamma}$	shear strain speed
$\dot{\gamma}^{el}$	elastic shear strain component speed
$\dot{\gamma}^{vp}$	viscoplastic shear strain component speed
δ	drift ratio
δ_{max}	maximum drift ratio
δ_{min}	minimum drift ratio
δ_u	ultimate drift ratio
δ_0	base drift ratio
ε_x	vertical strain
ε_y	horizontal strain
η^*	model viscosity-related parameter
κ	shear coefficient
λ	function to model the dependence of the viscoplastic strain speed on the state of stress
μ	friction coefficient
μ_{sl}	friction coefficient at the onset of sliding
ξ_{eq}	equivalent viscous damping ratio
σ	normal stress
σ_{bot}	normal stresses at the bottom cross sections of the wall
σ_{pc}	pre-compression stress
σ_{top}	normal stresses at the top cross sections of the wall
σ_2	principal compressive stress

202

τ	shear stress, average shear stress
τ_{bot}	shear stresses at the bottom cross sections of the wall
τ_{sl}	(average) shear stress at the onset of sliding
τ_{top}	shear stresses at the top cross sections of the wall
τ_y	shear stress at the elastic limit (yield shear stress)
$\dot{\tau}$	shear stress speed
Φ	yield function
φ	angle of internal friction
ψ	coefficient to account for the degradation of the multi-layer bed joint elastic response range stiffness with the number of performed loading cycles
ψ_1	coefficient to account for the degradation of the wall elastic response range stiffness with the number of performed loading cycles

References

[1]   Kelly JM. Seismic Isolation. In: Bozorgnia Y, Bertero V, editors. Earthquake Engineering: From Engineering Seismology to Performance-Based Engineering. Boca Raton: CRC Press; 2004.

[2]   Nikolić-Brzev S. Seismic protection of multi-storey brick buildings by seismic isolation technique. PhD thesis. University of Roorkee, India, 1993.

[3]   Vögeli C, Mojsilović N, Stojadinović B. Masonry wallettes with a soft layer bed joint: Behaviour under static-cyclic loading. Eng Struct 2015;86:16-32. doi:10.1016/j.engstruct.2014.12.038.

[4]   Petrović M, Mojsilović N, Stojadinovic B. Use of Soft Layers to Modify the Response of Masonry Structures: State-Of-The-Art Review. In: Proceedings of the 12th North American Masonry Conference, Denver: 2015.

[5]   Mojsilović N, Petrović M, Anglada XR. Masonry elements with multi-layer bed joints: Behaviour under monotonic and static-cyclic shear. Constr Build Mater 2015;100:149-62. doi:10.1016/j.conbuildmat.2015.09.065.

[6]   Joshi R. Striking behavior of structures in Assam earthquakes. In: Proceedings of the 2nd world Conference on Earthquake Engineering, Japan: 1964, p. 2143-58.

[7]   Li L. Base Isolation Measure for Aseismic Buildings in China. In: Proceedings of the 8th World Conference on Earthquake Engineering, San Francisco: 1984.

[8]   Ueda N, Onishi A, Shimizu M. Sanjusangen-do. 2004, accessed 13 November 2017 http://thekyotoproject.org/english/sanjusangen-do/.

[9]   Qamaruddin M, Chandra B, Arya AS. Dynamic testing of brick building models. In: Proceedings of the Institution of Civil Engineers, 1984;77:353-65.

[10]   Lou, Y; Wang, M; Su Z. Research of sliding shock absorbing of multi-storey brick buildings. In: Proceedings of 10th World Conference on Earthquake Engineering, Madrid: 1992, p. 2499-504.

[11]   Nanda RP, Agarwal P, Shrikhande M. Friction base isolation by geotextiles for brick masonry buildings. Geosynthetics International 2010;17:48-55. doi:10.1680/gein.2010.17.1.48.

204

[12] Nanda RP, Agarwal P, Shrikhande M. Suitable friction sliding materials for base isolation of masonry buildings. Shock and Vibration 2012;19:1327-39. doi:10.3233/SAV-2012-0675.

[13] Nanda RP, Shrikhande M, Agarwal P. Low-Cost Base-Isolation System for Seismic Protection of Rural Buildings. Pract Period Struct Des Constr 2016;21. doi:10.1061/(ASCE)SC.1943-5576.0000254.

[14] Sassu M. The Reinforced Cut Wall (RCW): A Low-Cost Base Dissipator for Masonry Buildings, Earthq. Spectra 2006;22(2):533–554. doi:10.1193/1.2193195.

[15] Mostaghel N, Tanbakuchi J. Response of sliding structures to earthquake support motion. Earthq Eng Struct Dyn 1983;11:729-48. doi:10.1002/eqe.4290110603.

[16] Li Z, Rossow EC, Shah SP. Sinusoidal forced vibration of sliding masonry system. ASCE J Struct Eng 1989;115:1741-55.

[17] Jangid RS. Response of pure-friction sliding structures to bi-directional harmonic ground motion. Eng Struct 1997;19:97-104. doi:10.1016/S0141-0296(96)00055-7.

[18] Suter GT, Ibrahim KS. Shear resistance of damp-proof-course materials in brick–mortar joints. In: Proceedings of the 6th Canadian Masonry Symposium, Saskatoon: 1992, p. 119-30.

[19] Zhuge Y, Mills J. The behaviour of masonry walls containing a damp proof course under cyclic loads. In: Proceedings of the 2nd Australasian Structural Engineering Conference, Auckland: 1998, p. 655-661.

[20] Griffith MC, Page A. On the seismic capacity of typical DPC and slip joints in unreinforced masonry buildings. Aust J Struct Eng 1998;1:133-40.

[21] Simundic G, Page AW, Chen Q. The cyclic and long term behaviour of slip joints in load-bearing masonry construction. In: Proceedings of the 12th International Brick/Block Masonry Conference, Madrid: 2000, p. 1409-20.

[22] Trajkovski S, Totoev Y. Shear strength of masonry including damp proof course: experimental determination at different strain rates. In: Proceedings of the 6th International Masonry Symposium, London: 2002, p. 487-492.

[23] Totoev Y, Simundic G. New test for the shear transfer capacity of horizontal slip joints in load-bearing masonry. In: Proceedings of the 10th Canadian Masonry Symposium, Banff: 2005, p. 863–872.

[24] Mojsilović N. Masonry elements with damp-proof course membrane: Assessment of shear strength parameters. Constr Build Mater 2012;35:1002-12. doi:10.1016/j.conbuildmat.2012.04.033.

[25] Mojsilović N, Simundic G, Page AW. Static-cyclic shear tests on masonry triplets with a damp-proof course membrane. In: Proceedings of the 12th Canadian Masonry Symposium, Vancouver: 2013.

[26] Mojsilović N, Simundic G, Page AW. Static-cyclic shear tests on masonry wallettes with a damp-proof course membrane. ETH Zurich, Institute of Structural Enginnering, IBK Report Nr. 319, Zurich: 2009, 87 pp.

[27] Mojsilović N, Simundic G, Page A. Masonry wallettes with damp-proof course membrane subjected to cyclic shear: An experimental study. Constr Build Mater 2010;24:2135-44. doi:10.1016/j.conbuildmat.2010.04.046.

[28] Mojsilović N, Stojadinović B, Barandun A, Vögeli C. Seismic behaviour of masonry walls with soft-layer wall bearings. In: Proceedings of the 5th International Conference on Structural Engineering, Mechanics and Computation, Cape Town: 2013, p. 1865-1870.

[29] Petrović M, Anglada XR, Mojsilović N. Shear tests on masonry elements with soft layer in bed joint. In: Proceedings of the 12th North American Masonry Conference, Denver: 2015.

[30] EN 1015-11. Methods of test for mortar for masonry - Part 11: Determination of flexural and compressive strength of hardened mortar. European Committee for Standardization (CEN), Brussels; 1999.

[31] EN 772-1. Methods of test for masonry units - Part 1: Determination of compressive strength. European Committee for Standardization (CEN), Brussels; 2000.

[32] EN 1052-3: Methods of test for masonry - Part 3: Determination of initial shear strength. European Committee for Standardization (CEN), Brussels; 2007.

206

[33] Jukes P, Riddington J. The failure of brick triplet test specimens. Mason Int 2001;15:30-3.

[34] Mojsilović N, Petrović M, Büchler R. Compressive strength of masonry with soft layers in bed joint. In: Proceedings of the 5th International Conference on Structural Engineering, Mechanics and Computation, Cape Town: 2016, p. 1691-701.

[35] EN 1052-1. Methods of test for masonry - Part 1: Determination of compressive strength. European Committee for Standardization (CEN), Brussels; 2002.

[36] Mojsilović N, Salmanpour AH. Masonry walls subjected to in-plane cyclic loading: application of digital image correlation for deformation field measurement. International Journal of Masonry Research and Innovation 2016;1:165-87. doi:10.1504/IJMRI.2016.077473.

[37] Salmanpour AH, Mojsilović N. Application of Digital Image Correlation for strain measurements of large masonry walls. In: Proceedings of the 5th Asia Pacific Congress on Computational Mechanics, Singapore: 2013.

[38] http://correlatedsolutions.com/vic-2d

[39] SIA 266. Mauerwerk. Schweizerischer Ingenieur- und Architektenverein (SIA), Zurich; 2015 [in German].

[40] Petrović M, Mojsilović N, Stojadinović B. Masonry walls with a multi-layer bottom bed joint: Behavior under static-cyclic shear. In: Proceedings of the 11th fib International PhD Symposium in Civil Engineering, Tokyo: 2016.

[41] Petrović M, Mojsilović N, Stojadinović B. Masonry walls with a multi-layer bed joint subjected to in-plane cyclic loading: An experimental investigation. Eng Struct 2017;143:189–203. doi:10.1016/j.engstruct.2017.04.025.

[42] Salmanpour AH, Mojsilović N. Simulation of boundary conditions for testing of masonry shear walls. In: Proceedings of the International Conference of Computational Methods in Sciences and Engineering, Athens: 2015. doi.org/10.1063/1.4938935

[43] Chopra AK. Dynamics of structures: theory and applications to earthquake engineering. New Jersey: Prentice Hall; 2012.

[44] Salmanpour AH, Mojsilović N, Schwartz J. Displacement capacity of contemporary unreinforced masonry walls: An experimental study. Eng Struct 2015;89:1-16. doi:10.1016/j.engstruct.2015.01.052.

[45] Salmanpour AH. Displacement capacity of structural masonry. PhD thesis. ETH Zurich, Switzerland, 2017. doi.org/10.3929/ethz-b-000172566

[46] Tomažević M. Earthquake-resistant design of masonry buildings. London: Imperial College Press; 1999.

[47] FEMA 356. Prestandard and commentary for the seismic rehabilitation of buildings. Federal Emergency Management Agency (FEMA), Washington; 2000.

[48] Assessment and improvement of the structural performance of the buildings in earthquakes. New Zealand Society for Earthquake Engineering (NZSEE), Wellington; 2006.

[49] Oberender PW, Puzrin AM. Observation-guided constitutive modelling for creeping landslides. Géotechnique 2016;66:232-47. doi:10.1680/jgeot.15.LM.003.

[50] de Souza Neto EA, Perić D, Owen DRJ. Computational methods for plasticity: theory and applications. Wiley; 2008.

[51] Paquette J, Bruneau M. Pseudo-dynamic testing of unreinforced masonry building with flexible diaphragm. ASCE J Struct Eng 2003;129:708-716. doi:10.1061/(ASCE)0733- 9445(2003)129:6(708).

[52] Moon FL, Yi T, Leon RT, Kahn LF. Recommendations for seismic evaluation and retrofit of low-rise URM structures. ASCE J Struct Eng 2006;132(5):663-672. doi:10.1061/(ASCE)0733-9445(2006)132:5(663).

[53] Yi T, Moon FL, Leon RT, Kahn LF. Lateral load tests on a two-story unreinforced masonry building. J Struct Eng 2006;132:643-52. doi:10.1061/(ASCE)0733-9445(2006)132:5(643).

[54] Russell AP, Elwood KJ, Ingham JM. Lateral Force–Displacement Response of Unreinforced Masonry Walls with Flanges. ASCE J Struct Eng 2014;140:4013087. doi:10.1061/(ASCE)ST.1943-541X.0000863.

[55] Khanmohammadi M, Behnam H, Marefat MS. Seismic behavior prediction of flanged unreinforced masonry (FURM) walls. J Earthq Eng 2014;18:759-84. doi:10.1080/13632469.2014.897273.

[56] Yi T, Moon FL, Leon RT, Kahn LF. Flange effects on the nonlinear behavior of URM piers. Mason Soc J 2008;26:31-42.

[57] Petrović M, Stojadinović B, Mojsilović N. Static-cyclic tests on I-shaped masonry wallettes with soft-layer bed joint. In: Proceedings of the 16th International Brick/Block Masonry Conference, Padova: 2016.

[58] Petrović M, Stojadinović B, Mojsilović N. I-Shaped unreinforced masonry wallettes with a soft-layer bed joint: Behavior under static-cyclic shear. ASCE J Struct Eng 2017;143(11):4017154. doi:10.1061/(ASCE)ST.1943-541X.0001884.

[59] ASCI/SEI 41-13. Seismic Evaluation and Retrofit of Existing Buildings. American Society of Civil Engineers (ASCE), Reston; 2014.

[60] Iyer H. The effects of shear deformation in rectangular and wide flange sections. Master thesis. Faculty of the Virginia Polytechnic Institute and State University, Blacksburg, VA, 2015. hdl.handle.net/10919/31421

[61] Eurocode 8. Design of structures for earthquake resistance - Part 3: Assessment and retrofitting of buildings. European Committee for Standardization (CEN), Brussels; 2004.

[62] National annex - Eurocode 8: Design of structures for earthquake resistance -Part 1: General rules, seismic actions and rules for buildings. DIN EN 1998-1/NA:2011- 01. National annex of Germany, Berlin; 2011.

[63] Norme tecniche per le costruzioni. Ministero delle Infrastrutture e dei Trasporti (MIT), Roma; 2008 [in Italian].

[64] Muttoni A, Schwartz J, Thürlimann B. Design of concrete structures with stress fields. Basel: Birkhäuser; 1997.

[65] Mojsilović N. Strength of masonry subjected to in-plane loading: A contribution. Int J Solids Struct 2011;48:865-73. doi:10.1016/j.ijsolstr.2010.11.019.

[66]   Salmanpour AH, Bitterli S, Mojsilović N. Compression tests on masonry wallettes with inclined bed joints. In: Proceedings of the 12th North American Masonry Conference, Denver: 2015.

[67]   Priestley M, Calvi GM, Kowalsky MJ. Displacement-based seismic design of structures. Pavia: IUSS Press; 2007.